IntechOpen

Tectonics

Problems of Regional Settings

Edited by Evgenii V. Sharkov

TECTONICS - PROBLEMS OF REGIONAL SETTINGS

Edited by **Evgenii V. Sharkov**

Tectonics - Problems of Regional Settings
http://dx.doi.org/10.5772/intechopen.68250
Edited by Evgenii V. Sharkov

Contributors

Mingliang Liang, Zongxiu Wang, Girish Chandra Kothyari, Ap Singh, Sneha Mishra, Raj Sunil Kandregula, Indu Chaudhary, Gaurav D Chauhan, Masaki Kanao, Bizhu He, Xiufu Qiao, Haibin Li, Dechen Su, Inna Derbeko, Boris Dyachkov, Marina Mizernaya, Yasuto Itoh, Guadalupe Arzadun, Renata Tomezzoli, Hugo Tickyj, Ernesto Cristallini, Leandro Gallo

Notice

First published in London, United Kingdom, 2018 by IntechOpen
eBook (PDF) Published by IntechOpen, 2019
IntechOpen is the global imprint of INTECHOPEN LIMITED, registered in England and Wales, registration number: 11086078, The Shard, 25th floor, 32 London Bridge Street
London, SE19SG – United Kingdom
Printed in Croatia

British Library Cataloguing-in-Publication Data
A catalogue record for this book is available from the British Library

Additional hard and PDF copies can be obtained from orders@intechopen.com

Tectonics - Problems of Regional Settings
Edited by Evgenii V. Sharkov

p. cm.

Print ISBN 978-1-78923-136-6

Online ISBN 978-1-78923-137-3

eBook (PDF) ISBN 978-1-83881-296-6

Meet the editor

Professor Evgenii Vitalievich Sharkov was born on October 25, 1937, in Leningrad (Saint Petersburg), USSR. He received his PhD degree from the Leningrad State University and DSc degree from the USSR Academy of Sciences (Moscow). Currently, he is working at the Institute of Geology of Ore Deposits, Petrography, Mineralogy, and Geochemistry (IGEM), Russian Academy of Sciences (Moscow), and is a lecturer at the Russian State Geological Prospecting University (RSGPU-MGRI), Moscow. He conducts research in igneous petrology and tectonics and has published about 620 papers in the field of Precambrian geology and petrology, layered intrusions, LIPs, evolution of tectonomagmatic processes throughout the Earth's history, and so on. He is an academician of the Russian Academy of Natural Sciences, a fellow of the Russian Petrographic Committee, and a member of the Russian Mineralogical Society, Geochemical Society (GS), and IAVCEI.

Contents

Preface XI

Chapter 1 **Seismological Implication to the Tectonic Evolution of the Lützow-Holm Bay Region (East Antarctica) 1**
Masaki Kanao and Vladimir D. Suvorov

Chapter 2 **Tectonic Insight in the Southwest Gondwana Boundary Based on Anisotropy of Magnetic Susceptibility 13**
Arzadún Guadalupe, Tomezzoli Renata Nela, Tickyj Hugo, Cristallini Ernesto Osvaldo and Gallo Leandro Cesar

Chapter 3 **Bureya-Jiamusi Superterrane: Tectonic and Geodynamic Processes in Late Mesozoic - Cenozoic 33**
Derbeko Inna

Chapter 4 **A Discussion on the Detachment Structural Deformation and Its Influence on Pore Structure Evolution in Shale on the Western of the Xuefeng Mountain, South China 47**
Mingliang Liang, Zongxiu Wang, Linyan Zhang, Huijun Li, Wanli Gao and Chunlin Li

Chapter 5 **Tectonics and Metallogeny of East Kazakhstan 67**
Boris Dyachkov, Marina Mizernaya, Oksana Kuzmina, Natalia Zimanovskaya and Tatiana Oitseva

Chapter 6 **Post-Opening Deformation History of the Japan Sea Back-Arc Basin: Tectonic Processes on an Active Margin Governed by the Mode of Plate Convergence 85**
Yasuto Itoh

Chapter 7 **Soft Sediment Deformation Structures Triggered by the Earthquakes: Response to the High Frequent Tectonic Events during the Main Tectonic Movements 103**
Bizhu He, Xiufu Qiao, Haibing Li and Dechen Su

Chapter 8 **Evolution of Drainage in Response to Brittle - Ductile Dynamics and Surface Processes in Kachchh Rift Basin, Western India 131**
Girish Ch Kothyari, Ajay P. Singh, Sneha Mishra, Raj Sunil Kandregula, Indu Chaudhary and Gaurav Chauhan

Preface

This book is devoted to different aspects of tectonic researches. New results and interpretations are presented here for diverse tectonic settings. Most of the chapters include up-to-date materials of detailed geological investigations, often combined with geophysical data, which can help understand more clearly the essence of mechanisms of different tectonic processes.

One half of the chapters are devoted to the evolution of tectonic processes of different regions. The chapter of M. Kanao and V.D. Suvorov "Seismological Implication to the Tectonic Evolution of the Lützow-Holm Bay Region, East Antarctica" dedicates to the problem formation of lithospheric mantle anisotropy considered with upwelling of the mantle plume associated with Gondwana breakup using teleseismic events that demonstrated heterogeneous structure in the studied region. A close examination of the problems is discussed in the chapter by G. Arzadún et al. "Tectonic Insight in the Southwest Gondwana Boundary Based on Anisotropy of Magnetic Susceptibility," however, from another position. Problems of tectonic locality of Bureja-Jziamusy superterrane (Mongol-Okhotsk orogenic belt) in the late Mesozoic-Cenozoic Era are covered in the chapter of I. Derbeko and tectonics and metallogeny of East Kazakhstan in the chapter of B. Dyachkov and his colleagues.

The second half of the chapters have to deal with different aspects of tectonic events. The chapter of Mingliang Liang represents a discussion on the influence of the detachment structural deformation on pore structure evolution in shale on the western of the Xuefeng Mountain, South China. Girish Ch Kothyari with his coauthors dealt with the problem of evolution of drainage in response to brittle-ductile dynamics and surface processes in Kachchh Rift Basin, Western India, and shows that the faults there are well connected at a deeper level and generated negative flower structures, significantly controlling the surface fluvial dynamics. According to Bizhu He et al., soft sediment deformation structures, triggered by the modern earthquakes observed in China, are the very likely response to the high-frequent tectonic events during the main tectonic movements. Prof. Yasuto Itoh covered the problem of the post-opening deformation history of the Japan Sea back-arc basin and shows that tectonic processes on an active margin are governed by the mode of plate convergence.

Prof. Evgenii V. Sharkov
Institute Geology of Ore Deposits, Petrology, Mineralogy and Geochemistry
Moscow, Russia

Chapter 1

Seismological Implication to the Tectonic Evolution of the Lützow-Holm Bay Region (East Antarctica)

Masaki Kanao and Vladimir D. Suvorov

Additional information is available at the end of the chapter

http://dx.doi.org/10.5772/intechopen.71972

Abstract

Passive source studies using teleseismic events demonstrated heterogeneous structure in the Lützow-Holm Bay (LHB) region, East Antarctica. Depth variations of upper mantle discontinuities (410 and 660 km) were derived from long-period receiver functions by local array stations. Shallow depths in topography of upper mantle discontinuity were cleared beneath the continental ice sheet back azimuth. These results reflect a paleo-upwelling of the mantle plume associated with Gondwana breakup. Lithospheric mantle anisotropy derived by shear waves' (SKS) splitting anticipated a relationship between "fossil" anisotropy and the past tectonics in NE-SW orientation. Origin of mantle anisotropy was assumed to be caused by supercontinent assembly rather than present asthenospheric flow parallel with absolute plate motion. The deep seismic surveys by active sources, moreover, were carried out over continental ice sheet and provided clear information on crust-mantle boundary, together with inner lithospheric mantle reflections. The extracted lithospheric cross-sectional images by seismic reflection analyses implied tectonic influence of compressive stress during Pan-African age.

Keywords: upper mantle structure, Lützow-Holm Bay region, East Antarctica, Gondwana supercontinent, tectonic evolution

1. Introduction

East Antarctic continent consists of several geological terrains as resultant of amalgamation and breakup of Rodinia and Gondwana [1, 2]. In wide areas of Western Enderby Land-Eastern Dronning Maud Land, inside the East Antarctica, several geological complexes are adjacent to each other from East to West: the Napier (Archaean), the Rayner (late Proterozoic), the Lützow-Holm (early Paleozoic), and the Yamato-Belgica (early Paleozoic) (**Figure 1**) [3–5]. Combined with other Gondwana component continents such as Africa, India, and Australia,

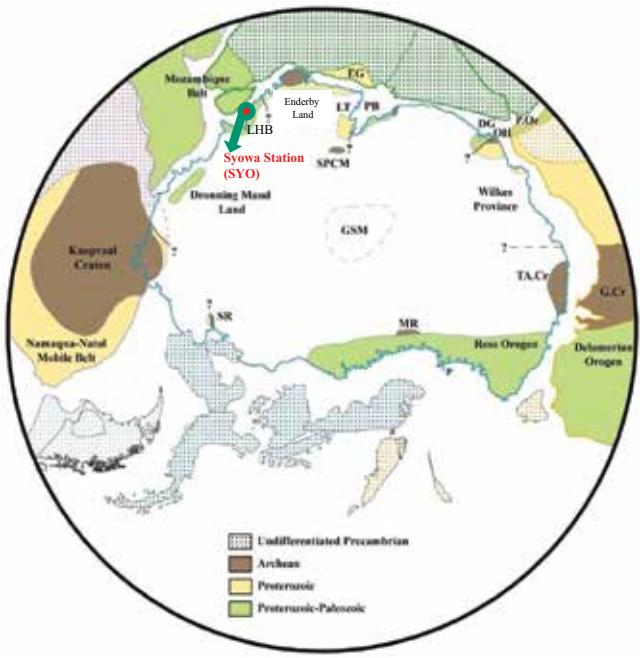

Figure 1. Gondwana reconstruction at 480 Ma, centered on East Antarctica (modified after [5]) showing the geologic ages of major exposed coastal outcrops [2]. The areas corresponding "undifferentiated Precambrian" terrains belonging to each continental blocks of Gondwanaland (Australia, Africa, South America, and Antarctica) are distinguished by different colors (yellow dot, green dot, brown dot, and light-blue dot), respectively. Abbreviations are as follows: SYO, Syowa Station; LHB, Lützow-Holm Bay; SR, Shackleton range; SPCM, Southern Prince Charles Mountains; LT, Lambert Terrane; EG, Eastern Ghats; PB, Prydz Bay; DG, Denman Glacier; OH, Obruchev Hills; P. Or, Pinjarra Orogeny; TA. Cr, Terre Adélie Craton; G. Cr, Gawler Craton; MR, Miller Range; GSM, Gamburtsev Subglacial Mountains.

the crust and lithospheric mantle architecture with relevant tectonic history of East Antarctica provide evidence of amalgamation and separation of the past supercontinents [6, 7]. The Lützow-Holm Bay (LHB) region, where the Japanese Syowa Station (SYO, 69S, 39E) is located, has been experiencing regional metamorphic events in early Paleozoic [8]. The metamorphic grade increases from amphibolite facies in eastern LHB to granulite facies in the western. During the Pan-African metamorphism, LHB was deformed under compression stress perpendicular to the thermal axis [9].

Seismological evidence with respect to the structure and tectonics of the upper mantle beneath LHB has been derived in the last few decades by both the computer modeling and field observations by the Japanese Antarctic Research Expedition (JARE). Teleseismic data detected at seismic stations in LHB have sufficient signal-to-noise quality for various kinds of analyses so as to clarify local seismicity, heterogeneities of the lithospheric structure, as well as deep interiors of the Earth [10–13]. Several studies had aimed at deriving static structure, tectonics, and dynamics within the crust and mantle depths, associated with geological evolution of the region [14, 15]. In this chapter, by taking into account the tectonic evolution around the Lützow-Holm Bay (LHB) region, passive and active seismic source studies were reviewed in

order to provide comprehensive understanding in formation of the upper mantle structure and dynamics beneath LHB, associated with evolving process of supercontinents in southern hemisphere during the Earth history.

2. Seismic investigations of the upper mantle

Seismological investigations in LHB demonstrated sufficient images of the structure and dynamics in the upper mantle underneath the Antarctic continent. The investigations by using passive seismic sources such as teleseismic events occurring over the globe had demonstrated strong heterogeneity existing in the upper mantle depths. Depth variations of the upper mantle discontinuities (410 and 660 km depths, respectively) were derived from long-period receiver function analysis (0.2 Hz low-pass filtered), which indicated shallow depths in the 660 km seismic discontinuity beneath continental back azimuths in LHB (**Figure 2**) [16]. The depth distributions of P-S conversion points were also revealed in particular for the 660 km discontinuity. The shallow depths in topography for the 660 km discontinuity were identified beneath the continental azimuths over the ice sheet. These results could provide an evidence of upwelling flow associated with mantle plume in terms of Gondwana breakup

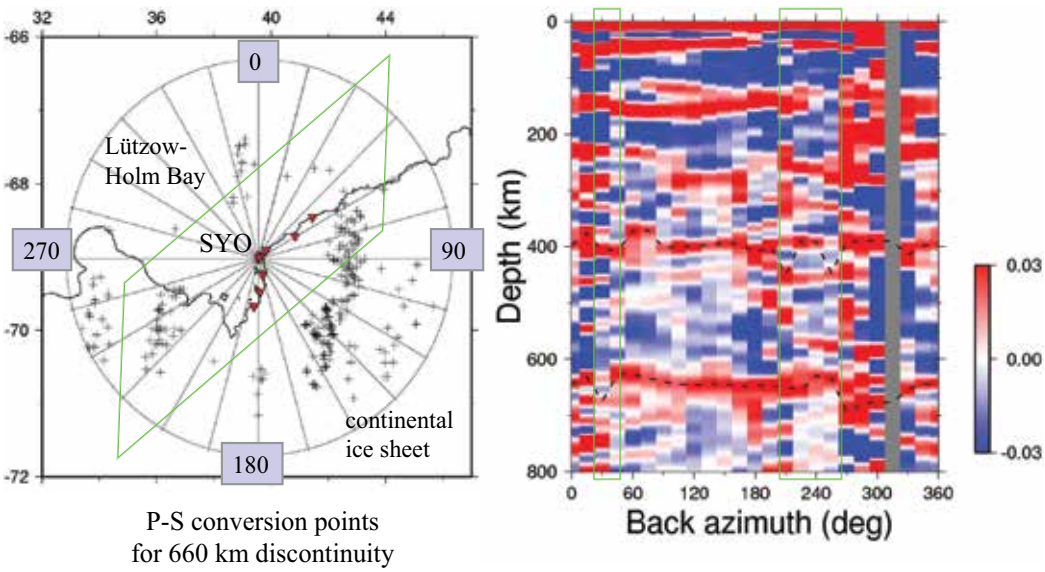

Figure 2. Back azimuth distribution of the depth variation in the upper mantle seismic discontinuities by receiver function analyses of broadband seismic data in LHB (modified after [16]). (Left) Location of the strong heterogeneous azimuths in LHB. The area for strong depth variations in upper mantle discontinuities is represented by the light-green open squares, which are almost parallel with the coastal line. Symbolic notation for the P-S conversion points at the mantle discontinuities around 660 km in depth. (Right) Color images represent the smoothed amplitudes of the long-period receiver functions. Two dashed lines are traced for the maximum amplitudes of both 410 km and 660 km depth discontinuities, respectively. Two back azimuth groups for strong depth variations in the upper mantle discontinuities are circled by the light-green open squares.

process. Moreover, strong heterogeneities were observed in both 410 km and 660 km discontinuities in back azimuths of 20–50° and 200–260°, respectively. These back azimuths are almost parallel to the coast line and are assumed to have a relationship with the breakup of Gondwana supercontinent.

Shear wave splitting analysis by using SKS waves [17], in addition, indicated clear association between "fossil" anisotropies relating to the past tectonics, which appeared to be in present lithospheric mantle structure beneath LHB. A two-layered structure model was assumed for upper mantle anisotropy; upper was supposed to be the "lithosphere," and lower corresponded to the "asthenosphere," respectively. By using the data from local seismic network in LHB, azimuthal variations of the shear wave splitting parameters were obtained (**Figure 3**). The fast polarization directions of the SKS waves were compared with those directions by an absolute plate motion, which are reflecting more recent mantle flow process of the Antarctic Plate (**Figure 3**) [18]. Since the fast polarization directions in lower layer were generally parallel to the directions of the absolute plate motion, the lower layer's anisotropy might reflect the asthenospheric anomalies due to horizontal mantle flow along the plate motion. On the other hand, the fast polarization directions of upper layers did not coincide with the absolute plate motion direction. It was supposed that anisotropic structure could be involved in the past tectonics; the origin of anisotropy was considered as "frozen" within the lithosphere. The Gondwana assembly in early Paleozoic age might be the major aspect in forming the present anisotropy [2].

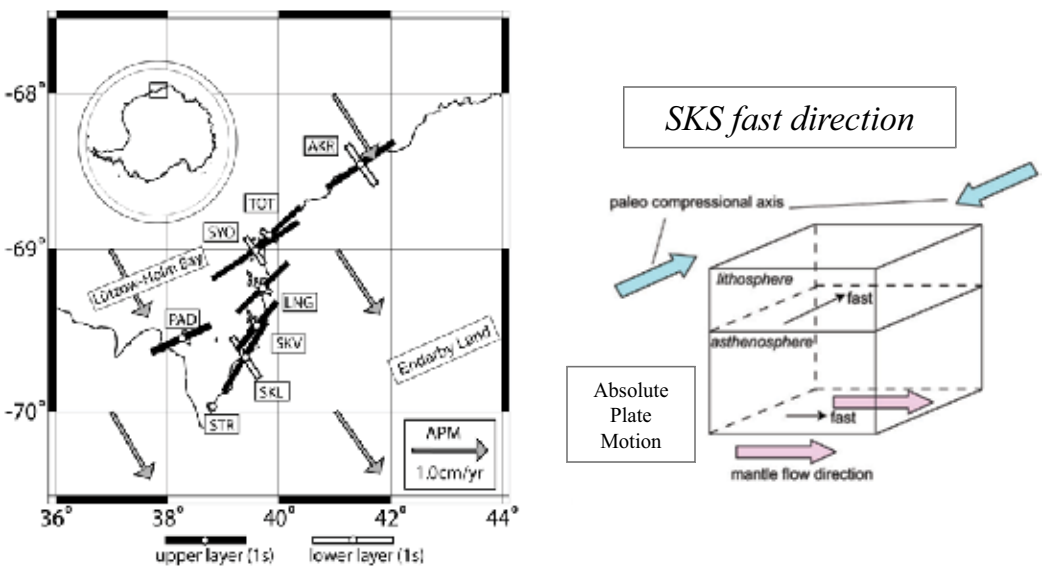

Figure 3. (Left) Upper mantle anisotropy in LHB derived from SKS splitting (modified after [17]). At the stations of AKR, LNG, SKL, SYO, and TOT, the lower layer anisotropy is supposed to be caused by recent asthenospheric flow. For almost all other stations, the direction of anisotropy in the upper layer (corresponds to the "lithosphere") is parallel to NE-SW convergence during the Pan-African age. (Right) Schematic illustration of a two-layered model of seismic anisotropy within the lithosphere and asthenosphere.

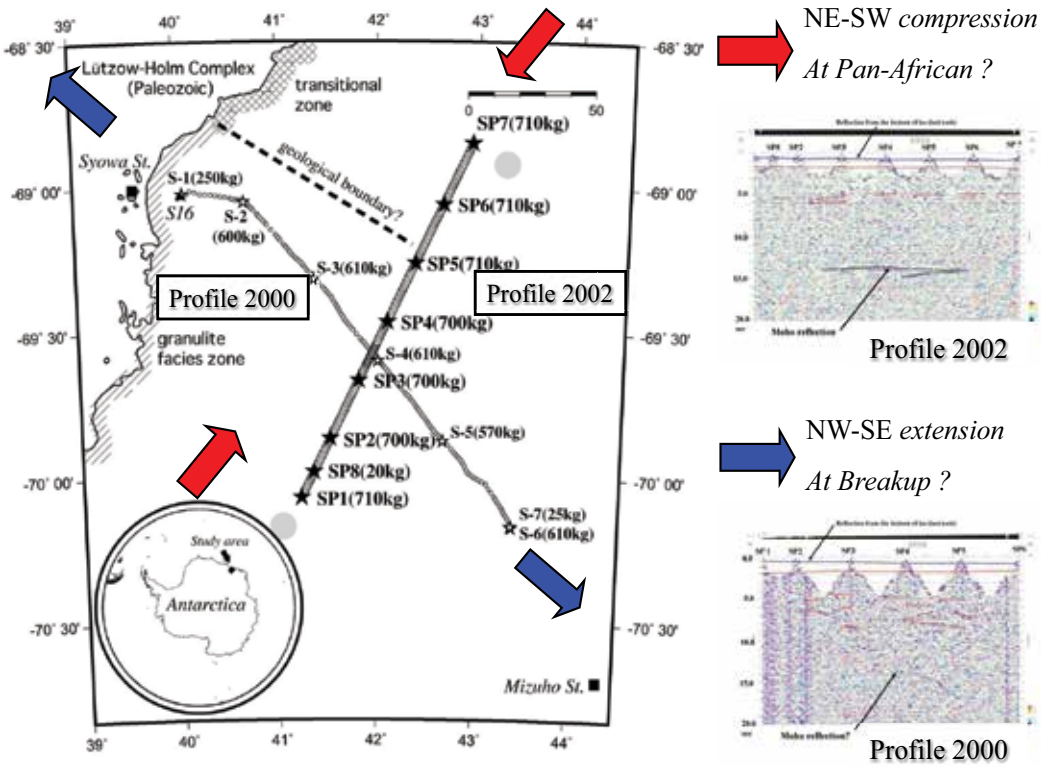

Figure 4. (Left) Map showing the location of deep seismic surveys conducted in LHB (modified after [19]). Solid and open stars indicate the shot locations in 2002 and 2000, respectively. Large and small circles represent the geophone stations on ice sheet for both the active seismic source operations. The size of each shot given is the weight of dynamite used. (Right) Tectonic interpretations of the seismic reflection cross sections. The CDP stack section with offset limited to traces within 120 km for the 2002 profile (upper) and to near traces for the 2000 profile (lower), respectively. Several seismic reflections in the crust and the Moho discontinuity are identified by broken lines and solid arrows. Moreover, reflections from the bottom of the ice sheet are traced by the broken line in the shallow layer of the topmost crust.

Furthermore, active seismic source investigations (wide-angle reflection/refraction and near vertical reflection studies) imaged striking lithospheric mantle reflection patterns involving regional tectonics during Pan-African and the next following extension regime at the continental margins of the breaking-upped supercontinent (**Figure 4**) [14, 19]. By these evidences, tectonic evolution model of LHB was estimated in order to explain the heterogeneities in the present upper mantle. For the 2000 active source profile on continental ice sheet in LHB, a single coverage of common depth point (CDP) with only nearer traces was identified in the lower-right panel of **Figure 4**. On the contrary, the CDP stack section with offsets less than 120 km was depicted for the 2002 active source profile. A laminated seismic velocity layer in the lower crustal depths, moreover, was modeled by comparing synthetic receiver functions with those of observed ones in short-period frequencies (0.1–1.0 Hz) [20]. The repetitive crust-mantle transition zone derived by 2002 profile suggested an influence of compression stress in NE-SW orientation during the Pan-African, which might occurred at the last stage of formation of a great mobile belt between East and West Gondwana [1]. Successive breakup of the

supercontinent in mid-Mesozoic could explain the formation of stretched reflection structure above the Moho discontinuity as imaged by the 2000 active source profile.

These seismic reflection cross sections were assumed to reflect multi-genetic origins, including igneous intrusions, lithologic/metamorphic layering, mylonite zones, shear zones, seismic anisotropy, and fluid layers [21, 22]. In spite of the multi-genetic origin, metamorphic layering could be principal candidates in the case of LHB. A strong reflectivity in the deeper crust-upper mantle might be expected by layered sequences of mafic and felsic rocks [23]. Moreover, such the reflectivity might be originated when the mafic rocks had been interlayered by a combination of the upper amphibolite and lower granulite facies metapelites [24]. In any continental terrains on the Earth, the primary causes for reflectivity might be enhanced by ductile stretching during a late tectonic extensional process [25]. The reflecting layers near the Moho, moreover, were predominantly identified at the crustal thinning tectonic regimes. In these regards, reflectivity in the lower crust and lithospheric mantle beneath LHB might be enhanced under extensional conditions by the last breakup of Gondwana.

3. Estimation of tectonic evolution

On the basis of the seismological evidence mentioned above, a regional tectonic model of LHB was estimated so as to explain formation process of the present upper mantle structure. A history of evolution, including major tectonic events in LHB, was summarized in **Figure 5**(**a, b**). Dedicated geological studies revealed regional metamorphism of the area during the Pan-African age [1, 2]. Metamorphic grade increased progressively from amphibolite facies in the NE to granulite facies in the SW of LHB. The maximum thermal axis runs through the southern LHB with a NNW-SSE striking direction [26]. From geological evidence, the LHB experienced deformation of compression stress oriented perpendicular to the thermal axis, almost parallel to the coast, during the last stage of deformation process within a mobile belt between East and West Gondwana [1, 2]. The high-amplitude magnetic anomalies occurring in LHB compared to those in surrounding terrains [27] indicated that the LHB might be located in one of the major suture zones of the Pan-African mobile belt. These major suture zones appeared to continue from LHB to the Shackleton Range of West Antarctica [1, 28].

Lower crust and upper mantle beneath LHB were characterized to have lateral as well as vertical variations as revealed by seismological studies mentioned in this paper. The gently inland dipping Moho discontinuity (38–42 km) beneath the 2000 deep seismic profile was inverted by travel time analysis from refraction and wide-angle reflection surveys [29]. The present structure was characterized to hold the past regional tectonics, in particular metamorphic activities during the Pan-African. Inferred thrust duplicated (similar to the wedge-shaped) lower crust-upper mantle transition structures interpreted on the 2002 seismic profile (**Figure 4**) [19] implied compressive stress regime along the profile oriented in NE-SW direction during the Pan-African events. In spite of these geophysical and lithologic information, LHB was assumed to be formed under convergence, perpendicular to the thermal axis, during the collision between supra terrains of the Gondwana at the last stage of supercontinent formation [15, 30]. When the LHB underwent NE-SW compression, related paleo-mantle flow

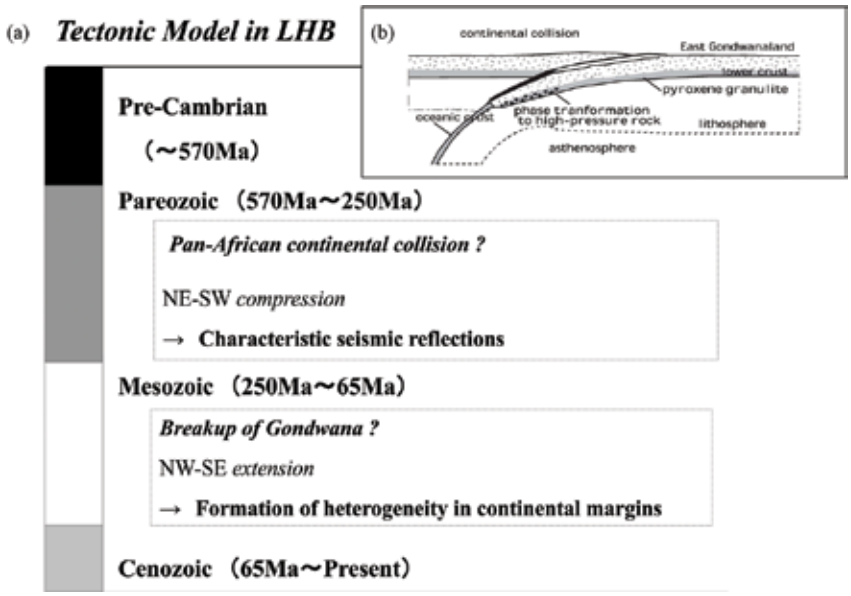

Figure 5. (a) Tectonic evolution model in LHB estimated by several seismological studies. Pan-African orogeny and mid-Mesozoic breakup could be the major two events affecting to form the present upper mantle structure. (b) Illustration of the collision tectonics around LHB at Pan-African orogeny in Eastern Dronning Maud Land-Western Enderby Land (modified after [30]). East Gondwana block includes the Archaean Napier Complex in the middle part of Enderby Land.

along the direction might produce well-defined seismic anisotropy associated with a thermal axis of the progressive metamorphism. Since the direction of paleo-compression was consistent with resultant fast polarization by SKS splitting [17], anisotropy in the upper layer in **Figure 3** could be explained by "lithospheric" deformation during the formation of LHB. **Figure 5b** illustrates the tectonic evolution of Pan-African orogeny in Eastern Dronning Maud Land-Western Enderby Land (modified after [30]). The tectonic evolution process is supposed to be divided into three stages: (1) collision of East Gondwana (Archaean Napier Complex), (2) LHB exhumation by wedge uplift of basement of underlying the Napier Complex, and (3) LHB exposure due to surface erosion, respectively.

At the breakup between Antarctica and Australia-India in 150 Ma [31], LHB experienced extensional stress, which caused thinning at the continental margins of Antarctic continent. The flat-lying reflectors above the crust-mantle boundary identified in the 2000 seismic profile (**Figure 4**) suggested the presence of an extensional stress regime in NW-SE direction resulting from the breakup. The seismic reflective layers at the crust-mantle boundary and lithospheric mantle might have been enhanced by extensional conditions during the final stages of the breakup. The LHB experienced regional high-grade metamorphism during the Pan-African age [32]; the metamorphic grade increased progressively from the north to the south, and the maximum thermal axis lied in the southernmost part of LHB [9]. The "fossil" anisotropy in the lithospheric mantle could be deformed by the past regional tectonics. A majority of the fast polarization directions in the upper layer, which corresponded to the "lithosphere," were orientated in a NE-SW direction (**Figure 3**). This direction was consistent with that of the paleo-compression

stress during Pan-African and the conversion stage between East and West Gondwana terrains at the age. In these concerns, it was proposed that the mantle anisotropy had been originated by lithologic orientation of the mantle minerals during amalgamation process of Gondwana rather than the current asthenospheric flow which parallel to the absolute plate motion.

The lattice-preferred orientation (LPO) induced mechanical anisotropy developed along the direction of preexisting lithospheric structure during continental rifting [33]. The origin of anisotropy beneath Western Dronning Maud Land was pointed out as the ancient lithospheric structure modified by rifting processes during breakup [34]. Since the spreading direction off the Enderby Land was NW-SE initial stage of breakup [35], a strike of the rift was generally parallel to the continental margin of LHB. The fast polarization directions of the upper layer ("lithosphere") in the SKS analysis were roughly parallel to the continental margin. In this regard, it was plausible that the breakup process affected the formation of anisotropy in the lithosphere. The preexisting lithospheric structure might also influence the formation of anisotropy in the succeeding breakup process.

4. Summary

Passive seismic source investigations using teleseismic data revealed heterogeneous structure in LHB. Depth variations of the upper mantle discontinuities (both for 410 and 660 km) were derived by long-period receiver functions by using local array network at the area. Shallow depths in topography of upper mantle discontinuity were identified at the continental back azimuth beneath the ice sheet. The evidence reflected the effect by paleo-upwelling flow associating the mantle plume with regard to the Gondwana breakup. Lithospheric mantle anisotropy derived by the SKS splitting was supposed to be formed by "fossil" anisotropy caused by the past tectonics in NE-SW orientation. The origin of the mantle anisotropy was assumed by the LPO involving the process of supercontinent assembly rather than present asthenospheric flow which parallel with the absolute plate motion on the Earth's surface. In addition, several results from deep seismic surveys by using active seismic sources which were carried out on the continental ice sheet provided clear information on crust-mantle boundary, in addition to the inner lithospheric mantle seismic reflections. After processing of deep seismic reflections, the extracted lithospheric cross section implied tectonic influence of compressive stress during Pan-African age.

Acknowledgements

The authors would like to express their appreciation to the involved JARE members for their great efforts to conduct seismic deployments around the LHB. The authors would also like to express sincere thanks to the geosciences staffs of NIPR, led by Prof. K. Shiraishi, the Director General, for their useful discussion. They would like to express their thankfulness to the reviewers, for their critical checks and useful comments. The authors would like to appreciate editors of this book series on "tectonics" as well as the editorial office of InTech Publisher.

Author details

Masaki Kanao[1]* and Vladimir D. Suvorov[2]

*Address all correspondence to: kanao@nipr.ac.jp

1 National Institute of Polar Research, Research (NIPR), Organization of Information and Systems (ROIS), Tokyo, Japan

2 Trofimuk Institute of Petroleum Geology and Geophysics of Siberian Branch, Russian Academy of Sciences, Novosibirsk, Russia

References

[1] Fitzsimons ICW. Grenville-age basement provinces in East Antarctica: Evidence for three separate collisional orogens. Geology. 2000;**28**:879-882

[2] Fitzsimons ICW. Proterozoic basement provinces of southern and southwestern Australia, and their correlation with Antarctica. Geological Society of London, Special Publication. 2003;**206**:93-130

[3] Harley S, Hensen BJ. Archean and proterozoic high-grade terranes of East Antarctica (40-80E): A case study of diversity in granulite facies. In: High Temperature Metamorphism and Crustal Anatexis. Dordrecht, Netherlands: Kluwer Academic Publishers. 1990. pp. 320-370

[4] Shiraishi K, Hokada T, Fanning CM, Misawa K, Motoyoshi Y. Timing of thermal events in eastern Dronning Maud Land, East Antarctica. Polar Geoscience. 2003;**16**:76-99

[5] Lawver LA, Dalziel IWD, Gahagan LM. Intercontinental migration routes for South American land mammals: Paleogeographic constraints. In: Origins and Evolution of Cenozoic South American Mammals. New York: Springer; 2014. 978-3-319-03700-4

[6] Storey BC. The role of mantle plumes in continental breakup: Case histories from Gondwanaland. Nature. 1995;**377**:301-308

[7] Goleby BR, Blewett RS, Fomin T, Fishwick S, Reading AM, Henson PA, Kennett BLN, Champion DC, Jones L, Drummond BJ, Nicoll M. An integrated multi-scale 3D seismic model of the Archaean Yilgarn Craton, Australia. Tectonophysics. 2006;**420**:75-90

[8] Shiraishi K, Dunkley DJ, Hokada T, Fanning MC, Kagami H, Hamamoto T. Geochronological constraints on the late Proterozoic to Cambrian crustal evolution of eastern Dronning Maud Land, East Antarctica: A synthesis of SHRIMP U-Pb age and Nd model age data. Geodynamic Evolution of East Antarctica: A Key to the East–West Gondwana Connection Special Publications. 2008;**308**:21-67

[9] Motoyoshi Y, Matsubara S, Matsueda H. P-T evolution of the granulite facies rocks of the Lützow-Holm Bay region, East Antarctica. In: Evolution of Metamorphic Belts. Oxford: Blackwell; 1989. pp. 325-329

[10] Isse T, Nakanishi I. Inner-Core anisotropy beneath Australia and differential rotation. Geophysical Journal International. 2001;**151**:255-263

[11] Kobayashi R, Zhao D. Rayleigh-wave group velocity distribution in the Antarctic region. Physics of the Earth and Planetary Interiors. 2004;**141**:167-181

[12] Usui Y, Hiramatsu Y, Furumoto M, Kanao M. Thick and anisotropic D″ layer beneath Antarctic Ocean. Geophysical Research Letters 2005;**32**:L13311

[13] Usui Y, Hiramatsu Y, Furumoto M, Kanao M. Evidence of seismic anisotropy and a lower temperature condition in the D″ layer beneath Pacific Antarctic ridge in the Antarctic Ocean. Physics of the Earth and Planetary Interiors. 2008;**167**:205-216 DOI: 10.1016/j.pepi.2008.04.006

[14] Kanao M, Ishikawa M, Yamashita M, Kaminuma K, Brown LD. Structure and evolution of the East Antarctic lithosphere: Tectonic implications for the development and dispersal of Gondwana. Gondwana Research. 2004;**7**:31-41

[15] Kanao M, Ishikawa M. Origins of the lower crustal reflectivity in the Lützow-Holm Complex, Enderby Land, East Antarctica. Earth, Planets and Space. 2004;**56**:151-162

[16] Kanao M, Usui Y, Inoue T, Yamada A. Broadband seismic deployments for imaging the upper mantle structure in the Lützow-Holm Bay region, East Antarctica. International Journal of Geophysics. 2011;**2011**:1-15

[17] Usui Y, Kanao M, Kubo A, Hiramatsu Y, Negishi H. Upper mantle anisotropy from teleseismic SKS splitting beneath Lützow-Holm Bay region, East Antarctica. In: Antarctica: A Keystone in a Changing World. U. S. Geological Survey and The National Academies. 2007 USGS OF-2007-1047:Short Res. Paper 013. DOI:10.3133/of2007-1047.srp013

[18] Gripp AE, Gordon RG. Young tracks of hotspots and current plate velocities. Geophysical Journal International. 2002;**150**:321-361

[19] Kanao M, Fujiwara A, Miyamachi H, Toda S, Tomura M, Ito K, Ikawa T. Reflection imaging of the crust and the lithospheric mantle in the Lützow-Holm Complex, Eastern Dronning Maud Land, Antarctica, derived from the SEAL transects. Tectonophysics. 2011;**508**:73-84

[20] Yamashita M, Miyamachi H, Kanao M, Matsushima T, Toda S, Takada M, Watanabe A. Deep reflection imaging beneath the Mizuho plateau, East Antarctica, by SEAL-2002 seismic experiment. In: Antarctica: Contributions to Global Earth Sciences. Berlin Heidelberg, New York: Springer-Verlag; 2006. pp. 147-154

[21] Hyndman RD, Shearer PM. Water in the lower continental crust: Modelling magnetotelluric and seismic reflection results. Geophysical Journal. 1989;**98**:343-365

[22] Smithson SB, Johnson RA. Crustal structure of the western U.S. based on reflection seismology: Geophysical framework of the continental United States. Geological Society London Special Publications. 1989;**172**:577-612

[23] Goff JA, Holliger K, Levander A. Modal fields: A new method for characterization of random velocity heterogeneity. Geophysical Research Letters. 1994;**21**:493-496

[24] Burke MM, Fountain DM. Seismic anisotropy of metapelites from the Ivrea-Verbano zone and Serie dei Laghi (northern Italy). Physics of the Earth and Planetary Interiors. 1990;**78**:301-317

[25] Warner M. Basalts, water, or shear zones in the lower continental crust. Tectonophysics. 1990;**173**:163-174

[26] Hiroi Y, Shiraishi K, Motoyoshi Y. Late Proterozoic paired metamorphic complexes in East Antarctica, with special reference to the tectonic significance of ultramafic rocks. In: Geological Evolution of Antarctica. Cambridge: Cambridge University Press. 1991. pp. 83-87

[27] Lawver LA, Scotese CR. A revised reconstruction of Gondwanaland. In: Gondwana Six: Structure, Tectonics and Geophysics. 1987. pp. 17-23

[28] Golynsky AV, Masolov VN, Nogi Y, Shibuya K. Magnetic anomalies of Precambrian terrains of the East Antarctic shield coastal region (20E–50E). Polar Geoscience. 1996;**9**:24-39

[29] Yoshii K, Ito K, Miyamachi H, Kanao M. Crustal structure derived from refractions and wide-angle reflections in the Mizuho plateau, East Antarctica. Polar Geoscience. 2004;**17**:112-138

[30] Ishikawa M, Kanao M. Structure and collision tectonics of Pan-African orogenic belt – Scientific significance of the geotransect for a supercontinent: Gondwanaland. Bulletin of the Earthquake Research Institute-University of Tokyo. 2002;**77**:287-302

[31] Anderson DL. Superplumes or supercontinents? Geology. 1994;**22**:39-42

[32] Shiraishi K, Ellis DJ, Hiroi Y, Fanning CM, Motoyoshi Y, Nakai Y. Cambrian orogenic belt in East Antarctica and Sri Lanka: Implication for Gondwana assembly. Journal of Geology. 1994;**102**:47-65

[33] Tommasi A, Vauchez A. Continental rifting parallel to ancient collisional belts: An effect of the mechanical anisotropy of the lithospheric mantle. Earth and Planetary Science Letters. 2001;**185**:199-210

[34] Müller C. Upper mantle seismic anisotropy beneath Antarctica and the Scotia Sea region. Geophysical Journal International. 2001;**147**:105-122

[35] Nogi Y, Seama N, Isezaki N. Magnetic anomaly lineations and fracture zones deduced from vector magnetic anomalies in the West Enderby Basin. In: Weddell Sea Tectonics and Gondwana Break-up, Geological Society of London, Special Publication. Vol. 108. 1996. pp. 265-273

Chapter 2

Tectonic Insight in the Southwest Gondwana Boundary Based on Anisotropy of Magnetic Susceptibility

Arzadún Guadalupe, Tomezzoli Renata Nela, Tickyj Hugo, Cristallini Ernesto Osvaldo and Gallo Leandro Cesar

Additional information is available at the end of the chapter

http://dx.doi.org/10.5772/intechopen.72825

Abstract

The anisotropy of magnetic susceptibility (AMS) is an effective tool to measure the rock petrofabric and it allow analyzing the tectonic stress. The southwest boundary of Gondwana in South America is the counter-part of the Cape fold belt of South Africa and its geological evolution is still a subject of debate. Samples of different localities of this sector were analyzed with the AMS technique, from Buenos Aires, La Pampa and Mendoza province. For rocks of Permian age, there is a clear regional magnetic signature indicating a NW-SE elongation direction and a NE-SW shortening. The ASM patterns obtained in the oldest rocks are complex, probably as the result of stress interference in the magnitudes, space and time with different pulses of the orogenic activity developed from the Middle Devonian to the Permian. In the southwest of Gondwana, small continental plates were accreted to the main continent mass during the Middle Devonian. The Permian deformation has been interpreted as the consequence of a paleogeographic re-organization of Gondwana that moves to lowest latitudes to makes the Pangea continent during the Triassic. This younger deformation evidences an orogenic front migration and attenuation to the foreland basin.

Keywords: tectonic, anisotropy of magnetic susceptibility, southwest margin of Gondwana

1. Introduction

The anisotropy of magnetic susceptibility (AMS) is an effective tool to measure the rock petrofabric, both of primary and secondary origin with the potential to identify the orientations

of the principal axes of finite strain to which the rocks were subjected [1, 2]. The base of the method is the measure of the orientation and intensity of the magnetic susceptibility (K) of a rock sample whose intensity is the sum of the diamagnetic, paramagnetic, antiferromagnetic and ferromagnetic responses of constituent minerals [3]. The diamagnetic response is typically very weak, and opposes the applied field; this response is typically contributed by iron-free silicates such as quartz and feldspar. The paramagnetic contribution is carried by Fe-bearing silicates [4], which in magmatic rocks includes the phyllosilicates (biotite, chlorite and Fe-muscovite), Fe-Ti oxides, amphiboles, pyroxene, cordierite, garnet and tourmaline. The antiferromagnetic contribution, typically provided by hematite and goethite, is negligible in practice. The ferromagnetic contribution is commonly a major component and it is associated with magnetite and occasionally with sulfides such as pyrrhotite [3, 5].

In deformed rocks, strain may control the orientation of ferromagnetic minerals. The AMS response in such rocks typically reflects the preferred crystallographic orientation of iron-bearing silicates and the shape and distribution of magnetite or hematite grains.

To determine the AMS, the response of a rock when it is affected by a weak magnetic field is measured, related to the acquired magnetization degree with the applied magnetic field, evidenced in the formula **K = M/H**, where K is the magnetic susceptibility, M is the acquired magnetization and H is the magnetic field applied.

The magnetic behavior of the rocks in a weak field of constant magnitude depends of some factors such as the preferential crystallographic orientation, the shape of the mineral fabric, the composition, the distribution and size of the mineral grains and the microfractures [6]. Therefore, a substance is isotropy, when the induced magnetization in a symmetric specimen, has the same intensity independent to the direction in which the field is applied. Instead, in the magnetic anisotropic rocks, the induced magnetization depends of the orientation of the sample in the magnetic field.

AMS measurement can be expressed by a second-rank tensor where eigenvectors/eigenvalues are geometrically represented as an ellipsoid (**Figure 1a**), with three perpendicular axis: K_{max}, K_{int} and K_{min}, (K_1, K_2 and K_3). The highest magnetic intensity is induced throughout the K_{max} major axis and the weakest intensity is induced according to the K_{min} minor axis; therefore, in an isotropic substance, the three axis are equal and the ellipsoid is in fact a sphere (**Figure 1a**). The shapes and orientations of these ellipsoids can be related to magmatic flow in igneous rocks and kinematics of deformation in metamorphic rocks [7]. Commonly, the flattening of the AMS ellipsoid (plane perpendicular to K_{min}) is parallel to the foliation in the rock, and the elongation of the ellipsoid (K_{max}) is parallel to the fabric lineation.

The parameters to consider are the anisotropy degree (P), the ellipsoid shape (T) and the spatial orientation of the main axis. Their most important properties are:

- The susceptibility ellipsoid tends to be coaxial with the total deformation ellipsoid with a correspondence to each principal axis (**Figure 1b**).
- The susceptibility ellipsoid tends to be coaxial with the petrofabric; the K_{min} axis is perpendicular to the foliation, to the bedding plane in sedimentary rocks, plane poles of magmatic foliation or foliation poles or cleavage in rocks deformed in solid stage.

http://dx.doi.org/10.5772/intechopen.72825

- If the magnetic fabric is only depositional origin, the angle between the K_{min} and the pole of the bedding plane is small.
- K_{max} is parallel to the lineation that could be tectonic origin, the direction of a magmatic flow or could be dominated by the paleocurrents direction.
- K_{min} is denominated by "magnetic foliation pole" and K_{max} "magnetic lineation".
- The ellipsoid shape is directly related with the rock fabric. In some rock types, there is a quantitative relation between L (lineation) and F (foliation), or any parameter that involve the relative length of the susceptibility axes and the intensity of the linear or planar orientations, respectively.
- In the case of the deformation in solid stage, there is a direct relation between the AMS and the deformation. A quantitative application of the AMS in this cases, it is only possible when a calibration is carry out with the stress and the original anisotropy of the rock, in other way, a qualitative ratio is only possible, as the rocks with major anisotropy are the more deformed.
- The ASM measurements are not affected by the natural or artificial remnant magnetizations.
- The simpler and quick way of visualize the obtained data about the directions of the main susceptibility axes is through a stereographic net. The most common is to use the inferior hemisphere and to plot the data of K_{max}, K_{int} and K_{min} with different symbols, so it is

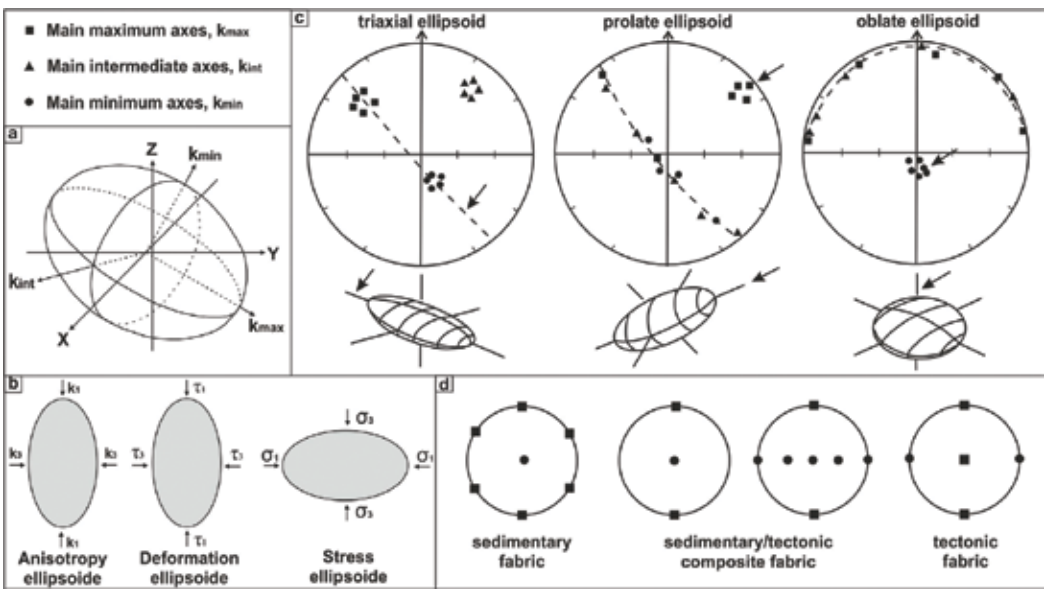

Figure 1. (a) Magnetic susceptibility ellipsoid, with three orthogonal axes that correspond to the maximum, intermediate and minimum [7]. The space orientation is defined in a coordinate system (x,y,z). (b) Ratio between the anisotropy, deformation and stress ellipsoids. K1: Maximum anisotropy axis; K3: Minimum anisotropy axis; τ1: Maximum deformation axis; τ3: Minimum deformation axis; σ1: Maximum stress axis; σ3: Minimum stress axis. (c) Directional data plotted in a stereographic net of triaxial, prolate and oblate ellipsoid [7]. (d) Stereographic net models of sedimentary fabric, sedimentary/tectonic composite fabric and tectonic fabric.

possible to distinguish the ellipsoid shape and to easily compare with structural data: cleavage, fractures, etc., and with the origin of the fabric: sedimentary, tectonic or sedimentary/tectonic composite (**Figure 1c**, **d**). On the other hand, the shape parameter (T) represents the ellipsoid shape: if the ellipsoid has oblate shape, then $T > 0$ and if it is prolate then $T < 0$ [7].

The AMS technique was applied in different localities along the southwest boundary of Gondwana (**Figure 2**), in diverse lithologies that ranges from Cambrian to Permian-Triassic ages, to study the kinematic history of this area and to distinguish multiple tectonic events that account for the fabrics of the outcropping rocks.

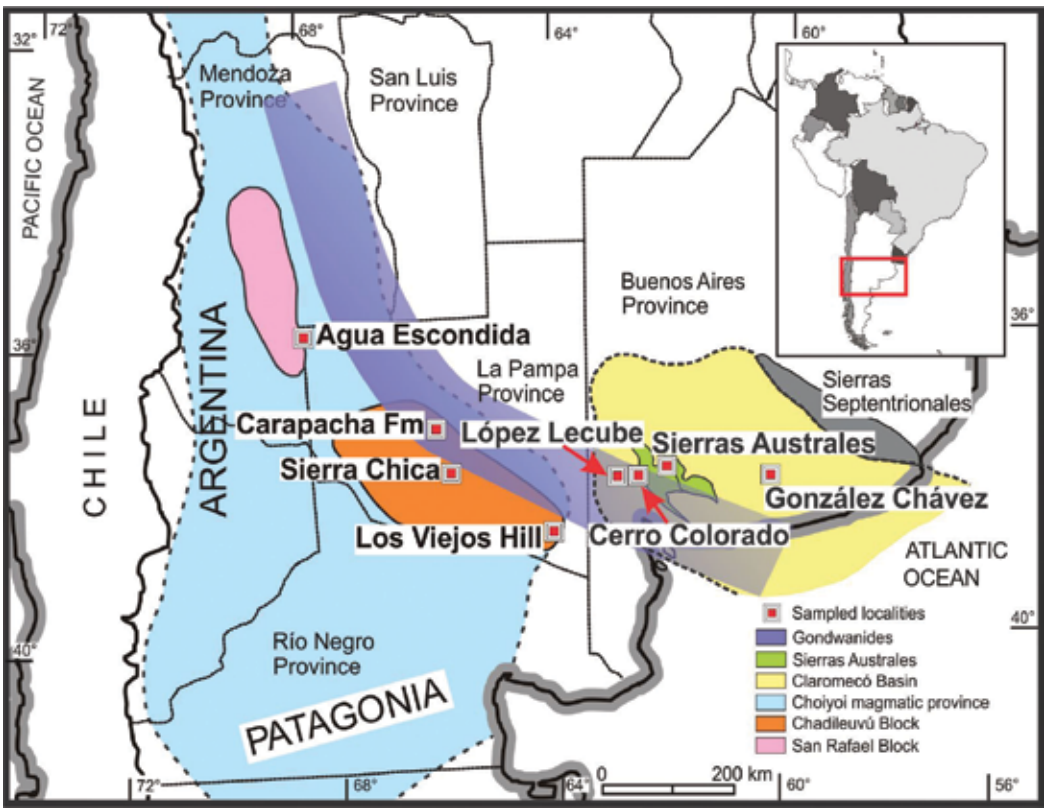

Figure 2. Location of the different localities and basin studied in the margin of Gondwana by the AMS technique. The Gondwanides fold and thrust belt is in purple, sierras Australes is in green, Claromecó Basin in yellow, Carapacha Basin in orange, San Rafael block in pink, and the Choiyoi magmatic province in light blue.

2. Geological setting

The southwest boundary of Gondwana in South America is the counter-part of the Cape fold belt of South Africa [8]. It is extended from Sierras Australes-Claromecó Basin in the Buenos Aires province to the San Rafael Block in the Mendoza province (**Figure 2**). This fold and thrust belt [9], known as Gondwanides [8], was subject to deformation during the Paleozoic.

Ramos (1984) propose [10] an ocean closed by subduction toward the northern boundary of Patagonia at the southern margin of Gondwana, and generated a collision during the late Paleozoic. However, the geological evolution of this region is still a subject of debate and doubts remain about the origin of Patagonia and the age of the main deformation and if it is related or not with this collision. Now there are new proposals that include collisional and intra-continental deformation mechanisms (Ref. [11]). According to some researchers, the deformation occurs in one phase during the late Permian-Triassic, instead other authors propose that it began in the late Devonian-early Carboniferous and continued up to the Permian [12].

With the aim of regionally analyze the magnitude of the deformation regionally, the stress directions that acted in the different geological moments and the time-space relations between the different localities of the Gondwanides, AMS studies were making along its margin. Rocks of different lithologies and ages ranging from Cambrian to Permian-Triassic were studied in different localities along this belt (**Figure 2**), from the Sierras Australes-Claromecó Basin, Chadileuvú Block (Carapacha Basin, Los Viejos Hill and Sierra Chica) and San Rafael Block (Agua Escondida).

2.1. Sierras Australes-Claromecó Basin, Buenos Aires province

The Sierras Australes are at the southwest of the Buenos Aires province and they represent the outcropping part of the Claromecó Basin (**Figure 2**). They are a fold and thrust belt [9] with a general northwest-southeast strike and a northwest vergence. The outcropping rocks are Pre-Cambrian to Permian, with the oldest units at the west and the most modern at the east.

The Cerro Colorado granite represents the basement of the Sierras Australes, and it is situated at 40 km to the west. It has a penetrative cleavage and a gneiss-milonitic structure [13]. Different authors calculated age data: Rb/Sr 427-392 Ma [14], Rb/Sr 487 $\pm$ 15 [15], Rb/Sr 381 $\pm$ 9 Ma [13], U/Pb 531 $\pm$ 4 Ma [16] and U/Pb 523 $\pm$ 4 Ma [17]. The López Lecube sienite is situated at 80 km at the west of Sierras Australes, and correspond to another intrusive body with apparently no deformation [18]. It was interpreted as post-tectonic origin because of its age data: U/Pb de 258 $\pm$ 2 Ma [19] and 251.5 $\pm$ 3.0 Ma [20], related with the Gondwanic magmatic cycle of La Pampa and Mendoza provinces (**Figure 2**).

The sedimentary rocks of the Sierras Australes is classified into three main orographic units: Curamalal, Ventana and Pillahuincó groups that have an important difference in the metamorphism degree and in the style of the deformation [21]. In the quartzites of the Curamalal, Bravard and Ventana groups, situated in the western sector (base of the sequence), there is a lower greenschist metamorphism [22, 23]. While in the Pillahuincó group, situated in the eastern sector (top of the sequence), there is a medium to high diagenesis degree [22, 24, 25]. Cenozoic deposits cover in discordance these units.

The west sector presents more deformed strata in the Sierras de Curamalal, Bravard and Ventana [21], while in the eastern sector, in the Sierras de las Tunas and Pillahuincó outcrops the Pillahuincó group, with a characteristic more open folding. Here the regional strike of the axes of the folds is northwest-southeast. However, there are visible differences between the base and the top inside the Pillahuincó Group. At the base, the folds tend to be cylindrical with shorter wavelength and more defined flanks, while toward the top of the sequence they tend to

expand and smooth their wavelengths [26]. The cleavage planes are nearly vertical, dipping toward the west at the bottom of the sequence and mostly east on the Bonete and Tunas formations (**Figure 3**).

The analyzed lithologies correspond to Cerro Colorado, López Lecube, to the Lolén Formation [21], and the Pillahuincó Group [21] in the Sierras Australes area, and a little outcrop that correspond to the Tunas Formation situated at the Claromecó Basin, at the east of Sierras Australes.

The Lolén Formation, of Devonian age [27], is at the top of the Ventana Group. It has micaceous sandstones, phyllites and shales with lenticular beds of fine conglomerate, with a strong cleavage in northwest-southeast direction.

The Pillhuincó Group is composed from base to top by the Sauce Grande, Piedra Azul, Bonete and Tunas formations. The carboniferous Sauce Grande Formation has diamictites and sandstones. The Piedra Azul Formation has mudrocks. The Bonete Formation, of Lower Permian age, has fine sandstones with white spots, interbedded with gray mudrocks. The Tunas Formation, of middle Permian age, has fine to medium sandstones interbedded with green and red mudrocks. There are some small outcrops of the Tunas Formation in the Claromecó Basin, close to the González Chávez locality. The Pillahuincó Group has the Carboniferous-Permian Glossopteris flora [28], and the Tunas Formation has zircon shrimp data of 291–280 Ma [29–31].

Paleomagnetic studies in the Tunas Formation indicate that the magnetizations are syntectonic, with shortening values of 32% at the base (to the west) and 90% at the top (to the east). This evidences a decrease in the deformation toward the top of the sequence and is consistent with the structural field observations [26]. Furthermore, anisotropy of magnetic susceptibility and compaction studies on Tunas Formation also show a decrease of the deformation toward the foreland [32].

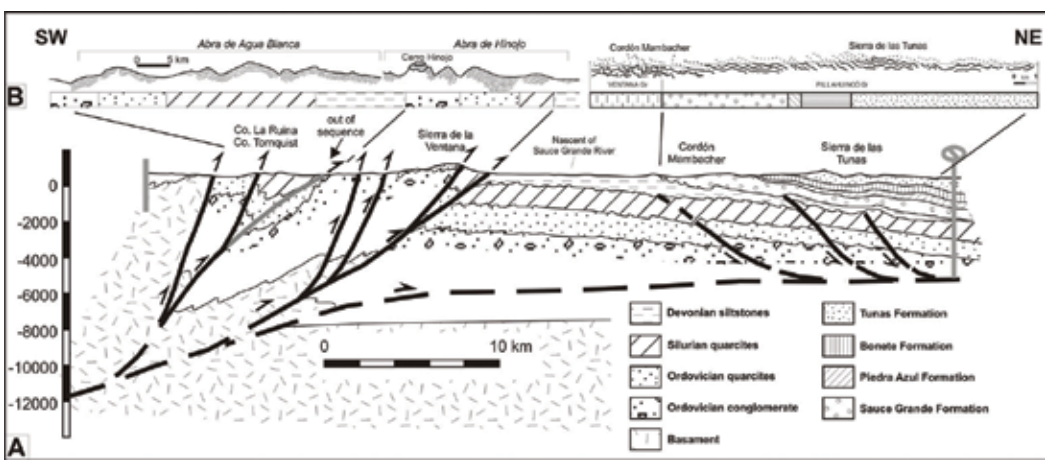

Figure 3. Structural cross-section of the sierras Australes: (a) general and, (b) detailed (taken from [11]). Notice that the western sector presents more deformed strata than the eastern sector, see shortening values.

The tecto-sedimentary [33] and paleomagnetic evidences [26], indicate that the deformation in the Tunas Formation occurs at the same time that the sedimentary deposition and it was related with the San Rafael orogenic phase defined by Azcuy and Caminos [34].

2.2. Chadileuvú Block, La Pampa province

Several localities that belong to the Chadileuvú Block were measured with the AMS technique: Los Viejos Hill, Sierra Chica and the Carapacha Formation. The igneous-metamorphic basement of the area includes Upper Cambrian to Lower Devonian metamorphic rocks (Las Piedras Metamorphic Complex, Paso del Bote Formation, El Carancho Igneous Complex and La Horqueta Formation), granitoids (Pichi Mahuida Group) and Late Paleozoic granite orthogneisses (Los Viejos Hill Complex) that outcrop in southeastern La Pampa province [35, 36]. In addition, there are sedimentary rocks outcrops belonging to the Carapacha Basin.

Los Viejos Hill is located at the southeast of La Pampa province (**Figure 2**). It belongs to the igneous-metamorphic basement considered by Linares et al. Linares et al. [37] as the southward prolongation of the Sierras Pampeanas geological province. It is part of a ductile deformation zone in low metamorphic degree with northeast vergence [38]. There are different deformation degrees, from little foliate granitic gneiss to mylonitic gneiss, with ages from 466.4 to 261 Ma, obtained by K-Ar and Rb-Sr dating in biotite and muscovite [35].

Sierra Chica is located at the center of La Pampa province (**Figure 2**). It is a volcanic rock outcrop belonging to the Choiyoi magmatic province. The Choiyoi Group in La Pampa is located in a tectonically stable environment adjacent to an active continental margin [39]. According to Quenardelle and Llambías [40], the sequence is composed of different units. The lowermost unit, at the north, consists of trachyandesitic pyroclastic flows of unknown thickness and extent. The other ones are rhyolitic units, divided into the lower unit, composed of well-bedded, thin pyroclastic units interbedded with thin fall deposit units, and the upper unit is composed of coarse bedded, thick pyroclastic layers with rheomorphic structures [40]. The Sierra Chica sequence is consistent with an eruption in an extensional tectonic regime immediately subsequent to a subduction-related compressional regime [40]. Rapela et al. [41] obtained an Rb-Sr whole-rock isochron age of 240 $\pm$ 2 Ma and Domeier et al. [42] obtained U-Pb ages of 263 $\pm$ 1.6 Ma.

The Carapacha Basin is a continental half-graben, located at the southern of La Pampa province, central Argentina (**Figure 2**; [43]). The basin filling is up to 630 m thick and it is entirely composed of clastic deposits of the Carapacha Formation, of Permian age. Red and gray arkosic or lithic sandstones, mudstones and scarce conglomerates compose the Carapacha Formation. It is divided into two members: the lower Calencó Member and the upper Urre-Lauquen Member [43]. The formation has yielded a typical Permian Glossopteris macroflora [44, 45]. The rocks of the upper Carapacha Formation along Río Curacó are gently folded, strike-slip, normal and reverse faults and extensional veins are also present. The structure and weak deformation of the upper Carapacha Formation was interpreted as reflecting left-lateral strike-slip deformation under a transpressive regime that it is associated with cessation of sedimentation in the basin [46]. The upper part of the formation is intruded by an andesite

assigned to El Centinela Formation, maybe associated with the Permian-Triassic volcanic rocks of the Choiyoi Magmatic Province.

2.3. San Rafael Block, Mendoza province

The Agua Escondida area is located at the southeast of the Mendoza province and it is situated at the south of the San Rafael Block (**Figure 2**). In this sector, the Piedras de Afilar Formation outcrops that is a pre-carboniferous granitic basement of 418.2 ± 3.1 Ma [47]. It is covered by carboniferous, siliciclastic sediments of the Agua Escondida Formation [48] and is intruded by the igneous rocks of the Permian Choiyoi magmatic Group. The Agua Escondida Formation [48] is composed by siliciclastic sediments of carboniferous-permian age due their flora remains deposited over the basement. In this sector, the Choiyoi magmatic Group is mainly composed by a metasilicic lower section with dacitic intrusive, andesitic lavas and tuffs. The silicic upper section has lavas, tuffs, ignimbrites and breccias of rhyolitic composition and granites that intrude the Agua Escondida Formation and the pre-carboniferous basement [49, 50]. The completely Paleozoic rocks are cover by plio-pleistocene basalts and recent sediments.

3. Methodology

Each sampled site consists at least of 4–5 hand samples or 6–7 cores obtained by portable drilling and orientated by magnetic (Brunton) and sun compass (Azimut 0–360° and dip 0–90°).

Kappabridge MFK-1A and KLY-2 (by Geofyzika Brno) were utilized to measure the AMS directions, at the Paleomagnetism Laboratory "Daniel A. Valencio" (IGEBA) of the Geologic Sciences Department of the Buenos Aires University (UBA) and at Colgate University, respectively. Previously to measure, it is necessary to ingress the field sample orientation because the AMS direction results are in specimen coordinates (without field correction) and in geographic coordinate (with field correction). The results were analyzed with the program Anisoft 4.2 (provided by Geofyzika Brno) to obtain directional results of AMS scalar axes represented in the ellipsoids and their statistic parameters, *in situ* and with structure correction, and the AMS degree (P) and the shape parameter (T) values. It is possible to make automatically the structure correction with the program, taking the bedding planes to the horizontal. The T and P parameter values were plotted in the diagram of Jelinek [51].

The AMS data obtained, were integrated with paleomagnetic and field structural data of each locality, to improve the interpretations.

4. Results of AMS in the southwest Gondwana boundary

Here the results of ASM from different localities along the Southwest Gondwana margin, from the Sierras Australes-Claromecó Basin to the San Rafael Block, are presented. Rocks of different

lithologies and ages ranging from Late Devonian to Permian-Triassic were studied. Each sampled locality has its own magnetic signature, but it is possible to identify a pattern related to the age.

4.1. Sierras Australes–Claromecó Basin

In this area were studied the Cerro Colorado granite, the López Lecube sienite, the Lolén Formation and the Pillahuincó Group, and a little outcrop in the González Chávez locality of possible upper Permain-Triassic age [18, 32, 52].

In all the analyzed localities, the AMS data show good internal consistence in each sample site and between them (**Figure 4**), and is almost possible to correlate the structural characteristics with the AMS patterns.

In López Lecube (Upper Permian), the magnetization is stable in all specimens with a reverse polarity [18], characteristic of the Kiaman superchron. In some specimens, the anisotropy of magnetic susceptibility was measured (**Figure 4**). They present prolate magnetic fabric, with the K_{max} axis parallel to the magmatic mineral lineation (**Figure 4**). This AMS spatial distribution axes were related with the magmatic conditions during the emplacement of the magma. However, the AMS fabric from Cerro Colorado (Cambrian) is oblate, with a tectonic signature instead of magmatic, in the distribution of the AMS axes with a northwest-southwest direction of the shortening (K_{min} in the northeast; **Figure 4**).

The specimens of the Lolén Formation (Devonian) show the K_{max} and K_{int} axes contained in the cleavage plane and aligned with the strike of the structure in the northwest-southeast

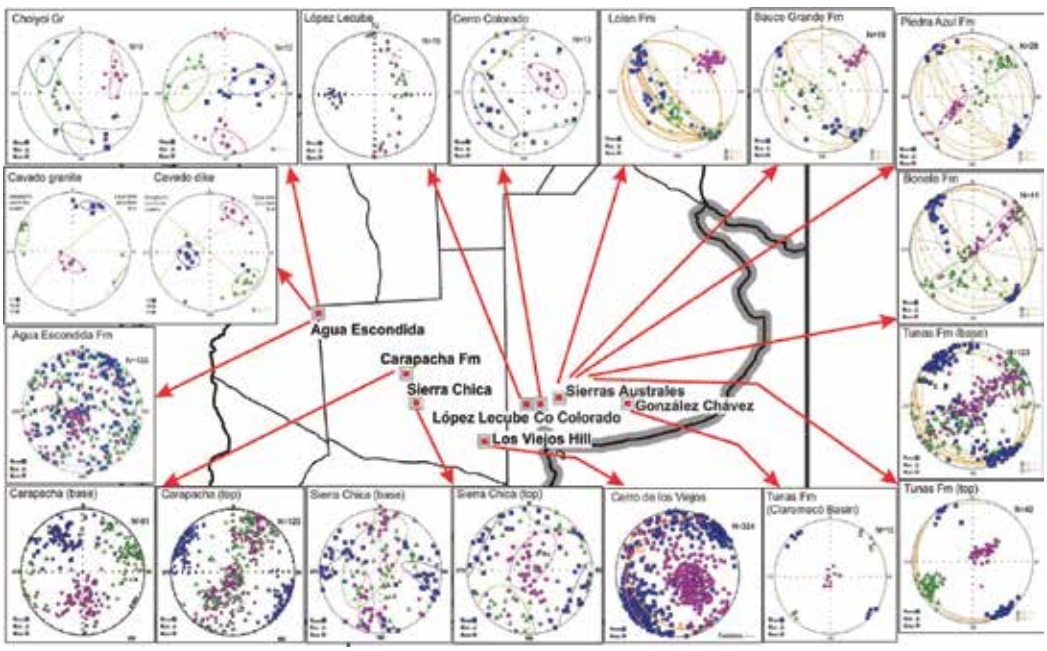

Figure 4. AMS ellipsoids results of the different sectors of the southwest margin of Gondwana, with the K_{max}, K_{int} and K_{min} axes and N the number of specimens. The stereographic nets are in geographic coordinate system and equal-area projection.

direction. The K_{max} tends to lie close to the horizontal. The K_{min} axes are always in the northeast direction close to the horizontal and parallel to the pole of the cleavages planes. The anisotropy degree (Pj) is low, minor than 10% and the susceptibility is minor than $2.52E^{-4}$ (SI), so the paramagnetic minerals control the magnetic fabric [7]. From the disposition of the AMS axes, its ratio with the cleavage planes and the ratio between the Pj and T parameters is deduced that the fabric is typically oblate of tectonic origin [53].

In the Pillahuincó Group, the Sauce Grande Formation presents oblate ellipsoids ($T < 0$), with K_{min} grouped in the first quadrant, almost horizontal, suggesting a flattening of the fabric with tectonic control. The Piedra Azul and Bonete formations show ellipsoids with prolate shapes ($T > 0$) and K_{min} axes in the first and third quadrant grouped toward the center of the stereographic net. The Tunas Formation has oblate ellipsoids with K_{min} axes tending to the vertical through the horizontal, suggesting a transition between tectonic to sedimentary fabric (**Figure 4**; [52]). The trend toward a fabric with a dominantly sedimentary control is clearly seen in the Gonzalez Chavez locality located at the Claromecó Basin (**Figure 4**).

The degree of anisotropy (P) shows a general decrease toward the younger formations and toward the east, with maximum values ranging from 11% in the Lolén Formation to 4.4% in Tunas Formation (**Figure 5**).

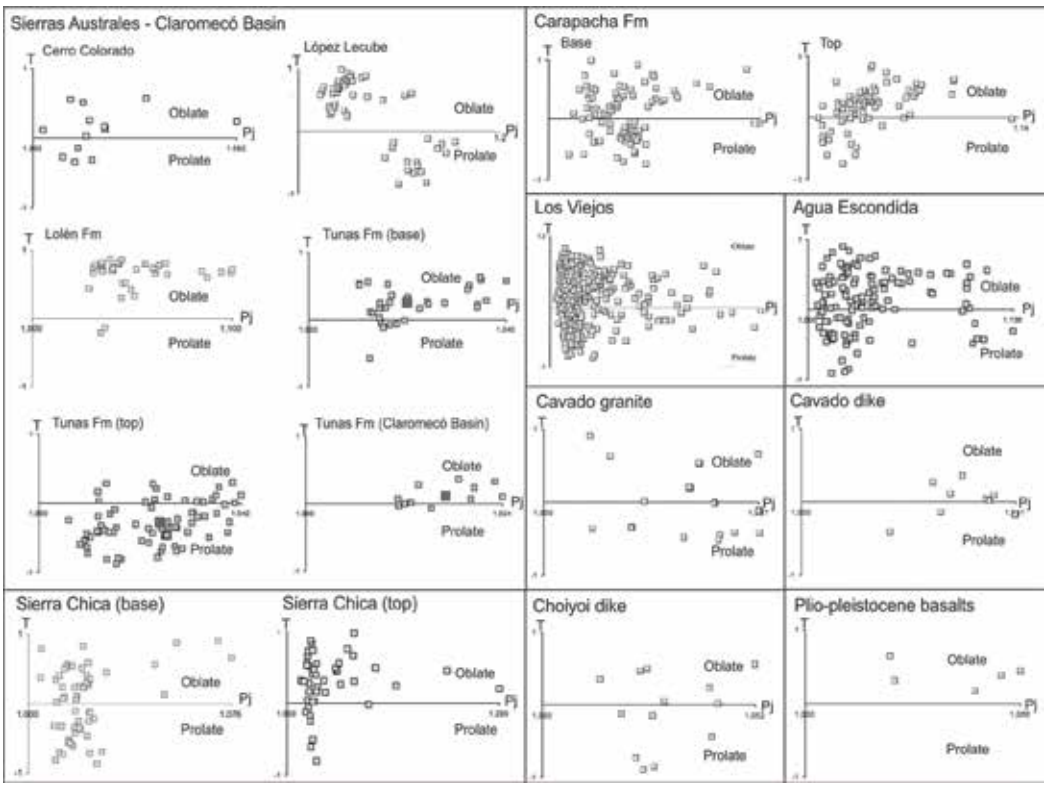

Figure 5. Ratio between the shape parameter (T) and the anisotropy degree (Pj) of the different localities, when $T < 0$ the ellipsoid is prolate and when $T > 0$ is oblate.

4.2. Chadileuvú Block, La Pampa province

In Los Viejos Hill, an AMS systematic sampling was made in a grid perpendicular to the main structures of the body [54]. Unexpectedly, it was found that the K_{min} poles deviate from the poles of the main foliation S_1 by about 25° (**Figure 4**). Similarly, but not so noticeably, the K_{max} poles trend northeast/southwest, with a near-horizontal plunge, whereas the principal lineation L_1 plunges gently southwest. This unusual situation is attributed to the existence of superimposed fabrics arising from S and C structures. The distribution of the paramagnetic and ferromagnetic minerals in "S-C" plane structures interferes in the expected anisotropy pattern, indicating the presence of a cryptic foliation. From the petrographic point of view [38] and the AMS studies, it is possible to infer that the zone was affected by different deformation episodes, evidencing by the presence of a secondary foliation S_2 subordinate to the S_1.

In all localities, the AMS signatures are predominantly triaxial, with well-defined axial groups and relatively small uncertainty ovals about means. Most of the sites exhibit oblate tendencies, and only a few are prolate (**Figure 5**). The T versus Pj diagram reveals an anisotropy degree mainly below 3%, with an ellipsoid more oblate than prolate (**Figure 5**).

A systematic sampling was made in localities situated at the southeast and south of the Carapacha Basin, to make paleomagnetic and AMS studies [55]. The paleopolar positions of both Carapacha Formation members are different [55]. According the AMS studies, the tectonic signature of the two members is different. The Calencó Member presents minor deformation than the Curacó Member (**Figure 4**). In the Curacó River samples, the K_{max} is more variable, not related with the folding axes except locally, and so it is probable that the primary sedimentary fabrics are more preserved; instead of in the Curacó River locality the K_{max} poles seem to be tectonically controlled because they have the same direction than the folding axes and the K_{min} are bimodal distributed as a typically prolate ellipsoid with a main maximum stress with a southwest-northeast dominant direction (**Figure 4**). The different paleomagnetic positions calculated in both members are concordant with the lithological, structural, biostratigraphic and AMS data differences. The AMS axial ratios of Carapacha are mainly characteristic of triaxial ellipsoids. The Pj versus T diagram reveal an anisotropy degree mainly below 4%, with ellipsoids more oblate than prolate (**Figure 5**).

The isolated magnetization of the Sierra Chica locality is syntectonic [56]. There are two different magnetic signatures: one in the base units and other one in the top units (**Figure 4**). These differences were interpreted as a tectonic discordance between both. The K_{min} is situated in a gird with south-southwest-north-northeast direction from horizontal (base) to vertical positions (top) (**Figure 4**), evidencing that the maximum stress direction is southwest-northeast. The anisotropy degree is Sierra Chica is low, minor than 11% and the magnetic susceptibility is low, minor than $2.5E^{-4}$(SI), indicating that it is carried by paramagnetic minerals. The Pj versus T parameters indicate a that predominate the oblate fabrics (**Figure 5**).

4.3. San Rafael block

The AMS pattern in the Agua Escondida area is complex. In the Piedras de Afilar Granite, of devonian age, the K_{min} axes have a north-northwest direction while the K_{max} are in east-west direction, indicating a secondary fabric and evidencing a deformation with a north-south

compression direction. Nevertheless, in the La Menta Granite (388.4 ± 3.1 Ma, [57]), that is part of the Piedras de Afilar Formation, the K_{min} has a west-southwest direction and the K_{max} a north-south direction, showing a secondary fabric and evidencing a compression direction from the west.

In the Permian Cavado Granite, the main AMS axes seem no follow a common spatial pattern; the magnetic fabrics seem to be primary and related to local effects of the emplacement conditions. The dikes that intrude the Cavado granite have a triaxial fabric, with the K_{max} in the third quadrant and close to the vertical and subparallel to the diaclases plane. The K_{min} tend to be in the northeast and the K_{int} in the southeast. From the statistic parameter analyses, the fabric is oblate. The anisotropy degree is 4% and the medium susceptibility is minor than $1E^{-4}$(SI) ([58]; **Figure 5**).

The sedimentary rocks from the Agua Escondida Formation (Upper Carboniferous) have K_{max} orientated to the northeast and contained in the bedding planes with northwest-southeast strike (**Figure 4**; [58]), while K_{min} is parallel to the pole of this plane. This arrangement of the axes does not respond to a "pure sedimentary fabric" (**Figure 4**), but on the contrary it would indicate interference of signatures.

The fabrics of the dikes and ignimbrites of Choiyoi are similar to the Piedras de Afilar and La Menta granites; they are secondary and produced by a deformation stress with east-west and north-south compression directions, following complex patterns of previous stress in the area.

The plio-pleistocene basalts have K_{max}-orientated northwest and close to the horizontal, indicating a primary fabric and a probable fluidity of the mineral components in a southwest-northwest direction. The anisotropy degree is minor than 13% in all the analyzed sites, and the fabric is in general oblate, although in each individual site there are oblate, prolate and triaxial shapes, depending of the lithology (**Figure 5**; [58]).

A rhyolitic dike of the Choiyoi Group has a K_{max} in northeast-southwest direction and contained in the diaclase planes. The K_{min} and K_{int} are in the second and fourth quadrant like a wreath. The fabric is prolate, the anisotropy degree is minor than 5% and the medium susceptibility is 43.5 E^{-4}(SI) (**Figure 5**; [58]).

4.4. Comparison with fold and thrust belt models

There are conceptual models of the AMS patterns proposed by Saint-Bezar et al. [59], Parés and Van Der Pluijm [6] and Weil and Yonkee [60], where weakly to strongly deformed sedimentary rocks in fold and thrust belts changed their AMS response (**Figure 6**). The AMS ellipsoids that have oblate shapes in the more tectonically deformed zones change to prolate-triaxial shapes and then to oblate shapes [6, 59, 60] (**Figure 6**). These changes indicate composite sedimentary/tectonic fabrics with layer parallel shortening (LPS). A secondary LPS [60] control the lineation (K_{max}), which indicates the maximum elongation direction.

The AMS patterns of the Sierra de la Ventana fold and thrust belt follow this model [32, 52]. In this area, the ratio between T and Pj parameters change with location in the stratigraphic succession and with shortening. In the western localities, at the base of the stratigraphic succession, with major tectonic deformation and syn-tectonic magnetizations (32% of unfolding), the ellipsoids

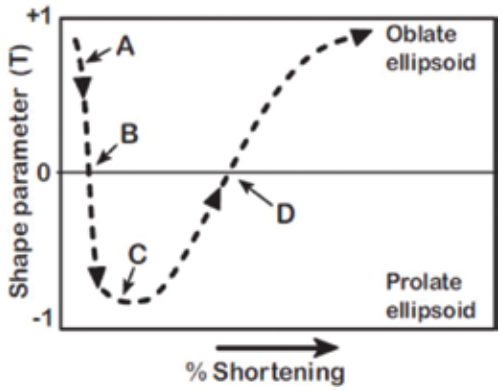

Figure 6. Conceptual model for evolution of AMS fabrics in weakly to strongly deformed sedimentary rocks in fold-thrust belts [6, 59, 60]. Idealized changes in AMS ellipsoid directions (relative to horizontal bedding) from a dominant bed-parallel sedimentary fabric (stage A), to mixed layer-parallel shortening (LPS) and sedimentary fabrics (weak LPS in stage B and moderate LPS in stage C), to strong tectonic fabric (stage D, with K_{max} either parallel to structural trend, D1, or down the dip of cleavage, D2). Changes in ellipsoid shape parameter (T).

tend to have prolate-oblate shapes. Toward the top of the sequence, with minor deformation and syn-tectonic magnetization (90% of unfolding), ellipsoids tend to have triaxial and prolate shapes. In the foreland basin, in the Claromecó Basin, with bed-parallel sedimentary fabric, the ellipsoids tend to have triaxial-oblate shapes (**Figure 5**).

All along the south margin of Gondwana, in the carboniferous-permian localities, the K_{max} axes trend northwest-southeast, parallel to the fold axes, clusters parallel to the intersection of the LPS fabric with bedding and tend to be constant in all sampled localities (**Figure 4**). The foliation (K_{min}) indicates that the shortening is related to the primary bedding. At the base of the sedimentary column, at the western most and also more deformed localities, the K_{min} axes are almost horizontal, trending southwest-northeast, perpendicular or scatter away from the bedding poles, showing a transition to a tectonic fabric with a maximum compressive stress ($\sigma 1$) parallel to that direction, indicating moderate LPS. In contrast, toward the foreland, to the eastern most localities, to the top of the stratigraphic succession, the K_{min} axes tend to orient vertically, showing a transition to a sedimentary fabric and indicating minor LPS (**Figures 4**, **6**).

5. Conclusions

Different rock types with different ages, from Devonian to Permian, were studied by AMS methodology, along the southwest margin of Gondwana, from the Sierras Australes-Claromecó Basin in the Buenos Aires province to Agua Escondida in the Mendoza province. Each sampled locality has its own magnetic signature according to their lithological and ages intrinsic characteristics. Nevertheless, in most samples there is a gradual tectonic development that overprinted differences of AMS patterns into and between the studied localities. In the Permian age rocks, as Pillahuincó Group, Carapacha Basin and Sierra Chica, there is a clear regional magnetic imprint that indicate northwest-southeast elongation directions (K_{max}) and therefore a northeast-southwest compression (K_{min}). This Permian deformation is linked to the

San Rafael orogenic phase. There is also a movement of the K_{min} from the horizontal, in the western sites at the base in the respective sequences, to the vertical in the eastern sites situated at the respective tops, and a change of the respective shape parameter. Thus, indicate a transition from a magnetic fabric with a clear tectonic imprint to transitional to sedimentary fabrics, similar to the conceptual models proposed by several authors in thrust and fold belts ([60], between others). The younger localities as Gonzales Chavez and Lopez Lecube, practically have no signature of deformation. These are evidencing pulses in the deformation intensity that diminish toward the east and an advance of the orogenic front toward the foreland basin, with the main stress from the southwest. This deformation coincides with an abrupt curvature in the apparent polar wander of Gondwana in the Upper Paleozoic ([61, 62]; **Figure 7**).

Nevertheless, in the patterns of the old rocks (Cerro de los Viejos, Cerro Colorado, Lolén Formation and Agua Escondida), the signature is no constant and the main stresses could be placed from the southwest, from the west or from the south. They have complex patterns that are related to the overlapping of different orogenic phases or to local lithological control of each locality.

In the Cavado granite and its dikes, of the Choiyoi Group, the fabrics are triaxial without axes situation common pattern, so the emplacement of these bodies seem to correspond to local effects. In the case of other dikes and the Choiyoi ignimbrite, the fabrics are similar, but they do not seem to have a clear relation with the diaclase planes. Probably the emplacement of these bodies corresponds to complex stress patterns previously installed in the region.

Figure 7. Apparent polar wander path of the south west Gondwana proposed by Tomezzoli [62] constructed from the paleomagnetic poles (PPs) selected from South America between the carboniferous and Triassic. Botton, plate accretion during Permian times.

All these data indicate that the deformation in the area came from the southwest and it attenuate during the Middle Permian, evidencing an orogenic front migration to the foreland basin at the northeast, with deformation re-activation during the Permian, indicating tectonic activity in Gondwana. Tomezzoli [12] interpreted that the Permian deformation, with a main stress from the southwest, is the consequence of a paleogeographic re-organization of Gondwana that moves to lowest latitudes to makes the Pangea continent during the Triassic. In the southwest of Gondwana, small continental plates were accreted to the main center of the continent during the Medium Devonian (**Figure 7**). This devonian deformation known as Cháñica orogenic phase in Argentina [34] have been related by Tomezzoli [12] with the Chilenia and Patagonia collision with Gondwana from the west or southwest respectively. Based on that, Tomezzoli [12] proposed the possibility that Chilenia and Patagonia where the same allochthonous plate.

The AMS data allowed interpreting, by the analysis of different localities, the regional tectonic of the southwest margin of Gondwana. It is clear that, in the cases where there is an important tectonic imprint, the technique of the AMS is very useful for the interpretation of the efforts magnitude and direction, and their variability.

Author details

Arzadún Guadalupe[1,2]*, Tomezzoli Renata Nela[2,3], Tickyj Hugo[4],
Cristallini Ernesto Osvaldo[1,2,5] and Gallo Leandro Cesar[2]

*Address all correspondence to: guadalupe.arzadun@gmail.com

1 Laboratorio de Termocronología (LaTe Andes), Vaqueros, Salta, Argentina

2 Consejo Nacional de Investigaciones Científicas y Técnicas (CONICET), Argentina

3 Departamento de Geología, Facultad de Ciencias Exactas y Naturales, Instituto de Geociencias Básicas y Aplicadas de Buenos Aires (IGEBA), Laboratorio de Paleomagnetismo D.A. Valencio, Universidad de Buenos Aires, Argentina

4 Departamento de Geología, FCEyN, Universidad Nacional de La Pampa, Argentina

5 Departamento de Geología, Facultad de Ciencias Exactas y Naturales, Laboratorio de Modelado Geológico (LAMOGE), Universidad de Buenos Aires, Argentina

References

[1] Borradaile GJ. Magnetic susceptibility, petrofrabrics and strain. Tectonophysics. 1988;**156**:1-20

[2] Graham JW. Magnetic susceptibility, an unexploited element of petrofabric. Geological Society of American Bulletin. 1954;**65**:1257-1258

[3] Gleizes G, Nédélec A, Bouchez JL, Autran A, Rochette P. Magnetic susceptibility of the mount Louis-Andorra ilmenite type granite (Pyrenees): A new tool for the petrographic

characterization and regional mapping of zoning granite plutons. Journal of Geophysical Research. 1993;**98**:4317-4331

[4] Rochette P. Magnetic susceptibility of the rock matrix related to magnetic fabric studies. Journal of Structural Geology. 1987;**9**:1015-1020

[5] Jover O, Rochette P, Lorand JP, Maeder M, Bouchez JL. Magnetic mineralogy of some granites from the French massif central: Origin of their low-field susceptibility. Phys. Earth Plant. Inter. 1989;**55**:79-92

[6] Parés JM, Van der Pluijm BA. Phyllosilicate fabric characterization by low-temperature anisotropy of magnetic susceptibility (LT-AMS). Geophysical Research Letters. 2002; **29**(24):2215

[7] Tarling DH, Hrouda F. The Magnetic Anisotropy of Rocks. London: Chapman and Hall; 1993. p. 217

[8] Keidel J. La geología de las Sierras de la provincia de Buenos Aires y sus relaciones con las montañas del Cabo y los Andes. Ministerio Agricultura Nacionale, Anales, Dirección Nacional Geología Minera, IX, 3. Buenos Aires; 1916

[9] Tomezzoli RN, Cristallini EO. Nuevas evidencias sobre la importancia del fallamiento en la estructura de las Sierras Australes de la Provincia de Buenos Aires. Revista de la Asociación Geológica Argentina. 1998;**53**(1):117-129

[10] Ramos VA. Patagonia: un nuevo continente paleozoico a la deriva? 9° Congreso Geológico Argentino (S. C. Bariloche). Actas 2. Buenos Aires; 1984. pp. 311-325

[11] Tomezzoli RN, Cristallini EO. Secciones estructurales de las Sierras Australes de la provincia de Buenos Aires: Repetición de la secuencia estratigráfica a partir de fallas inversas? Revista de la Asociación Geológica Argentina. 2004;**59**(2):330-340

[12] Tomezzoli RN. Chilenia y Patagonia: un mismo continente a la deriva? Revista de la Asociación Geológica Argentina. 2012;**69**(2):222-239

[13] Massabie A, Rossello EA, Linares E, Párica C, Powell CA. Granito Los Chilenos: una nueva unidad granítica jurásica en Cerro Colorado, Sierras Australes de Buenos Aires. Implicancias tectónicas. Revista de la Asociación Geológica Argentina. 1999;**54**:281-289

[14] Cingolani CA, Varela R. Examen geo-cronológico por el método Rubidio - Estroncio de las rocas ígneas de las Sierras Australes Bonaerenses. 5 Congreso Geológico Argentino, Actas 1; 1973. pp. 349-371

[15] Varela R, Cingolani CA, Dalla Salda LH. Edad del granito del Cerro Colorado y su implicancia geotectónica. Sierras Australes de Buenos Aires. 11° Congreso Geológico Argentino, Actas 2; 1990. pp. 279-282

[16] Rapela CW, Pankhurst RJ, Fanning CM, Grecco LE. Basement evolution of the sierra de la Ventana Fold Belt: New evidence for Cambrian continental rifting along the southern margin of Gondwana. Journal of the Geological Society. 2003;**160**:613-628

[17] Tohver E, Cawood PA, Rossello EA, Jourdan F. Closure of the Clymene Ocean and formation of west Gondwana in the Cambrian: Evidence from the sierras Australes of the southernmost Rio de la Plata craton, Argentina. Gondwana Research. 2012;**21**:394-405

[18] Tomezzoli RN, Vilas JF. Paleomagnetismo y fábrica magnética en aforamientos cercanos a las Sierras Australes de la provincia de Buenos Aires (López Lecube y González Chaves). Revista de la Asociación Geológica Argentina. 1997;**52**:419-432

[19] Pankhurst RJ, Rapela CW, Fanning CM, and Márquez M. Gondwanide continental collision and the origin of Patagonia. Earth-Science Reviews. 2006;**76**:235-257

[20] Tohver E, Cawood PA, Rossello E, López de Luchi MG, Rapalini A, Jourdan F. New SHRIMP U-Pb and $^{40}Ar/^{39}Ar$ constraints on the crustal stabilization of southern South America, from the margin of the Rio de Plata (Sierra de Ventana) craton to northern Patagonia. American Geophysical Union, Fall Meeting, Abstract T23C-2052, San Francisco; 2008

[21] Harrington HJ. Explicación de las Hojas Geológicas 33m y 34m, Sierras de Curamalal y de la Ventana, Provincia de Buenos Aires. Servicio Nacional de Minería y Geología, Boulletin. 1947;**61**

[22] Buggisch W. Stratigraphy and very low grade metamorphism of the sierras Australes de la provincia de Buenos Aires (Argentina) and implications in Gondwana correlation. Zentralbatt für Geologie und Paläontologie. 1987;**5**:819-837

[23] Cobbold PR, Massabie AC, Rossello EA. Hercynian wrenching and thrusting in the sierras Australes Foldbelt, Argentina. Hercynica. 1986;**2**:135-148

[24] Iñiguez AM, Andreis RR. Caracteres sedimentológicos de la Formación Bonete, Sierras Australes de la provincia de Buenos Aires. Reunión Geológica de las Sierras Australes Bonaerenses. Provincia de Buenos Aires. Comisión de Investigaciones Científicas. La Plata; 1971. pp. 103-120

[25] Von Gosen W, Buggisch W, Krumm S. Metamorphism and deformation mechanisms in the sierras Australes fold and thrust belt (Buenos Aires Province, Argentina). Tectonophysics. 1989;**185**:335-356

[26] Tomezzoli RN. La Formación Tunas en las Sierras Australes de la Provincia de Buenos Aires. Relaciones entre sedimentación y deformación a través de su estudio paleomagnético. Revista de la Asociación Geológica Argentina. 1999;**54**(3):220-228

[27] Cingolani CA, Berry CM, Morel E, Tomezzoli RN. Middle Devonian Lycopsids from high southern palaeolatitudes of Gondwana (Argentina). Geological Magazine. 2002;**139**:641-649

[28] Archangelsky S, Cúneo R. Zonación del Pérmico continental de Argentina sobre la base de sus plantas fósiles, 3° Congreso latinoamericano Paleontológico, México. Memoria; 1984. pp. 143-153

[29] Alessandretti L, Philipp RP, Chemale F, Brückmann MP, Zvirtes G, Metté V, Ramos VA. Provenance, volcanic record, and tectonic setting of the Paleozoic Ventania Fold Belt and the Claromecó Foreland Basin: Implications on sedimentation and volcanism along the southwestern Gondwana margin. Journal of South American Earth Sciences. 2013;**47**:12-31

[30] López Gamundi OR, Fildani A, Weislogel A, Rossello E. The age of the tunas formation in the sauce Grande basin-Ventana fold belt (Argentina): Implications for the Permian evolution of the southwestern margin of Gondwana. Journal of South American Earth Sciences. 2013;**45**:250-258

[31] Ramos VA, Chemale F, Naipauer M, Pazos PJ. A provenance study of the Paleozoic Ventania system (Argentina): Transient complex sources from western and eastern Gondwana. Gondwana Research. 2013;**26**:719-740

[32] Arzadún G, Tomezzoli RN, Cesaretti NN. Tectonic insight based on anisotropy of magnetic susceptibility and compaction studies in the sierras Australes thrust and fold belt (southwest Gondwana boundary, Argentina). Tectonics. 2016a;**35**(4):1015-1031

[33] López Gamundi OR, Conaghan PJ, Rossello EA, Cobbold PR. The tunas formation (Permian) in the sierras Australes fold belt, east central Argentina: Evidence for syntectonic sedimentation in a foreland basin. Journal of South American Earth Sciences. 1995;**8**(2): 129-142

[34] Azcuy CL, and Caminos R. 1987. Diastrofismo. En Archangelsky S., (ed.) El Sistema Carbonífero en la República Argentina, Academia Nacional de Ciencias, Córdoba: 239-251

[35] Tickyj H. Estructura y petrología del basamento cristalino de la región centro - sur de la provincia de La Pampa, Argentina. Tesis Doctoral. La Plata: Universidad Nacional de La Plata; 1999. p. 228

[36] Zappetini EO, Chernicoff CJ, Santos JO, Mc Naughton NJ. Los esquistos neoproterozoicos de Santa Helena, Provincia de La Pampa, Argentina: edades u-pb shrimp, composición isotópica de hafnio e implicancias geodinámicas. Revista de la Asociación Geológica Argentin; 2010

[37] Linares E, Llambías EJ, Latorre CO. Geología de la provincia de La Pampa, República Argentina y Geocronología de sus rocas metamórficas y eruptivas. Revista de la Asociación Geológica Argentina. 1980;**35**(1):87-146

[38] Tickyj H, Dimieri LV, Llambías EJ, Sato AM. Cerro de los Viejos (38° 28′ S - 64° 26′O): cizallamiento dúctil en el sudeste de La Pampa. Revista de la Asociación Geológica Argentina. 1997;**52**(3):311-321

[39] Llambías EJ, Quenardelle S, Montenegro T. The Choiyoi group from Central Argentina: A subalkaline transitional to alkaline association in the craton adjacent to the active margin of Gondwana continent. Journal of South American Earth Sciences. 2003;**16**:243-257

[40] Quenardelle SM, Llambías EJ. Las riolitas de Sierra Chica (37°S, 65°O): un centro eruptivo gondw'anico en el bloque del Chadileuvú, provincia de La Pampa. Revista de la Asociación Geológica Argentina. 1997;**52**(4):549-558

[41] Rapela CW, Pankhurst RJ, Llambías EJ, Labudía C, Artabe A. "Gondwana" magmatism of Patagonia: Inner cordilleran calc-alkaline batholiths and bimodal volcanic provinces, Proc. Third Int. Symp. Andean Geodynamics; 1996. pp. 791-794

[42] Domeier M, Van der Voo R, Tohver E, Tomezzoli RN, Vizan H, Torsvik TH, Kirshner J. New late Permian paleomagnetic data from Argentina: Refinement of the apparent polar wander path of Gondwana. Geochemistry, Geophysics, Geosystems. 2011;**12**(7). DOI: 10.1029/2011GC003616

[43] Melchor RN. Redefinición estratigráfica de la Formación Carapacha (Pérmico), Provincia de La Pampa, Argentina. Revista de la Asociación Geológica Argentina. 1999;**54**(2):99-108

[44] Melchor RN, César SN. Algunos elementos paleoflorísticos de la Formación Carapacha (Pérmico inferior), provincia de La Pampa, República Argentina. Ameghiniana. 1991;**28**:347-352

[45] Melchor RN, César SN. Permian floras from Carapacha Basin, la Pampa Province, central Argentina. Description and importance. Geobios. 1997;**30**(5):607-633

[46] Melchor RN. Sedimentología de las unidades paleozoicas aflorantes del centro–oeste de la provincia de La Pampa, Argentina. Tesis doctoral inédita. La Plata: Universidad Nacional de La Plata; 1995. p. 272

[47] Tickyj H, Tomezzoli RN, Basei MA. Edad U-PB del Granito Lomas de las Piedras de Afilar, Distrito Minero Agua Escondida, Mendoza. XII Jornadas Pampeanas de Ciencias Naturales. CD Resúmenes. Santa Rosa, La Pampa, Argentina; 2016

[48] González Díaz EF, García HH. El hallazgo del neopaleozoico plantífero en el área de Agua Escondida (SE de Mendoza y NO de La Pampa). 3° Jornadas Geológicas Argentinas (Comodoro Rivadavia 1966), Actas, 1; 1968. pp. 341-354

[49] González Díaz EF. Descripción Geológica de la Hoja 30e, Agua Escondida, provincias de Mendoza y La Pampa. Servicio Nacional Minero Geológico, Boletín. 1972;**135**:1-78

[50] Narciso V, Mallimacci H, SantaMaría G, Sepúlveda E, Zanettini JM. Hoja geológica 3769-II, Agua Escondida. Provincias de Mendoza y La Pampa. Vol. 300. Buenos Aires: Instituto de Geología y Recursos Minerales, Servicio Geológico Minero Argentino. Boletín; 2007. p. 39

[51] Jelinek V. Characterization of the magnetic fabrics of rocks. Tectonophysics. 1981;**79**:63-67

[52] Arzadún G, Tomezzoli RN, Cesaretti NN. Evidencias de avances y retrocesos en la deformación a partir del estudio de la anisotropía de susceptibilidad magnética. Grupo Pillahuincó (Sierras Australes, Argentina). LatinMag Letters; 2016b. p. 4

[53] Tomezzoli RN, Arzadún G, Cristallini EO. Anisotropía de susceptibilidad magnética y paleomagnetismo en la Formación Lolén de edad devónica, Sierras Australes de la provincia de Buenos Aires. Revista de la Asociación Geológica Argentina. 2017;**74**(3):326-337

[54] Tomezzoli RN, MacDonald WD, Tickyj H. Composite magnetic fabrics from S-C granitic gneiss of Cerro de los Viejos, la pampa province, Argentina. Journal of Structural Geology. 2003;**25**(2):159-169

[55] Tomezzoli RN, Melchor R, MacDonald WD. Tectonic implications of post-folding Permian magnetizations, Carapacha basin, Argentina. Paleomagnetism in Latinoamerica, Special Volume. Earth and Planets Space. 2006;**58**:1235-1246

[56] Tomezzoli RN, Saint Pierre T, Valenzuela C. New Palaeomagnetic results from late Paleozoic volcanic units along the western Gondwana in la pampa, Argentina. Earth and Planets Space. 2009;**60**:1-7

[57] Tickyj H, Tomezzoli RN, Basei MA. Geología de la Formación Piedras de Afilar, basamento granítico del Distrito Minero Agua Escondida, Mendoza. III Simposio de Petrología Ignea y Metalogénesis Asociada, General Roca, Argentina. CD Resúmenes; 2015. pp. 158-159

[58] Battler JM. Fábrica magnética en el área de Agua Escondida, Bloque de San Rafael, Mendoza. Tesina de Licenciatura. Universidad Nacional de La Pampa; 2015. p. 95

[59] Saint-Bezar B, Herbert RL, Aubourg C, Robion P, Swennen R, Frizon de Lamotte D. Magnetic fabric and petrographic investigation of hematite bearing sandstones within ramp-related folds: Examples from the south atlas front (Morocco). Journal of Structural Geology. 2002;**24**:1507-1520

[60] Weil AB, Yonkee A. Anisotropy of magnetic susceptibility in weakly deformed red beds from the Wyoming salient, Sevier thrust belt: Relations to layer-parallel shortening and orogenic curvature. Lithosphere. 2009;**1**(4):235-256

[61] Gallo LC, Tomezzoli RN, Farjat AD and Hernández RM. Revisión de la Curva De Deriva Polar aparente de Gondwana durante el Paleozoico superior, Implicancias sobre la configuración de Pangea. Latinmag Letters, v. 6, Special Issue, Proceedings of Fourth Biennial. Sao Pablo, Brasil; 2015

[62] Tomezzoli RN. The apparent polar wander path for South America during the Permian-Triassic. Gondwana Research. 2009;**15**:209-215

Chapter 3

Bureya-Jiamusi Superterrane: Tectonic and Geodynamic Processes in Late Mesozoic - Cenozoic

Derbeko Inna

Additional information is available at the end of the chapter

http://dx.doi.org/10.5772/intechopen.72538

Abstract

Bureya-Jiamusi superterrane (BJS) is a component of the Amur plate. This is one of the most complex and controversial structures of the eastern Asia. The bulk of the "body" superterrane is located in China, where it is actively researched by the Chinese scientists. The northern border of the structure is directly on the territory of the Amur region and is defined by the boundary of the Mongol-Okhotsk orogenic belt. By Parfenov, the superterrane is bordered by the Paleozoic-early Mesozoic orogenic belts and the North China plate. But there are other ideas about the spatial location of the BJS. All the suggested geodynamic reconstructions of the studied region take into account the interdependence between North-Asian and China-Korea plates and plates of the Pacific basin oceanic crust. The suggested work attempts to show the dependence of the evolution of the Bureya-Jiamusi superterrane on the surrounding geological objects in the late Cretaceous-Cenozoic interval.

Keywords: tectonic, geodynamic, Bureya-Jiamusi superterrane, Mongol-Okhotsk orogenic belt, late Mesozoic, Cenozoic

1. Introduction

Bureya-Jiamusi superterrane is a component of the Amur plate [10, 11, 24, 25, 33]. It is situated in the southern frames of Mongol-Okhotsk orogenic belt, which was formed as a result of closure of Mongol-Okhotsk orogenic belt. The structure of the Mongol-Okhotsk orogenic belt, closure time of the basin and, correspondingly, so is the structure-tectonical situation of the framing structures at that moment have no certain definition by the scientists. One of the most difficult and debatable structures of the region is Bureya-Jiamusi superterrane. A significant part of the superterrane body is situated in the territory of China, where it is actively studied by the scientists of the country [2, 12, 14, 19, 20, 39, 42, 44–47].

The northern border of the Bureya-Jiamusi superterrane is situated directly at the territory of Amur region (Russia) and correlates with its border with Mongol-Okhotsk orogenic belt [26]. According to [25], superterrane borders with Paleozoic early Mesozoic orogenic belts on west and south: South Mongol-Khingan, Solonker, Wundurmiao and China-Korea plate (**Figure 1**). The Bureya-Jiamusi superterrane situation by [19] is the same as by [25].

As the author states [19], the southern border of superterrane is cut by Suolunshan-Central Jilin orogenic belt, which is an intermediate suture between the superterrane and the China-Korea plate. Li [19] suggests that Solonker orogenic belt includes the Bureya-Jiamusi superterrane in its structure. But there are also other ideas of the location of the Bureya-Jiamusi superterrane (**Figure 1**).

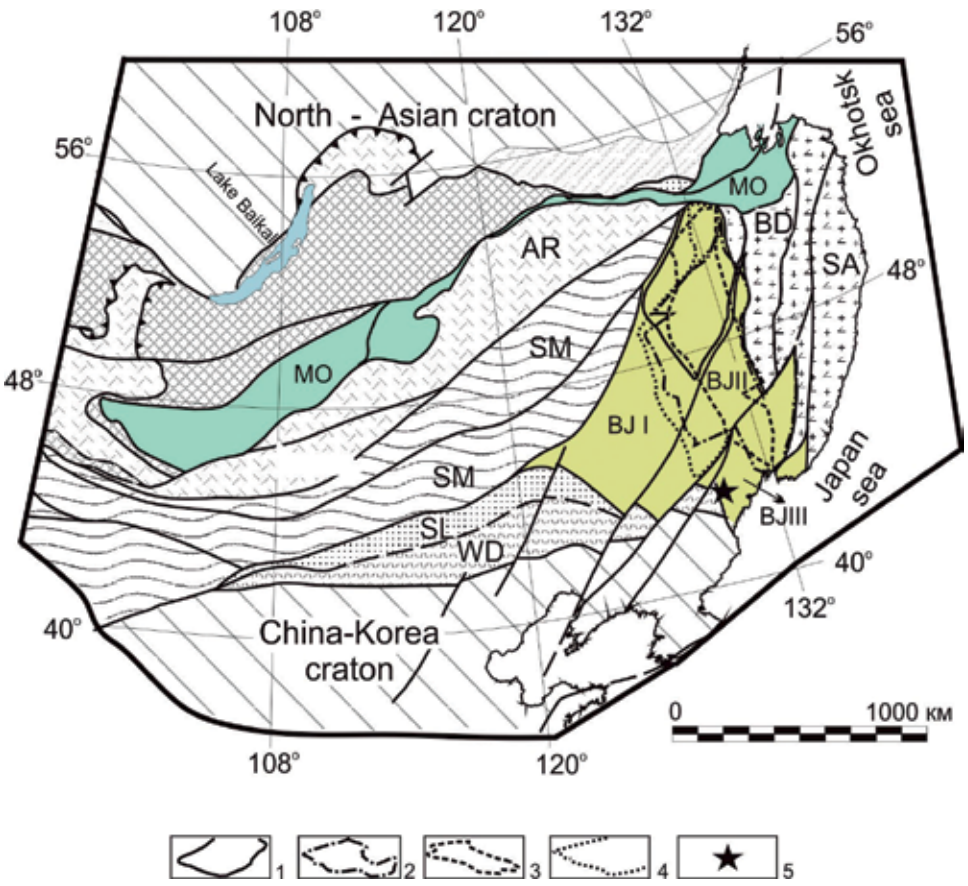

Figure 1. Scheme of the structurally tectonical composition of the Mongol-Okhotsk orogenic belt and its southern framing according to [25]. BJ – Bureya-Jiamusi superterrane and its forming terrains: I – Bureya, II – Jiamusi, III – Khanka. The outlines of the Bureya-Jiamusi superterrane are according to the data: 1 – [12]; 2 – [43]; 3 – [39]. 4 – The outline of Mudanjianiang belt is according to the data [31]. Adacitic fields with age 55.5 Myr are according to the data [2] – 5. Other alphabetic designations: MO – Mongol-Okhotsk orogenic belt, AR – Argun superterrane, SM – South Mongolian-Khingan orogenic belt, SL – Solonker orogenic belt, WD – Wundurmiao orogenic belt, BD – Badzhal terrain, SA – Honshu-Sikhotealin orogenic belt.

http://dx.doi.org/10.5772/intechopen.72538

According to the idea, the spreading of the superterrane formations is significantly limited in the southwest direction [2, 12, 14, 20, 39, 40]. The author of the suggested article attempts to analyze the geodynamic processes in late Mesozoic-Cenozoic time, which could affect the structure-tectonical formation of Bureya-Jiamusi superterrane.

2. Geological structure of the Bureya-Jiamusi superterrane

It is considered that the Bureya-Jiamusi superterrane is formed with the comparable in geological structure terrains (**Figure 1**): I – Bureya, II – Jiamusi, III – Khanka [16, 25–27].

Previously, it was stated that the foundations of these terrains are the metamorphic complexes of the Archean-Proterozoic [17, 22]. But at this time, data on the age of protoliths of metamorphic rocks of these complexes are obtained.

According to the data, the formation of the foundation occurred not earlier than late Proterozoic. Superimposed structural-metamorphic transformations are connected not with the Precambrian events but are the result of processes that occurred in the territory of Bureya-Jiamusi superterrane in Paleozoic-Mesozoic [34, 35, 40, 41].

Significant part of the Bureya-Jiamusi superterrane territory (more than 50%) is built with granitoids of Paleozoic age [17].

It is believed that the Paleozoic granites along with Devonian, Permian, and Silurian volcanogenic and terrigenous formations played a "stitching" and overlapping role in the structure of the studied terrains.

They built up more ancient formations. In turn, they were blocked and injected with Mesozoic rocks (Triassic and Cretaceous) [16]. According to the research results of the biota characteristics from terrigenous deposits of early Mesozoic (Triassic-Jurassic) of Bureya-Jiamusi superterrane, it was stated that the rocks were formed in the sea basin under conditions of significant climate changes. Such changes are characteristic of mid-latitude [21]. The formations of the Sikhote-Alin terrains that are the neighboring territory at the east were formed under tropical conditions of the marine environment of low latitudes. With all that, it was shown that the sedimentation accumulation of the rocks occurred in the single oceanic basin [21]. As the authors consider, the fact is "an important, evidence in favor of the interpretations, according to which, a number of Sikhote-Alin terrains, experienced large-scale displacement in the northern direction" [21]. Shallow marine sediments, which are replaced by coarse continental material, begin to form in Jurassic. The end of Jurassic is marked with magmatic activity in the region.

3. Stages of magmatic activity in the Bureya-Jiamusi superterrane territory

On the territory of the Bureya-Jiamusi superterrane, the continental volcanism correlates with the fore time periods: trachyriolithic complex was formed in the interval of the end of

Jurassic—135–136 Myr; the formation of calc-alkaline complexes of rocks of andesite composition occurred at 120–105 Myr. One of the complexes is a fragment of the island arc which is preserved along the border of Mongol-Okhotsk orogenic belt on Russian territory (**Figure 2**) [7]. The formation of an intraplate volcano-plutonic complex of rhyolites-alkaline trachydacytes and their plutonic comagmatites occurred 101–99 Myr [3]. According to the geochronology data, the beginning of the fourth stage can be counted since 56 Myr till our time, practically. Impulsive outpouring of volcanites, predominantly of basic composition, occurs from this moment [2, 16].

3.1. First stage: late Jurassic to 135 Myr

The beginning of the magmatic activity of late Mesozoic is marked with the formation of trachyriolite volcanic complex. These are the rocks of Itikut complex located on Russian territory. It is represented by stratified volcanogenic-terrigenous formations and subvolcanic bodies [4, 16, 22]. Stratified formations perform rift-like depressions in the north–north eastern direction. The lower part of the cut is made with tuff terrigenous rocks. Belonging of the acid volcanites to the intraplate post-collisional formations is confirmed by petro-geochemical features of the rocks [4].

According to the findings of macro- and micro-palaeoflora from the tuff-terrigenous part of the section of the cover part of the complex, the time interval might be stated as the end of Jurassic-Hauterivian [16]. The age of the volcanites of the Itikut complex is 135–136 Myr ($^{40}Ar/^{39}Ar$ method) [37] by the geochronological data. According to these data, the time of the Itikut complex rocks formation was accepted as the end of the Jurassic—135 Myr.

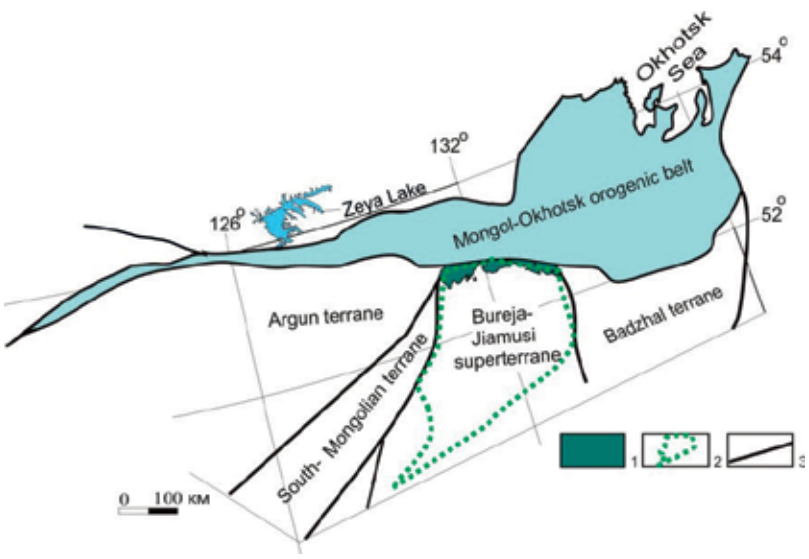

Figure 2. Spatial position of the rocks of the volcano-plutonic Burunda complex, according to the data [7] and Mudanjianiang magmatic belt, according to data [31]. The rock of the Burinda volcano-plutonic complex—(1). Outline of the northern flank Mudanjianiang belt—(2). Tectonic boundaries—(3).

3.2. Second stage: 120–105 Myr

The most widely spread volcanic complexes are of andesite composition and were formed 120–105 Myr. Geochronological data on volcanites and plutonic comagmates of the complexes correspond to the 118–105 Myr interval [2, 5]. Considering the stage of the accumulation of tuff-terrigenous coagulation at the base of stratigraphic sections of these complexes and the presence of fossil biological remains of Aptian age in the sediments, the time interval of the rock forming of the complexes is stated as 120–105 Myr [5]. Three volcanic complexes of this age have been identified on Russian territory: Pojarka, Stanolir, and Burunda [5, 16]. Rocks of Burunda complex correspond to island-arc formations by the petrochemical and geochemical characteristics [7].

It can be stated that the island arc was formed in late Mesozoic along the northern margin of superterrane (on the border with the Mongolo-Okhotsk orogenic belt in modern coordinates). Nowadays, it represents a fragment of the island arc that lies at a significant depth (about 3000 km) of the coastal-marine sediments [5, 7] (**Figure 2**). Concerning this, highlighting of the Mudanjianiang belt is of interest in the region of the Burunda rock complex island-arc development (**Figure 1**).

Age data of the Mudanjianiang belt rocks are ambiguous, which is shown by the researchers [43]. But the authors state that these formations are the analog of Burunda volcano-plutonic island-arc complex. The age interval of formation for the magmatites of Burunda complex is stated by the precision ($^{40}Ar/^{39}Ar$, Rb-Sr) methods as 111–105 Myr [5].

The volcanic formations aged 118–105 Myr are widely developed within the Jiamusi terrain in China [2]. The authors subdivide the rocks into four formations here: Tuntianying—118–116 Myr, Sanxianling—117–115 Myr, Huoshanyan—108 Myr, Jingouling—106 Myr. The affinity of these formations with the rocks of the volcanic complexes listed above that was studied in the territory of Bureya terrain (Russia) and is not only limited by age compatibility. This is confirmed by their petro- and geochemical affinity. The volcanites of the Jiamusi terrain are also moderately enriched in Sr., Zr, Hf, Ti, Y, REE and depleted in Ta and Nb according to [2].

3.3. Third stage: 101–99 Myr

The third stage of the history of geological development of the Bureya-Jiamusi was the shortest one. Apparently, some catastrophic events took place at that period. They evoke the formation of the volcanic-plutonic complex of rhyolites-alkaline trachydacytes (Solonechny). The complex is represented with the rocks of the cover, vent, subvolcanic facies and plutonic comagmates. They are depleted in Ba and Sr. and are enriched in Rb, Th, Nb, Hf, and Zr. The age of the volcanites determined by the $^{40}Ar/^{39}Ar$ method is 99–101 Myr [8, 36], which corresponds to the alb.

3.4. Forth stage: 56 Myr to Cenozoic

In the interval 99–56 Myr, the territory of Bureya-Jiamusi superterrane is in a state of rest; in fact, it is a platform where coarse clastic terrigenous deposits accumulate. Impulsive outpouring of volcanites, predominantly of basic composition, occurs about 56 Myr ago and, in

fact, up to our time—260 years ago (bass Nemarhe river—mineral spring Udalyanchi, China). Herewith, typical adakites were formed in the frames of the southern flank of the superterrane—on the border with the orogenic belt of Wundurmiao [2]. The age of adakitic rocks is 55 Myr. All the following magmatites (less than 20 Myr) correlate with the intraplate formations by their geochemical characteristics.

4. Tectonic position of the Bureya-Jiamusi superterrane

Ideas about the location of the Bureya-Jiamusi superterrane in the Late Mesozoic-Cenozoic are quite various. Thus, according to [33] the joining of Bureya-Jiamusi superterrane to Argun superterrane (through South Mongolian-Khingan belt or Sungliao block according to the views of the Chinese geologists) occurred in the second half of Paleozoic. It accreted to the Chinese-Korean craton in late Permian [46]. And later, being a part of Amur plate, together with the Chinese-Korean craton, superterrane moved north and accreted to Siberian platform, forming Mongol-Okhotsk orogenic belt and provoking closure of Mongol-Okhotsk basin. Different authors suggest various time stages of the process of the basin closure: in the early Cretaceous [32], in the Late Jurassic [46], or at the end of the Paleozoic [26].

It is known that the union of large geological objects, as a rule, is accompanied (fixed) by magmatic manifestations. The following stages of volcanic activity are set for the northern flanks of the Argun superterrane and the South Mongolian-Khingan (Sunglao) orogenic belt: 147–138 Myr—volcano-plutonic complex of adakite granites—trachyriolites; 140–122 Myr—differentiated calc-alkaline volcano-plutonic complex; 119–97 Myr—bimodal volcano-plutonic complex; 94-cognac (88?)—absarokite-trachyandesite intraplate [3, 6, 37]. Absolutely other age sequence of Bureya-Jiamusi superterrane magmatic activity is noted in late Mesozoic.

In the author's opinion, the final closure of the Mongolian-Okhotsk basin occurred in the interval 119–97 Myr and was accompanied by the formation of bimodal volcano-plutonic complexes in the frames of the Mongolo-Okhotsk belt [3]. So far, it can be stated that an entirely different age sequence of magmatic activity is noted in the late Mesozoic within the Bureya-Jiamusi superterrane. And the magmatites formed at the same time have disparate material characteristics with late Mesozoic volcanites of the Argun superterrane and the South Mongolian orogenic belt. The fact that the closure of Mongol-Okhotsk orogenic belt was accompanied by the formation of riftogenic structures in its frames, made by the bimodal complexes formations, is confirmed by the evolution of the western flank of the Mongol-Okhotsk orogenic belt [1]. The absence of bimodal complexes in the territory of Bureya-Jiamusi superterrane [4, 5] can be an evidence of the fact that the studied superterrane did not participate in the closure of the Mongol-Okhotsk basin, that this geological object represented an independent structure in the late Mesozoic.

The idea of the tectonic boundary of the Bureya-Jiamusi superterrane with the Badzhal and Honshu-Sikhotealin orogenic belts is almost unambiguous for all authors. And the ideas of the researchers of the eastern structures and the Bureya-Jiamusi superterrane collision time, which fits into the interval 155–125 Myr [16], are close.

http://dx.doi.org/10.5772/intechopen.72538

5. Geodynamic evolution of the Bureya-Jiamusi superterrane

The Bureya-Jiamusi superterrane tectonic development scheme for the territory of China was developed back in 1994 by Liu Zhaojun with co-authors [47]. According to this scheme, the stretching prevailed in the region in late Jurassic-early Chalk. It was triggered by changes in the movement of the Izanagi ocean plate. As a result, rift-like structures were formed about 135 Myr ago. These structures were filled with of coal-bearing precipitates and volcanites of acid composition. In the territory of Russia, within the Bureya-Jiamusi superterrane, a similar volcanic complex with an age of magmatic component of 136–135 Myr [4, 37] is formed during this period. The territory of Bureya-Jiamusi superterrane represented a passive continental margin and, probably, was at rest approximately 135–120 Myr. According to palinspastic reconstructions (Bretshtein and Klimov [16] and Didenko with coauthors [9]), Bureya-Jiamusi superterrane was an independent geological body during this period. It drifted on the Izanagi oceanic plate in the northwestern (close to northern) direction with a speed of 30–20 cm per year [23]. Magmatic activity occurred throughout the territory of Bureya-Jiamusi superterrane during the interval of 120–99 Myr actually [4, 5, 30, 38].

According to the palinspastic data of Bretshtein and Klimov [16], the Bureya-Jiamusi superterrane accretion to the Badzhal terrain occurred in post-Jurassic. It was shown that the formation of volcanites with geochemical marks of the suprasubduction type took place 120–105 Myr [2, 4, 5, 7]. Based on the data, it can be assumed that the subduction processes covered almost the entire territory of the Bureya-Jiamusi superterrane during this period. We can consider the following as one of the possible tectonic scenarios: subduction processes are caused by the displacement of a younger and, therefore, more plastic Badzhal terrain to older formations of the Bureya-Jiamusi superterrane, which has more power and rigidity.

What was the cause of this? According to paleomagnetic definitions [23], the Izanagi plate reversed its direction from north-west to northeast 119 Myr. And although the angle of rotation was insignificant, and the speed changed by only 0.6 cm per year (from 21.1 to 20.5 cm/year), it could be enough for the interaction of these geological objects to occur. Proceeding from such a tectonic scenario, the next stage of magmatic activity will be more understandable. Catastrophic events that were accompanied by the formation of an intraplate volcano-plutonic complex of acidic-alkaline rocks at the contact of Bureya-Jiamusi superterrane and Badzhal terrain occurred about 101–99 Myr [8, 36]. Therefore, it is assumed as the most likely scenario, that during the subduction process a sharp break (breakage) and a plunge of the slab of Badzhal terrain into the asthenospheric "window" occurred. This was, naturally, accompanied by an active and short-term formation of the rocks of the intraplate volcano-plutonic complex [4, 8, 36] (**Figure 3**).

According to paleomagnetic data, for the main tectonic units of the Far East south [16] in the Jurassic-Neogenic interval, the Bureya-Jiamusi superterrane was at a very considerable distance from the continental margin of Asia. Similar research works [18] prove that the width of the Mongolo-Okhotsk paleobasin in the late Jurassic was about 3000 km. Paleomagnetic

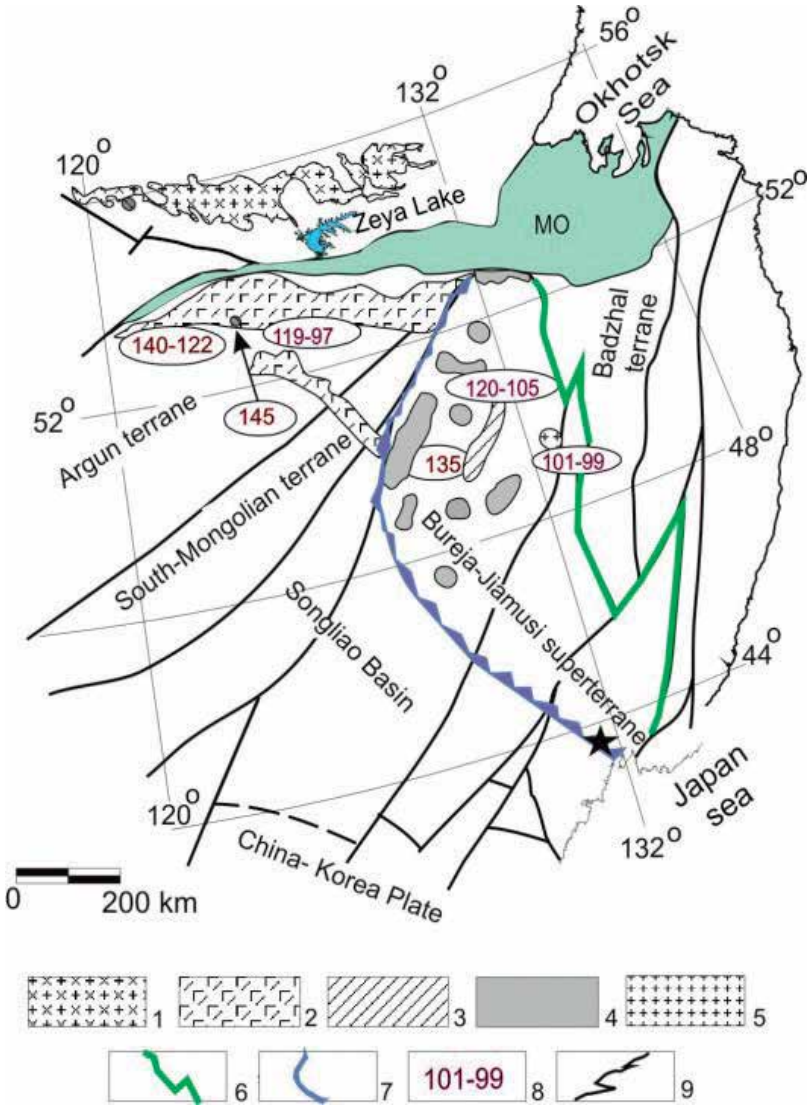

Figure 3. Hypothetical scheme of the spatial position of the Bureya-Jiamusi superterrane, compiled from original data and materials [2, 12, 25, 31, 39, 43]. Areas of distribution of rocks of late Mesozoic volcano-plutonic complexes: (1–2) differentiated and bimodal: mainly plutonic (1), mainly volcanic (2); volcano-plutonic complexes of Bureya-Jiamusi superterrane; (3–5) with the late Jurassic age—135 Myr (3), 120–105 Myr (4), 101–99 Myr (5). The boundaries of superterrane (6–7): subduction boundaries (6), transforming boundaries (7). Age of the magmatic rocks (8). Other tectonic boundaries (9).

determinations for the terrains of the Sikhote-Alin orogenic belt structures bordering the superterrane from the east [9, 28, 29] showed that they were much more south of the 30th parallel 123 ± 22 Myr. All this confirms the assumption that Bureya-Jiamusi superterrane was located at a considerable distance from its current location and was an independent geological object in late Mesozoic. Any magmatic activity in the Bureya-Jiamusi superterrane is absent (not established) in the interval 99–56 Myr.

Most likely, the drift of a collage of terrains, now, according to the motion of the ocean plate Izanagi, occurred in this period. The Izanagi plate moved to the northwest at a speed of 23.5 cm per year, and then in the western direction (85–74 Myr) at a speed of 20.2 cm per year [23] during 100–85 Myr time period. It can be assumed that this movement continued until the final joining of the Bureya-Jiamusi superterrane to the eastern edge of the Asian continent. If we accept the fact that tectonic rearrangements are usually accompanied by magmatic events, it can be stated that its accession to the east of the Asian continent took place approximately 56–55 Myr. This is confirmed by the appearance of adakite fields in the accretion place of the Bureya-Jiamusi superterrane and the orogenic belt of Wundurmiao and the China-Korean plateau (**Figure 1**) aged 55.5 Myr [2].

Mesozoic adakite granitoids and their volcanic analogs are identified and studied during the last decade in such regions as Romania, Turkey, Korea, East, and Southwest China. According to the generalized analysis of petro- and geochemical characteristics, these rocks are associated with subduction processes [13].

Complex tectonic rearrangements comparable to the transformational situation of the Californian type occurred when the Bureya-Jiamusi superterrane collided with the continental margin of Asia [15]. Surely, the subduction moments were present among the processes accompanying the transformational interaction of the two continental margins. And farther, the pulsation outflow of lavas of the main-medium composition with increased alkalinity and geochemical characteristics of intraplate magmatism [4] takes place actually up to now.

6. Conclusion

All the suggested geodynamic reconstructions of the studied region take into account the interdependence between North-Asian and China-Korea plates and plates of the Pacific basin oceanic crust [16]. The suggested work attempts to show the dependence of the evolution of the Bureya-Jiamusi superterrane on the surrounding geological objects in the late Cretaceous-Cenozoic interval. As a result of the analysis of the original and extensive literature, it is suggested that magmatic activity—its manifestations and activity changes—in the Bureya-Jiamusi superterrane territory correlates quite well with the geodynamic events occurring in the late Mesozoic-Cenozoic, not only on the continental margin of Asia but also within the evolution of oceanic plates of the Pacific basin (plate Izanagi). Comparison of the time stages, material composition, and tectonic positions of the Bureya-Jiamusi superterrane in this time interval indicates its belonging to the structures of the Pacific mobile belt.

Author details

Derbeko Inna

Address all correspondence to: derbeko@mail.ru

Laboratory of Geodynamic and Petrogenesis, Institute of Geology and Nature Management, FEB RAS, Russia

References

[1] Bogatikov OA, Kovalenko VI, editors. Magma Types and their Sources in the Earth's History. Moscow: IGEM RAS; 2006;**2**:278

[2] ChaoWen L, Feng G, WeiMing F, XiaoFeng G. Ar-Ar geochronology of Late Mesozoic volcanic rocks from the Yanji area, NE China and tectonic implications. Science in China Series D Earth Sciences. 2007;**5**(4):505-518. DOI: 10.1007/s11430-007-2046-9

[3] Derbeko IM. Bimodal volcano-plutonic complexes in the frames of Eastern member of Mongol-Okhotsk orogenic belt, as a proof of the time of final closure of Mongol-Okhotsk basin. In: Stoppa F, editor. Updates in Volcanology – A Comprehensive Approach to Volcanological Problems. Rijeka, Croatia: In Tech; 2012. pp. 99-124. DOI: 10.5772/23281

[4] Derbeko IM. Later Mesozoic volcanism of Mongol-Okhotsk belt (eastern end and the southern framing of eastern member of the belt). Saarbruken, Germany: LAP LAMBERT Academic Publishing GmbH&Co.KG; 2012. 97 p

[5] Derbeko IM. The role of the andesitic volcanism in the understanding of Late Mesozoic tectonic events of –Jziamysi superterrane, Russian Far East. In: Nemeth K, editor. Updates in Volcanology – New Advances in Understanding Volcanic Systems. Croatia: In-Tech; 2013. pp. 91-115. DOI: 10.5772/51908

[6] Derbeko IM. Adakitic magmatism as an indicator of the onset of the subduction regime along the southern edging of the eastern link of the Mongol-Okhotsk orogenic belt. In: Geological Processes in the Lithospheric Plates Subduction, Collision, and Slide Environments. Proceedings of Third Russian Conference with Foreign Participants. 20-23 September 2016, Vladivostok. Vladivostok: Dalnauka; 2016. pp. 268-271

[7] Derbeko IM, Agaphonenko SG. Formations of the Island Arc of the southern flank of the eastern flank of the Mongol-Okhotsk orogenic belt. In: Proceedings of the IV All-Russian Symposium on Volcanology and Paleovolcanology, Volcanism and Geodynamics, 22-27 September, Petropavlovsk-Kamchatsky. Petropavlovsk-Kamchatsky: IVS FEB ARS. Vol. 1. 2009. pp. 344-347

[8] Derbeko IM, Sorokin AA, Ponomarchuk VA, Sorokin AP. Timing of Mesozoic magmatism in Khingan-Okhotsk volcano-plutonic belt (Russian Far East). Geochimica et Cosmochimica Acta. 2004;**68**(11):A226

[9] Didenko AN, Efimov AS, Nelyubov PA, Sal'nikov AS, Starosel'tsev VS, Shevchenko BF, Goroshko MV, Gur'yanov VA, Zamozhnyaya NG. Structure and evolution of the Earth's crust in the region of junction of the Central Asian fold belt and the Siberian platform: Skovorodino–Tommot profile. Geology and Geophysics. 2013;**54**(10):1583-1599

[10] Gatinsky YG, Rundquist DV. Geodynamics of Eurasia – Plate tectonics and block tectonics. Geotectonics. 2004;**38**(1):3-20

[11] Gatinsky YG, Rundquist DV, Vladova G, Prochorova T. Up-to-date geodynamics end seismicity of Central Asia international. Journal of Geosciences. 2011;**2**:1-12. DOI: 10.4236/ijg/2011.21001

[12] Guo F, Fan W, Gao X, Li C, Miao L, Zhao L, Li H. Sr-Nd-Pb isotope mapping of Mesozoic igneous rocks in NE China: Constraints on tectonic framework and Phanerozoic crustal growth. Litos. 2010;**120**:563-578. DOI: 10.1016/j.lithos.2010.09/020

[13] Gusev AI. Petrology of Adakite Granitoids. Publishing House: Academy of Natural History; 2014. 242 p

[14] Huang B, Piper JDA, Zhang C, Li Z, Zhu R. Paleomagnetism of Cretaceous rocks in the Jiaodong Peninsula, eastern China: Insight into block rotations and neotectonic deformation in eastern Asia. Journal of Geophysical Research. 2007;**112**:1-21. DOI: 10.1029/2006JB004462

[15] Khanchuk AI. Paleogeodynamic Analysis of Ore Deposit Formation in the Russian Far East. 2009. Available from: http://w.w.w.fegi.ru/FEGI/sbornik2/art00/art00.htm

[16] Khanchuk AI, editor. Geodynamics, magmatism and metallogeny of East of Russia. Book 1. Vladivostok: Dalnauka; 2006. 572 p

[17] Krasnyi LI, Peng Yungbiao, editors-in-chief. Geologycal map of Priamurie and neighbouring territories. Scale 1:2 500 000. Explanatory note, St. Petersburg – Blagoveschensk – Harbin: Ministry of nature resources of Russian Federation, Ministry of geology and mineral resources of China. 1999. 135 p

[18] Kravchinsky VA, Cogne J-P, Harbert W, Kuzmin MI Evolution of the Mongol-Okhotsk ocean with paleomagnetic data from the suture one. Geophysical Journal International 2002;**148**:34-57

[19] Li J-Y. Permian geodynamic setting of Northeast China and adjacent regions: Closure of the Paleo-Asian Ocean and subduction of the Paleo-Pacific plate. Journal of Asian Earth Science. 2006;**26**:207-224. DOI: 10.1016/j.jseaes.2005.09.001

[20] Ma Q, Xu Y-G, Griffin W, Ma L. Coexisting early cretaceous high-mg andesites and adakitic rocks in the North China Craton: The role of water in intraplate magmatism and cratonic destruction. Journal of Petrology. 2016;**6**:1-30. DOI: 10.1093/petrology/egw040

[21] Markevich PV, Zacharov YD, editors. Triassic and Jurassic of the Sikhote-Alin.: volcanogenic-sedimentary complex, paleobiogeography. Book 2. Vladivostok: Dal'nauka; 2008. 300 p

[22] Martiniuk MV, Ryamov SA, Kondrateva VA. Scheme of the Correlation Magmatic Complexes Khabarovsk Region and Amur Region. Khabarovsk: IGU "Dalgeologia"; 1990. 215 p

[23] Maruyama S, Seno T. Orogeny and relative plate motions: example of the Japanese Islands. Tectonophysics. 1986;**127**:305-329. DOI: 0040-1951/86/$03.50

[24] Natalin BA. Mesozoic accretion and collision tectonics of the Far East south of the USSR. Russian Journal of Pacific Geology. 1991;**5**:3-23

[25] Parfenov LM, Berezin NA, Khanchuk AI, Badarch G, Belichenko VG, Bulgatov AN, Dril SI, Kirillova GL, Kuzmin MI, Nokleberg U, Prokopiev AV, Timofeev VF, Tomurtogoo O,

Yan H. The model of the formation of the orogenic belts of Central and Northern-Eastern Asia. Russian Journal of Pacific Geology. 2003;**22**(6):7-41

[26] Parfenov LM, Bulgatov AN, Gordienko IV. Terrains and the formation of the orogenic belts of Transbaikal. Russian Journal of Pacific Geology. 1996;**15**(4):3-15

[27] Parfenov LM, Popeko LI, Tomurtogoo O. Problems of tectonic of Mongol-Okhotsk orogenic belt. Russian Journal of Pacific Geology. 1999;**18**(5):24-43

[28] Peskov AY, Archipov MV, Didenko AN. Paleomagnetic studies of the Mesozoic sedimentary rocks of the Kiselev-Manominsk and Kemsky terranes of the Sikhote-Alin orogenic belt, tectonics of modern and ancient suburbs. In: Proceedings of the XLIX Tectonic Meeting; 3-7 February 2017. Moscow: GEOS; 2017. pp. 58-60

[29] Pisarevsky SA. New edition of the Global Paleomagnetic Database. EOS Transactions American Geophysical Union. 2005;**86**(17):170

[30] Rasskasov SV, Ivanov AV, Travin AV, Brandt IS, Brandt SB. ^{40}Ar-^{39}Ar and K-Ar dating of the volcano rocks of Albian of Priamuria and Transbaikal. In: Isotopic Geochronology in Solving Problems of Geodynamics and Ore Genesis. St. Petersburg: Center of Information Culture; 2003. pp. 410-413

[31] Shao J, Tang KD. Terranes in Northeast China and Evolution of Northeast Asia Continental Margin. Chinese, Beijing: Seismic Press; 1995. p. 185

[32] Sharov VN, Fefelov NI, Jablonovsky BV. Dating of the low Proterozoic stratificated formations of Patomsky plateau Pb/Pb method. Doklady of the Earth Science. 1992; **324**(5):1081-1084

[33] Sonenshein LP, Kuzmin MN, Natapov LM. Tectonics of Lithosphere Plates on the Territory of USSR. Vol. 1. Moscow: Nedra; 1990. p. 328

[34] Sorokin AA, Kotov AB, Sal'nikova EB, Sorokin AP, Yakovleva SZ, Fedoseenko AM, Plotkina YV. First data on the age of the Early Paleozoic granitoids of the Malohingan terrane Central Asian fold belt. Doklady Earth Sciences. 2010;**431**(2):228-232

[35] Sorokin AA, Kotov AB, Sal'nikova EB, Sorokin AP, Yakovleva AM, Plotkina YV, Grochvsky BM. Early Paleozoic age of granitoids of the Kivillian complex of the terrane (eastern flank of the central Asian folded belt). Doklady Earth Sciences. 2011;**440**(3):392-396

[36] Sorokin AA, Ponomarchuk VA, Derbeko IM, Sorokin AP. Geochronology and geochemical peculiarities of Mesozoic associations of Khingan-Olonoisk volcanic zone (the Far East). Stratigraphy and Geological Correlation. 2005;**13**(3):63-78

[37] Sorokin AA, Ponomarchuk VA, Kozirev SK, Sorokin AP, Voropaeva MS. New isotopic-geochronology data for Mesozoic magmatic formation of the north-east outskirts of Amur superterrane. Geology of the Pacific Ocean. 2003;**22**(2):3-6

[38] Sorokin AA, Sorokin AP, Ponomarchuk VA, Travin AV, Kotov AB, Melnikova OV. Basaltic andesites of Amur-Zeja depression in Aptian: New geochemical and ^{40}Ar/^{39}Ar – Geochronological data. Doklady on Earth Science. 2008;**421**(4):525-529

[39] Wang K-L, William LG, Kovach VP, Iizuka Y. Ancient mantle lithosphere beneath the Khanka massif the Russian Far East: In situ Re-Os evidence. [Internet]. 2015. Available from: hatp://www.researchgate.net/publication/276150676. DOI: 10.1111./ter.12157

[40] Wilde SA, Wu F. Timing of granite emplacement in the Central Asian orogenic belt of Northeastern China. Gondwana Research. 2001;**4**(4):823-824

[41] Wilde SA, Wu F-Y, Zhang X. Late Pan-African magmatism in the northeastern China: SHRIMP U-Pb zircon evidence from granitoids in the Jiamusi Massif. Precambrian Research. 2003;**122**:311-327

[42] Wu F-Y, Sun D-Y, Ge W-C, Zhang Y-B, Grant ML, Wilde SA, Gahn B-M. Geochronology of the Phanerozoic granitoids in north-eastern China. Journal of Asian Earth Sciences. 2011;**41**:1-30. DOI: 10.1016/j.jseaes.2010.11.11.014

[43] Wu F-Y, Yang J-H, Lo C-H, Wilde A, Sun D-Y, Jahn B-M. The Heilongjiang Group: A Jurassic accretionary complex in the Jiamusi massif at the western Pacific margin of northeastern China. Island Arc. 2007;**16**:156-172. DOI: 10.1111/j.1440-1738.2007.00564.x

[44] XingZhou Z, Guo Ye G, JianBo Z, Zhen Z, JianBin P, QiuLin P. Late Paleozoic-early Mesozoic tectonic evolution in the east margin of the Jiamusi massif, eastern Northeastern China. Russian Journal of Pacific Geology. 2015;**34**(1):3-12

[45] Yang B, Liu Cai, Zhou Yang, Liang Tiecheng, Tang Dayi. Study of the crust structure in the Anda-Zhaozhou-Harbin transect region using deep reflecthion method. M-SGT geophusical research group ed. Research on geophusical field and deep structural characteristics of Manzhouli – Suifenhe geoscience transekt region of China. Beijing: Seismic Publishing House. 1995. P. 100-113

[46] Zhao X, Coe RS, Gilder SA, Frost GM. Paleomagnetic constrains on the paleogeography of China: Implications for Gondwanaland. Australian Journal of Earth Sciences. 1994;**3**:643-672

[47] Zhaojun L, Xiaolin W, Wanghu L, Fang X, Manping Z. Formational mechanism of the Songliao and Hailaer Mesozoic basins of Mongholui – Suifenhe geoscience transekt region. In: M-SGT Geological Research Group, editor. Geological Research on Lithosphere Structure and its Evolution of Mongholui – Suifenhe Geoscience Transekt Region of China. Beijing: Seismic Publishing House; 1994. pp. 14-25

Chapter 4

A Discussion on the Detachment Structural Deformation and Its Influence on Pore Structure Evolution in Shale on the Western of the Xuefeng Mountain, South China

Mingliang Liang, Zongxiu Wang, Linyan Zhang, Huijun Li, Wanli Gao and Chunlin Li

Additional information is available at the end of the chapter

http://dx.doi.org/10.5772/intechopen.72245

Abstract

Detachment structures occur widely in the crust, and it is the commonest and most important deformation type developed in the region between orogenic belts and basins. Organic-rich shale, as the weak layers, usually acts as slippery layers in detachment structural deformation systems. The "comb-like" and "tough-like" fold belts on the western side of the Xuefeng Mountain result from the multilayer detachment, and their formation is different from the typical Jura type structures. The reason is that there are several detachment layers and detachment systems in the stratigraphic column from the Neoproterozoic upwards to the Mesozoic in the study area. As the stress decoupling role, the shale slippery layers tend to undergo strong deformation in the detachment systems and impacted on pore structure evolution in the shale. In order to obtain the detachment structural deformation and its influence on pore structure evolution in shale on the Middle and Upper Yangtze, the structural and textural, geochemical and mineralogical properties analysis, porosity and pore structure feature investigations are performed using shale samples collected from the same shale bed of the Longmaxi Formations (Lower Silurian) of Western of the Xuefeng Mountain, South China.

Keywords: Western of the Xuefeng Mountain, detachment deformation, tectonic deformed shale, Longmaxi shales, pore structure evolution

1. Introduction

Detachment structures occur widely in the crust, which is the result of the shearing occurring between a competent rock and an uncompetent rock, include many different types of

structures such as detachment folds and hybrid fault-propagation folds. Recently, a series of models of the detachment has been brought forwards, and the kinematics and mechanism of detachment folds is also an important branch in the studies of the thrust tectonics [1–6]. The typical detachment folds are those in the Jura Mountain in the Alps orogenic belt, in the foreland region of the Appalachian orogenic belt and in the foreland region of Cordillera orogenic belt [1, 7, 8]. And, many researches have also been carried out on the thrust tectonics in China since 1960 [9–19]. The main characteristic of these detachment folds is that they formed on the uncompetent layers such as the Triassic evaporates in the Jura Mountain [20–22]. However, most studies focus on the structure with single detachment layer, with few studies on the effects of the multilayer detachment on the derived structures except for those researches in the Jura Mountain and the Zagros Mountain [23, 24].

The deformation zone between the Huayin Mountain and Xuefeng Mountain in the eastern Sichuan, located in Middle and Upper Yangtze, is characterized by the multilayer detachments in the late Mesozoic, with discordant features in various structural styles (**Figure 1**). In the study region, the strata from the Cambrian up to the Jurassic are all covering layers in the basin, and the "comb-like" and "tough-like" fold belts result from the multilayer detachment. In terms of basic structural styles and mechanism, Liu argued that these thin-skinned structures resulted from differential erosion of box folds under the stress outside [25]. Ding et al. and Ding and Liu suggested that the folds in this region [26, 27], especially those comb-like folds, were the kink bands controlled by the buckling at the regional scale. Liu and Liu preferred that these folds were produced by the compression in the early Mesozoic and superimposed by the late

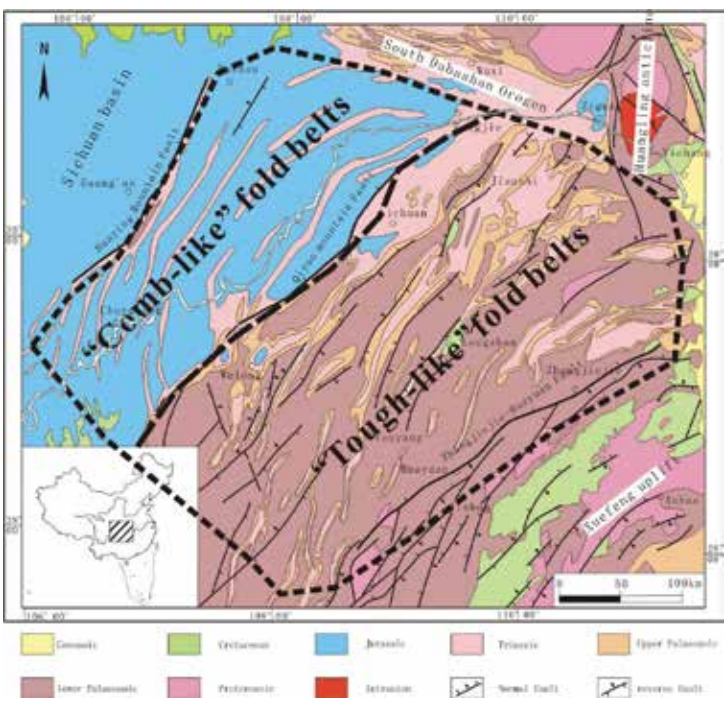

Figure 1. Geological map of western of the Xuefeng Mountain, South China.

extension [28]. Xu et al. divided this region into three structural layers [29], among which duplexes and fault-bend folds mainly form in the lower one, fault-bend folds and fault-propagation folds mainly form in the middle one and the detachment folds, fault-propagation folds and break-through structures mainly occur in the upper layer. Guo et al. further pointed out discordance occurring in various layers [30]. Yan et al. argued that multi-detachment thrusting due to the progressive compression from the southeast to the northwest resulted in the development of the structures in the study region. Two major detachment layers occur in these covering layers [10, 31], comprising the Lower Cambrian Niutitang Formation and Lower Silurian Longmaxi Formation (**Figure 2**). Organic-rich shale, as the weak layers, usually acts as slippery layers in detachment structural deformation systems in this study. The detachment layers in the study region show a wide range of deformation styles caused by shearing along the layers: A-type; S-C fabric; sheared puddings; cleavage and thrusts. The primary structure of deformed shale is damaged and the parallel bedding has almost disappeared due to deformation.

Previous studies have shown that the Upper and Middle Yangtze Plates have superior marine hydrocarbon geological conditions and immense potential for shale gas. Compared to North America, the geological conditions of gas shale reservoirs in South China are highly diversified and complicated due to the detachment structural deformation, which transformed the structure of shale seams and resulted in structure deformed shale with unique reservoir properties [32–35]. For example, as the first commercial shale gas field outside the North America, one of the most important controlling geological factors in the Fuling shale gas field in southeastern margin of the Sichuan Basin was strong structural deformation of shale [32, 33, 36]. It is necessary to study how pore structure develops in gas shale influenced by tectonic deformation. Ma et al. investigated the pore structure of the mylonitized shale sample by FESEM and N_2 adsorption analysis and found that the mylonitized shale has high specific surface area and high methane adsorption capacity [34]. Ibanez and Kronenberg have explained the deformational and microstructural changes under variable confinement

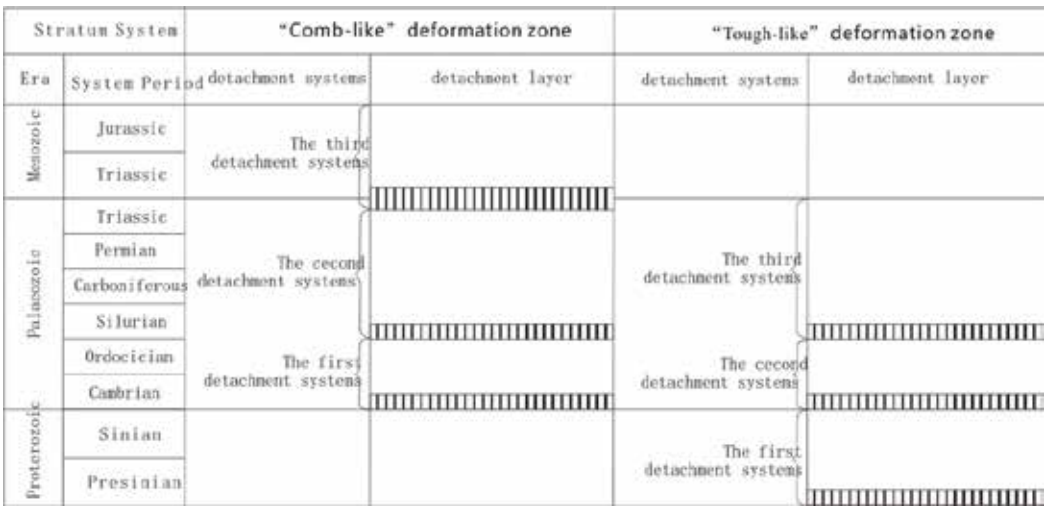

Figure 2. Distribution of detachment layers and constitution of detachment systems in western of the Xuefeng Mountain, South China.

for illite-rich shale [37]. Shale gas and coalbed methane (CBM) reservoirs are in formally grouped as unconventional because gas is trapped in part by sorption processes [38]. Several previous workers have focused on the pore characteristics and adsorption gas characteristics of tectonically deformed coals [39, 40], which provide references to the study on deformed shale. Although previous studies have provided useful insight to evolution of pore structure in shale during thermal maturity and in CBM related to deformation structures, the prediction of structural deformation change in pore structure of shale in geological condition still remains quite challenging. In the present study, pore structure feature investigations are performed using two sets of shale samples (deformed shale and undeformed shale) collected from the typical shale bed of the Longmaxi Formations (Lower Silurian) of Western of the Xuefeng Mountain, South China. The influence of structural deformation on pore structure was discussed.

2. Deformation of the detachment layers

There are two main detachment layers of shale in the covering layers in the study region, i.e., the Lower Cambrian Niutitang Formation and Lower Silurian Longmaxi Formation. These two detachment layers controlled the strong deformation of the study region during the late Mesozoic and showed different roles in different zones.

2.1. Deformation of the Cambrian system

The detachment layer is the Niutitang Formation ($\in_1$n) in the Lower Cambrian, which is mainly composed of black carbonaceous shale and black shale and about 70–200 m thick. This layer crops out in the region between Shizhu and Anhua-Xupu Fault, but the strong shearing along the layer only occurred in the region between the Cili-Dayong Fault and the Anhua-Xupu Fault.

Different types of small shear folds and thrust faults character the deformation of the detachment layer, including angular folds, congruous inverted folds, sheath folds and recumbent folds. B-type and A-type folds can be found (**Figures 3** and **4**). The fold hinges strike mainly northeast-southwest. However, the fold hinges of sheath folds trend northwest-southeast, which indicated the direction of shearing. The axial planes of these folds mainly dip to the southeast at the angle of 40–70°. Combined with sheath folds, top-to-the-northwest thrusting occurred along this detachment layer, which is similar to the deformation of the Xuefeng Mountain.

2.2. Deformation of the Silurian detachment layer

The Silurian detachment layer is composed of the Longmaxi Formation (S_1l) of the Lower Silurian. It is the thickest detachment layer (more than 2000 m) in the study region, which is mainly composed of shale with some silty mudstone and siltstone. This layer mainly distributes in Shizhu and Baojing; it also crops out to the west of Anhua-Xupu Fault. Field observations showed that the deformation of this layer mainly occurred in the region between Shizhu and Baojing (the region where the so-called narrow syncline style folds developed).

The B-type folding characters the deformation of the Silurian detachment layer. The congruent inverted fold is the main type of the folds in this layer (**Figure 5**). Most fold hinges strike

http://dx.doi.org/10.5772/intechopen.72245

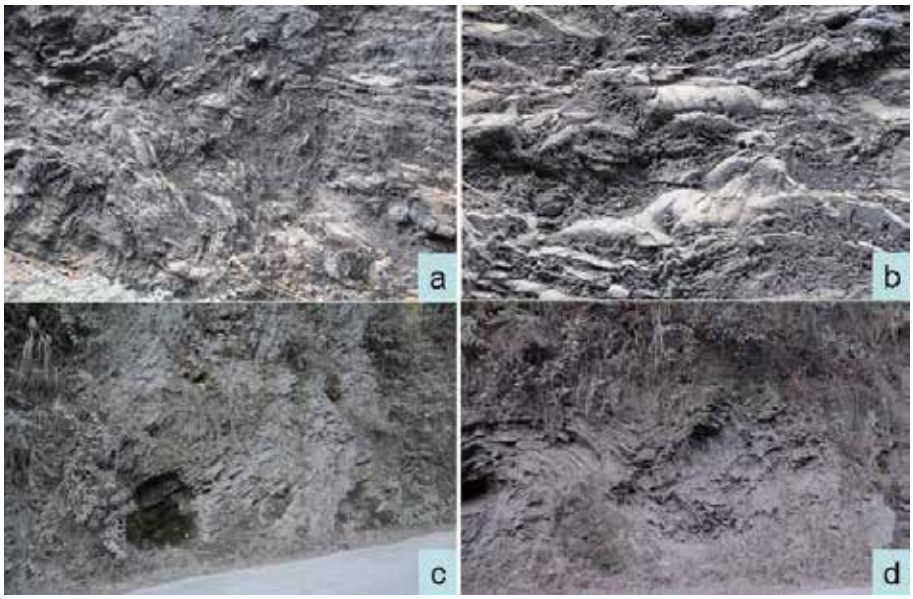

Figure 3. Shear folds formed by shear deformation in the lower Cambrian detachment layer. (a) A-type shear folding; (b) pencil structure indicates SE-NW shear (location: Labachong, Luoyixi Town, Yongshun County, Hunan); (c, d) B-type shear folding (location: Mengfu Village, Liangshuijing Town, Yuanling County, Hunan).

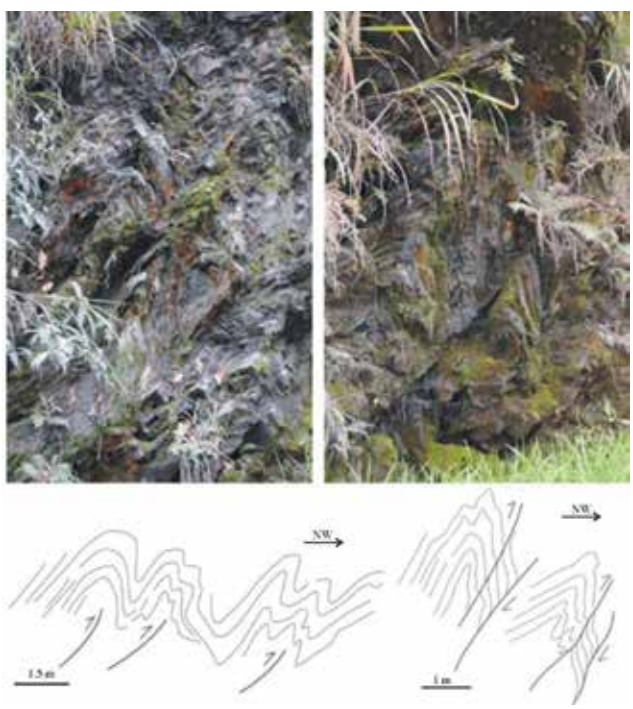

Figure 4. Assemblage of thrust faults and shear folds in the lower Cambrian (location: Fumeng Village, Liangshuijin Town, Yuanling County, Hunan).

Figure 5. B-type shear folds with SE dipping axial planes in the Silurian detachment layer (location: (a, b) Shaoha Village, Shaoha Town, Yongshun county, Hunan; (c, d) Heixi Town, Pengshui county, Chongqing).

northeast-southwest; some AB-type inverted folds whose hinges strike north-east are also found. The axial planes of these folds mainly dip to the southeast with dip angle ranging from 20 to 60°. And some inverted folds with axial plane dipping to the northwest are also developed. In addition, many minor thrust faults top to the northwest are also developed in the layer. These structures imply that the top-to-the-northwest thrusting parallel to the bedding is the main deformation mechanism, and the inverted folds with axial plane dipping to the northwest resulted from the back thrusting.

3. The discussion on mechanism of regional tectonic deformation

Many previous studies divided the deformation between the eastern Sichuan Basin and the Xuefeng Shan into the narrow anticline style fold belt, narrow syncline style fold belt and the basement-involved fold belt, which mainly resulted from the detachment folding and thrusting [10, 26, 27, 41–45]. This study showed that the so-called narrow-anticline style and narrow-syncline style folds in the eastern Sichuan Basin were named just after their geometries at regional scale; the exact original mechanism for these folds is different from that of the Jura type structures.

As mentioned in above sections, the deformation in the study region could be divided into two parts, one is the deformation of the detachment layers and the other is the deformation of rocks in the hanging walls. The bedding parallel detaching and many small-scale A-type,

http://dx.doi.org/10.5772/intechopen.72245

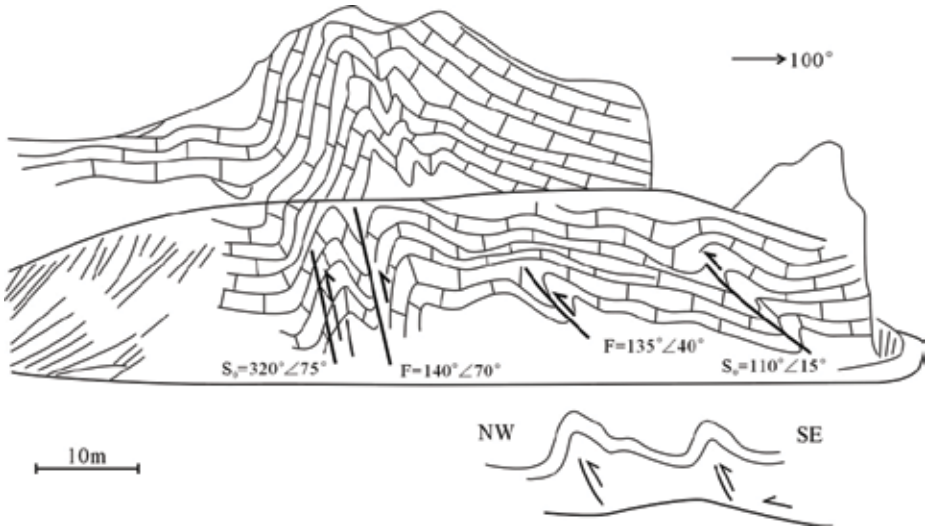

Figure 6. Widespread thrust folding in the eastern Sichuan Basin (location: Wanfo Village, Gaoleshan Town, Xianfeng County, Hubei).

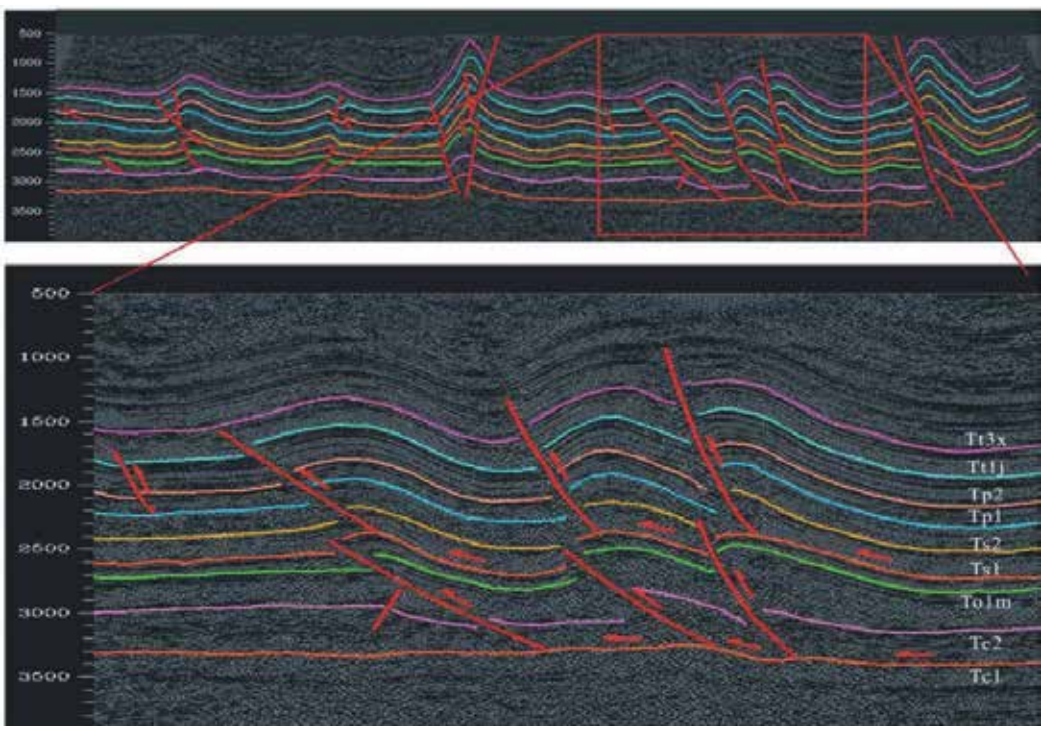

Figure 7. Multi-layer detaching-thrusting deformation section shown by the seismic reflection. Tt_3x, upper Triassic Xujiahe Fm; Tt_1j, lower Triassic Jialingjiang Fm; Tp_2, upper Permian; Tp_1, lower Permian; Ts_2, middle Silurian; Ts_1, lower Silurian; To_1m, lower Ordovician Meitan Fm; $T\epsilon_2$, middle Cambrian; $T\epsilon_1$, lower Cambrian.

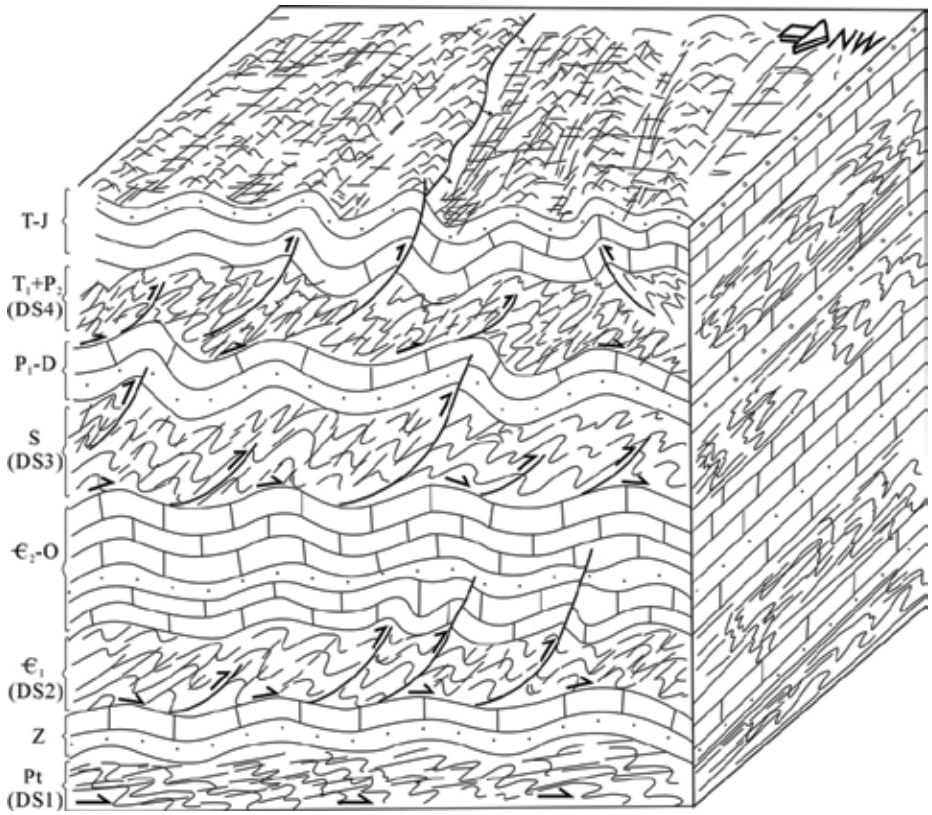

Figure 8. Block model of the deformation assemblage of multi-layer detachment and thrust fault between the Huayin Mountain and the Xuefeng Mountain. T-J, Triassic-Jurassic; T_1-P_2, lower Triassic-upper Permian; P_1-D, lower Permian-Devonian; S, Silurian; $Є_2$-O, middle Cambrian-Ordovician; $Є_1$, lower Cambrian; Z, Sinian; Pt, Precambrian (Banxi Gp); DS1, detachment layer and its number.

B-type and AB-type inverted folds, recumbent folds and small thrust faults character the deformation of the detachment layers, which generally imply the top-to-the-northwest detachment. And, the symmetrical large open folds and large reclined folds character the deformation of the non-detachment layers, and most geomorphic highs are located at the large reclined folds, such as the Huayin Shan, Tongluo Shan, Mingyue Shan, Fangdou Shan and Qiyao Shan.

Most anticlines between the Fangdou Shan and the Huayin Shan (where the narrow-anticline style folds developed) are narrow with steep northwest limbs dipping at 70–85° and shallow dipping southeast limbs dipping at 40–65°. Between the anticlines are the open synclines. And most northeast trending anticlines between the Fangdou Shan to the west and the Xuefeng Shan to the east (where the narrow-syncline style folds formed) are large open asymmetrical folds with steep northwest limbs and shallow southeast limbs except for some folds with steep southeast limbs such as the asymmetrical folds in Wanzhou along the east bank of the Yangtze River. The field observation showed that thrust faults often developed in the cores and steep limbs of these asymmetrical folds, and the thrust faults in the cores did not cut through the folds (**Figure 6**); similar characteristics could be found in the seismic profiles (**Figure 7**). These large reclined folds resulted from the thrusting; however, the thrust faults

derived from the bedding parallel shearing along the underlying detachment layers led to the deformation of overlying rocks. The above deformation was the results of thrusting and detachment, called as detachment-thrusting mechanism.

The deformation between the Huayin Shan and the Xuefeng Shan is the typical of multi-layer detachment. From the Cambrian System to the Jurassic System, the different deformations between four detachment layers and strata between detachment layers are discordant (**Figure 8**). The detachment and thrusting in every detachment layer controlled the deformation of the overlying strata. The main detachment layers controlling the deformation are different in different belts from the east to the west in the study region. Previous studies suggested that the so-called narrow-anticline style fold belt between the Huayin Shan and the Xuefeng Shan was controlled by the Silurian detachment, and the narrow-syncline style fold belt was controlled by the detachment layer between marine covering layers and the metamorphic basement, and these two types of folds are all typical Jura type detachment folds [10, 46].

4. Detachment layers in shale of Longmaxi Formation and its structural deformation characteristics

To obtain information about the influence of tectonic deformation on shale pore characteristics, the geochemical, mineralogical, structural and textural properties analysis, porosity and pore structure feature investigations are performed using two sets of shale (deformed shale and undeformed shale) collected from the same shale bed of the Longmaxi Formation (Lower Silurian) of southeast of Sichuan Basin, China. Previous studies have shown that the Upper and Middle Yangtze plates have superior marine hydrocarbon geological conditions and immense potential for shale gas. Compared to North America, the geological conditions of gas shale reservoirs in South China are highly diversified and complicated due to the detachment structural deformation, which transformed the structure of shale seams and resulted in structure deformed shale with unique reservoir properties. The detachment layers in the study region show a wide range of deformation styles caused by shearing along the layers: A-type; S-C fabric; sheared puddings; cleavage and thrusts. As the main detachment structure belt [35], the Longmaxi Formations shale layer developed multilayer subdivided slip structural deformation. The primary structure of deformed shale is damaged and the parallel bedding has almost disappeared due to deformation. The plastic deformation of shale is obvious, and the cleavage structure and cleavage surface are smooth with fine-grained powder coatings. The detachment fault mirrors (FMs), scratches and micro-fold deformation phenomena were commonly present in Longmaxi shale outcrops. A suite of samples were subset to two sets of deformed shale and undeformed shale for this study due to their variability of texture, fabric and structure properties (**Figures 9** and **10**). To evaluate the influence of detachment deformation on shale reservoir characteristics by comparing the deformed shale and undeformed sample subsets, 14 shale samples (9 undeformed samples from 3 beds) were collected from this Yongshun outcrop (**Figure 9**). However, not all the 14 samples were examined. All samples were analyzed to determine the organic geochemistry and mineralogy, the undeformed samples taken from same bed have similar composition

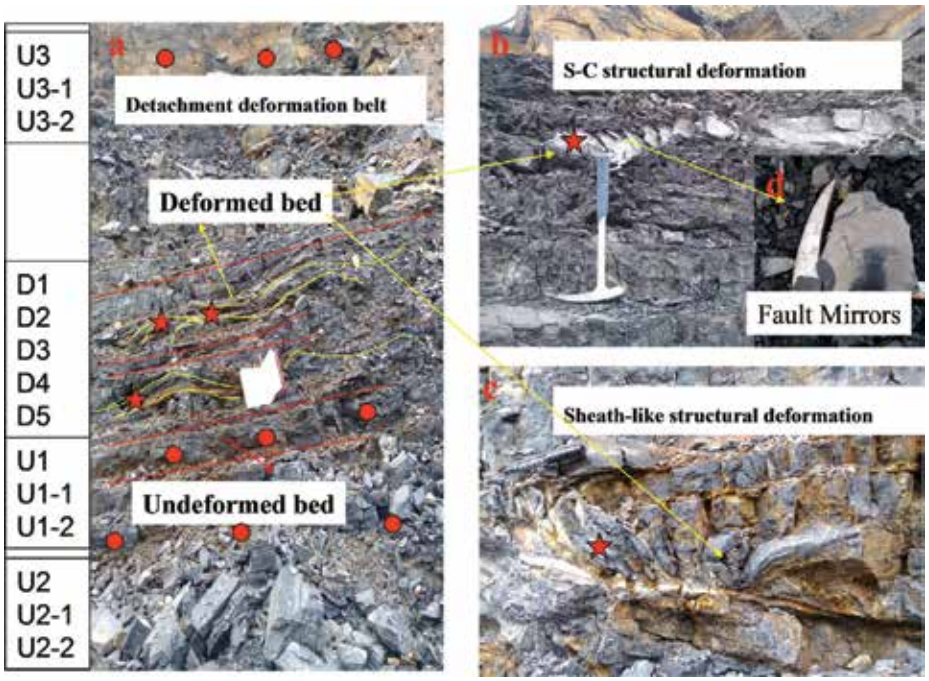

Figure 9. Location of study area is in southeastern Sichuan Basin, Yongshun, China. And the detachment structural deformation control across the Longmaxi Formations shale in this area. (a) The stratigraphic relationships and structural deformation characteristics of the samples, (b) S-C structural deformation shale, (c) Sheath-like structure deformation shale (d) Fault mirrors (FMs) of the deformed shale. ★ : Deformed shale samples, ● : Undeformed shale samples. The height of the notebook is 20 cm (a), length of the hammer is 38 cm (b) and the length of the pen is 14 cm (c). See **Figure 2** and **Table 1** for texture and structure properties of these deformed samples.

characteristics and eight samples (three undeformed samples and five deformed samples) were selected for mercury injection capillary pressure (MICP) and low-pressure gas (LPG) adsorption to determine the pore structure, including the porosity, pore-size distribution (PSD), surface area (SA) and pore volume (PV).

The sample number was abbreviated as U1, U2, U3 (Undeformed shale) and D1, D2, D3, D4, D5 (Deformed shale), the deformed samples subsets to strong deformed shale (D1, D2, D3) and weak deformed shale (D4, D5). The samples of U3 were collected from the thick sandy shale, and the other samples were collected from the thin siliceous shale. The stratigraphic relationships of the samples are shown in **Figure 9**. The features of the experimental samples are shown in **Table 1**. Before geochemical and mineralogical analyses, samples crushed to 180–200 mesh. The TOC content was collected using a Leco C/S-344 Carbon/Sulfur analyzer. The stable carbon isotope was determined using a Finnigan MAT 252 mass spectrometer. A 3Y–Leica DMR XP microscopy equipped with a microphotometer was used to measure the vitrinite reflectance values (VRo) of samples. Each sample was determined at least by 30 measurements on vitrinite particles. The crushed samples were mixed with ethanol, hand ground in a mortar and pestle and then smear mounted on glass slides for X-ray diffraction (XRD) analysis using a D/Max-III analyzer at 40 kV and 30 mA. The relative mineral contents were estimated and semi-quantified using the area under the curve for the major peaks.

http://dx.doi.org/10.5772/intechopen.72245

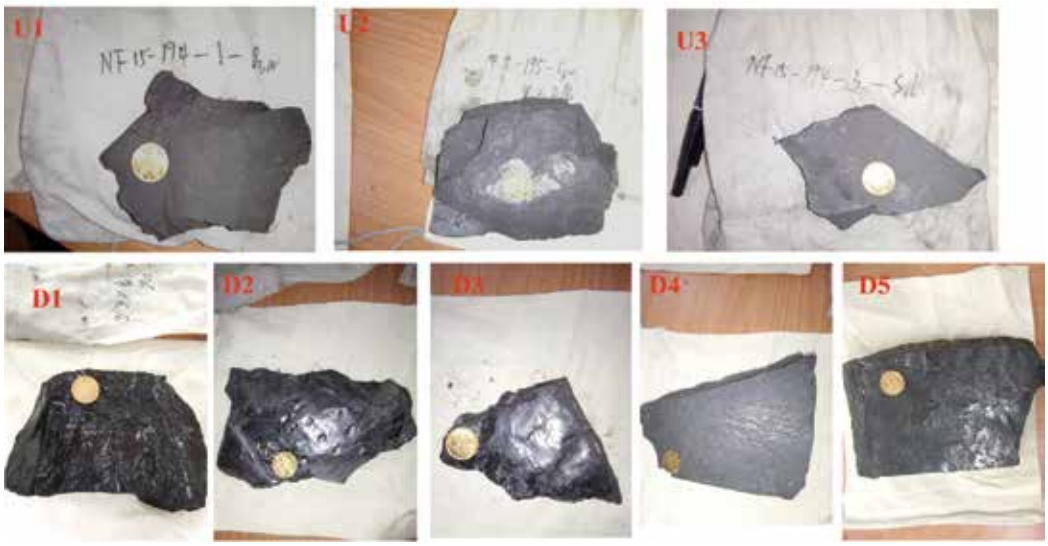

Figure 10. Undeformed shale and deformed shale samples; the sample ID was abbreviated as U1, U2, U3 (Undeformed shale) and D1, D2, D3, D4, D5 (Deformed shale). The undeformed shales have original parallel bedding, and the primary structure of shale can be observed. The detachment fault mirrors (FMs) can be observed on the deformed shales. And the deformed samples were subset to two sets of strong deformed shale and weak deformed shale due to their difference on the degree of deformation strength. The D1, D2 and D3 were strong deformed shales that the primary structure was damaged and the parallel bedding has almost disappeared due to deformation, and the fractures and mineral filling development in the strong deformed shales. The D4 and D5 were weak deformed shales that have original parallel bedding, and FMs developed in the surface of fault. The coin diameter is 20.5 mm.

Sample ID	TOC (%)	VRo (%)	δC_{13} ‰ (PDB)	Quartz (%)	Carbonate (%)	Clay (%)	Texture and fabric features of macroscopic hand specimens
U1	3.9	2.57	−30.4	41	nd	44	Undeformed shales. Shale primary structure can be observed. Shale has original parallel bedding
U2	2.5	2.78	−30.8	40	2	41	
U3	2.0	2.77	−30.9	34	11	33	
U-mean (9)	2.8	2.76	−30.7(3)	42	4.6	38	
D1	2.1	3.01	−30.6	77	nd	14	Strong deformed shales. The primary structure of shale is damaged and the parallel bedding has almost disappeared due to deformation. Fractures and mineral filling development. The plastic deformation of shale is obvious. Shale shows cleavage structure and cleavage surface is smooth with fine-grained powder coatings
D2	6.6	2.86	−31.0	64	nd	26	
D3	1.0	2.91	−31.3	77	nd	16	
D4	1.8	2.90	−30.6	46	nd	41	Weak deformed shales. Shale has original parallel bedding. Shale shows cleavage structure and cleavage surface is smooth with fine-grained powder coatings
D5	3.0	3.00	−31.1	71	nd	20	
D-mean (5)	2.9	2.93	−30.9	67	nd	23	

TOC, total organic carbon (%); VRo, vitrinite reflectance values (%); (Number), number of measured samples.

Table 1. The features of the experimental samples.

Sample ID	Gas absorption		MICP			Relative content* (%)		
	Micropore (μL/g)	Mesopore (μL/g)	Mesopore (μL/g)	Macropore (μL/g)	Porosity (%)	Micropore (%)	Mesopore (%)	Macropore (%)
U1	6.4	4.8	186.7	231.9	2.0	37.6	27.9	34.6
U2	5.7	8.4	175.5	122.9	1.6	28.5	42.0	29.4
U3	10.4	20.9	2198.4	330.0	7.5	30.3	60.6	9.1
D1	4.5	2.2	73.9	185.7	1.3	36.6	18.1	45.4
D2	5.3	6.7	73.8	143.3	1.6	21.2	26.8	52.0
D3	2.2	0.4	14.2	273.2	3.8	22.6	3.8	73.5
D4	4.5	3.8	148.7	172.1	2.5	28.5	23.8	47.7
D5	5.2	4.4	214.3	387.4	4.5	15.1	12.9	71.9

*The relative contents of different pore size distributions with PV were calculated by set the mesopore PV as referenced value.

Table 2. Pore volume characteristics of the samples.

To fully evaluate the pore size distribution and porosity, samples were crushed (2–5 mm), dried at 110°C and then preformed both mercury porosimetry and low pressure gas adsorption analyses. The mercury injection capillary pressure (MICP) analysis using a Poremaster GT60 and intruded with mercury from 1.5 to 60,000 Psi, the measured pressure range equates to the pore diameter range of 0.003–1000 μm (7–120,000 nm in this study). The pore size distributions of mesopores and macropores were determined using the Washburn equation [47]. The minimal pore diameter limit of 7 nm is within the mesopore range, and mercury porosimetry cannot detect micropores within the pore structure. Porosity is determined by mercury immersion (bulk density) coupled with helium pycnometry (skeletal density). Low pressure gas adsorption analyses have been used to measure the PSD both micropores and mesopores using both nitrogen adsorption at −196°C and carbon dioxide adsorption at 0°C by a Micromeritics ASAP 2020 HD88 analyzer. The PSD, PV and SA analysis of combined the N_2 and CO_2 gas adsorption by the same calculation models of density function theory (DFT) [48, 49]. The development of DFT models has led to a better understanding of adsorption processes in well-ordered systems compared to the more conventional models, used in the present study to analyzed N_2 and CO_2 gas adsorption data. The pore characteristics including SA, PV and PSD will be different between the two techniques (MICP and gas adsorption analyses) because of sample preparation, analytical models and calculation models; analysis method of combined the mercury intrusion and gas adsorption only used to determine the relative content percentage of micro-, meso- and macropores in this article by set the mesopores as a referenced values (**Table 2**).

5. Evolution of pore structure in the shale of detachment layers

It is believed that the shale composition controlled the pore structure character, and the diagenetic processes controlled the shale composition [38, 48, 50]. In the previous analysis, we

discussed the pore characteristic data obtained by different analytical methods of MICP and LPG separately [51]. **Figure 11** shows the correlation between porosity and pore volume for different pore diameters, indicating the positive relationship between porosity and micro- and mesopores PV ($R^2 > 0.85$) for undeformed shale, while the porosity of deformed shale was only related to the macropores PV ($R^2 = 0.77$). Such difference between the deformed and undeformed samples indicated that the micropores and mesopores (nanoscale pores) dominate the total porosity and controlled the diagenetic processes and shale compositions in the primary shale reservoir, while the macropores controlled the total porosity in the intense tectonic deformation shale. It is found that there were no significant changes in porosity between deformed and undeformed shale samples. In order to further study the evolution of pore size distribution in deformed shales, analysis method of combined the mercury intrusion and gas adsorption was used to determine the relative content percentage of micro-, meso- and macropores in this article by set the mesopores as a referenced value (**Table 2** and **Figure 12**). The balance of micro-, meso- and macropores were weakened in deformed shale samples, and the percentages of PV in different pore diameters were changed as macropores increased and mesopores decreased.

Organic matter can affect the evolution of pore structure, especially for different organic matter types and organic matter maturity. Jiang et al. reported the pore structure of a lacustrine oil shale in the Ordos Basin and indicated that the mesopores are dominant in samples [52]. Chen and Xiao measured the evolution of pore structure of artificially matured samples during an anhydrous pyrolysis, finding that the microporosity and mesoporosity increase with thermal maturity after the oil window stage [53]. The effect of organic matter on shale pore structure is mainly concentrated on micropore and mesopore [53–55] and achieved by the difference type and maturity. In the present study, all samples have a similar kerogen type and maturity stage, consistent with the similar micropores. Clay minerals can influence pore structure evolution and always have comparable organic contents. As compared to the deformed shale samples, the undeformed shale samples have higher values in micro-, meso-, total pore SA and adsorption quantity, because they have a higher clay content

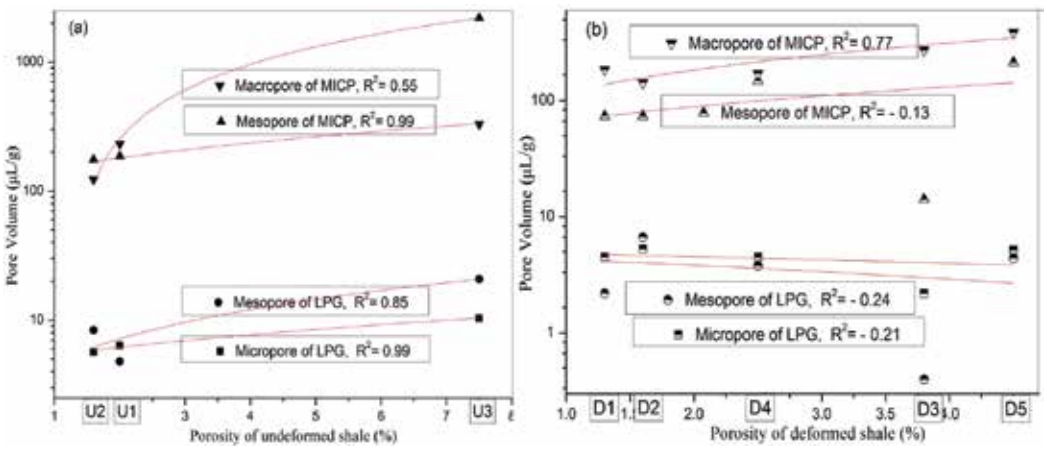

Figure 11. Relationship between total porosity and pore volume of micro-, meso- and macropores in shale samples from different analytic methods of LPG and MICP.

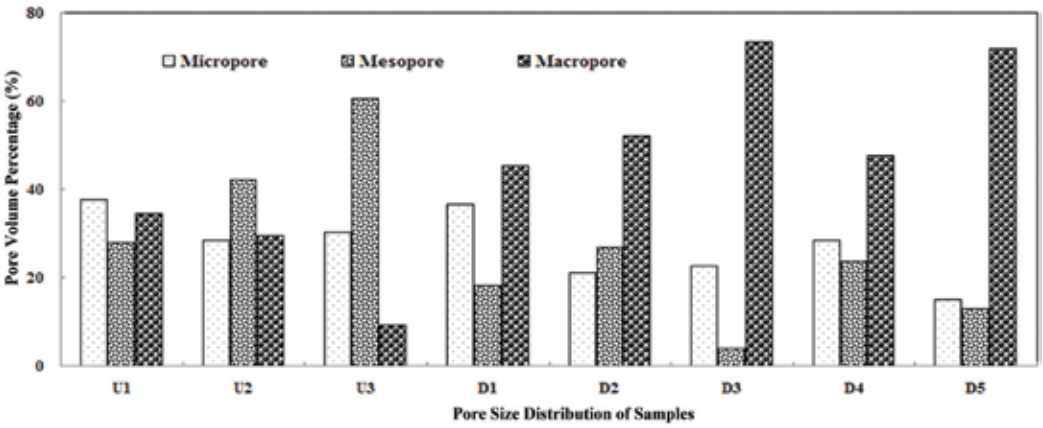

Figure 12. The pore volume percentages for shale samples.

rather than because of their undeformation. Ross and Bustin suggested that shales enriched in both clays and organics have the largest micropore volumes, suggesting a micropore contribution from both the organic and clay fractions. In the present study, the shale sample of D3, which is poor in clay and TOC, has the least micro- and mesopores. Kareem et al. found that the clay minerals are over-represented at the pore surfaces and in pore spaces compared to the other major minerals such as quartz and feldspar [56]. The knowledge of effective mineralogy complicated the influence of clay minerals on the pore structure. The biogenic quartz produced by precipitation during diagenesis with silica is derived from graptolite and radiolarians [57], which may also control the pore volume and structure in shales. This type of quartz affects microporosity significantly and has certain correlation to TOC content. There are no clearly defined relationships between quartz mineralogy and pore structure, because the micropore characteristics of the samples did not change with the quartz content in this study. Furthermore, the parts of extra quartz content in fracture filling of deformed shale may come from the hydrothermal source, after the tectonic deformation and fracture generations. The relationship between shale compositions and pore structure is not well reflected in the change of shale pore structure in deformed shale samples for the present study. There is no significant difference in organic matter content in deformed and undeformed samples, which agrees with a similar microporosity on all of the samples. All-scale pore structure analysis reveals that the deformed shale had notable higher macropores percentages than undeformed shale. At the same time, the total porosity and micropores were constant, suggesting that the evolution of pore structure in structural deformed shale was due to part of mesopores was disappeared due to compression of the tectonic stress, and macropores were generated due to the development of microcracks.

6. Conclusions

A series of comb-like folds and trough-like folds in eastern Sichuan Basin were the deformation controlled by multilayer detachment, which is different from the typical Jura type

detachment folds. Although the deformations between the Jura Mountain and eastern Sichuan look similar at the regional scale, their deformation mechanisms are different. There are many detachment layers occurring in the strata from the Neoproterozoic to the Mesozoic in the study region that controlled the deformation. Due to the multi-tectonic movement, shale reservoirs in China are highly diversified and complicated, which transformed the texture of shale beds and resulted in structure deformed shale with unique pore properties. The structural deformation has a significant effect on the evolution of pore size distribution, especially for the increase in the proportion of macroporous.

Acknowledgements

This research was funded by the Science and Technology Research and Development Program of China Petroleum and Chemical Corporation (No. P06088), Nonprofit Special Research Program (No. 200811015), Land Resource Survey Project of the Ministry of Land and Natural Resources, China (No. 1212010782003), Major State Research Development Program of China (No. 2016YFC0600202) and the China Geological Survey (CGS, No. DD20160183).

Author details

Mingliang Liang, Zongxiu Wang*, Linyan Zhang, Huijun Li, Wanli Gao and Chunlin Li

*Address all correspondence to: wangzongxiu@sohu.com

Institute of Geomechanics, Key Lab of Shale Oil and Gas Geological Survey, Chinese Academy of Geological Sciences, Beijing, China

References

[1] Suppe J. Geometrv and kinematics of fault-bend folding. American Journal of Science. 1983;**283**:684-721

[2] Jamison WR. Geometric analysis of fold development in overthrust terranes. Journal of Structural Geology. 1987;**9**:207-219

[3] Poblet J, McClay K, Storti F, Munoz JA. Geometries of syntectonic sediments associated with single-layer detachment folds. Journal of Structural Geology. 1997;**19**:369-381

[4] Marrett R, Bentham PA. Geometric analysis of hybrid fault-propagation/detachment folds. Journal of Structural Geology. 1997;**19**(3-4):243-248

[5] Liu C, Zhang YK, Shi B. Geometric and kinematic modeling of detachment folds with growth strata based on Bézier curves. Journal of Structural Geology. 2009;**31**:260-269

[6] McClay KR. Glossary of thrust tectonics terms. In: McClay KR, editor. Thrust Tectonics. Chapman and Hall; 1992. pp. 419-433

[7] Rich JL. Mechanics of low-angle overthrust faulting illustrated by Cumberland thrust block, Virginia, Kentucky and Tennessee. Bulletin of the American Association of Petroleum Geologists. 1934;**18**:1584-1596

[8] Collet LW. The Structure of the Alps. Glasgow University Press; 1964

[9] Zhu ZC. On Jura-type fold (S. China) and its mechanism. Earth Science-Journal of China University of Geosciences. 1983;**3**:45-53

[10] Yan DP, Zhou MF, Song HL, Weng WX, John M. Origin and tectonic significance of a Mesozoic multi-layer over-thrust system within the Yangtze block (South China). Tectonophysics. 2003;**361**(3-4):239-254

[11] Chen HJ, Yin YN. Calling for opening up oil/gas exploration frontiers in overthrust belt-a discussion on the distribution of oil controlled by the southern Jiangsu Overthrust Belt. Petroleum Geology and Experiment. 1983;**2**:5-15

[12] Zhu ZC, Ye JL, Yang KG. On thrust-nappe and gliding-detachment on both sides of Mufushan-Jiuling uplift and asymmetrical tectonic architecture of mountain. Earth Science-Journal of China University of Geosciences. 1987;**5**:55-62

[13] Li BL, Sun Y, Zhu WB, Guo JC, Wen SH. Study on the layer slip parameter systems in the eastern Sichuan. Journal of Southwest Petroleum Institute. 2001;**23**:29-33

[14] Sun Y, Jia CZ, Jiang YJ. Determination of physical parameters of rocks and establishment of regional layer-slip systems in the northern Tarim area. Chinese Journal of Geophysics. 1996;**39**(5):660-671

[15] Gao XS, Liu SG, Guo GA. Structural styles and relationships to hydrocarbon accumulation in the northeast of Central Sichuan. Journal of Mineralogy and Petrology. 1998;**18**:167-170

[16] Feng CM, Liu J, Song LJ. Formation mechanism of the tectonic deformation belt and the prognosis of favorable oil and gas exploration areas in the middle and upper Yangtze Valley. Acta Geoscientica Sinica. 2008;**29**(2):199-204

[17] Tang LJ, Yu YX, Yang WJ, Peng GX, Lei GL, Jin WZ, Wan GM. Internal deformation features of detachment layers in the front of the Kuqa foreland fold-thrust belt. Geology in China. 2006;**33**:944-951

[18] Tang LJ, Guo TL, Jin WZ, Yu YX, Li RF. Main structural styles and deformation mechanisms in the Northern Sichuan Basin, Southern China. Acta Geologica Sinica (English edition). 2008;**82**:543-553

[19] Wang GL, Wang X, Wang WJ. Study on Detachment Structures. Beijing: Science Press; 1992

[20] Buxtorf A. Prognosen und befunde beim Hauesnsteinbasis und Grenchenberg-tunnel und die geologie des Juragebirges. Ver-handlungen der Naturforschenden Gesellchaft in Basel. 1916;**27**:184-205

[21] De Sitter LU. Structural Geology. New York: McGraw-Hill; 1956

[22] Laubscher HP. Fold development in the Jura. Tectonophysics. 1977;**37**:337-362

[23] Donatella M, Hemin AK, Massimiliano RB. Structural evolution of a fold and thrust belt generated by multiple decollements: Analogue models and natural examples from the northern Apennines (Italy). Journal of Structural Geology. 2006;**28**:185-199

[24] Hemin AK, Bruno CV. The effect of decollement dipongeometry and kinematics of model accretionary wedges. Journal of Structural Geology. 2003;**25**:1445-1450

[25] Liu SZ. My opinion of structural pattern of thin-skinned structure in East Sichuan. Acta Geologica Sichuan. 1995;**15**:264-267

[26] Ding DG, Guo TL, Zhai CB. Kink structure in the West Hubei and East Chongqing. Petroleum Geology and Expeximent. 2005;**27**:205-210

[27] Ding DG, Liu GX. Progressive deformation in Yangtze plate-series 2 of the southern structure studies. Petroleum Geology and Expeximent. 2007;**29**:238-246

[28] Liu XF, Liu CX. Analysis of structural styles at the juncture of Chongqing, Hubei and Hunan. Journal of Jianghan Petroleum Institute. 2002;**24**:1-4

[29] ZY X, Li DC, WZ L, Lin K, Liu CY. Pattern analyses and genetic interpretation about the geotectonics of Yudong (East Chongqing). Geotectonica Et Metallogenia. 2004;**28**:15-22

[30] Guo JH, Zhu MH, Liu CS, Liu XF, Zhang HD, Wang MY. Structural characteristics of the corridor section in Sangzhi-Shimen synclinore. Geotectonica Et Metallogenia. 2005;**29**:215-222

[31] Yan DP, Wang XW, Liu YY. Analysis of fold style and its formation mechanism in the area of boundary among Sichuan, Hubei and Hunan. Geoscience. 2000;**14**:37-43

[32] Liu SG, Deng B, Zhong Y. Unique geological features of burial and superimposition of the lower Paleozoic shale gas across the Sichuan Basin and its periphery. Earth Science Frontiers. 2016;**23**:11-28

[33] Guo TL, Zeng P. The structural and preservation conditions for shale gas enrichment and high productivith in the Wufeng-Longmaxi formation, southeastern Sichuan Basin. Energy Exploration and Exploitation. 2015;**33**:259-276

[34] Ma Y, Zhong NN, Han H. Definition and sturcture characteristics of pores in mylonitized organic-rich shales. Science China: Earth Sciences. 2014;**44**:2202-2209

[35] Wang ZX, Zhang J, Guan HM. A discussion on the structural deformation and oil/gas traps on the western side of the Xuefeng Mountain. Geological Bulletin of China. 2012;**31**:1812-1825

[36] Guo TL. Discovery and characteristics of the Fuling shale gas field and its enlightenment and thinking. Earth Science Frontiers. 2016;**23**:29-43

[37] Ibanez WD, Kronenberg AK. Experimental deformation of shale: Mechanical properties and micromechanical indicators of mechanisms. International Journal of Rock Mechanics and Mining Sciences & Geomechanics. 1993;**30**:723-734

[38] Ross DJK, Bustin RM. The importance of shale composition and pore structure upon gas storage potential of shale gas reservoirs. Marine and Petroleum Geology. 2009;**26**:916-927

[39] Pan JN, Hou QL, YW J, et al. Coalbed methane sorption related to coal deformation structures at different temperatures and pressures. Fuel. 2012;**102**:760-765

[40] Pan JN, Zhu HT, Hou QL. Macromolecular and pore structures of Chinese tectonically deformed coal studied by atomic force microscopy. Fuel. 2015;**139**:94-101

[41] Yan DP, Jin ZL, Zhang WC, Liu SF. Rock mechanical characteristics of the multi-layer detachment fault system and their controls on the structural deformation style of the Sichuan-Chongqing-Hunan-Hubei thin-skinned belt, South China. Geological Bulletin of China. 2008;**27**:1687-1697

[42] Feng XY, Meng XG, Shao ZG, Wang JP, Zhu DG. A preliminary discussion on features and dynamics of sequence deformation in South China and neighboring areas. Acta Geosicientia Sinica. 2003;**24**:115-120

[43] Wang YJ, Zhang YH, Fan WM, Peng TP. Structural signatures and 40Ar/ 39 Ar geochronology of the Indosinian Xuefengshan tectonic belt, South China block. Journal of Structural Geology. 2005;**27**:985-998

[44] Cai XL, Cao JM. The deformation structures framework control function on earthquake in Sichuan Basin. Earthquake Research in Sichuan. 1998;**3**:26-34

[45] Hu GC, Xie YX. The Steep Structures in the Carboniferous Gas Fields, Eastern Sichuan, China. Beijing: Petroleum Industry Press; 1997

[46] Wang YS, Wang XB, Gou L, Jia JD. Several progress of deep-shallow structure interpretation by MT along Songpan-Shaoyang cross section. South-to-north water transfers and. Water Science and Technology. 2007;**5**:70-77

[47] Washburn EW. The dynamics of capillary flow. Physics Review. 1921;**17**:273-283

[48] Clarkson CR, Haghshenas B, Ghanizadeh A. Nanopores to megafractures: Current challenges and methods for shale gas reservoir and hydraulic fracture characterization. Journal of Natural Gas Science and Engineering. 2016;**31**:612-657

[49] Thommes M, Kaneko K, Neimark AV. Physisorption of gases, with special reference to the evaluation of surface area and pore size distribution (IUPAC technical report). Pure and Applied Chemistry. 2015;**87**:1051-1069

[50] Chalmers GRL, Bustin RM, Bustin AAM. Geological controls on matrix permeability of the Doig-Montney hybrid shale-gas–tight-gas reservoir, northeastern British Columbia (NTS 093P). In: Geoscience BC Summary of Activities. Geoscience BC, Report 2012-1, 2011. pp. 87-96

[51] Liang ML, Wang ZX, Gao L. Evolution of pore structure in gas shale related to structural deformation. Fuel. 2017;**197**:310-319

[52] Jiang FJ, Chen D, Wang ZF. Pore characteristic analysis of a lacustrine shale: A case study in the Ordos Basin, NW China. Marine and Petroleum Geology. 2016;**73**:554-571

[53] Chen J, Xiao X. Evolution of nanoporosity in organic-rich shales during thermal maturation. Fuel. 2014;**129**:173-181

[54] Curtis ME, Cardott BJ, Sondergeld CH. Development of organic porosity in the Woodford shale with increasing thermal maturity. International Journal of Coal Geology. 2012;**103**:26-31

[55] Sun LN, Tuo JC, Zhang MF. Formation and development of the pore structure in Chang 7 member oil-shale from Ordos Basin during organic matter evolution induced by hydrous pyrolysis. Fuel. 2015;**158**:549-557

[56] Kareem R, Cubillas P, Gluyas J. Multi-technique approach to the Petrophysical characterization of Berea sandstone Core plugs (Cleveland quarries, USA). Journal of Petroleum Science and Engineering. 2017;**149**:436-455

[57] Luo QY, Zhong NN, Dai N. Graptolite-derived organic matter in the Wufeng–Longmaxi formations (upper Ordovician–lower Silurian) of southeastern Chongqing, China: Implications for gas shale evaluation. International Journal of Coal Geology. 2016;**153**:87-98

Chapter 5

Tectonics and Metallogeny of East Kazakhstan

Boris Dyachkov, Marina Mizernaya,
Oksana Kuzmina, Natalia Zimanovskaya and
Tatiana Oitseva

Additional information is available at the end of the chapter

http://dx.doi.org/10.5772/intechopen.72745

Abstract

General regularities in the formation of tectonic and metallogenic structures are considered as a scientific basis for forecasting new deposits of nonferrous, precious and rare metals in the territory of East Kazakhstan and are considered on the basis of modern geotectonic concepts of the Earth self-development. Regular connections between the main ore-bearing structures and the leading geological-industrial types of deposits are determined with features of the deep crustal structure and certain geodynamic settings of various geotectonic cycles and eras (from the Precambrian to the Quaternary). The belt placement of ore deposits is emphasized with the identification of four ore belts: Rudny Altai (Cu, Pb, Zn, Au), West Kalba (Au, Ag), Kalba-Narym (Ta, Nb, Be, Li, Sn, W) and Zharma-Saurs (Cr, Ni, Co, Au, TR). In the location of gold ore deposits, the Zaisan suture zone, formed in the collision zone of the Kazakhstan and Siberian lithospheric plates, is the ore-controlling value. Spatial-genetic connections of rare metal and rare-earth deposits with granitoid belts formed in post-collision (orogenic) geodynamic conditions of Permian time are determined. The research is aimed at strengthening the mineral and raw material base for the operating enterprises of the East Kazakhstan region.

Keywords: Central-Asia, Zaisan zone, suture, ore-bearing structures, deposits

1. Introduction

The beginning of the twenty-first century was marked by a sharp increase in fundamental geological research in the world to create a modern scientific basis for further development of mineral and raw materials sector of the world economy. Mineral resources are still the backbone of the economies of many countries, but there is a general tendency for their depletion as a result of mining the deposits discovered in previous years. The most important task is to open new mineral deposits on the basis of modern geotectonic concepts of geological

structure development and processes of ore formation with the aim to develop new technologies of deep earth prognosis and prospect for ore deposits [1].

The territory of East Kazakhstan is a unique geological area, in which many deposits of copper, lead, zinc, gold, silver, rare metals and rare earths, titanium, hydrocarbon raw materials and other minerals are concentrated. A powerful industrial infrastructure of mining and metallurgical works and plants has been built in the region on their basis.

The novelty of the study is further development of scientific idea of the Greater Altai (GA) geostructure formation during the Hercynian collision (C_1-C_3) of Kazakhstan and Siberian paleomicrocontinents, horizontal displacement and coalescence of large tectonic blocks of the earth's crust (terranes) during the Irtysh-Zaisan paleobasin (a part of the Paleo-Asiatic ocean) degradation. A significant ore-controlling importance is attached to justification of belt placement of ore-bearing structures and deposits which were formed in various geodynamic settings and regimes.

The tendency of ore deposit's belt distribution is manifested in the North American, Mexican, South China, Urals metallogenic provinces and other regions of Kazakhstan [4, 6]. Revealed ore belts within the territory of the Greater Altai regional ranks offer new opportunities for deposit forecasting and prospecting especially on poorly studied and closed territories.

2. Geotectonic position of the Greater Altai geological structures

The Hercynian geostructure of the Greater Altai is located in the Central Asian mobile belt, in the northwest of the Altai-Alashan Modal Zone, and is bounded by deep faults in the northwestern direction (Loktevsko-Karairtyshsky and Chingiz-Saursky) which separate it from the Caledonides of the Gorny Altai (in the northeast) and Chingiz-Tarbagatai (in the southwest). The territory under consideration unites the geological structures of the Rudny Altai, Kalba-Narym, Western Kalba, Zharma-Saur and adjacent areas of Russia and China, the total length of which is more than 100 km with an average width of 3000 km in modern coordinates (**Figure 1**).

According to geotectonic zoning, they are separate blocks of the earth's crust or terranes that were welded together during the Hercynian collision and separated by a system of deep faults or structural zones (the Northeast, Irtysh, Zaisan, and so on). The latter are also considered as zones of upwelling and the entry of mantle material, and ore-bearing fluid flows into the earth's crust [2].

The deep structure of the region in terms of geological and geophysical data is sharply heterogeneous and is characterized by a multilayered earth crust (up to 50–55 km thick) with heterogeneous linear-mosaic blocks complicated by folded and discontinuous deformations.

The model of the GA deep structure is presented at the geological and geophysical section of the Altai geotraverse compiled by Lyubetskiy et al. (**Figure 2**) [2, 3]. The upper mantle (UM) is characterized by an inhomogeneous structure, and it lies at a depth of 38–55 km and has a dissected relief. Mohorovichich's (M) raising of the surface is also recorded in the northwestern flank of the suture zone (Gornostaevsk) and its southeastern continuation (Zaisan), and in the Rudny Altai (Rubtsovsk) [2].

http://dx.doi.org/10.5772/intechopen.72745

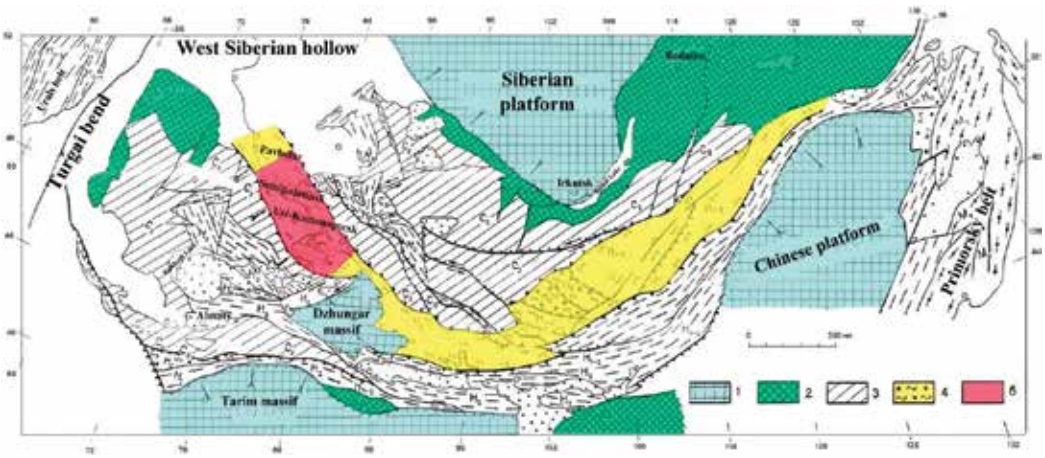

Figure 1. The Greater Altai geotectonic position in the structures of the Central Asian belt. 1—Ancient platforms and massifs; 2—Baikal; 3—Caledonian orogeny region; 4—Altai-Alashan area; and 5—position of the Greater Altai.

Deep mobile zones (DMZs) and associated systems of longitudinal-transverse faults which caused intensive transformations of the entire section of the EC and the upper mantle played a decisive role in magmatism origin and evolution, the spatial arrangement of volcanic and intrusive belts. The real differentiation of the upper mantle and the level of foci nucleation in the EC reformation column determined the composition and geochemical specialization of magmatism. The influence of the mantle plume evidently played a decisive role in the metallogenic specialization of Charskaya, West Kalbinsk and Zharma-Saur tectonic zones (Cr, Ni, Fe, Cu, Pb, Zn, Au, and so on).

These data are consistent with the views of a number of researchers on the relationship between plume magmatism and metallogeny in Tarim, Siberian, Emeishan, Central European and other large magmatic provinces (R.D. Dzhenchuraeva, 2015).

In fact, small deposits of magmatic Cu-Ni formation C_{2-3} (Maksut et al.) are known in the territory of East Kazakhstan, and the earlier action of the asthenolite plume was recorded in the Rudniy Altai (in the Devonian) and Chara zone during the stage of the Hercynian collision of C_1-C_3 [3]. Later, in the lower Triassic, the Semeytauska volcano-tectonic construction of the trachybasalt-trachyriolite composition was formed under the influence of a local mantle plume. Therefore, the manifestation of mantle plumes in East Kazakhstan occurred, probably, repeatedly, and the mantle source of ore matter (Cr, Ni, Pt, Ir, Hg) is fixed in deposits of different types (copper-polymetallic, gold ore, rare metals and others). Consequently, it is also necessary to take into account the mantle plume models of the formation of ore-magmatic systems for metallogenic constructions in the territory of the Greater Altai.

The metabasalt layer (K surface) is fixed by amphibolites and hyperbasites fragments in the deep melange of Charskii, Irtysh-Markakol and other faults. In the axial part of the Rudny Altai, according to G.P. Nakhtigal's materials, the crust surface is elevated (at a depth of 22–24 km) bounded by Kalba-Narymsky (26–28 km) and Belousinsk-Sarymsaktin (28–30 km) edge deflections [2, 4, 5]. Metabasaltic layer elevations are also noted in the core zones of

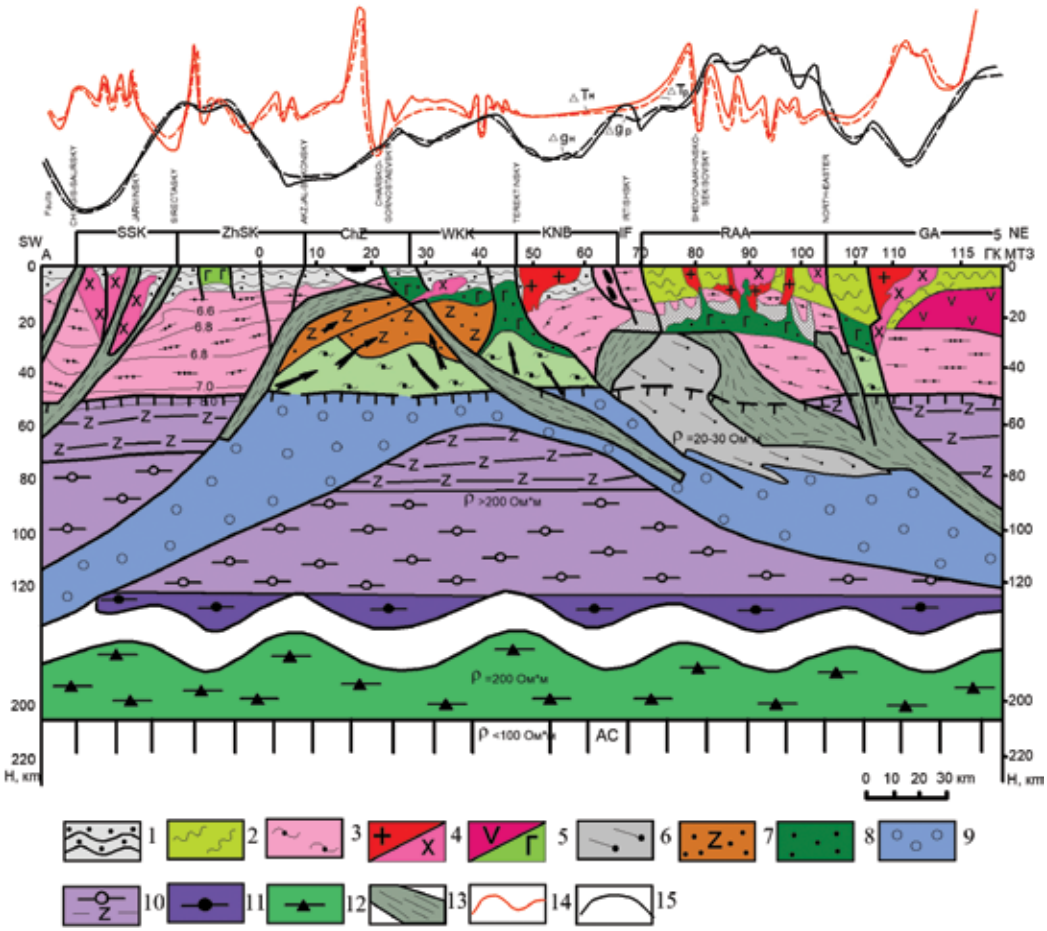

Figure 2. Geological and geophysical section of the lithosphere at the Greater Altai according to Aleisk geotraverse. Granite-metamorphic layer: 1—Hercynides; 2—Caledonian; 3—Proterozoic. Intrusive bodies: 4—granites and granodiorites, plagiogranites; 5—diorite and gabbro; 6—metamorphic carbonaceous rocks. Meta basalt layer: 7—amphibolites; 8—granulites. The upper mantle: 9—primary; 10—ultrabasites; 11—eclogite garnet; 12—diamondiferous eclogite; 13—upwelling zones; 14—gravity field curves (Δg); (15) curves of the anomalous magnetic field (ΔT). Metallogenic zones: SSK, Syrektas-Sarsazan-Kobukskaya; ZhSK, Zharma-Saur-Kharatungskaya; ChZ, Charco-Zimunayskaya; WKK, West-Kalbinsk-Koksentauskaya; KNB, Kalba-Narym-Burchumskaya; IF, Irtysh-Fuyunskaya; RAA, Rudnoaltaisko-Ashalinskaya; GA, Gornyi Altai.

Zharma-Saursky and Chingiz-Tarbagatai belts. Evidently, this is a general pattern for the entire East Kazakhstan region.

The analysis of represented geological and geophysical data emphasizes the transverse heterogeneity of the deep structure of East Kazakhstan territory and different maturity of the EC in its different parts. Typical models of EC tectonic zone structure are reconstructed accordingly: (1) femic with increased capacity of metabasalt to 24–28 km (Chingiz-Tarbagatai, Rudnoaltayskaya and Zharma-Saurskaya zones); (2) sialic with a high thickness of metagranite layer up to 12 km and the EC up to 50–55 km (Kalba-Narymskaya, Syrektas-Sarzanskaya zone, Gorny Altai) and (3) interbedded femichesical—saliches on a heterogeneous (Precambrian-Caledonian) base

http://dx.doi.org/10.5772/intechopen.72745

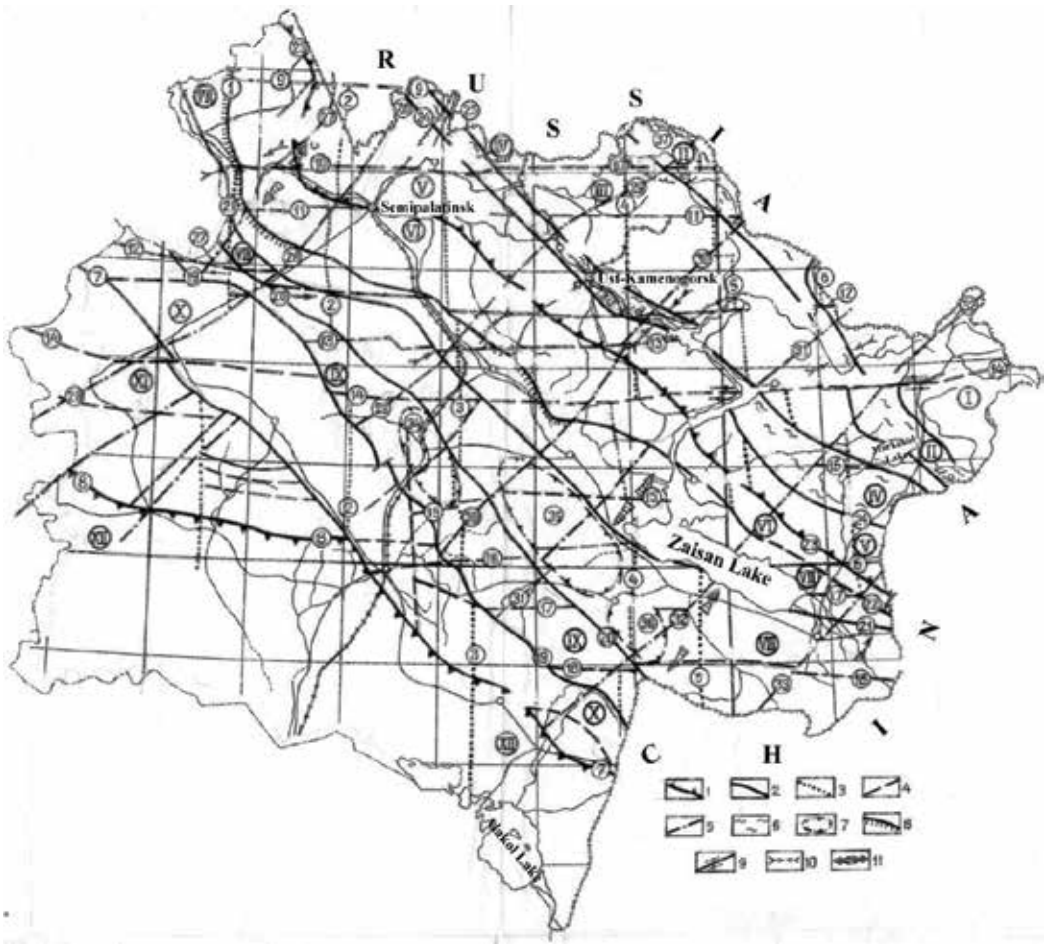

Figure 3. The layout of the faults of the Eastern Kazakhstan (by B.A. Dyachkov, G.P. Nakhtigal). 1—Deep longitudinal faults restricting tectonic structures and 2—their structure-formation zone; 3 and 4—regmatic system longitude-latitude prehercinian structural fault occurrence; 5—transverse deep faults of the Hercynian activation; 6—crushing zones; 7—ring structures; 8—thrusts; 9—fault-shifts; 10—direction of prevailing tectonic compression and 11—tension. Structural area (roman number in circles): I—Mountain Altai (Charyshskaya, Holzunsko-Chuiskaya), II—Beloubinsko-Sarymsaktinskaya (northeastern zone crumpling), III—Rudnoaltayskaya, IV—Irtyshskaya (Irtysh zone crumpling), (V) Kalba-Narymskaya, VI—Western Kalbinskaya, VII—Charskaya, VIII—Zharma-Saurskaya, IX—Sirektasskaya, X, XI—Chengis Tarbagataiskaya, XII—Pribalhashkaya.

with a suboceanic EK type of section (Charskaya, West Kalbinsk, the Irtysh zones). These tectonic zones, which have unequal tectonic magmatic activity, were saturated with basaltoid and granitoid matter in different ways with different geochemical specialization.

Thus, the geodynamic model of the GA mobile belt development reflects a long and complex history of geological structure formation and emphasizes the intensity of ore-magmatic processes and metallogeny. As a result of polycyclic development of tectonic magmatic processes, the main epochs of ore formation have been outlined, reflecting vertical and lateral zonation within the ore belts and in general for East Kazakhstan. During the stepwise EC transformation and the migration of magmatic foci from the upper mantle, a homodromic evolution of the magmatic formations

and associated mineralization occurred. The change of sidero-chalcophile mineralization (Fe, Mn, Cu, Pb, Zn, Au, Ag) by chalcophile (Pb, Zn, Au, Ag, Bi, Sb, etc.) and lithophilic (Ta, Nb, Sn, W, Mo, TR, etc.) occurred from early to late epochs [6]. System analysis of the materials shows that in each metallogenic zone the maximum outburst of mineralization (with the formation of industrial deposits) occurred only in a certain geodynamic regime and in the age interval.

The role of deep faults in the development of geological structures and metallogeny was considered in the works of many researchers (G.D. Azhgirey, A.V. Peive, N.P. Nekhoroshev, G.N. Shcherba, P.F. Ivankin, et al.). Deep faults had a long history of development, among which the Proterozoic, Caledonian and Hercynian fault systems as well as Cimmerian and Alpine (new and refurbished) are distinguished by age (location or intensive activation). The following systems also differ in direction: (1) longitudinally transverse (northwestern and northeastern), (2) longitude-latitudinal (regmatical), (3) diagonal, and (4) annular (according to space images interpretation) (**Figure 3**).

3. Peculiarities of metallogeny

3.1. The geological history of development of structures

In recent years, some common patterns of geological structure formation of Central Asian belt have been addressed in a number of publications from the theoretical standpoint of mobilism [6–10]. Particular attention has been given to determining the role of the mantle in tectogenesis, magmatism and ore formation processes, sources of magmatic melts and ore matter, clarifying geotectonic positions, age and ore content of granitoid batholiths and their connection with large Siberian and Tarim mantle plumes. General orientation of evolution of geology and metallogeny of the Greater Altai and skirting structures (Gorny Altai and Chingiz-Tarbagatai) occurred over a long geological history (from Precambrian to Quaternary time) in various geodynamic regimes and conditions.

In the Precambrian, near-fault intrusions of hyperbasites were accompanied by mineralization of magmatic formation under oceanic rifting conditions—Cr, Ni, Co, Cu (Charco-Gornostaevsky belt). In the early stages of caledonides and hercinides, stratiform iron-manganese, polymetallic, and copper-pyrite volcanogenic sedimentary deposits of the Ural and Rudno-Altai types (Fe, Mn, Pb, Zn, Cu, Au, Ag, etc.) were formed under rift-arc island geodynamic conditions (Chingiz-Tarbagatai, Rudny Altai).

Predominantly small intrusions and dikes of the gabbro-diorite-granodiorite-plagiogranite series are localized under collision geodynamic conditions, productive for copper-nickel sulfide, copper-porphyry and gold mineralization—Ni, Co, Mo, Au, Ag, etc. (Chingiz-Tarbagatai, Zharma-Saur, Western Kalba, the Rudny Altai). Southeastern zones formed in the process of lithospheric plate collision with oceanic and continental earth crust types are fixed by a system of deep crust–mantle faults, ophiolite belts, blocks of metamorphic rocks and thrust-melange structures which have ore-controlling importance. They are accompanied by many minerals (Cr, Ni, Co, Cu, Hg, Au, etc.), including large gold deposits (Bakyrchik, Vasilkovskoe, Suzdalskoe, etc.) [11, 12].

The post-collisional (orogenic) situation in the Permian was characterized by the activation of intra-plate tectonics and powerful development of granitoid magmatism, which is associated with deposits of rare metals and rare earths (Ta, Nb, Be, Li, Sn, W, Mo, TR, and so on). Deposits of rare metals are concentrated in the Kalba-Narym zone, Zharma-Saur, the Gorny Altai and other regions of Central Asia (China, Mongolia, the Urals, and so on) [13–15].

In the Cimmerian cycle, residual weathering crusts of nontronite profile (Ni, Co) accumulated in the Chara zone, kaolinite-hydromica (Au) in Western Kalba and Zharma-Saur, kaolinite (Ti, Zr) in northern Prizaisan (Karaotkel deposit) under continental rifting conditions. Deposits of coal and oil shale were formed in intermontane depressions (Karazhyra, Kenderlyk). Deposits of various minerals including placer gold, ilmenite, monazite, cassiterite and other minerals were formed in a Mesozoic-Cenozoic platform cover.

3.2. Metallogenic zoning

As a result of study, it has been determined that geotectonic and metallogenic zoning is fully consistent and the following ore-bearing structures have been identified: a metallogenic province, ore belt, metallogenic zone (subzone), ore region, ore zone, ore site and ore field. The Hercynian geostructure of the Greater Altai which covers the territory of the Rudny Altai, Kalba-Narym, Western Kalba, Zharma-Saur and adjacent regions of Russia and China is the largest.

Four ore belts have been determined within the Greater Altai by metallogenic zoning (**Figure 4**):

1. Rudnoaltai copper-polymetallic (Fe, Mn, Cu, Pb, Zn, Au, Ag, and so on)
2. Kalba-Narym rare metal (Ta, Nb, Be, Li, Cs, Sn, W).
3. West Kalbinsky gold ore (Au, Ag, As, Sb).
4. Zharma-Saursky multimetal (Cs, Ni, Co, Cu, Au, Hg, Mo, W, TR).

Chingiz-Tarbagatai belt in the southwest of the GA unites two metallogenic zones (West-Chingiz and East-Chingiz), and in the northeast there are Charyshskaya, Kholzun-Chuysko-Sicikhe and Tsunghu-Chihuye zones adjacent to the Gorny Altai [8].

The Rudny Altai belt was formed on the destructured continental crust of the Gorny Altai during the Hercynian cycle, and the change of geodynamic regimes from the initial rifting (D1e) to the island-arc (D_3-C_1) was accompanied by a collision (C_2-C_3), orogenic activation (P_1-T_1) and stabilization (Mesozoic-Cenozoic). The ore-control importance is given to a system of echeloned deep faults in the northwestern direction penetrating the activated upper mantle, which contributed to the entry of mantle-crustal magma and ore-bearing fluxes into the upper parts of the EC [3, 16]. Industrial copper-pyrite and pyrite-polymetallic deposits are concentrated in the core Rudny Altai zone of increased femininity of the EC section, the magmatic saturation and the density of mineralization and are clearly correlated with the elevation of the upper mantle, the metabasaltic layer, and the blocks of the Proterozoic and Caledonian basement.

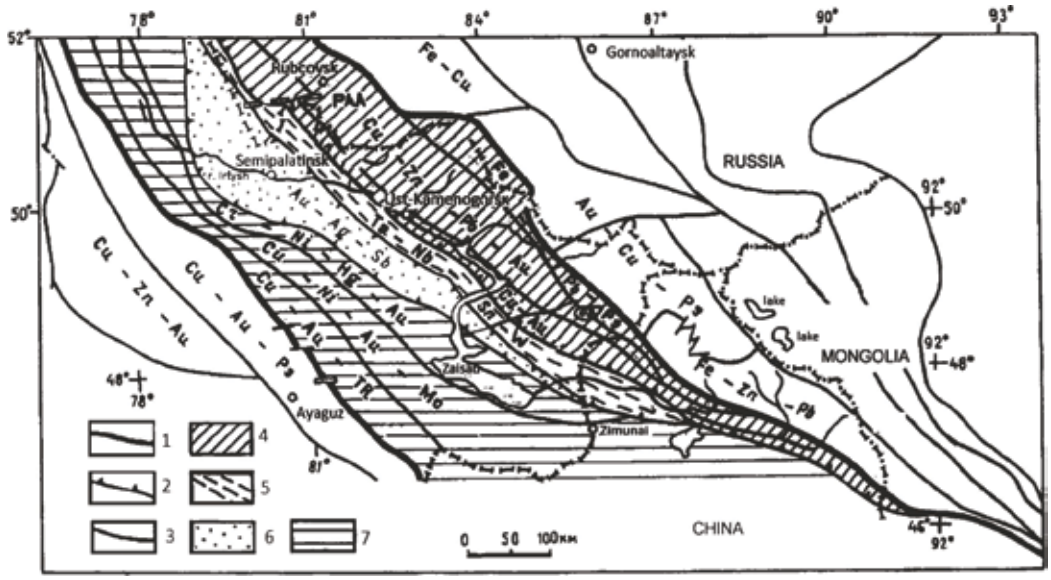

Figure 4. Greater Altai metallogeny division into areas. 1—Border of Greater Altai; 2—of ore belts and 3—of metallogenic zones; 4—Rudnoaltaisk gold-copper-polymetal; 5—Qalba-Narym rare metal; 6—West Qalba gold bearing and (7) Zharma-Saur multimetal.

Pyrite-copper-polymetallic mineralization is genetically associated with a group of basalt-andesite-rhyolite formations (D_{1-3}), differentiated and contrasting antidirectional series, forming several productive geochronological levels from D_1e to D_3fr_1 (**Figure 5**). Accordingly, multi-rhythmic zoning and high-level distribution of mineralization in ore zones, ore sites and, in general, the ore belt (with a vertical span of ores up to 1000–1500 m) are manifested. There is a concentration of deposits in the Devonian volcanic arcs of ring structure framing the Caledonian paleo-elevations (Sinyushinsky, Revnushinsky, Alei and Rubtsovskoye), characterized by volcanic processes and ore formation duration.

The linear cluster distribution of volcanic-tectonic structures with pyrite-polymetallic deposits in longitudinal ore zones (Leninogorsk, Zyryanovskaya, Orlovsky-Belousovskaya, etc.) with a step of ore nodes at the intersection of faults of 20–40 km is also characteristic. Sublatitudinal ore-control faults played an important role (Leninogorskii and others), especially at the junctions of their intersection with breaks in other directions, where volcanogenic ore centers were created (according to G.F. Yakovlev, 1976).

Ore formation took place under submarine conditions, evidently with an ascending water-and-hydrothermal system of solutions with a juvenile source of metals (Fe, Cu, Pb, Zn, S, Au, Ag, etc.) and dissolved gases (CO_2, N_2, H_2S, S, Cl and others) (Dyachkov, Titov, 2005).

Two types of ores differ in origin:

1. stratiform hydrothermal sedimentary, characterized by the accumulation of ore matter at the bottom of the basin among sedimentary-pyroclastic rocks with the formation of stratified rhythmically layered ores (Ridder-Sokolnoye, Verkh-Ubinskoe, Nikitinsky deposits, and so on);

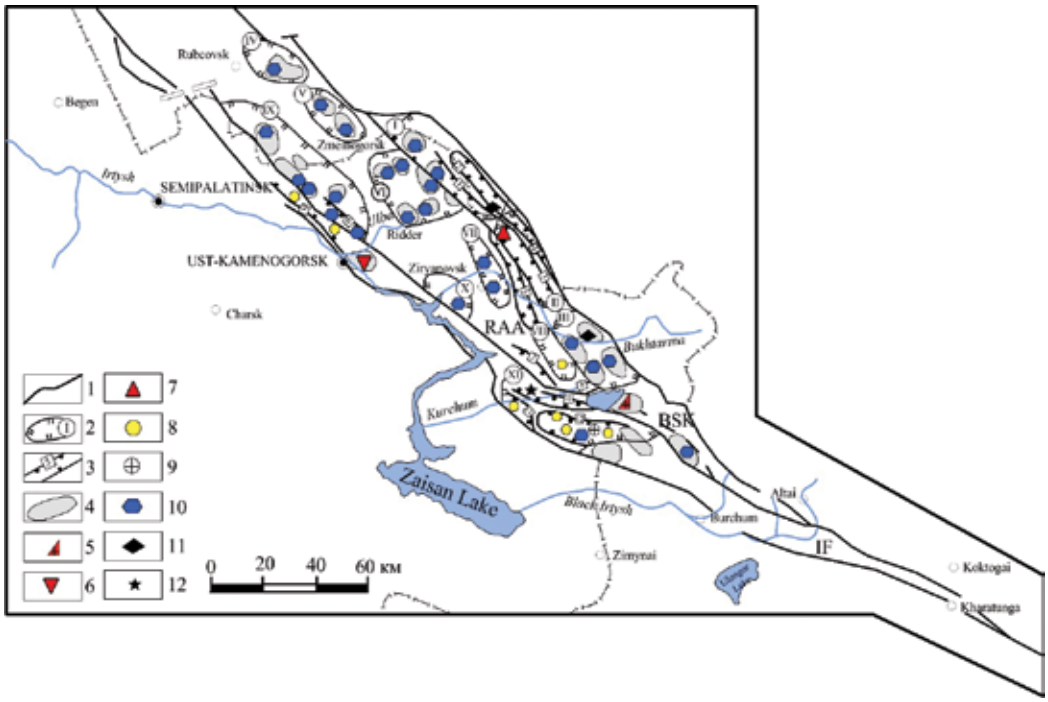

Figure 5. Rudny Altai copper-polymetallic belt. 1—Boundary of metallogenic zones; 2—ore district; 3—ore zone; 4—ore node; 5 to 12—ore formations: 5—epimagmatic; 6—skarn; 7—greisen-quartz-vein; 8—quartz vein golden; 9—gold-quartz berezitic; 10—pyrite-polymetallic; 11—volcanogenic-sedimentary iron-manganese; 12—metamorphogenic (golden). Metallogenic zones: IF—Irtysh-Fuyun; RAA—Rudny Altai-Ashalinsk; BSK—Belousinsk-Sarymsaktin-Kurstinskaya. Ore regions (roman numerals in circles): I—Beloubinsky; II—Khamirsky; III—South Altai; IV—Rubtsovsky; V—Zmeinogorsky; VI—Leninogorsk; VII—Zyryanovsky; VIII—Maymyr; IX—Priirtyshsky; X—Bukhtarminsky; XI—Kurchum-Caldzhirsky.

2. hydrothermal metasomatic, associated with changes in volcanic-sedimentary rocks and fluid-porphyry complexes on the path of ore-bearing flows. The latter type includes the majority of commercial pyrite-polymetallic deposits (Zyryanovskoye, Maleevskoe, Belousovskoye, and so on).

The Rudny Altai is the main raw material base of nonferrous metallurgy in Kazakhstan. As a result of studies, the overall large scale of the Rudny Altai gold-copper-polymetallic belt is renewed, the belt continues in Russia on the northwestern flank (Rubtsovskoye, Zmeinogorskoye, Talovskoye, etc.), and in the southeast, with a sharp narrowing, it is traced to the territory of China Aschaly, Koktal, Timurty, and so on [8, 17]. This regional position of high productivity ore zone shows that the Rudny Altai prospects are not yet exhausted.

The West Kalbia belt is the main gold-bearing structure in East Kazakhstan, in which more than 450 deposits and gold ore occurrences of various geological and industrial types are concentrated [18].The general regularity of the spatial confinedness of gold ore deposits to Zaisan southeast zone formed during the Hercynian collision of Kazakhstan and Siberian lithospheric plates has been established (**Figure 6**). The Charsko-Gornostaevsky ophiolitic belt, which fixes the zone of deep mantle fault, was localized as a result of complex geodynamic development in the southeast zone; fold-melange, overlying thrust and ruptural structures were formed.

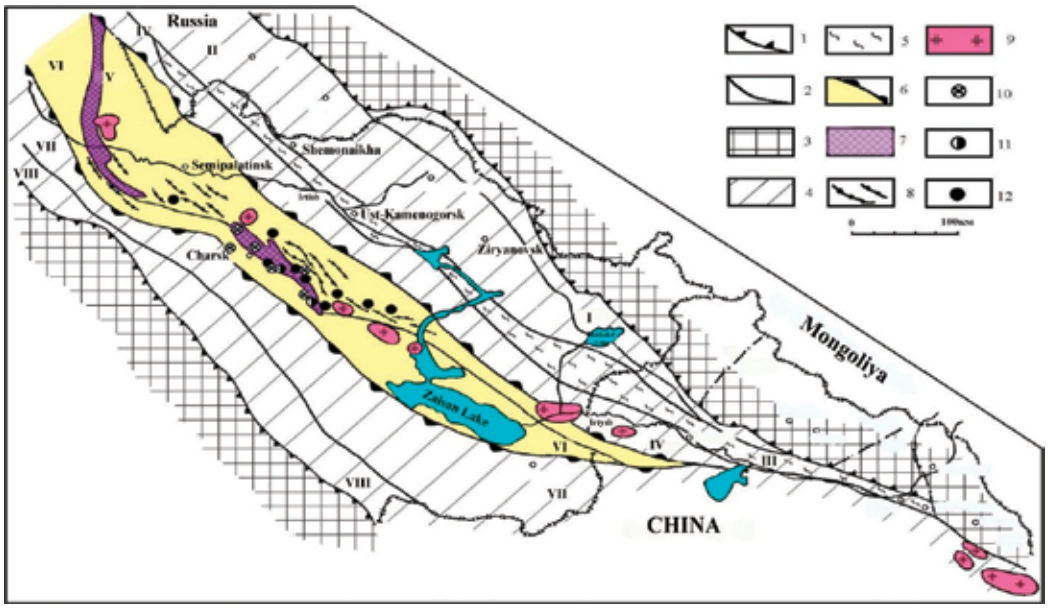

Figure 6. Location of Zaisan suture zone. 1—Borders of Greater Altai and 2—borders of metallogeny zones; 3—Caledonian, and 4 and 5—Hercynian structures; 6—Azaisansky suture; 7—protrusion of hyperbasites; 8—dikes and 9—dubalkalic granitoids; 10 to 12—Cr, Au, Hg deposits. Metallogenic zones (I—Beloubinsko-Sarymsaktinskaya, II—Rudno-Altaiskaya, III—Irtysh-Fyunskaya, IV—Kalba-Narym, V—West-Kalba, VI—Charsko-Zimunaiskaya, VII—Zharma-Saurs, VIII—Syrektas-Sarsazan).

The system of diagonal deep faults in the west-north-west direction (West Kalbinsky, Charskiy, Terektinsky and Baiguzin-Bulaksky) had ore-controlling importance along which the belts of the near-fault small intrusions and dikes of the gabbro-diorite-granodiorite-plagiogranite series (C_{2-3}-C_3) in association with ore-bearing fluid flows were formed.

It was here that, at the junction of continental margins in a collision geodynamic situation, favorable conditions were created for the formation of gold-bearing structures and deposits (Zapadno-Kalkinskaya, Zhanan-Boko-Zaisanskaya, Yuzhnoaltaiskaya and other ore zones), which, according to geological and geophysical data, frame the Charko-Gornostaevsky uplift from the northeast and southwest).The patterns of formation and the criteria for predicting gold ore deposits in the region under study (geotectonic, geological-structural, magmatic, mineralogical-geochemical and others) have been considered in a number of publications [11, 12]. One of the main regularities is belt placement of ore zones and gold ore objects which we unite into a large East Kazakhstan gold belt of regional ranks [1]. The arc belt has a considerable length (length of about 800 km with a width of 40–60 km), and in the northwestern flank, it has a gateway in the meridional direction and is covered with loose sediments in Kulunda depression; in the southeast, it is intersected by rare-metal granites of the Kalba-Narym pluton and it further penetrates into the territory of the Southern Altai and is traced to China (**Figure 7**).

Such a regional position of the gold belt allows us to reevaluate the prospects of Semipalatinsk Priirtyshye to identify gold deposits under the cover of loose sediments of the Kulunda depression (**Figure 8**).

http://dx.doi.org/10.5772/intechopen.72745

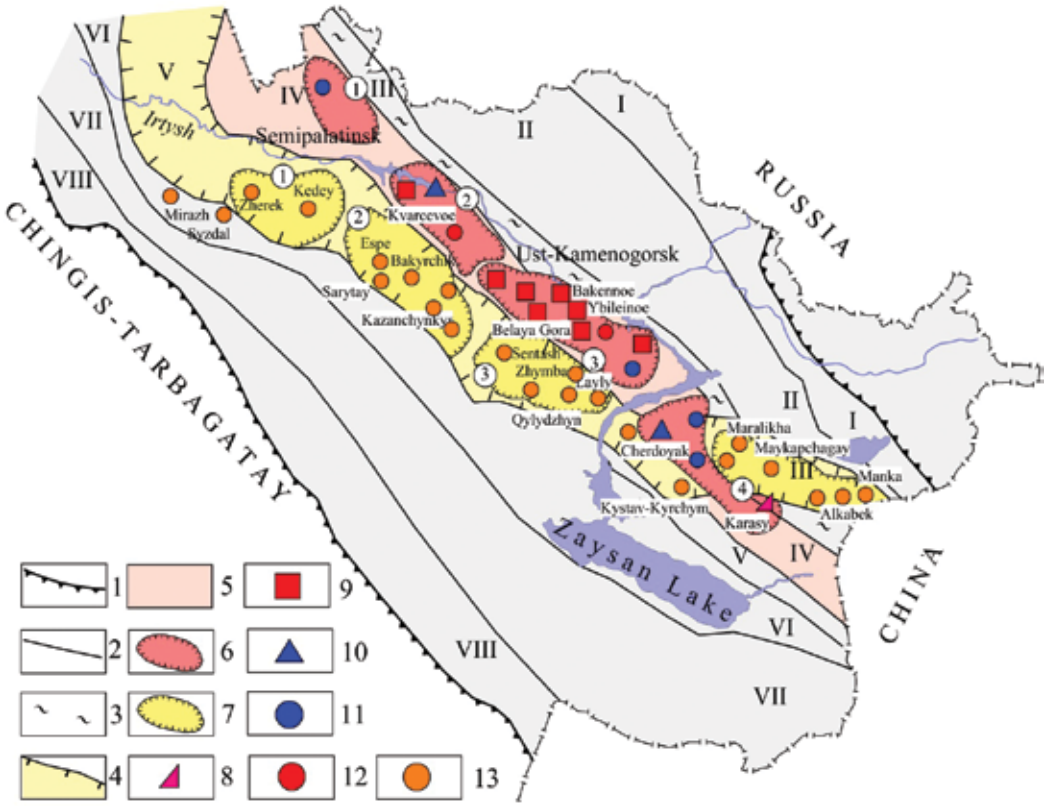

Figure 7. Scheme of placement of rare metal and gold-ore belts. 1—The boundaries of the Greater Altai and 2—metallogenic zones; 3—Irtysh crush zone; 4—East Kazakhstan gold ore, and 5—Kalba-Narym rare metal belt; 6—rare metal ore regions (1—Shulbinsk; 2—North-West-Kalba; 3—Central-Kalba; 4—Narym); (7) gold ore regions (1—Mukursky; 2—Bakyrchik; 3—Kuludjun; 4, South Altai); (8–13) types of deposits: 8—albitite-greisen (Sn, Ta); 9—rare metal pegmatites (Ta, Nb, Be, Li, etc.); 10—greisen-quartz-vein (Sn, W); 11—quartz vein tin (Sn, W); 12—tungsten; 13—gold ore deposits. Metallogenic zones (I—Beloubinsko-Sarymsaktinskaya; II—Rudy Altai; III—Irtysh; IV—Kalba-Narym; V—West-Kalba; VI—Charsk; VII—Zharma-Saurs; VIII—Syrektas-Sarsazan). Deposits of the Kalba-Narym zone: 1—quartz; 2—Bakennoye; 3—Jubilee; 4—Belaya Gora; 5—Cherdoyak; 6—Karasu. Deposits of the West Kalba zone: 1—Kazanchunchur; 2—Kuludjun; 3—Layla; 4—Kystav-Kurchum; 5—Maralikha; 6—Maykapchagay; 7—Alkabek; 8—Manka.

An important ore-petrological criterion is determined in establishing paragenetic connection of gold with small intrusions and dikes of Kunushsky complex C3 and its analogues (Saldyrminsky and Katoy complexes). The leading geological and industrial types of gold deposits are: (1) gold-listenitic (Maralakha deposit); (2) gold-sulfide (Suzdalskoe, Mirage, etc.); (3) gold-quartz (Kuludzhun, Sentash, Kystav-Kurchum); (4) gold-quartz beresit (Baladzhal, Manka); (5) gold-arsenic-carbonaceous (Bakyrchik, Bolshevik); (6) crust weathering (Zhanan, Mukur) and (7) gold-placer (West Kalba, the South Altai).

The Bakyrchik deposit is the largest world-level object of the "black shale type" represented by zones of gold-arsenic-carbon mineralization and vein silicification [3, 11, 12]. Depositions of molasses, limnic formations (Buconian suite C_{2-3}) which are subject to intense dynamometamorphic and hydrothermal-metasomatic changes in the zone of latitudinal Kyzylovskiy deep fault (overthrust) are ore-bearing (**Figure 9**).

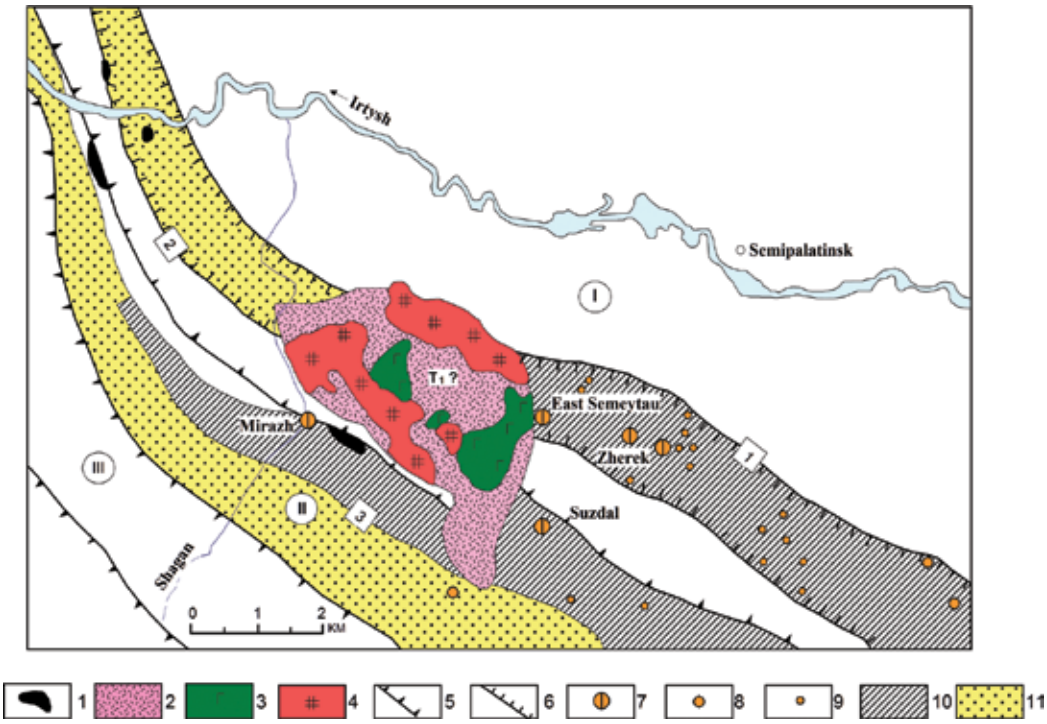

Figure 8. Forecast-metallogenic scheme of Semipalatinsk Priirtysh. 1—Precambrian hyperbasite formation; 2 to 4—volcano-plutonic trachybasal-trachyriolithic formation T1? (2—trachybasalt-trachyriolithic; 3—gabbro-monzonite; 4—granosyenite-granite-porphyry subformation; semeitauskaya series); 5—boundary of metallogenic zones (I—West Kalba; II—Charsk; III—Zharma-Saur); 6—boundary of ore zones (1—Mukur; 2—Shagan; 3—Mirage-Suzdal); 7 to 9—gold ore objects (7—deposits; 8—ore occurrences; and 9—mineralization points); 10 to 11—prospective areas (10—high degree of prospects; 11—predictive).

Ore bodies are represented by lenticular and ribbon-like deposits, stockworks of hydrothermally altered sedimentary rocks with veins and nests of metasomatic quartz and abundant dissemination of gold-bearing pyrite and arsenopyrite. Their thickness varies from 0.6 to 20 m, and gently sloping deposits are traced by a drop of 1700 m. The average gold content is 8–9 g/t. The Bakyrchik ore region retains high prospects for the increasing of forecast gold resources, which makes it possible to bring them to a number of world super-large objects.

The Kalba-Narym belt is the main rare-metal structure in East Kazakhstan. According to new geodynamic schemes, it is regarded as a foreign block of EC (terrain) which has become connected to the Greater Altai during the Hercynian collision (C_1 and later). Based on analysis and generalization of deep geophysical studies, it is assumed that the Kalba-Narym granitoid belt is located in the head part of a giant tectonic magmatic zone, steeply falling to the northeast under the Rudny Altai (to a depth of more than 100 km). The centers of magma formation originated, judging by the composition of the granite smelting, in a metagranite layer or on its boundary with metadiorite. The zones of transit heat-mass flows penetrated from the lower parts of the EC and the upper mantle through the system of deep faults.

The Kalba-Narym granitoid belt unites many deposits and ore occurrences of pegmatite, albit-greisen, greisen-quartz, and other ore-forming types. Well-known industrial deposits

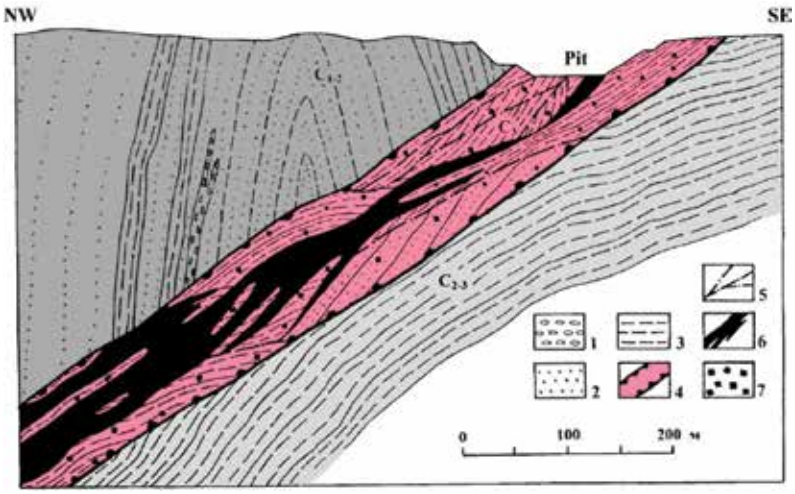

Figure 9. Geological section of gold-sulfide deposit Bakyrchik through the central ore body (based on the materials of V. M. Yanovsky, Y.V. Chudikova). 1–3 carboniferous sediments: 1—conglomerates, gravelites; 2—sandstones; 3—carbonaceous siltstones and shales; 4—Kyzylovskaya zone of deep fault; 5—faults, tectonic cracks; 6—ore body; 7—diffuse sulfide mineralization.

(Bakennoye, Yubileynoye, Belaya Gora, etc.) were developed by Belogorsk mining and dressing plant in previous years, but at present they are mothballed. The main source of rare metals is deposits of rare metal pegmatite (Ta, Nb, Be, Li, Cs, Sn) genetically associated with the granites of the Kalbinsk complex (P_1) [13].

Deep faults and feathering faults that functioned for a long period of time were of decisive importance in the location of the Kalba-Nyrym granitoid belt. The most magmatically submissive role of the northwestern deep faults is manifested in the late Herzinian post-collision (orogenic) stage of development. The Kalba-Narymsky and Terektinsky deep faults served as the largest magma guides. Granite intrusions which formed in a mobile geodynamic environment turned out to be the most ore-bearing; it contributed to more intensive ore formation processes in nonequilibrium PT—conditions and, ultimately, the formation of industrial deposits (Bakennoe, Ybileinoe, and so on). On the contrary, quieter tectonic conditions of crystallization of relatively inactive and viscous granite melts lead to dispersion of RE and poor ore content of granites (the massifs of Dubygaly, Sibinsky, and so on). On this basis, ore-magmatic systems with different degrees of productivity were identified, ore-petrochemical typification of granitoids was performed and geological-genetic models of ore formation were constructed as the leading factors for forecasting new rare metal deposits [19].

Importance is attached to ore-controlling role of latitudinal deep faults of ancient deposits and long-term activation, especially at clusters at their intersection with northwestern, northeastern or meridional disjunctives (Gremyachinsko-Kiinsky, Asubulaksky, Belogorsky, Mirolyubovsky, and so on).

Thus, Asubulak latitudinal fault controls pegmatite field location in which two ore-bearing strips of sublatitudinal strike separated by a fault are distinguished: (1) Ungur (northern), including ore objects in Carmen-Kuus, Akkesen, Ungursai and Plachgor, and (2)

Krasnokordonskaya (southern), uniting the Yubileynoye industrial deposit and ore occurrences in Red Cordon, Rock and Budo in 1.5 km increments.

Mirolyubovsky latitudinal long-term activation fault had a decisive role in distribution of tungsten-greisens and hydrothermalites of the same granite massif, in which the main ore bodies were localized in meridional discontinuities that cut across Kalbin granites and leucogranites of the monastirskiy complex. At the final stage of the Hercynian tectonic magmatic cycle, the Mirolyubovsky fault was transformed into a fault-shift with displacement of all intrusive formations and ore bodies with an amplitude of 3 km.

Favorable factors of ore formation include the multistage structure of the Kalba-Narym pluton in the form of alternating cross sections of granite plates and enclosing sedimentary rocks, which caused formation of structural traps and screens for pegmatite fields. Apical parts and above intrusive zones of granite massifs, their apophyses, hidden domes and tectonically weakened zones saturated with vein formations are the most promising for the concentration of rare metal mineralization. According to geological and geophysical data, the main ore sites and ore fields are spatially located in a thickened part of granite massifs, above the magmatic-leading roots or along their periphery [4, 20].

The Zharma-Saursky belt was formed on the northeastern outskirts of the Kazakhstani massif, and it is characterized by complex geodynamic development and polycyclic metallogeny. It unites three metallogenic zones: Charskaya, Zharma-Saurskaya and Sariktas-Sarsazanskaya.

Charskaya zone is a structure of regional or planetary rank, and it has a long and complex history of development. Within its limits, the Charsko-Gornostaevsky ophiolite belt is distinguished which is fixed by separate fragmentary outcrops of Precambrian metamorphic rocks, protrusions of hyperbasites, thrust zones and serpentinite melange [2, 18, 21]. In the Precambrian cycle, the primary ores (Cr, Ni, Co, Cu) formed in the oceanic geodynamic environment are associated with the hyperbasite formation (Charsky complex, PR?). The ores belong to the hysteromagmatic chromium, magmatically liquation and hydrothermal copper-cobalt-nickel formations.

Zharma-Saurskaya zone, located in the central part of the ore belt, developed under the influence of a deep mobile zone (DMZ), was characterized by an elevation of the upper mantle and a high-power metabasalt layer (24 km). The focal part of the DMZ was characterized by high magmatic saturation with a strong development of syncollision intrusions of gabbro-diorite-granodiorite-plagiogranite series (C_1 and C_{2-3}) productive for copper-porphyry, sulfide copper-nickel and gold mineralization. Copper-porphyry type of mineralization is manifested in a volcano-plutonic belt of intrusions of Saursky complex C_1 (the Kyzylkain deposit in Saursky ore district) [3]. Maksut deposit is genetically associated with stratified intrusions and dike-like bodies of the late-collision activation stage, controlled by deep faults. Gold ore objects are associated with small intrusions and collision-type dikes (C_3) and are fixed by quartz-vein and stockwork zones (Ashaly, Daubai, Chang, and so on).

Syrektas-Sarsazan zone is a margin southwestern structure in Zharma-Saur, and it is bounded by Syrektas (East Tarbagatay) and Chingiz-Saur deep faults. It is characterized by a section of the EC of increased syality and copper-rare metal-rare earth specialization (Cu, Mo, W, Nb, Zr, TR) [3, 19].

4. Discussion of results

Cardinal changes in views on the Earth development and world geological science have occurred in recent years on the basis of provisions of modern geotectonic hypotheses (new global tectonics, tectonics of lithospheric plates, terranean tectonics, plumectonics, and so on). Identification of regular relationships between cyclically directed self-development of geological structures and ore formation processes in certain geotectonic cycles and epochs is of fundamental importance [11]. Mineral and raw materials sector continues to be the basis of economies in many countries, but experts point to the depletion of the world's mineral resources. The most important task is to open new mineral deposits taking into account current trends in world geological science. This is of particular importance for East Kazakhstan region territory—a unique geological test site, where there is an urgent need to replenish ore reserves of deposits exploited by mining and metallurgical enterprises.

The considered territory of East Kazakhstan, located in the Central Asian mobile belt, is a unique geological providing ground that unites many deposits of ferrous, nonferrous, precious, rare metals and other minerals. For decades, accumulated large factual material on geology, tectonics and metallogeny has been traditionally tied up from the positions of classical geosynclinal hypothesis [22]. The Irtysh-Zaisan and Chingiz-Tarbagatai fold systems were distinguished here, including structural-formational zones, ore-bearing structures with their own set of geological and ore formations. In recent years, from the new theoretical positions, the main problematic issues of geodynamic and metallogenic development of geological structures have been considered in a trilogy "Big Altai" (BA) and a number of other publications [2, 3, 6, 20, 21, 23, 24]. Based on these studies results, the emergence and formation of large geological structures in Kazakhstan, Siberia, the Urals and other regions are associated with Eurasian continent disruption into individual slabs, geoblocks, massifs and detachments in the late Proterozoic that migrated and experienced complex development in the evolution of the Paleo-Asian ocean (Buslov, 2011; Geodynamics, 2007). According to paleomagnetic and geodynamic reconstructions, it is assumed that modern geological structures (the Rudnyi Altai, Kalba-Narymskaya, West-Kalbinsky Zones and others) are erratic masses of paleocontinents (Eastern Gondwana, etc.), possibly terranes, that drifted in the Paleo-Asiatic ocean and interlocked in the collision stage (C_1-C_3) when Kazakhstan and Siberian lithospheric plates collided. Paleogeodynamic analysis of the BA structure formation was carried out from the Precambrian to the Cimmerian and Alpine cycles inclusive. As a result of a complex polycyclic development of tectonic magmatic processes and metallogeny in the region, a system of ore belts and metallogenic zones that unite many types of mineral deposits was formed.

5. Conclusion

On the basis of theoretical positions of mobilism, the BA represents a single system of parallel ore belts of regional ranks in the northwestern direction (Rudnoaltayskiy, Kalba-Narymsky, Zapadno-Kalkinsky and Zharma-Saursky) formed as a result of the Hercynian collision of Kazakhstan and Siberian lithospheric plates and the degradation of the Irtysh-Zaisan paleobasin (parts of the Paleo-Asiatic ocean). According to geological and geophysical data, the

ore belts are characterized by a large-scale development along their length and depth, which reflects their high material and energy potential and opens new prospects for forecasting and prospecting works within their boundaries.

In each ore belt, the maximum mineralization productivity was manifested in certain geodynamic settings and regimes. In the Rudnyi Altai, the main pyrite-polymetallic deposits were formed in a riftogenic geodynamic environment, genetically related to the Devonian basalt-andesite-rhyolite volcanism (D_1e-D_3fr) and were controlled by a system of echeloned deep faults in the northwestern direction.

Gold-bearing deposits of Western Kalba, the Southern Altai and Zharma-Saur were formed in the Middle Gerzinian stage (C_1-C_3) in a collision geodynamic situation under conditions of horizontal displacement, jointing and turning of Kazakhstan and Siberian lithospheric plates, manifestations of main folding phases, thrust and melange structures and introduction of gold-bearing small intrusions and dikes (C_{2-3}-C_3). The ore-controlling role of diagonal deep faults system of mantle-crustal location and the regmatic system of renewed sublatitudinal deep faults in location of gold ore objects has been determined. The main gold deposits (Bakyrchik, Bolshevik, Suzdal, Kuludgun, Maralikha, etc.) were located in the Zaisan suture zone forming East Kazakhstan gold belt of regional ranks.

Rare-metal deposits are formed mainly in the Hercynian cycle in post-collision (orogenic) geodynamic situation as a result of vertical arched motions and a powerful development of Permian granitoid magmatism. They are spatially placed in granitoid belts of the northwestern direction formed in tectonically weakened blocks of EC of increased syality. The main importance is given to rare-metal and rare-earth deposits (pegmatite, albitite-riebeckite, etc.) formed in certain nonstandard geological settings and nonequilibrium PT conditions for granite massif formation.

As a result of study, regular relationships of tectonic and metallogenic development of geological structures in East Kazakhstan have been determined. The revealed mineralogical specialization of geodynamic environments is one of the main methods for forecasting and searching for new deposits along with detailed structural and physical studies of geological formations. The setting of detailed prognostic-metallogenic works in selected perspective structures at modern scientific and technical level is recommended for forecast implementation.

Author details

Boris Dyachkov, Marina Mizernaya*, Oksana Kuzmina, Natalia Zimanovskaya and Tatiana Oitseva

*Address all correspondence to: mizernaya58@bk.ru

D. Serikbaev East Kazakhstan State Technical University, Ust-Kamenogorsk, Republic of Kazakhstan

References

[1] Innovations and perspective technologies of geological exploration in Kazakhstan. In: Materials of the International Scientific and Practical Conference; Almaty. 2017. p. 254

[2] The Great Altai: (Geology and Metallogeny). Book 1. Geological Structure ed. Almaty: Gylym; 1998. 304 p

[3] The Great Altai: (Geology and Metallogeny). Book 2. Metallogeny ed. Almaty: Gylym; 2000. 400 p

[4] Dyachkov BA, Titov DV, Sapargaliev EM. Ore belts of the Greater Altai and an assessment of their prospects. Geology of Ore Deposits. 2009;**51**(3):222-238

[5] Dyachkov BA, Ganzhenko GD, Sapargaliev EM. Geodynamic Conditions for the Formation of Ore-bearing Structures of the Greater Altai. Almaty: KazGeo; 2016. pp. 9-21

[6] Shcherba GN. Global mobilism (main provisions). Geodynamics and Minerageny of Kazakhstan. 2000;**RIVOVAKRK**(1):40-45

[7] Berzin NA, Kolman RG, Dobretsov NL, et al. Geodynamic map of the western part of the Paleo-Asiatic ocean. Geology and Geophysics. 1994;**35**(7, 8):8-29

[8] Bespaev KhA, Polyansky NV, Ganzhenko GD, Dyachkov BA, et al, editors. Geology and Metallogeny of the South-Western Altai (Within the Territory of Kazakhstan in China). Almaty: Gylym; 1997. 288 p

[9] Kuzmin MI, Yarmolyuk VV. Early history of the earth, possible mechanisms of the first granitoid rocks of the continental crust in the Gadeysko-eoarchaean time. In: Granites and Earth Evolution: Mantle and Crust in Granite Formation. Ekaterinburg: IGG UrB RAS; 2017. pp. 156-158

[10] Dyachkov BA, Mizernaya MA, Mayorova NP, et al. Geotectonic position and metallogeny of the great Altai structures in the system of the central-Asian imobil belt. In: New-Frontiers in Tectonic Research General Problems, Sedimentary Basins and Island Arcs. Croatia: InTech; 2011. pp. 73-92

[11] Narseev VA, Rafailovich MS, Dyachkov BA. Gold mining potential of Kazakhstan Giant gold deposits of Central Asia. Strengthening the gold ore potential of Kazakhstan. In: Materials of the International Symposium; Almaty. 2014. pp. 10-22

[12] Rafailovich MS. Metallogeny of gold in Kazakhstan: State and prospects. In: Earth Sciences in Kazakhstan; Almaty. KazGeo; 2008. pp. 195-206

[13] Dyachkov BA. Genetic Types of Rare Metal Deposits of the Kalba-Narym Belt. Ust-Kamenogorsk: EKSTU; 2012. 130 p

[14] Fershtater GB, editor. Paleozoic Intrusive Magmatism of the Middle and Southern Urals. Ekaterinburg: RIO UB RAS; 2013. 368 p

[15] Cao M-J, Zhou Q-F, Qin K-Z, Tang D-M, Evans NJ. The tetrad effect and geochemistry of apatite from the Altay Koktokay no. 3 pegmatite, Xinjiang, China: Implications for pegmatite petrogenesis. Mineralogy and Petrology. 2013;**107**(6):985-1005

[16] Parilov YS, editor. Genesis of the main types of deposits of non-ferrous metals in Kazakhstan (based on the results of studying fluid inclusions). Almaty; 2012. 266 p

[17] Han C, Xiao W, Zhao G, Su B, Sakyi PA, Ao S, Wan B, Zhang J, Zhang Z, Wang Z. Mid-Late Paleozoic metallogenesis and evolution of the Chinese Altai and East JunggaiOiogenic Belt, NW China, Central Asia. Journal of Geosciences. 2014;**59**:255-274

[18] Dyachkov BA, Amralinova BB, et al. Laws of formation and criteria for predicting nickel content in weathering crusts of East Kazakhstan. Journal of the Geological Society of India. 2017;**89**(5):605-609

[19] Dyachkov BA, Mataibaeva IE, Frolova OV, Gavrilenko OD. Types of rare metal deposits in East Kazakhstan and their appraisal. Gornyi Zhurnal. 2017;**8**:45-50

[20] Sherba GN, Dyachkov BA, Nakhtigal GP, editors. Metallogeny of Rudny Altai and Qalba. Almaty: Nauka; 1984. 240 p

[21] Safonova I. The Russian-Kazakh Altai orogen: An overview and main detatable issues. Geoscience Frontiers. 2014;**5**:537-552

[22] Geology of the USSR. Volume XLI. Eastern Kazakhstan. Part I—A Geological Description ed. Moskow: Publishing House "Bosom"; 1967. 467 p

[23] Tkachev A. Evolution of metallogeny of granitic pegmatite associated with orogens throughout geological time. Geological Society London Special Publication. 2011; **350**(1):7-23

[24] Vladimirov AG, Kruk NN, Khromykh SV. Permian magmatism and deformations of the Altai lithosphere as a consequence of thermal processes in the crust and mantle. Geology and Geophysics. 2008;**49**(7):636

Chapter 6

Post-Opening Deformation History of the Japan Sea Back-Arc Basin: Tectonic Processes on an Active Margin Governed by the Mode of Plate Convergence

Yasuto Itoh

Additional information is available at the end of the chapter

http://dx.doi.org/10.5772/intechopen.71953

Abstract

Three-dimensional structure of the Japan Sea back-arc basin is investigated based on an extensive reflection seismic survey. The process of the Oligocene to early Miocene rifting is described in reference to a geologic database, and the most likely paleoreconstruction of rifted continental fragments is presented. The back-arc region has been subjected to intermittent post-opening deformation events, which the author regards as side effects of temporal shifts in the convergence mode of the Philippine Sea Plate (PSP). The southern shelf of the Japan Sea appears to have suffered North-South strong contraction for a short period of time during the latest Miocene. Resumed convergence of the PSP was responsible for the regional tectonic event because frequent igneous intrusions within the upper Miocene series upon the back-arc shelf, which was confirmed by a borehole stratigraphic study, are suggestive of revitalized arc volcanism linked to dehydration of the subducted slab. During the Quaternary period, confined structure in varied forms developed on the shelf, which is related to the dextral wrench deformation of southwest Japan and the eventual arc-parallel crustal breakup along the back-arc region. Simultaneous highly oblique subduction of the PSP provoked the prevailing shear stress and conspicuous neotectonic deformation.

Keywords: convergent margin, back-arc opening, back-arc basin, seismic survey, Japan Sea, Philippine Sea Plate, eastern Eurasia

1. Introduction

Back-arc opening specifically occurs on convergent plate margins of the globe. Since the phenomenon inevitably impacts geographical and environmental conditions, numerous researchers have pursued evolutionary processes of back-arc basins.

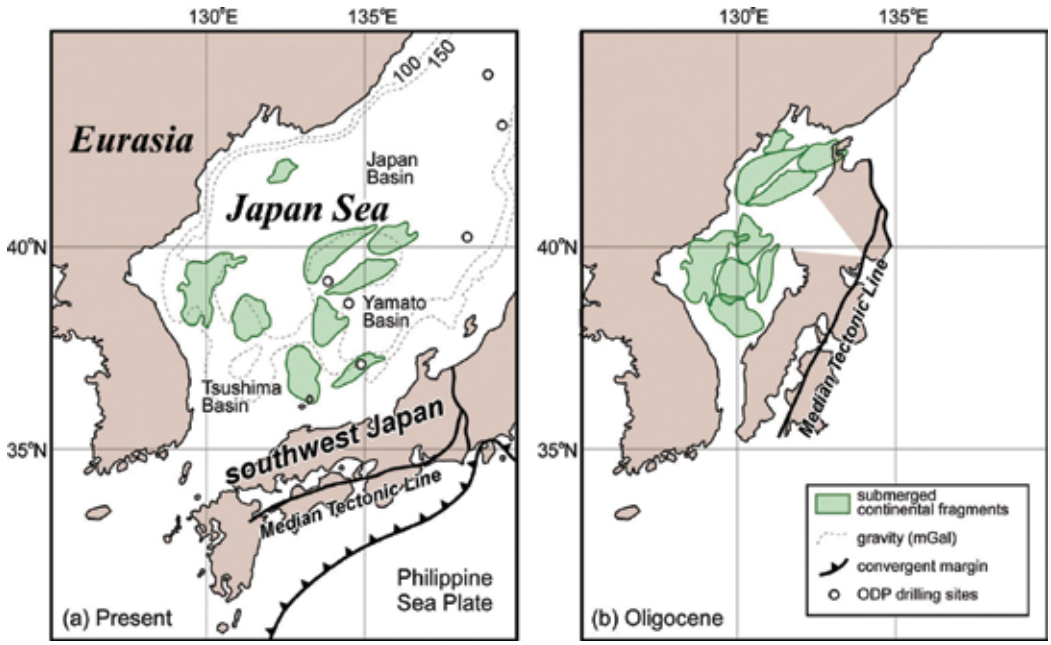

Figure 1. (a) Present configuration of southwest Japan and (b) its paleogeographic reconstruction before opening of the Japan Sea following [4]. Bending of the southwestern Japan arc caused by the middle Miocene collision event has been restored referring to paleomagnetic studies, expressed as the straightforward trend of the Median Tectonic Line.

The eastern Eurasian margin has been a site of vigorous basin formation related to long-standing convergence of major oceanic plates since the late Mesozoic [1]. The Japan Sea is located around mid-latitudes on the margin and is interpreted as a late Cenozoic back-arc basin based on the geological affinity between the Japanese Archipelago and the continental rim. In a series of pioneering paleomagnetic studies by Otofuji et al. (e.g., [2, 3]), a fan-shaped opening mode was advocated to explain the large rotation of the rifted block. **Figure 1** shows the most probable paleoreconstruction of the southern part of the Japan Sea [4], in which jigsaw fitting of subsea continental fragments is carefully taken into account.

In this chapter, the author focuses on the southwestern shelf of the back-arc basin. The three-dimensional architecture of the shelf is visualized by means of detailed seismic data, and its development process is described referring to stratigraphic data of deep boreholes. The spatio-temporal variety in the structural styles reflects intermittent changes in the converging sense of the Philippine Sea Plate (PSP). In other words, deformation records around the arc are a key to elucidating the transient motion of the marginal sea plate.

2. Geophysical survey

In 1989, the Ministry of International Trade and Industry (MITI) conducted an extensive offshore seismic campaign around the Japan Sea and the East China Sea (see **Figure 2**) by using the M/V

http://dx.doi.org/10.5772/intechopen.71953

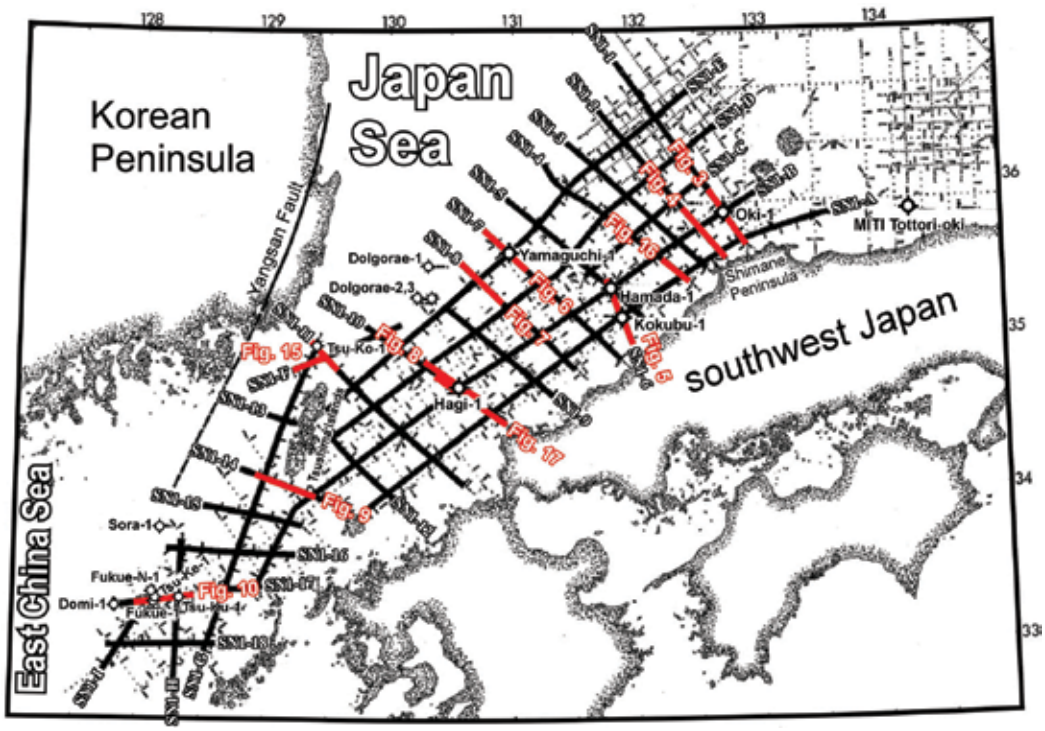

Figure 2. Index map showing geophysical survey tracks (dotted lines) around the southwestern shelf of the Japan Sea. The thick solid lines and larger open symbols are the seismic lines analyzed in the present study and key stratigraphic boreholes, respectively.

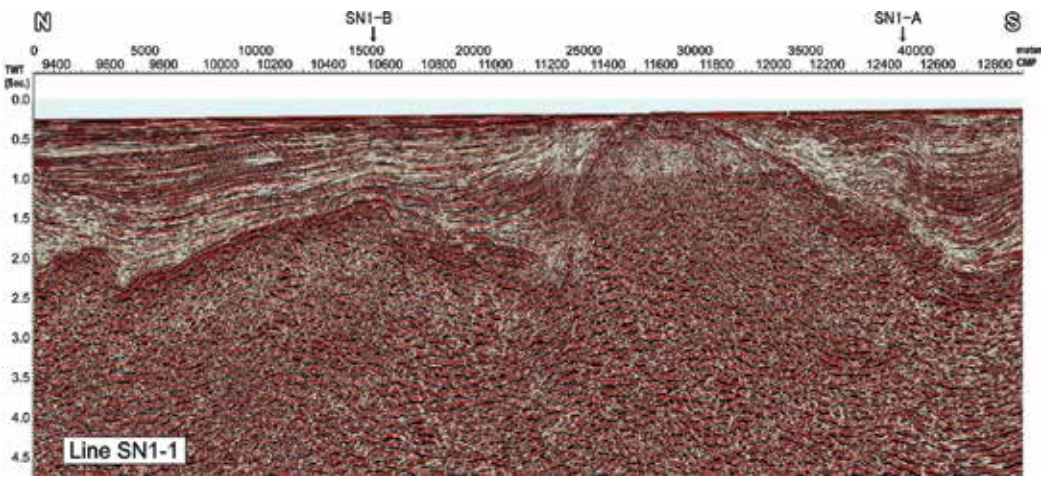

Figure 3. Reflection seismic profile (time migration; SN1-1) on the southwestern shelf of the Japan Sea. See **Figure 2** for line locations.

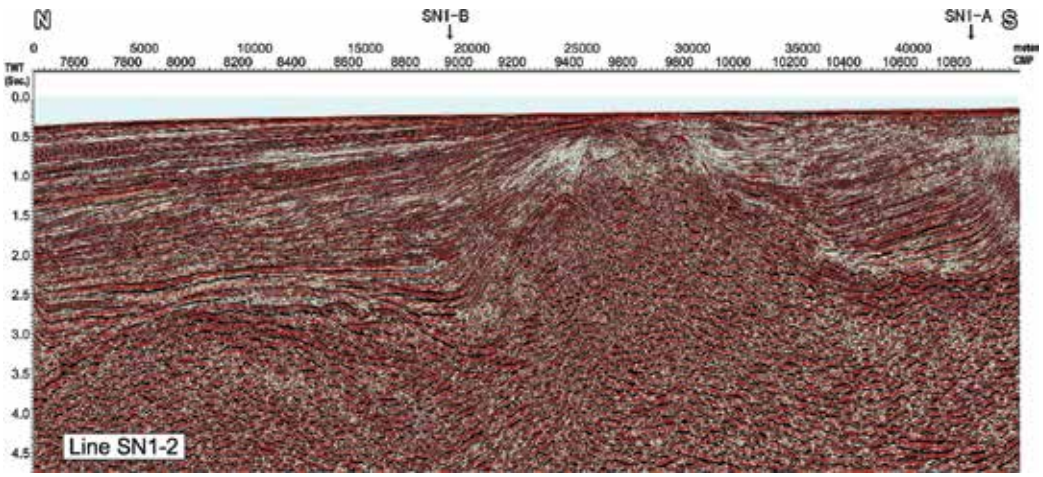

Figure 4. Reflection seismic profile (time migration; SN1-2) on the southwestern shelf of the Japan Sea. See **Figure 2** for line locations.

GECO MY. During the shooting of survey lines, 240 channels of hydrophones (12.5-m intervals) recorded the energy released from a tuned air-gun array (total: 78 l), which was shot at 25-m intervals. Raw field data were stacked and then subjected to a processing sequence for the enhancement of resolution. Regional seismic reflectors were traced throughout the study area and were correlated with the results of a previous seismic survey [5]. Basically, the back-arc shelf consists of an acoustic basement (pre-Neogene metamorphosed sedimentary complex and early Miocene volcaniclastics) and Neogene-Quaternary marine sediments. In the following section, we investigate the characteristic features of the seismic profiles.

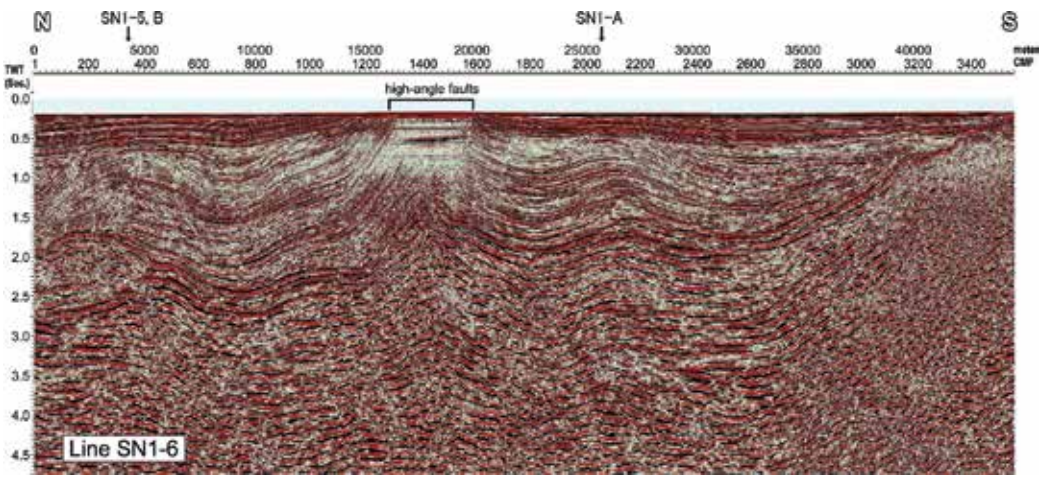

Figure 5. Reflection seismic profile (time migration; SN1-6) on the southwestern shelf of the Japan Sea. See **Figure 2** for line locations. The bracket indicates the recent high-angle faults discussed in the chapter.

http://dx.doi.org/10.5772/intechopen.71953

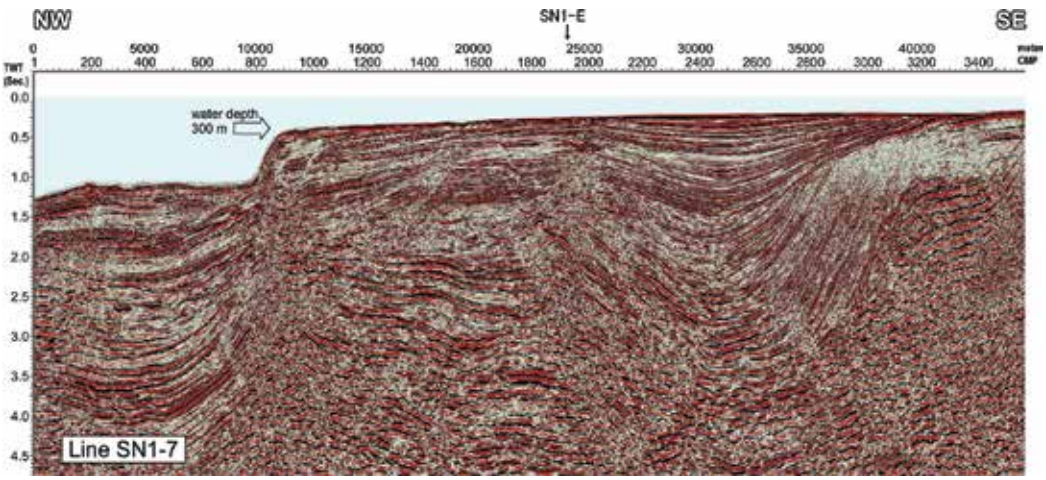

Figure 6. Reflection seismic profile (time migration; SN1-7) on the southwestern shelf of the Japan Sea. See **Figure 2** for line locations. The arrow indicates the location at which the water depth exceeds 300 m.

The morphology of the top of the acoustic basement is well preserved in the eastern part of the survey area. **Figure 3** (line SN1-1) shows the tilted blocks of the basement, which imply dominant normal faulting in the incipient stage of the back-arc rifting. On occasion, thinly layered younger sediments are tilted and dragged upon the fault scarps reflecting subsequent tectonic events (**Figure 4**; SN1-2).

The most remarkable and traceable event around the survey area is an unconformity in the upper portion of the sediment pile (**Figure 5**; SN1-6). The east-northeastward (namely arc-parallel) axis of the folds coincides with the latest Miocene deformation trend on land [6]. The strong contraction appears to almost reach the northern shelf break (**Figure 6**; SN1-7). As

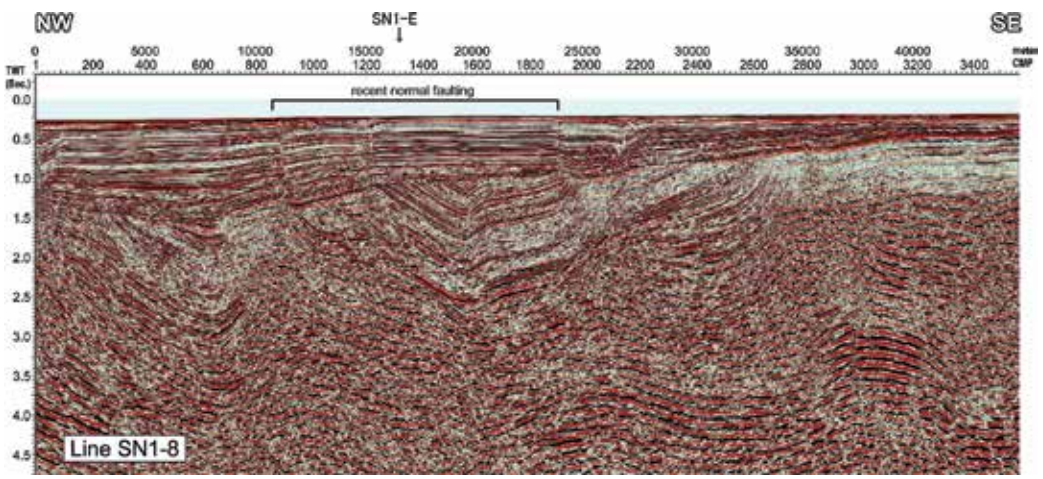

Figure 7. Reflection seismic profile (time migration; SN1-8) on the southwestern shelf of the Japan Sea. See **Figure 2** for line locations. The bracket indicates the range of recent normal faulting discussed in the text.

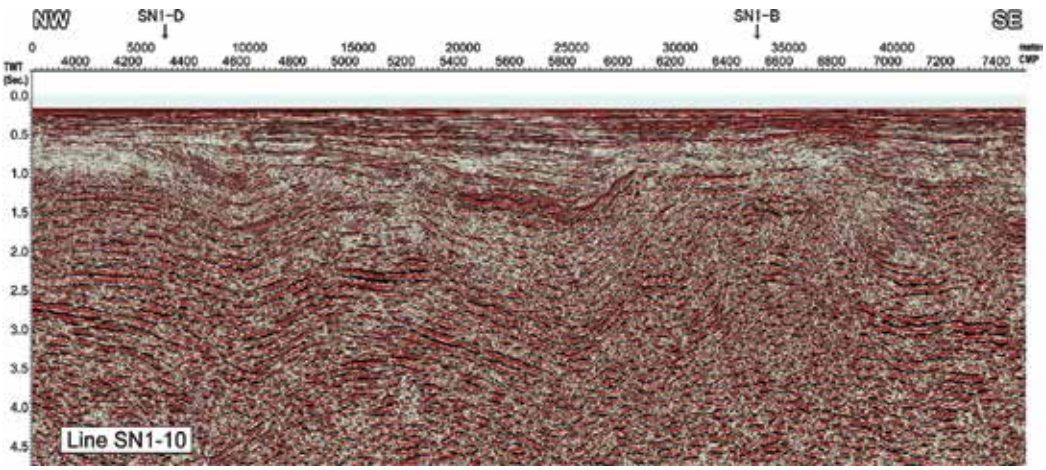

Figure 8. Reflection seismic profile (time migration; SN1-10) on the southwestern shelf of the Japan Sea. See **Figure 2** for line locations.

shown in **Figure 5**, undulation of the erosional surface and truncation near the surface are indicative of younger tectonic events.

We notice a change in the recent stress regime around the westernmost part of the shelf. **Figure 7** (line SN1-8) demonstrates that the latest Miocene unconformable boundary is cut by normal faults. Separation along these faults grows through the Plio-Pleistocene. The areal extent and neotectonic context of this intriguing feature is discussed in the following section.

Deformation trends around the westernmost shelf are partially obscured by strong discontinuous reflectors in shallow horizons (**Figure 8**; SN1-10). Such disturbances are spatially coincident

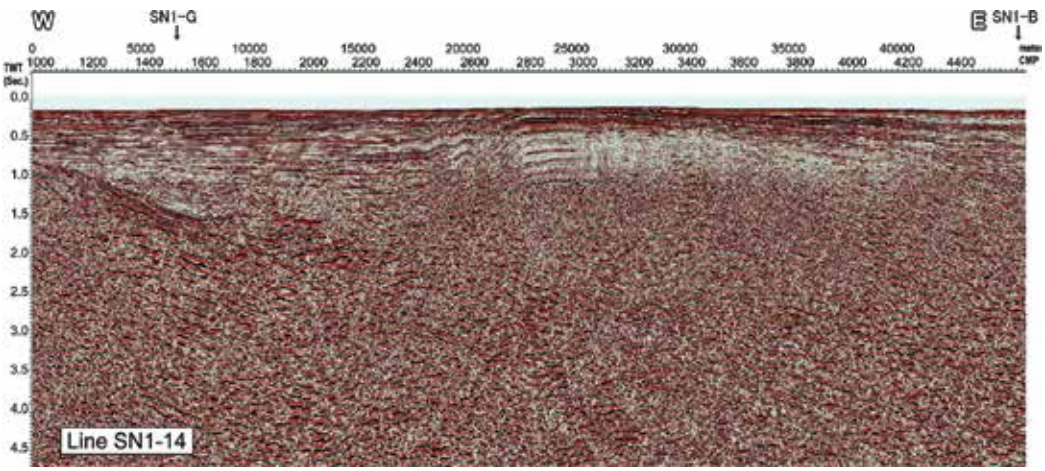

Figure 9. Reflection seismic profile (time migration; SN1-14) around the eastern end of the East China Sea. See **Figure 2** for line locations.

http://dx.doi.org/10.5772/intechopen.71953

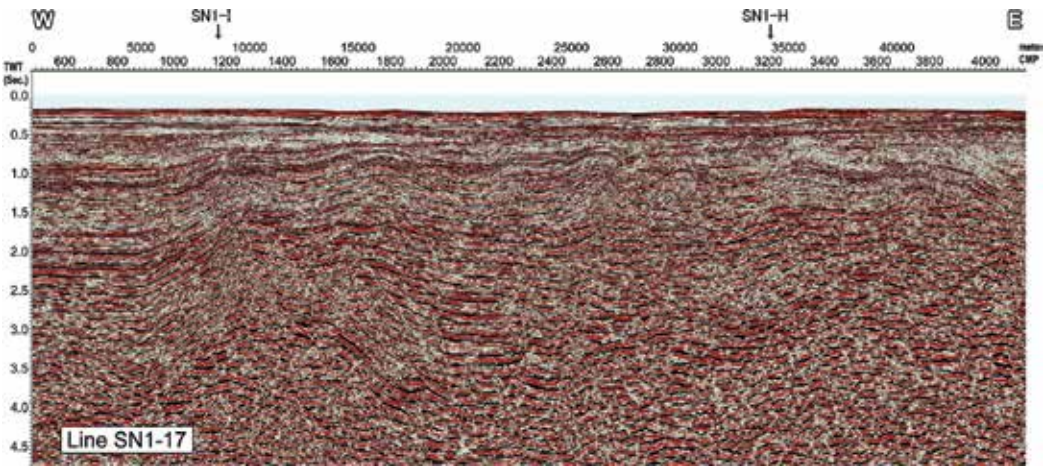

Figure 10. Reflection seismic profile (time migration; SN1-17) around the eastern end of the East China Sea. See **Figure 2** for line locations.

with sporadic geomagnetic anomalies [7]. Together with borehole lithology described in the next section, post-opening volcanic activities may be responsible for the phenomenon.

The regional contraction zone abruptly ends as the pivot of a folding fan to the west. Back-arc folds change their azimuth to counterclockwise and converge into the anticlinoria of Tsushima [7]. The islands along the Japan-Korea border are accompanied by a deep half-graben developed beneath an east-dipping thrust (**Figure 9**; SN1-14) and are regarded as the product of the highest level of transpressive stress around the end of the Miocene.

In contrast with the strong deformation on the Japan Sea shelf, the easternmost portion of the East China Sea is underlain by intact sediments in shallow horizons (**Figure 10**; SN1-17). Short-wavelength deeper undulations are bounded by high-angle ruptures.

3. Stratigraphy

For the purpose of oil exploration, five deep drilling surveys were performed in the study area. **Figure 11** shows their locations (columns 1–5) along with an auxiliary nearby borehole (column 6). Based on detailed stratigraphic assessments [5, 8], lithologic piles penetrated by these boreholes are divided into four units. In ascending order, the X Group corresponds to the acoustic basement and is collectively defined as a mixture of early Miocene nonmarine sediments and pyroclastic rocks and older granitic intrusives. The N Group rests unconformably on the basement and consists of early Miocene marine sediments with numerous tuff intercalations. Nonvolcanic monotonous sediments of the K Group yield foraminiferal assemblages correlated with Blow's [9] zone N14~N16 (late middle Miocene-early late Miocene) and are overlain by sandy clastics of the D Group, the basal part of which is assigned to zone N19 (early Pliocene) of [9]. Thus, the angular unconformity at the K/D boundary is identified to be

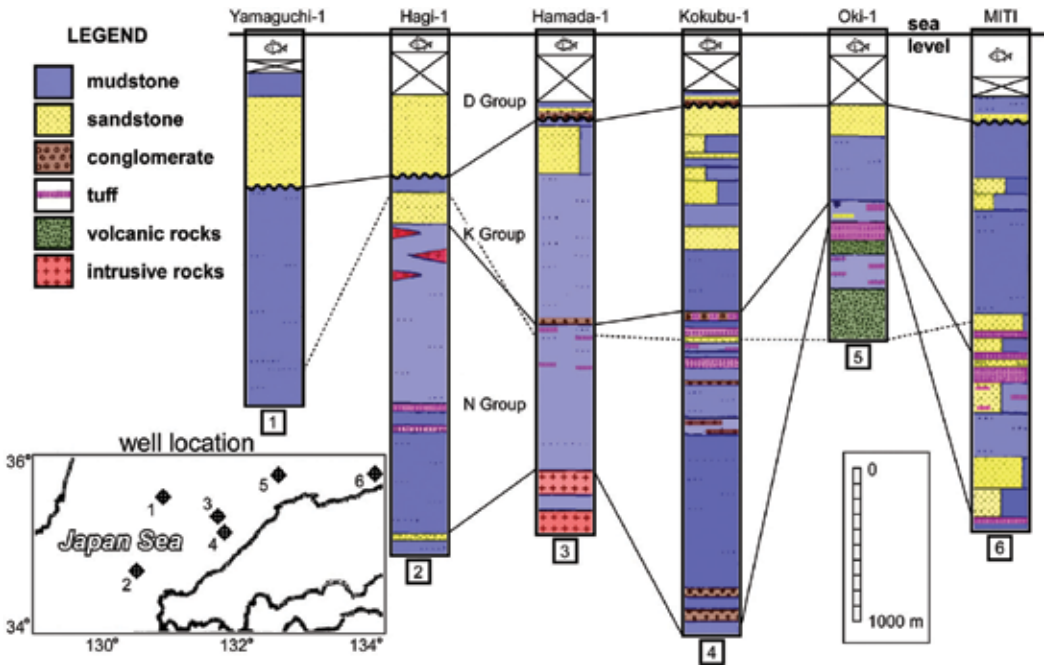

Figure 11. Stratigraphy of the offshore boreholes described by [5, 8]. Their localities are also shown in **Figure 2**. The solid and broken lines indicate unit boundaries and the 0.6% Ro (vitrinite reflectance) contour, respectively.

of the late Miocene, which is in good agreement with the formation age of a remarkable folded zone on land [6].

4. Discussion

After the abovementioned overview of the structural and stratigraphic characteristics of the southwestern Japan Sea shelf, we now discuss the evolutionary processes of the study area following the back-arc opening event. In this section, the author discusses structural features governed by a unique opening mode, regional inversion provoked by resumed underthrusting of the Philippine Sea Plate, and stress-strain concentration on the shelf under the influence of an emerging simple shear regime, in this order.

4.1. Back-arc opening governed by the divergent rift system

As mentioned earlier, the southern Japan Sea is unique, in that the oceanic basin is studded by a number of submerged highlands composed of massive continental crust. Therefore, in order to force the sea floor to spread, a radial rift system presumably developed on the eastern Eurasian margin from the Oligocene to early Miocene. The normal faults in **Figures 3** and **4** are relics of the prevalent extension. **Figure 12** shows a paleoreconstruction map in the early Miocene stage. As suggested by [4], such a divergent breakup is endorsed by the presence of the early Miocene rift-margin type volcanism along the normally faulted scarp. In comparison to the pre-rifting paleogeography in **Figure 1**, the separated southwest Japan block drifted

http://dx.doi.org/10.5772/intechopen.71953

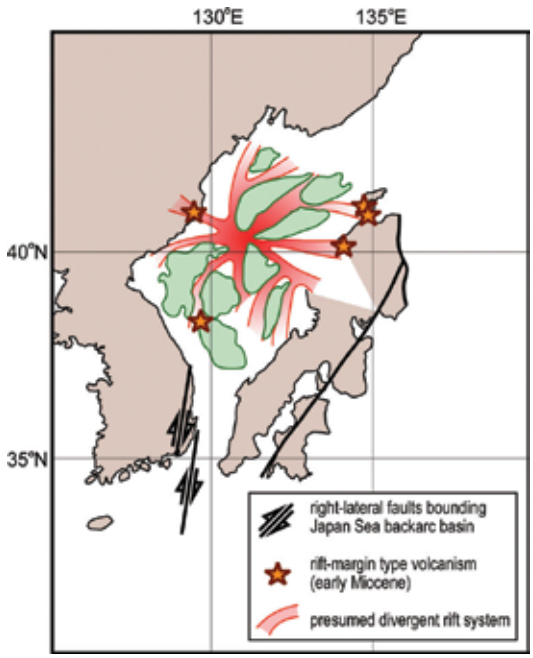

Figure 12. Paleoreconstruction map of the southern Japan Sea in the syn-rifting stage (early Miocene) modified from ref. [4].

southward and rotated clockwise as a result of differential effective spreading rates determined by rift geometry. Coeval development of N-S high-angle ruptures around the easternmost portion of the East China Sea (**Figure 10**) is interpreted as dextral faults to compensate for rapid spreading of the Japan Sea back-arc basin [10].

Another troublesome but highly intriguing problem is the plate configuration in the Pacific Northwest during the Japan Sea opening. **Figure 13** shows two paleogeographic reconstructions around the southern Japan Sea in the Neogene period. Based on the detailed geologic research of the Sundaland, Hall [11] adopted lingering expansion and rotational motion of the Philippine Sea Plate. On the other hand, Itoh et al. [12] advocated an earlier migration of the marginal sea plate. Their kinematic model is dependent on the collision of the easternmost tip of the clockwise-rotating southwest Japan against the Izu-Bonin arc along the eastern margin of the Philippine Sea Plate from 15 to 12 Ma [13].

The rotational processes of the marginal sea plate remain unsettled. Hall [11, 14] argued that the Philippine Sea Plate began to rotate clockwise at the earliest Miocene (ca. 24 Ma) with a relevant sinistral motion around north New Guinea. An incipient spreading center at that time is identified along the northeastern margin of the plate. Based on rapid crustal growth in southwest Japan, Kimura et al. [15] recently insisted that the plate swiftly rotated clockwise nearly simultaneously with the oceanward drift of the Japanese island arc driven by the Miocene Japan Sea opening. On the other hand, the significant rotation phase of the Philippine Sea Plate has been assigned before 25 Ma based on newly obtained paleomagnetic data from the northwestern part of the plate [16]. However, the present author believes that further geochronological information is necessary in order to clarify these processes.

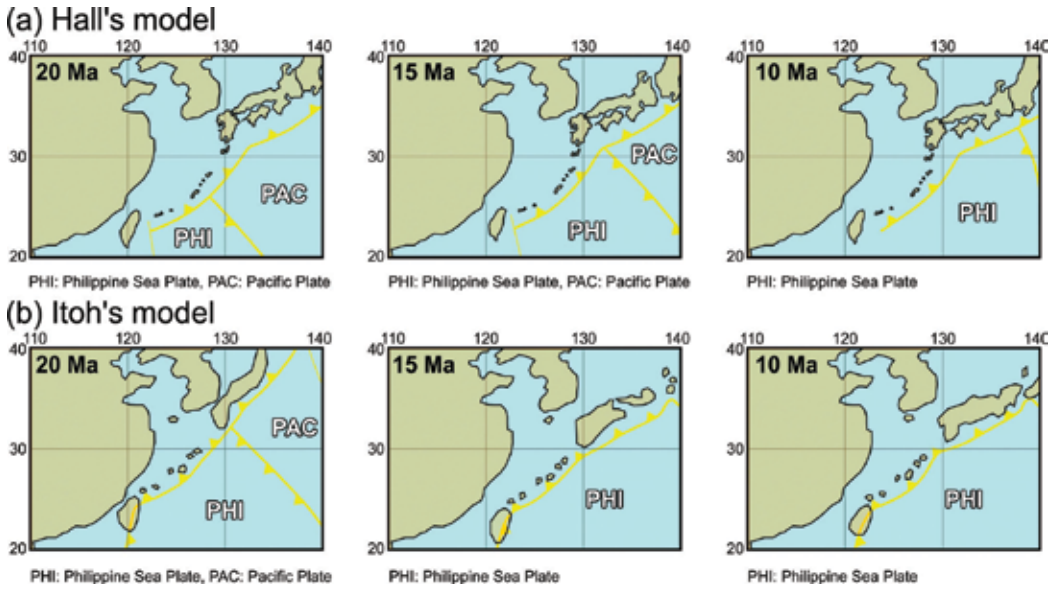

Figure 13. Comparison of two Neogene paleogeographic reconstruction models around the southern Japan Sea. (a: top) Model of lingering (delayed relative to the Japan Sea opening) migration of the Philippine Sea Plate [11]. (b: bottom) Model adopting earlier migration of the Philippine Sea Plate [12].

4.2. Extensive inversion: Structural contrast between forearc and back-arc regions

North-South strong contraction is the most notable post-opening event around the southern Japan Sea and southwest Japan. Although the amplitude of the folds tends to diminish toward the intra-arc region [7], arc-parallel gentle undulation was ubiquitous along the late Miocene convergent margin. Based on the spatiotemporal distribution of tectonic events related to contraction/extension found mainly in intra-/forearc areas, Itoh et al. [17] argued that compressive stress propagated progressively westward through the Plio-Pleistocene and attributed the change in the stress-strain state to the shift of the Euler pole of the subducting Philippine Sea Plate. Itoh [18] redefined their Quaternary epochs based on detailed structural analysis of an event sedimentary sequence. **Figure 14** shows a series of compiled illustrations depicting variable tectonic regimes around southwest Japan.

Compared to the transient history of southwest Japan, the back-arc shelf appears to have been uniformly deformed throughout its extent, considering the subsurface structures described by Itoh and Nagasaki [7], Itoh et al. [19], and the author of the present study (**Figures 5**, **6**, and **9**). The seismic characteristics at the bottom of the D Group do not exhibit clear time-transgressive terminations onto the K/D erosional surface. Thus, the Japan Sea back-arc region appears to have suffered synchronous deformation in a short period.

Nevertheless, it is plausible that resumed convergence of the Philippine Sea Plate was responsible for the regional contraction because frequent igneous intrusions within the upper part of the K Group (**Figures 8** and **11**) are suggestive of revitalized arc volcanism linked to dehydration of the subducted slab. Not only the change in relative motions of the marginal sea plate

http://dx.doi.org/10.5772/intechopen.71953

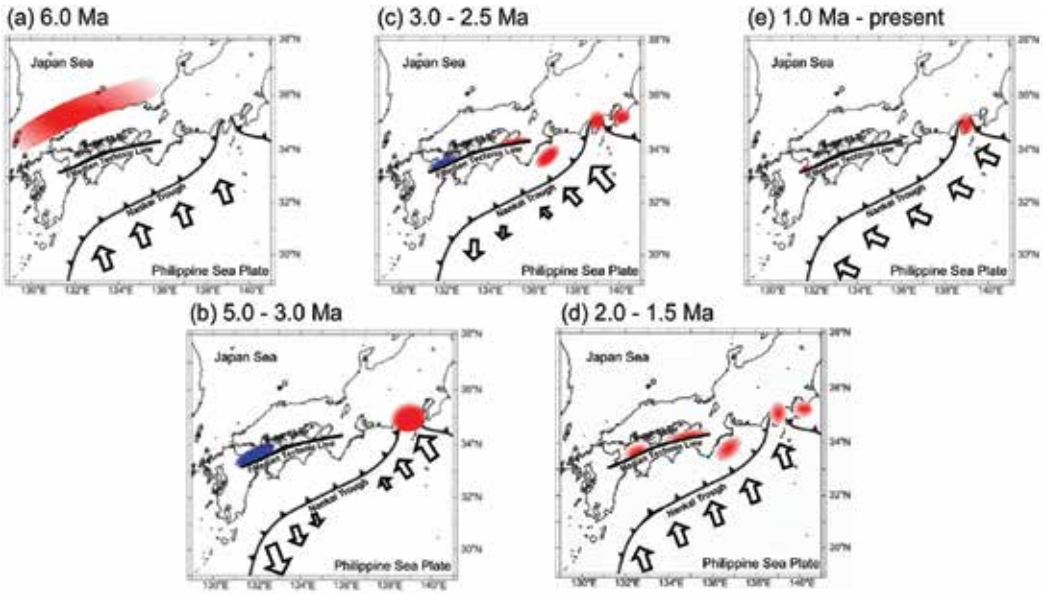

Figure 14. Spatiotempora distribution of stress-strain regimes in southwest Japan, the southern Japan Sea shelf, and a kinematic model of the Philippine Sea/Eurasian plate convergence since 6 Ma (a to e) compiled from [17, 18]. The red and blue areas represent areas of compressive (contractional) and tensile (extensional) stress (strain), respectively. Modes of the Philippine Sea Plate convergence are shown schematically by the length and azimuth of the arrows.

but also spatial variations in the coupling on the slab surface may be a key to understanding these complicated tectonic processes.

4.3. Confined deformation on the back-arc shelf: Emerging Quaternary back-arc break

Seismic data for the westernmost part of the back-arc shelf imply the emergence of an extensional regime during a recent period. The K/D interface as the product of an impulsive contraction is cut by normal faults, which have been active since the Pliocene (**Figure 7**). The shelf break partly reaches a depth of 300 m (**Figure 6**) and exceeds the limit of the eustatic sea-level fluctuation. **Figure 15** shows a conspicuous depression on the north side of the Tsushima Islands. As mentioned earlier, the border islands originated from a strong transpressive regime around the latest Miocene. However, the depression appears not to have been generated as a foreland basin related to the nearby reverse faulting that became dormant in the early Pliocene. Deformation of superficial sediments in the seismic profiles requires the subsea landforms to originate from neotectonic stress relief. Such a drastic shift from contraction to extension may be linked to an episodic change of the Philippine Sea Plate's motion in the Quaternary. Nakamura et al. [20] suggested that the plate changed its converging direction to be counterclockwise at ca. 2–1 Ma, which inevitably enhanced the right-lateral wrench deformation of southwest Japan and the eventual arc-parallel crustal breakup, such as that at the Median Tectonic Line (MTL in **Figure 16**). Itoh et al. [21] found an embryotic right-lateral rupture along the Japan Sea margin (Southern Japan Sea Fault Zone; SJSFZ in **Figure 16**). The area of confined subsidence is coincident with a propagating tensile termination of the lateral fault

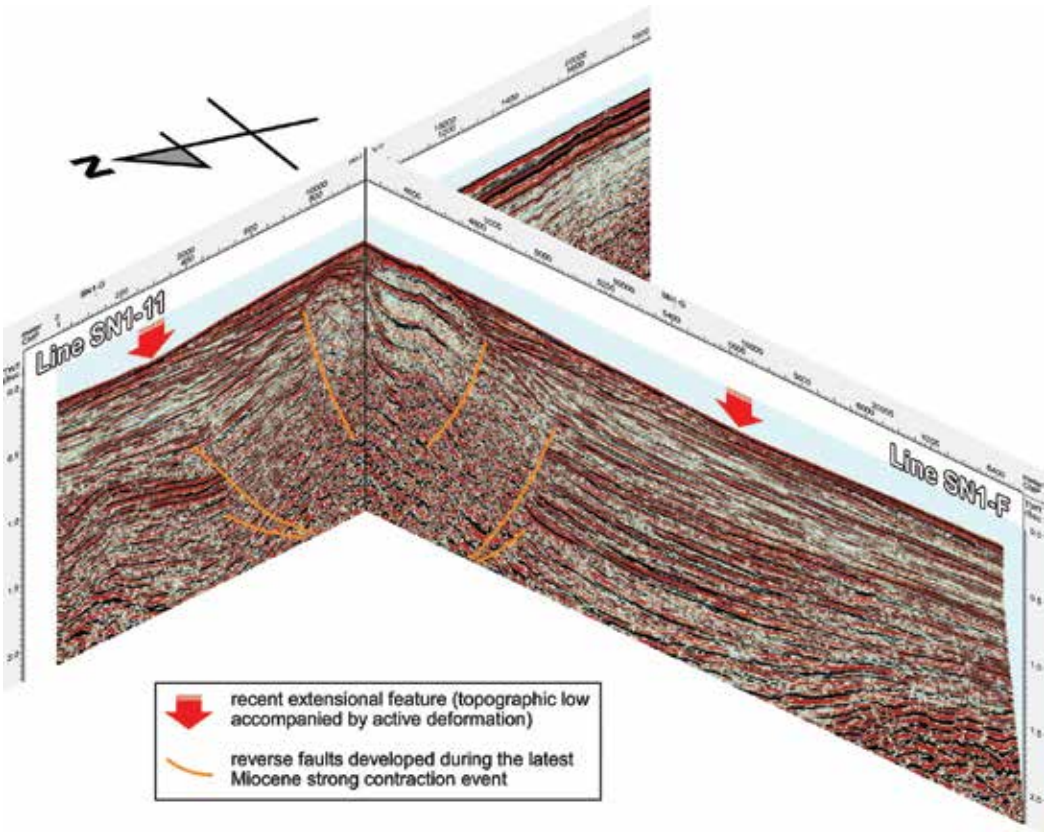

Figure 15. Confined recent depression north of the Tsushima Islands confirmed by seismic profiles. See **Figure 2** for line locations.

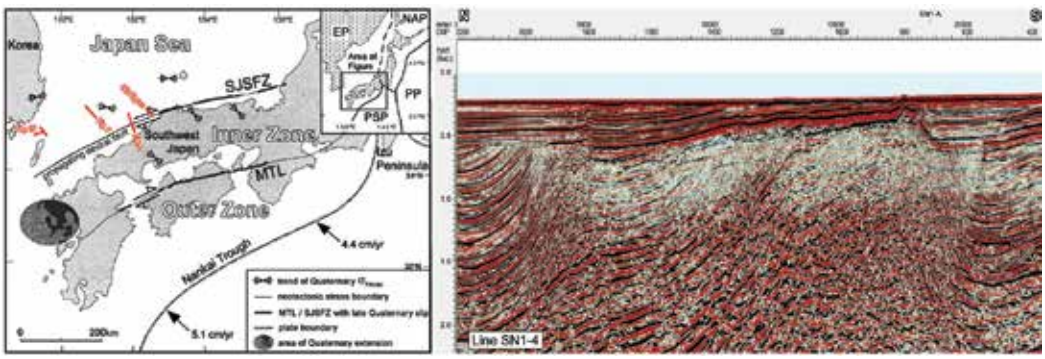

Figure 16. Neotectonic synthesis around the southwestern Japan arc together with a seismic section (time migration; SN1-4) showing high-angle faults along the trace of the Southern Japan Sea Fault Zone (SJSFZ). EP, NAP, PP, and PSP in the regional inset represent the Eurasian Plate, the North American Plate, the Pacific Plate, and the Philippine Sea Plate, respectively. The location of the seismic section is also shown in **Figure 2**.

http://dx.doi.org/10.5772/intechopen.71953

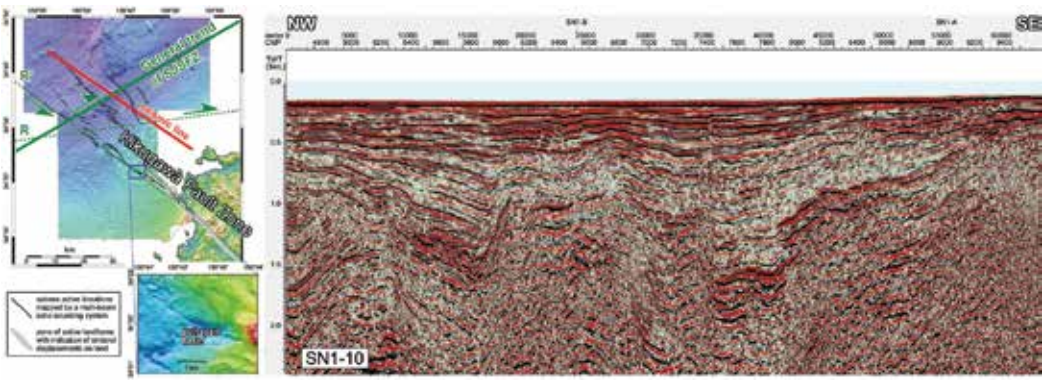

Figure 17. Subordinate shear deformation developed around the Southern Japan Sea Fault Zone (SJSFZ). Subsea topographic maps were compiled using a multibeam echo sounding system [25]. R and R′ with their strike-slip senses (arrows) in the topographic index are the azimuths of the Riedel shear and the conjugate Riedel shear, respectively, provoked by recurrent dextral activities on the SJSFZ. The location of the seismic line (time migration; SN1-10) is also indicated in **Figure 2**.

[22], as shown in **Figure 16**. A closer look at the seismic records indicates high-angle faults cutting the sediment surface on the trace of the SJSFZ (see the seismic inset of **Figure 16** and the active horst in **Figure 5**, which is indicated by a bracket).

Figure 17 shows another side effect of the SJSFZ's activity. A northwest-trending sinistral rupture, called the Kikugawa Fault [23], extends to the back-arc shelf. The seismic and geologic investigation of the Kikugawa Fault [24] confirmed recurrent slips during the late Pleistocene. Recent sounding of subsea topography [25] delineated an active pull-apart sag on a releasing (i.e., leftward) bend of the rupture. The azimuth and slip sense of the active lineament agree with those of the conjugate Riedel shear provoked by the dextral motion on the arc-bisecting fault, as shown in the figure. The multichannel seismic record shown in **Figure 17**, acquired parallel to the Kikugawa Fault, is cut by several high-angle faults that can be interpreted as dextral Riedel shear adjacent to the SJSFZ.

Thus, the present research demonstrates that the change in the convergence modes of the Philippine Sea Plate triggered a series of episodic deformation around the rim of the overriding plate. The latest mode of highly oblique subduction promotes the development of extensive wrenching in fore-, intra-, and back-arc regions as well as the formation of a crustal sliver sandwiched between the MTL and SJSFZ. This mode also enhances the compartmentalization of the Japan Sea back-arc basin.

5. Conclusions

The present seismic study has fully described the following tectonic epochs of the Japan Sea back-arc basin.

1. The Oligo-Miocene back-arc opening of the southern Japan Sea was governed by a divergent rift system. The southwestern Japan block drifted southward and rotated clockwise as a result of differential effective spreading rates determined by the rift geometry.

2. The Japan Sea back-arc region appears to have synchronously suffered North-South strong contraction during a short period of the latest Miocene. Resumed convergence of the Philippine Sea Plate was responsible for the regional tectonic event because frequent igneous intrusions within the upper Miocene series on the shelf are suggestive of revitalized arc volcanism linked to dehydration of the subducted slab.

3. Confined and complicated deformation on the back-arc shelf during the Quaternary is related to the dextral wrench deformation of southwest Japan and the eventual arc-parallel crustal breakup along the back-arc region. Recent highly oblique subduction of the Philippine Sea Plate provoked the prevailing shear stress.

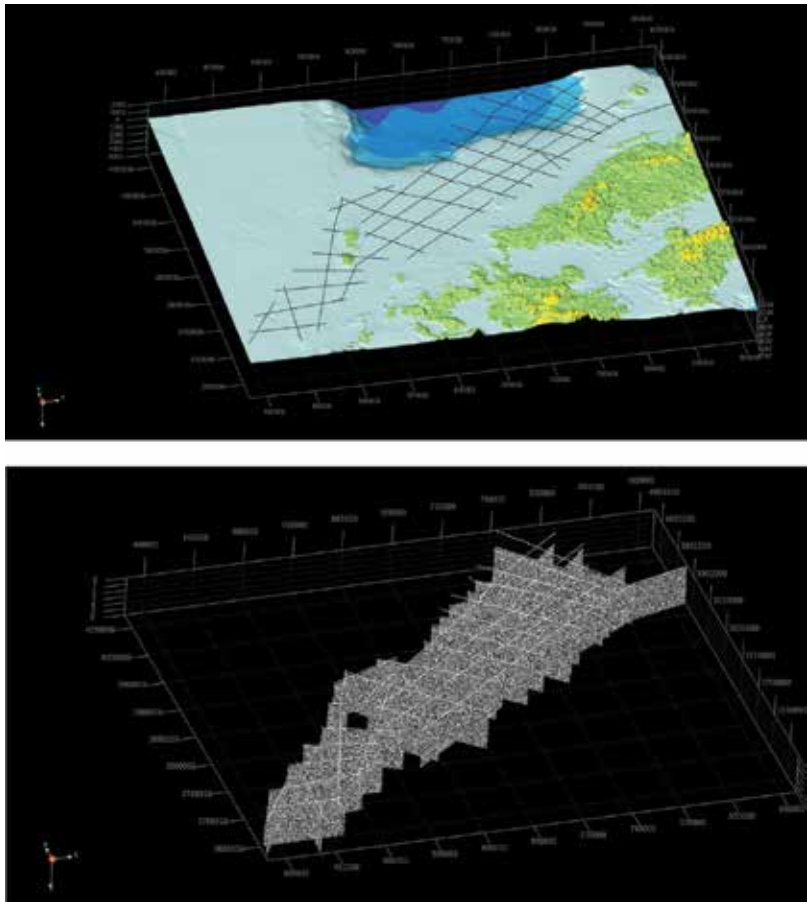

Figure 18. Bird's eye topographic vista (from southwest) around the southern Japan Sea (top) and the subsurface structural architecture (bottom). See **Figure 2** for seismic line locations. Although the total accommodations shown on the seismic data (bottom) of the northern and western back-arc of southwest Japan are in the same level, the present study integrating structural and stratigraphic knowledge has revealed that the shelf to the east of the Tsushima Islands was built up in a short period reflecting intensive post-opening deformation events since the Miocene.

http://dx.doi.org/10.5772/intechopen.71953

The three-dimensional architecture around the southern Japan Sea has been visualized, as shown in **Figure 18**. A bird's eye view movie of the subsurface structure based on seismic interpretation and high-resolution original figures in this chapter are available from the Osaka Prefecture University Education and Research Archives (OPERA) (http://hdl.handle.net/10466/15505).

Acknowledgements

The author would like to thank the Ministry of Economy, Trade, and Industry (METI), and the Japan Oil, Gas, and Metals National Corporation (JOGMEC) for permission to publish this paper.

Author details

Yasuto Itoh

Address all correspondence to: itoh@p.s.osakafu-u.ac.jp

Graduate School of Science, Osaka Prefecture University, Japan

References

[1] Engebretson DC, Cox A, Gordon RC. Relative motions between oceanic and continental plates in the Pacific Basin. Geological Society of America Special Paper. 1985;**206**:1-59

[2] Otofuji Y, Hayashida A, Torii M. When was the Japan Sea opened?: Paleomagnetic evidence from Southwest Japan. In: Nasu N, Uyeda S, Kushiro I, Kobayashi K, Kagami H, editors. Formation of Active Ocean Margins. Tokyo: Terra Publishing Co.; 1985. pp. 551-566

[3] Otofuji Y, Matsuda T. Amount of clockwise rotation of Southwest Japan – Fan shape opening of the southwestern part of the Japan Sea. Earth and Planetary Science Letters. 1987;**85**:289-301

[4] Itoh Y, Uno K, Arato H. Seismic evidence of divergent rifting and subsequent deformation in the southern Japan Sea, and a Cenozoic tectonic synthesis of the eastern Eurasian margin. Journal of Asian Earth Sciences. 2006;**27**:933-942

[5] Minami A. Distribution and characteristics of the sedimentary basin offshore San-in to Tsushima Island. Journal of the Japanese Association for Petroleum Technology. 1979;**44**:89-96 (in Japanese with English abstract)

[6] Tai Y. On the 'Shinji folded zone'. Memoir of Geological Society of Japan. 1973;**9**:137-146 (in Japanese with English abstract)

[7] Itoh Y, Nagasaki Y. Crustal shortening of Southwest Japan in the Late Miocene. The Island Arc. 1996;**5**:337-353

[8] Furukawa T, Tomizawa A. Offshore stratigraphic test well 'MITI Tottori-Oki'. Journal of the Japanese Association for Petroleum Technology. 1985;**50**:43-52 (in Japanese)

[9] Blow WH. Late Middle Eocene to Recent planktonic foraminiferal biostratigraphy. In: Bronnimann P, Renz HH, editors. Proceedings of 1st International Conference of Planktonic Microfossils. Leiden: Brill; 1969. pp. 199-422

[10] Itoh Y. A Miocene pull-apart deformation zone at the western margin of the Japan Sea back-arc basin: Implications for the back-arc opening mode. Tectonophysics. 2001;**334**:235-244

[11] Hall R. Late Jurassic-Cenozoic reconstructions of the Indonesian region and the Indian Ocean. Tectonophysics. 2012;**570-571**:1-41

[12] Itoh Y, Takano O, Takashima R. Tectonic synthesis: A plate reconstruction model of the NW Pacific region since 100 Ma. In: Itoh Y, editor. Dynamics of Arc Migration and Amalgamation – Architectural Examples from the NW Pacific Margin. Rijeka: InTech; 2017. pp. 93-111. DOI: 10.5772/67358

[13] Itoh Y. Differential rotation of the eastern part of southwest Japan inferred from paleomagnetism of Cretaceous and Neogene rocks. Journal of Geophysical Research. 1988;**93**:3401-3411

[14] Hall R. Cenozoic geological and plate tectonic evolution of SE Asia and the SW Pacific: Computer-based reconstructions, model and animations. Journal of Asian Earth Sciences. 2002;**20**:353-431

[15] Kimura G, Hashimoto Y, Kitamura Y, Yamaguchi A, Koge H. Middle Miocene swift migration of the TTT triple junction and rapid crustal growth in southwest Japan: A review. Tectonics. 2014;**33**:1219-1238. DOI: 10.1002/2014TC003531

[16] Yamazaki T, Takahashi M, Iryu Y, Sato T, Oda M, Takayanagi H, Chiyonobu S, Nishimura A, Nakazawa T, Ooka T. Philippine Sea plate motion since the Eocene estimated from paleomagnetism of seafloor drill cores and gravity cores. Earth, Planets and Space. 2010;**62**:495-502

[17] Itoh Y, Kusumoto S, Takemura K. Evolutionary process of Beppu Bay in central Kyushu, Japan: A quantitative study of the basin-forming process controlled by plate convergence modes. Earth, Planets and Space. 2014;**66**:74. DOI: 10.1186/1880-5981-66-74

[18] Itoh Y. Gunchu Formation – An Indicator of Active Tectonics on an Oblique Convergent Margin. Germany: LAP LAMBERT Academic Publishing; 2015 76 p

[19] Itoh Y, Nakajima T, Takemura A. Neogene deformation of the back-arc shelf of Southwest Japan and its impact on the palaeoenvironments of the Japan Sea. Tectonophysics. 1997;**281**:71-82

[20] Nakamura K, Renard V, Angelier J, Azema J, Bourgois J, Deplus C, Fujioka K, Hamano Y, Huchon P, Kinoshita H, Labaume P, Ogawa Y, Seno T, Takeuchi A, Tanahashi M, Uchiyama A, Vigneresse JL. Oblique and near collision subduction, Sagami and Suruga troughs – preliminary results of the French-Japanese 1984 Kaiko cruise, leg 2. Earth and Planetary Science Letters. 1987;**83**:229-242

[21] Itoh Y, Tsutsumi H, Yamamoto H, Arato H. Active right-lateral strike-slip fault zone along the southern margin of the Japan Sea. Tectonophysics. 2002;**351**:301-314

[22] Kusumoto S, Itoh Y, Takano O, Tamaki M. Numerical modeling of sedimentary basin formation at the termination of lateral faults in a tectonic region where fault propagation has occurred. In: Itoh Y, editor. Mechanism of Sedimentary Basin Formation – Multidisciplinary Approach on Active Plate Margins. Rijeka: InTech; 2013. pp. 273-304. DOI: 10.5772/56558

[23] Research Group for Active Faults. The Active Faults in Japan: Sheet Maps and Inventories. Rev. ed. Tokyo: University of Tokyo Press; 1991

[24] Abe S, Arai R, Okamura Y. Fault distribution and activity in the offshore extension of the Kikugawa fault system, western Japan. Annual Report on Active Fault and Paleoearthquake Researches. 2010;**10**:81-118 (in Japanese with English abstract)

[25] Japan Coast Guard. The Seafloor Topography of the Kikukawa Fault Zone Off Yamaguchi Prefecture [Internet]. 2010. Available from: http://cais.gsi.go.jp/YOCHIREN/report/kaihou83/09_13.pdf [Accessed: July 29, 2017] (in Japanese)

Chapter 7

Soft Sediment Deformation Structures Triggered by the Earthquakes: Response to the High Frequent Tectonic Events during the Main Tectonic Movements

Bizhu He, Xiufu Qiao, Haibing Li and Dechen Su

Additional information is available at the end of the chapter

http://dx.doi.org/10.5772/intechopen.72941

Abstract

Typical cases of the soft-sediment deformation structures (SSDSs), triggered by the modern earthquakes to the oldest of paleo-earthquakes in the Mesoproterozoic, have been observed in China. These deformation structures have various geometry morphology, different interior structural architectures and sediment compositions, in centimetre to metre-scales. They are intercalated with the undeformed layers, which are composed of similar sediments of lithology and sedimentary environments. SSDSs are formed during sediments deposited but incompletely consolidated. And they exist in different periods and are closely related to the active or paleo-active faults. They occur nearby the faults and usually have the characteristics nearer to the faults and more. And they distribute parallel to the trending of the active faults and have the characters of the vertical duplication. They have responded to the high-frequency activity of different faults in tectonic movement and are the perfect records of the paleo-active faults.

Keywords: soft sediment deformation structure, triggering mechanism, records of earthquakes, high-frequent tectonic events, paleo-active faults

1. Introduction

Under regional tectonic stress, the earth's interior might become imbalanced and the stored elastic strain energy inside the earth would be released quickly, and so the seismic events occur and cause devastating disasters to the life and environment [1–3]. Earthquakes are derived from plate tectonic movements [4–6]. Earthquakes occur primarily at the boundaries between lithospheric plates, such as divergence zone, transform zone and convergence zone,

and also occur at the pre-existing fault or weak stress belt in the plate and can be triggered by impacting of meteorites [7].

Paleo-seismic records are induced by earthquakes during geological history and reserved in strata. They include two categories: fault rocks and seismites. The fault rocks are composed of cataclastic rocks, mylonites, pseudotachylytes and fault gouge. They can occur and have been preserved at active fault zones and their adjacent areas in different geological times. The fault rocks are formed in different focal mechanisms of normal faults, thrust faults and strike slip faults [8–12, 5, 13]. Pseudotachylytes can be thought of as "an earthquake fossil". The fault rocks can be as the records of the active fault during different times. But the fault zone is often located in the long-term tectonic activity areas, and the later tectonic activities are often superimposed on the previous activities. Therefore, it is difficult to distinguish them for different time and determine the activity of faults.

Seismites are the soft-sediment deformation structures (SSDSs) produced by strong earthquakes. SSDS is deformation that originates in unconsolidated sediments and usually occurs rapidly at or close to the surface during or shortly after deposition and before lithification takes place. During the deformation process, the original sediment particles are rearranged and migrated, the compositions are not changed and no new minerals would be produced. The triggers for SSDS are tectonism, glaciogenic, mass movement, collapse and some other physical and biological processes, and the earthquake trigger is one of important dynamic drives. Seismites had been observed from 1780s [14], and the liquefaction triggered by modern earthquakes were mainly studied. But the term 'seismites' was first proposed by A. Seilacher to interpret an effect of strong earthquakes on paleoslope for fault-graded beds in the Monterey Shales (Miocene), the north of Santa Barbara, California (USA) [15]. From the 1970s to 2000, several SSDSs triggered by earthquakes were identified and the formation mechanisms were primarily analysed [16–18]. In the last 20 years, they have been widely developed and classified [14, 19–21]. The special SSDSs (seismites) with inconsistence are preserved in the normal sedimentary strata, which provide opportunities to understand tectonic activity at different times.

In this chapter, we introduce the typical SSDSs observed in China, which are triggered by the recent to the Mesoproterozoic earthquake activities, and formed in different deposition environments and are composed of different sedimentary rocks. Especially, the structural styles, preserved positions, occurrence times, formation mechanisms and relationship with the activities of faults are discussed. The aim of the chapter is to reveal the high-frequency active events of the faults in different geological history and provide evidences for the paleotectonic and paleogeographic reconstruction.

2. Genetic mechanisms of soft-sediment deformation structures

Soft-sediment deformation structures (SSDSs) are deformations that originated in unconsolidated sediments [16, 18, 19]. SSDSs can occur in different tectonic settings, e.g., passive continental margins, deep (trench) subduction zones and strike-slip tectonic transitions,

and they can form in almost all sedimentary environments, preferably in shallow-marine, lagoonal, lacustrine and fluvial environments.

There are mainly four deformation mechanisms: (1) intergranular shear [22, 23]; (2) plastic or hydroplastics [24, 25]; (3) liquefaction [18, 24, 27] and (4) fluidization [24, 26]. The driving forces of deformation mechanisms include the tectonism, gravity acting on slopes, disequilibrium loading caused by topographical irregularities in the sediment-water interface, gravitational instabilities due to a reverse density gradient where denser sediments overlie less dense sediments, shear waves or other currents, and biological and chemical agents [14, 15, 18, 27–29]. The various morphology and deformation styles of the SSDSs can be formed with respect to sedimentation in different lithology, driving forces, sediment rheology and deformation mechanisms of the deformation [20, 27, 30–33].

Numerous schemes of classification of SSDSs have been proposed [14, 24, 26, 28, 29, 32]. The formation mechanisms of deformations induced in earthquake may be classified into five main categories, which include liquefaction, thixotropic deformation, hydroplastication, superposed gravity driving deformation and brittle deformation. And the secondary classification is also proposed according to genetic types, sediment compositions and deformation styles (**Figure 1**).

The strict criteria of SSDSs triggered by seismic events (seismites) have been discussed [14, 15, 18, 20, 27, 28, 34]. The commonly received criteria include (1) the deformation emerges in laterally continuous, vertically recurring layers, separated by undeformed layers; (2) the deformation occurs in marine, lacustrine or fluvial sediments; (3) deformed and undeformed beds have similar lithologies and facies features; (4) the deformation is related to a seismically or tectonically active area; (5) the deformation shows systematic increases in frequency or intensity toward a likely epicentral area. "Liquefied deformation" as a seismic record is associated with many modern and ancient seismogenic deposits and is related to surface-wave magnitudes Ms > 5 [20, 30, 32, 35].

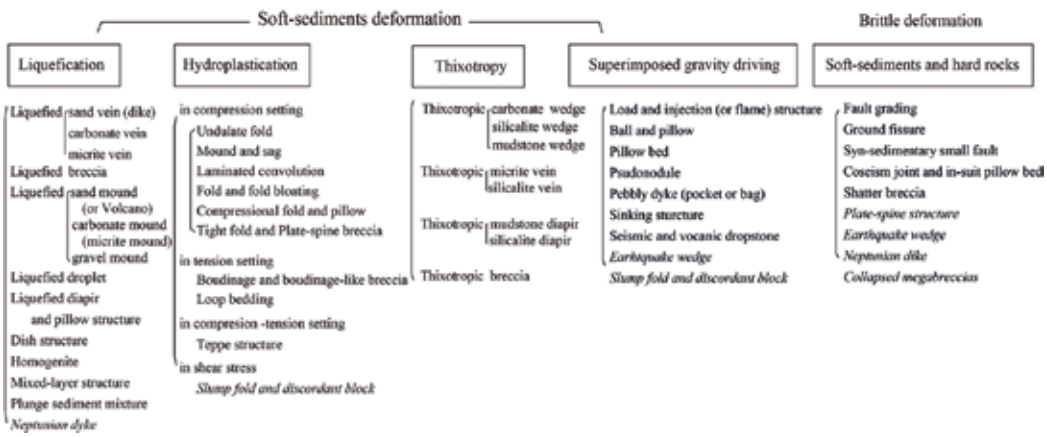

Figure 1. Classification of SSDSs according to the genetic mechanism (modified from [14, 18, 20, 21]). The deformations in italics are triggered by more than two mechanisms.

3. Typical cases of the SSDSs triggered by earthquakes during the geological history

3.1. Triggered by the modern earthquakes of the Yingxiu-Beichuan active faults

The MS 8.0 Wenchuan earthquake struck the Longmenshan area on 12 May 2008, the transition zone between the eastern margin of the Tibetan Plateau and the Sichuan Basin, China. Besides the huge casualties and property losses, a most complicated yet longest thrust-type co-seismic surface rupture zone was developed in the quake-hit area. The surface rupture extends over lengths of 270 km and 80 km along the NE-SW trending Yingxiu-Beichuan fault (hereafter YBF) and Guanxian-Anxian fault (hereafter GAF) (**Figure 2**), which are high-angle

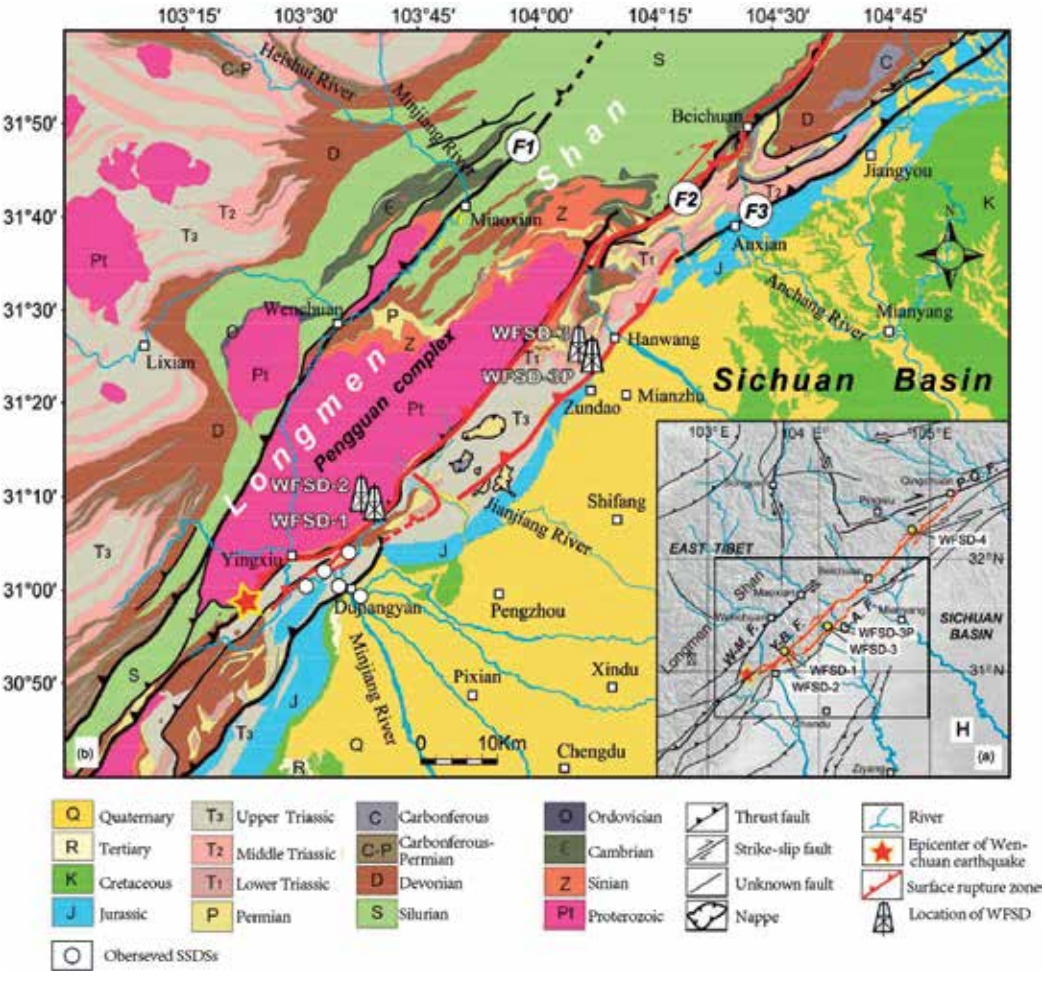

Figure 2. Simplified geologic and active tectonic map of the Longmen Shan and its adjacent area (adapted from 1:500,000 geologic maps, Ministry of Geology and Mineral Resources, 1991; [36, 37]) and observed SSDS sites during post-disaster investigation soon after the Wenchuan earthquake. F1, Maoxian-Wenchuan Fault; F2, Yingxiu-Beichuan Fault; F3, Anxian-Guanxian Fault.

and low-angle thrusts in the Longmen Shan, respectively [36–38]. The largest surface vertical displacements were attained at 12 m in the northern segment in the Beichuan area [39, 40]. There also occurred several soft-sedimentary deformation structures in the YBF and the terraces of the Mingjiang River, including liquefaction, gravitational and hydroplastic deformations and other related deformations. There is a need to mention that most SSDSs were observed soon after the Wenchuan earthquake had disappeared or been destroyed, because these SSDSs were distributed in the farmlands, river terraces or lawn and sandy areas of town. Prof. Li Haibing, one of the authors of this paper, pays attention to the liquefaction of sand deformations during the investigation of the Wenchuan earthquake in Longmen Mountain and its adjacent area, and makes a preliminary study on the soft-sediment deformation shortly after earthquake.

3.1.1. Sand volcanos and liquefied mounds

Various sand volcanos and liquefied mounds (**Figure 3**) have been observed in the Mingjiang terraces and adjacent areas of the Yingxiu-Beichuan Fault. They possessed different shape styles and internal sediment compositions. Unconsolidated saturated sedimentary sand layers are liquefied and flow upwards along vertical conduits and form mound-shape uplifts on the surface when the shaking occurred. The underground sands and gravels are brought by extrusion liquefied sand flow to the surface, and they form sand cones (**Figure 3D**) or gravel mounds (**Figure 3C** and **E**). Some of them are ejected out of the liquefied sands completely and form the craters (**Figure 3A**). Liquefied sand cones and gravel mounds usually occur in line along the Yingxiu-Beichuan faults (**Figure 3C** and **D**). The gravel mounds or cones are 1.5 m in diameter and 0.5 m high. If the thin gravel layer is covering the liquefaction layer, the upward sand flow entrainment gravels can form larger mounds. The largest one can reach 3.5 m in diameter and 1.5 m high. There are also small sand cones, which are parallel with the large mounds.

3.1.2. Liquefied sheet sands and collapse pits

Multiple liquefied sheet sands in a large area accompanied by ground fissures occurred in the Mingjiang terraces during the 2008 Wenchuan earthquake. The trending of ground fissures are parallel or perpendicular to the terrace margin, and the two groups of ground fissures constitute the netlike fissures. The underground liquefied sand flowed upwards and overflowed along the fissures to form the liquefied sheet sands (**Figure 3B**). The liquefied sheet sands also occurred from ring and radial cracks along the low sand dune.

There were many linear collapse pits in the farmland (**Figure 3F** and **G**), and the orientation of arrangement was usually paralleled to the Yingxiu-Beichuan Fault. They resulted from the liquefied sand dunes. The underground liquefied sand upwelling towards the ground, due to the process of liquefaction, ceased; the density of local underground layers changed to smaller; the sediments changed looser, even the underground caves occurred; and the collapse pits were formed due to downwards suction. Some undeveloped collapse pits also have the ring and ring and radial cracks (**Figure 3F**).

Figure 3. Sand volcano, liquefied dune, sand sheet, liquefied deformation of sand bed, triggered by May 12, 2008 Wenchuan earthquake (photographed by Li Haibing). (A) Sand volcano in the terraces of Mingjiang river; (B) liquefied sand sheets in the terraces of Mingjiang river; (C) a higher liquefied sand mounds in the Yingxiu-Beichuan fault zone; (D) liquefied sand dunes distributed in the lineal arrangement and parallel with the fault trend of the Yingxiu-Beichuan; (E) a liquefied sand and gravel mound, the gravels have been carried over the top of mound; (F) collapse sink resulted from liquefaction; (G) linear arrangement of the collapse sinks, diameter of collapse sinks are about 80–90 cm, the orientation is also parallel to the Yingxiu-Beichuan fault, showing the orange colour dot line.

3.1.3. Formation mechanism of SSDSs' response to the Yingxiu-Beichuan activity

Sand volcanos, liquefied mounds and collapse pits are recognised in the earliest earthquake records. And the liquefaction and ejection of fluid induced by the big earthquakes are key to fluid escape structures (sand boiling and sand volcano), which are composed of gas (often sulphur emanations), water, mud and sand, and under unstable fluidization environments [14, 30]. Nichols's experiments demonstrated the lower part material was fluidized and was blocked by the overlying non-fluidization layer, and when the grain size is more than 15% compared to the overlying layers, the biggest ejections can be produced [41]. But in huge modern earthquakes, sand volcanos and liquefied mounds are published little: first, because it is smaller than the earthquake rupture zone; second, it is easy to be destroyed by human activities and cannot be preserved. The liquefaction mounds and other SSDSs induced by the Wenchuan earthquake are extremely valuable geological records. Liquefied sand dunes, sand volcanos and liquefied gravel mounds reflect the process of the liquefaction, and the size and driving force of deformation structures are increased largely.

The Wenchuan earthquake produced the Yingxiu-Beichuan fault and Guanxian-Anxian faults with the NE-trending NW-dipping occurred surface rupture on the Longmenshan Fault Belts and with dextral-slip thrusting [36, 37]. The Longmenshan Fault Belts are the main margin fault of the West Sichuan foreland basin to the Songpan-Ganze terrane, and it is activated since the Triassic. From the distance of observed SSDSs to the faulted belts, range from 5 to 30 km, induced that the reactivated faults and triggered fault is the Yingxiu-Beichuan Faults (see **Figure 4**). These liquefied gravel mounds and sand volcanos are the records of events of the activity of the Longmenshan Fault Belts, and it is a response to the Indo-Asia collision and eastern extrusion of the Qinghai-Tibetan Plateau terrane. The activities of the Longmenshan Fault Belt is a result of the stress that originate from the Qinghai-Tibetan Plateau terrane converging to the north and escaping to the southeast, which were driven by the continent-continent collision between the India and Asian continent.

3.2. Triggered by the early Jurassic earthquake activities of the Talas-Ferghana strike-slip fault (TFSSF)

3.2.1. Soft-sediment deformation structures at the southeast end of TFSSF

Talas-Ferghana strike-slip fault has been active since the Mesozoic, but the initial time of strike-slip is still in dispute [42–44]. The Wuqia pull-apart basin of the Lower Jurassic was controlled by this huge fault (**Figure 5a**), with NW-trending, which is located at the south-east end of the significant Talas-Ferghana fault, SW Tianshan. Soft-sediment deformations were preserved in sandstone layers at top of the Lower Jurassic Kangsu Formation, and three earthquake-induced deformation sequences have been recognised within 10 m thickness of sandstones deposited in the lacustrine environment (**Figure 5b**). They are included as load cast, ball-and-pillow, droplet, cusps, homogeneous layer, and liquefied unconformity.

Load casts and ball-and-pillow are the main types of deformation in the third layer of SSDSs in the Kangsu formation. The parental sand layer providing load casts to subside is 80-cm-thick laminated siltstone and consists of limonite debris, feldspar, quartz and muscovite. The

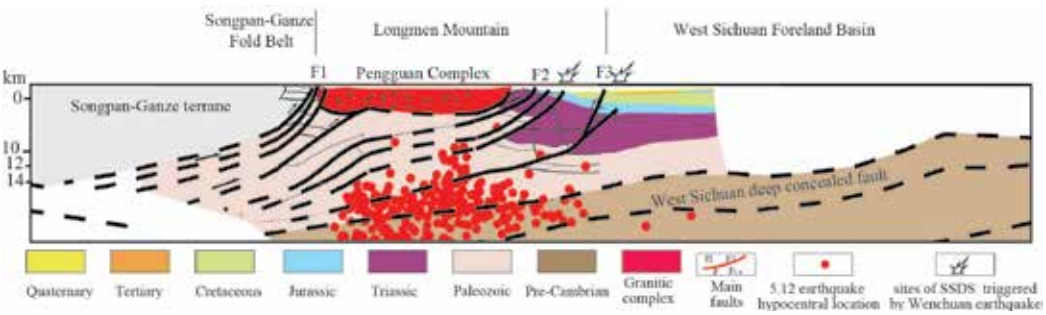

Figure 4. Sketch tectonic model of the Longmen Mountain and Sichuan Basin (modified from [47]), showing the main fault belts and 5.12 earthquake hypocentral locations and SSDS triggered by this earthquake. F1, Maoxian-Wenchuan Fault; F2, Yingxiu-Beichuan Fault; F3, Anxian-Guanxian Fault.

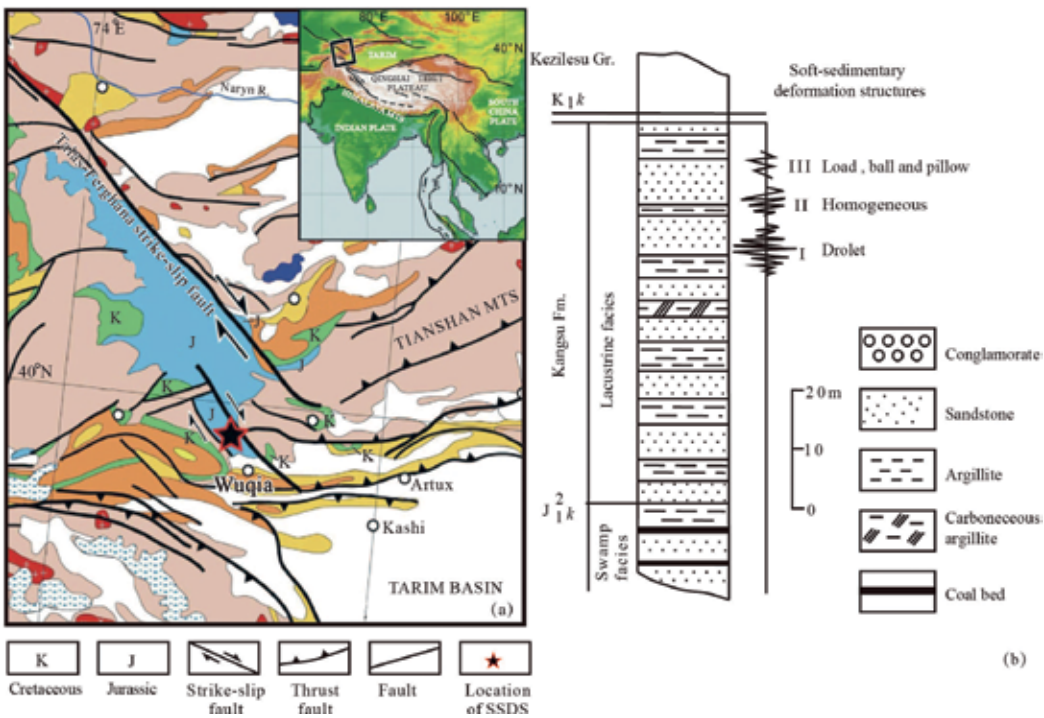

Figure 5. Geological sketch map (a) and stratigraphic column (b) showing the Wuqia Basin, southwest Tianshan Mts., Xinjiang (modified from [20, 47, 48]), and location of the SSDS in the Kangsu Formation in Jurassic. I, II and III presented the three layers of seismic events and composed a paleo-earthquake episode. The star marks the positions of these layers.

grain sizes range from 0.01 to 0.05 mm, with minor less than 0.5–0.1 mm, displaying distinct feature of seasonal lacustrine lamination (**Figure 6A** and **B**). The deformation structures resulted from the static pressure of the unconsolidated silt beds that were destroyed while

http://dx.doi.org/10.5772/intechopen.72941

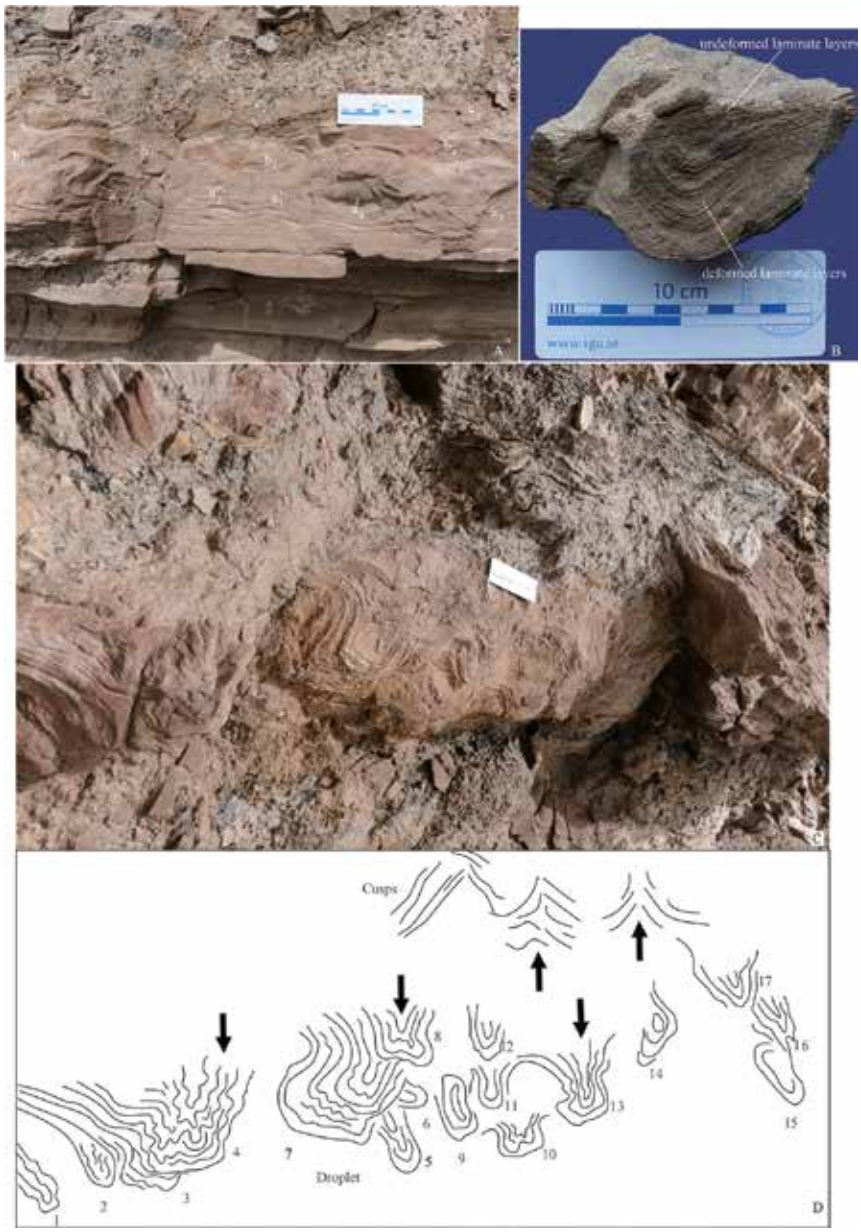

Figure 6. Soft-sediment deformation structures in the Kangsu Formation, Wuqia Basin, Southwest Tianshan Mountains. (A) Load cast and ball-and-pillow in the third layer of seismic event; a, b and c represent orders of load cast structures submerged. a_3 displays spindle, concentric laminae in ball-and-pillow. a_4 shows the intact stereo configuration of ball-and-pillow (oblate ellipsoid body). (B) Load cast showing syncline-like laminated layers resulted from subsidence of sand beds. (C and D) Long section morphology of droplet and upward cusps in the first layer of seismic event; arrows mark the directions of liquefying movement.

shaking, and gravity differentiation took place and sands or silts (the denser material) sank into the underlying (less dense) mud beds to form load-cast structures that evolved into 'ball-and-pillow structures' or pseudonodules [28, 32, 35].

Droplets and cusp anticlines occurred in the first event layer, about 60-cm-thick sandstone layer, of the Kangsu formation. Droplets and cusp anticlines resulted from strongly liquidised sandstone grains migrated vertically up and down during earthquake [45]. Seventeen intensively-distributed droplets can be seen within a distance of 170 cm along the sandstone layer (**Figure 6C** and **D**). They are revealed as cylinders and drops, with elongated U-type synclines in vertical cross sections and wavy laminates, presenting the trace of liquefaction flowing. Directions of axial planes of syncline-shaped laminae in each droplet are out of order, upright, oblique and curve, suggesting that downward displacement of sand grains is random and without sliding of sand bodies on slope. Cusp anticlines are similar to diapirs in configuration of structures but different to diapiric structures. The diapiric structure refers to the underlying liquefied sand bed puncture into overlying soft sediments, while cusps are the result of liquefaction sands migrated upwards within liquefied sand layer with corn-shape body and without distinct xenolith in nucleus (**Figure 6C** and **D**). Droplets and cusp anticlines are formed under the duel effects by liquefaction and gravity. Groups of droplets resulting from superimposition of droplets and cusp anticlines resulting from upward movement of liquefying sandstone constitute multilayer complex deformation layers, which are generally explained to be triggered by earthquakes.

3.2.2. The activity of Talas-Ferghana strike-slip fault during the late early Jurassic

Three deformation layers of the Kangsu formation in the Lower Jurassic in Wuqia Basin had differences of deformation mechanisms (**Figure 5b**). The first deformation layer was characterised by droplet and cusp structures resulted from vertical liquefied displacement; the second was mainly homogeneous layers of liquefied sands and local unconformity and the third was mainly load casts and ball-and-pillow resulted from the effects of gravity and seismic shaking. Therefore, three seismic events suggest that the Talas-Ferghana strike-slip fault zone occurred due to at least three times large-scale active events during the late early Jurassic, with the different paleo-stresses imposed on soft sediments and made them deformed. According to the recorded data of liquefaction of sand layers by modern earthquakes and previous earthquakes [20, 30, 46], the SSDS were 45 to 50 km away from the Talas-Ferghana fault, and Ms 6.5–7 of the paleo-earthquake magnitudes were estimated.

3.3. Triggered by the early Palaeozoic activities of interior faults of the Tarim Basin

3.3.1. SSDSs in the deep drilling cores in the Manjiaer depression and Tazhong uplift

Tarim Basin is the largest, very complex, oil-bearing, superimposed marine facies and continental facies basin (560,000 km^2), in north-western China. It is surrounded by the Tianshan-Beishan, West Kunlun and Altyn Tagh mountain belts to the north, south, and southeast, respectively (**Figure 7**). The basin has undergone a long geological evolution with multi-phase tectonic movements from the Neoproterozoic to the Quaternary. The

http://dx.doi.org/10.5772/intechopen.72941

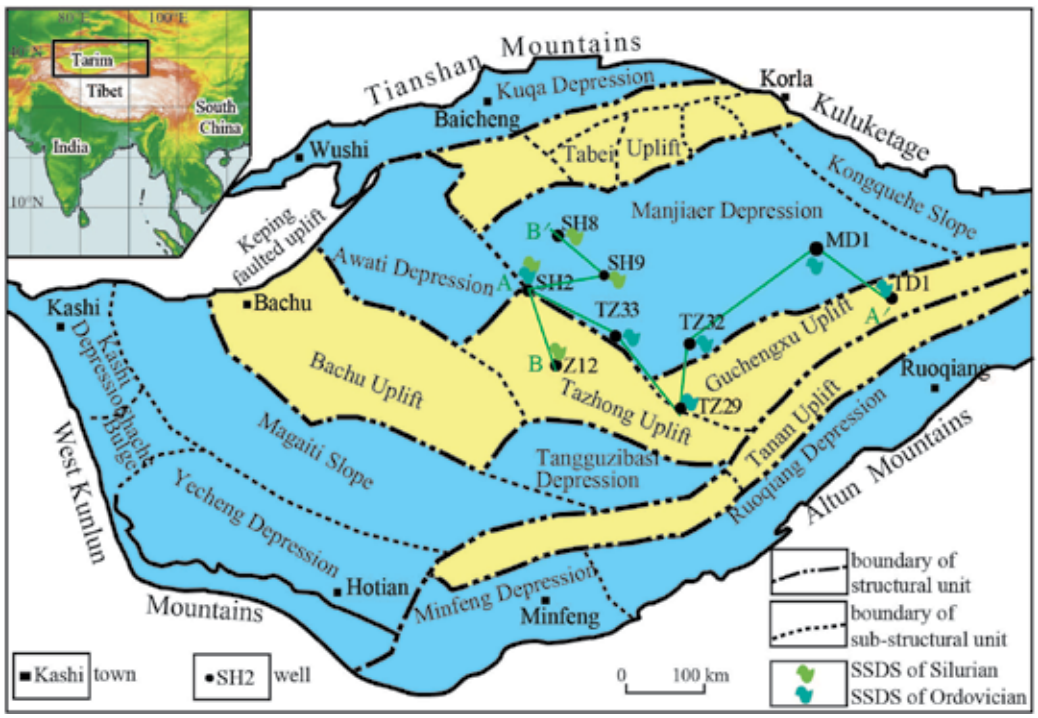

Figure 7. Schematic map of the structural units of the Tarim Basin, showing the location of deep drilling wells in Tazhong uplift and Manjiaer depression, in which various SSDSs of the Ordovician and Silurian are observed.

early Palaeozoic is the main period of development, especially in the central parts of the basin. During the first tectonic cycle, which is from the latest Neoproterozoic to the Middle Devonian, two unconformities that are Silurian/Upper Ordovician and Upper Devonian-Carboniferous/pre-Upper Devonian unconformity were formed during the middle and late Caledonian tectonic movements [49–53]. The properties of main faults changed from the normal faulting to reverse faulting during the middle Caledonian movement. The paleo-tectonic activities of this area are key issues and remain enigmatic for understanding the basin reconstructions and hydrocarbon explorations.

From the Ordovician to Silurian, the sedimentation (**Figure 8**) took place in a marine basin facies, shelf-and-platform (**Figure 8b**) and tidal-flat facies (**Figure 8a**) depositional environment in the Tazhong Uplift and the Manjiaer Depression. Various millimetre-, centimetre- and metre-scale soft-sediment deformation structures (SSDSs) have been identified in the Upper Ordovician and Lower-Middle Silurian from deep drilling cores in the Tazhong Uplift and the Manjiaer Depression (**Figure 7**). They include liquefied sand veins, liquefaction-induced breccia, boudinage-like structures, load and diapir- or flame-like structures, dish and mixed-layer structures, hydroplastic convolutions and seismic unconformities (**Figure 8**). They were commonly mistaken for worm traces, mud cracks or storm deposits since they have abrupt contacts with the surrounding sedimentary rock (according to the geological well reports).

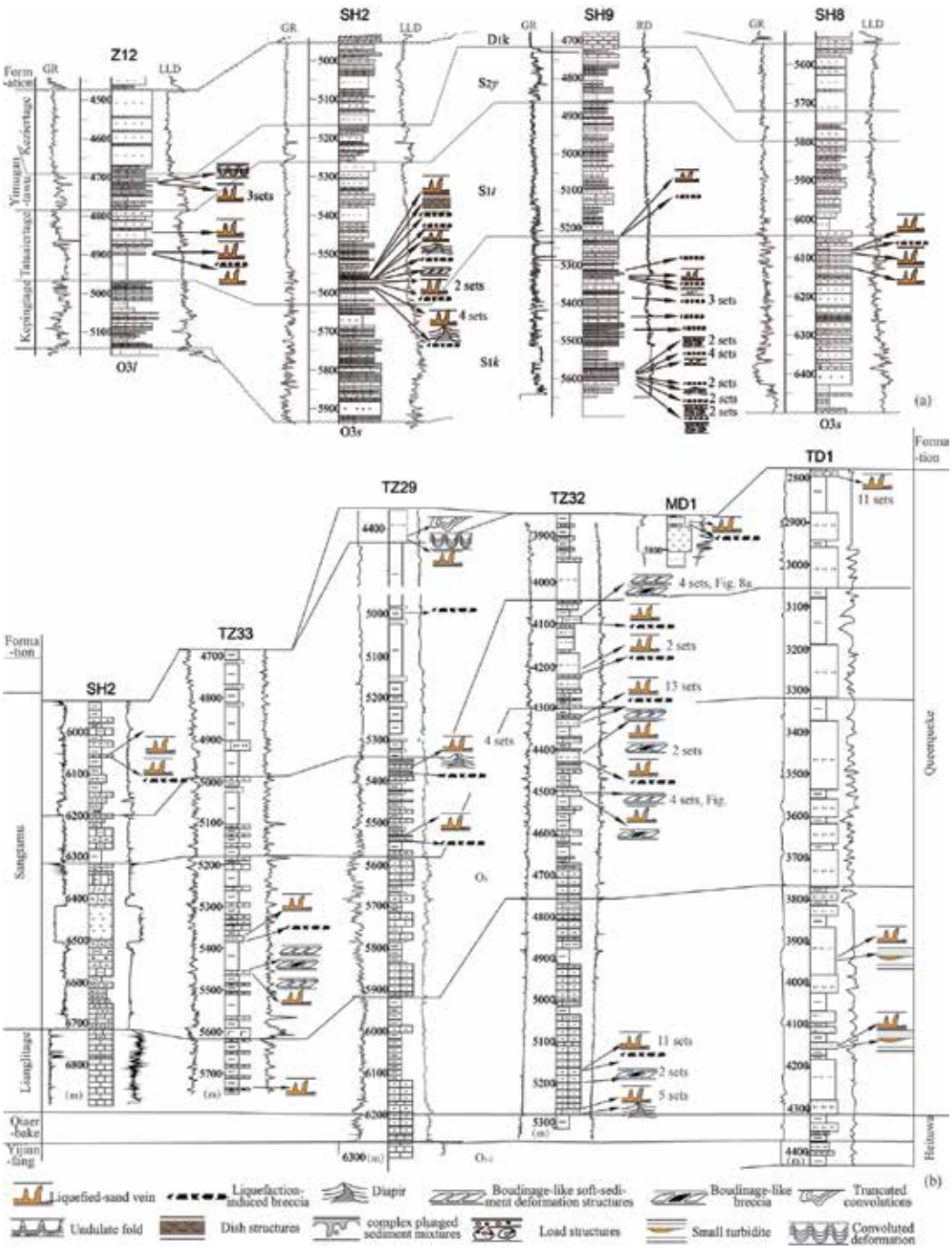

Figure 8. Correlation of strata and paleo-seismic records in the Silurian (a) and Upper Ordovician (b) in the central part of the Tarim Basin (modified from [54]), showing the types and layers of observed SSDS.

3.3.1.1. Liquefied sand veins and liquefaction-induced breccias

Liquefied sand veins are common in the studied cores and have been identified in many wells (**Figure 8**). These liquefied sand veins are a vein-type structure that is formed by injection of liquefied sand flow. Unconsolidated near-surface sands that are water-saturated may liquefy when are abruptly loaded or shaken. This results in overpressure of the pore water, which may then escape to adjoining lower pressure intervals by forming injection features in otherwise undisturbed deposition. Liquefied sand veins in the MD1, TZ29, SH2 and Z12 wells range in width from 2 mm to ~ 3 cm and their length ranges from 1 cm to over 10 cm. They consist of laminated thick horizontal mud layers interbedded with thin silty or fine sand layers, the grey silty sand liquefied and emplaced grey black mud beds. Liquefied sand flows have two occurrences: vertically liquefied (**Figure 8B**) and lateral liquefied (**Figure 9A**). The veins are irregularly curved, with bifurcation in cross section, and without a uniform planar direction as plate in 3D morphology. The textures and components of the sand veins are similar and differ obviously from the surrounding mudstones. Liquefied sand veins cut through mud beds and trigger arching or concave bending (**Figure 9A**, **D** and **E**) of the surrounding laminated mud beds. Thin interbedded sand and mud can form multilayered, interpenetrated and complex vein, like the liquefied sand veins of SH2 well on Silurian composed of ochre sands (fine sands or silty sands) liquefied and invaded in the over- and underlying brown muds. Some of the liquefied sand veins are associated with liquefaction-induced breccias.

Liquefaction-induced breccias are produced by liquefaction of sands that are both overlain and underlain by mud layers. Liquefaction of the sand causes disruption of the surrounding mud beds into gravel-sized, clayey breccia fragments. Liquefaction-induced breccias occur together with liquefied sand veins (**Figures 9A** and **10A**). Grey silty gravels were confined by black grey mudstones; breccias are components of grey green silty mudstones and siltstone fragments with angular and assorted sizes of gravel particles ranging from 0.3 to 1 cm. Such breccias have been interpreted as genetic of storm flow (taken from the final well report) by the mixed and disorderly sedimentary breccias intercalated into the undeformed stable layers. However, the breccias were formed in the mud layers by invasion, ripping up and truncating by liquefied sand veins. The breccias are in-situ and non-transportation. **Figure 10D** shows a liquefied gravel-bearing sand veins and a micro-thrust fault coexisted deformation structure.

3.3.1.2. Boudinage-like SSDS and boudinage-like breccias

Boudinage-like soft-sediment deformation structures (BSSDS) are for the first time identified in the Upper Ordovician in Manjiaer depression and the metre-scale deformation structures in vertical stratigraphic sequences. They consist of thin, light grey calcareous siltstones interbedded with dark grey calcareous mudstones deposited in mixing siliciclastic and carbonate shelf environment. The unconsolidated sediments under horizontal shear stress form boudinage-like structures, rapid depositing sediments with large thicknesses and undeform layers with similar properties on lithology and sedimentary intervals. Multiple cycles of BSSDS are identified in the TZ32 and TZ33 wells (**Figures 8B** and **9B**). The calcareous sand beds with

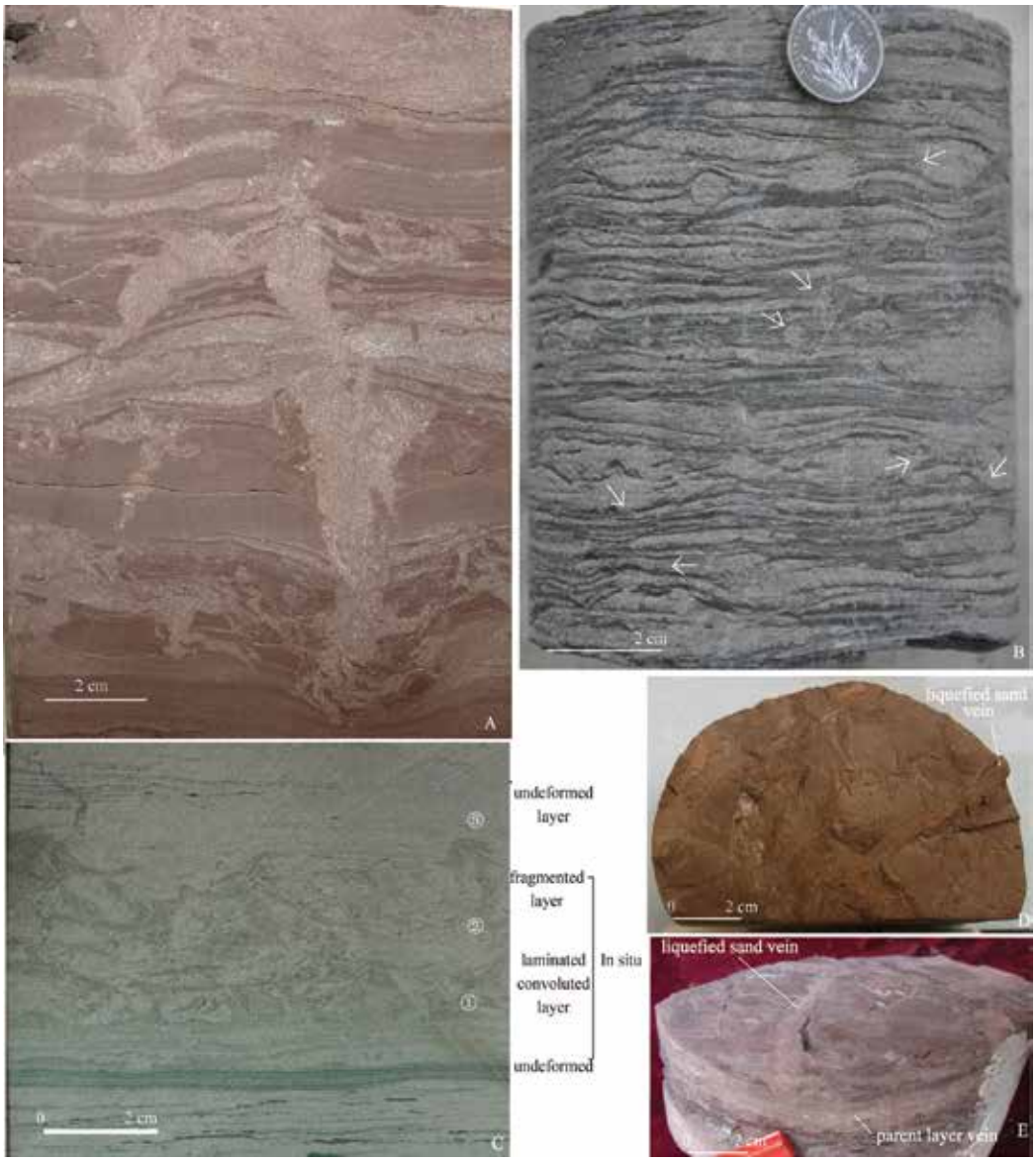

Figure 9. Typical SSDSs in the deep drilling cores (1), in the central part of the Tarim basin. (A) Concentration of sand veins, well SH2, depth 5567.3 m; Yimugantawu Formation of the Middle Silurian (S2*y*). (B) Boudinage-like soft-sediment deformation structures (B-SSDS) and small liquefied sand veins, well TZ32, depth 4507.5 m, Upper Ordovician. (C) Mixed-layer structures, well Z12, depth 4713.8 m; Yimugantawu Fm. Of the middle Silurian. (D and E) Sand veins in cross section and plane, well SH2, depth 5573.1 m; stratigraphical unit S2*y*.

comparatively higher cohesive muds were sheared and cut off, to form lenticular sand bodies under tensional shear stresses.

3.3.1.3. Plunged sediment mixtures

Plunged sediment mixtures refer to the deformation that occurs near or on the boundary between two different unconsolidated stratigraphic units [54]. These two units usually have

http://dx.doi.org/10.5772/intechopen.72941

little difference of the upper and lower sediments. The discontinuous undulate surfaces are easily produced at the boundary, and the sediments of the upper unit form ground fissure, load cast, ball-and-pillow at the top of the lower unit. Spherical, mushroom-shaped and ellipsoidal bodies (**Figure 10B**) of the lower unit also invaded the upper unit by liquefaction and diapirism.

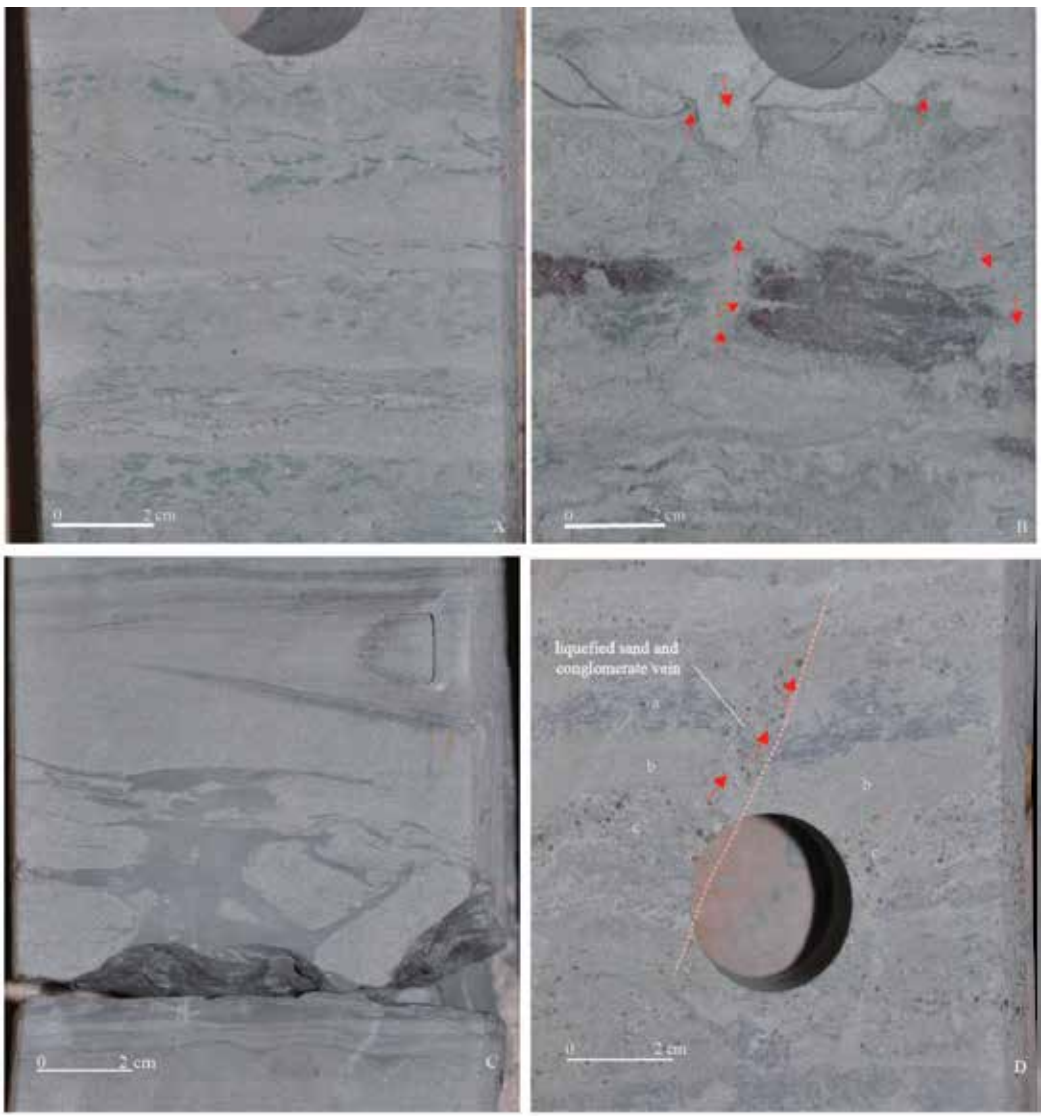

Figure 10. Typical SSDSs in the deep drilling cores (2) of Kepingtage Formation of the Lower Silurian, in well SH9, central part of the Tarim basin. (A) Liquefied breccia and liquefied sand veins, dark grey muds were brecciaed vertically or horizontally by light grey silts emplaced, depth 5590.15 m. (B) Complex plunged sediment mixtures, the wavy interface and load cast were formed, with some light sand layers and light celadon liquefied sand veins, depth at 5342 m. (C) Thixotropic diapir, showing that the dark grey muds experienced thixotropy upward movement to the upper light grey silt sands and formed diapir structures, which were intercalated by the overlying and underlying non-deformation flatting dark grey mud layers and light grey silt layers, showing a complete non-seismic, in-seismic, and non-seismic sequence vertically; well SH9, depth 5606 m. (D) Liquefied gravel-bearing sand veins and a micro-thrust fault, liquefied light grey sand with brown fine gravels and cut the laminated grey mud layer, and superimposed by mini-type thrust fault, depth 5339.69 m. Red arrows indicate the orientation of rheology of particulate matter.

3.3.1.4. Thixotropy wedge and diapir

Thixotropic wedges usually develop in fine-grain sediments, which are thixotropic flow deformation triggered by an earthquake activity [14, 20]. While the soft sediments (mud, soft siliceous sediment and carbonate ooze) with the grain size are less than 0.005 mm, the strength of fine-grain sediments and clays decrease owing to seismic shear stress effect, resulting in the complex rheological phenomenon that occurs (**Figure 10C**). Three axis vibration test of saturated soft soil presents when the seismic intensity is 7 or greater (amount to the earthquake magnitude is 5.6), and muds usually do not be liquefied but it happens with thixotropic flow, which is triggered by shocking [55, 56]. The earthquake magnitude for thixotropic deformation is higher than liquefied deformation [57]. Many deformation structures in argillaceous rocks, silica rocks and micritic of carbonate rocks can be interpreted by the thixotropic mechanism (**Figure 10C**).

The wedges may be very narrow and are recurrent. Thixotropic wedges are obviously different with the ground fissure in hard rock layers. Thixotropic diapir indicates that mud layers flow upwards with thixotropy owing to shock and intrude or emplace in the fine sand or silt layers (**Figure 10C**).

3.3.2. SSDSs triggered by the paleo-activities of the Tazhong 1 and secondary faults

During the late Ordovician to early Silurian, the Tarim Basin underwent conversion from a tensional to a compressive flexural tectonic environment. Accompanied by the Proto-Tethys Ocean subducted in a northward direction since early Ordovician [58], the middle Kunlun terrain collided with the Tarim plate and the South Altun Ocean closured during the late Ordovician [59, 60]. The southern parts of the Tarim Basin was the strong deformation area, especially the southeast area [52, 53], and the main faults in the Tazhong uplift and Tangguzibas depression were activated strongly (**Figure 11**) and responded to the orogenic activities. The NW-trending Tazhong 1 fault (TZ1F) was the boundary fault between the Tazhong Uplift and the Manjiaer Depression during the late Ordovician to Middle Devonian and the paleo-active strength of fault movement was strongest during the Ordovician, with a vertical fault displacement in excess of 2 km (**Figure 11a** and **c**). The property of the TZ1F changed from the normal fault to the reverse fault at the end of the late Ordovician. The west segment of TZ1F ceased activity before or in early Silurian depositing, and the middle and south segments remained active to the early Carboniferous. The activities of the secondary reverse faults of the TZ1F were dominated during the Silurian. At the same time, a series of NE-trending small faults were active but the displacements were little (**Figure 11b**). The normal and strike-slip property of these small faults had been recognised in the 3D seismic data.

These SSDSs, which are intercalated by undeformed layers with similar lithology and sedimentary facies, are observed with wide distribution near the faults (**Figures 7, 8** and **11**). So the SSDSs resulted from the bursting events after they were deposited but incompletely consolidated. Most of them (Well SH2, TZ33, TZ29 and TZ32) in the Upper Ordovician are in the drilling cores nearby the TZ1F and a little in the farther wells (MD1 and TD1). About 51 layers of SSDSs have been observed in the 1500 m sedimentary layers of the Upper Ordovician (deposited during 447–444 Ma) and 26 layers of SSDSs have been observed in about 800 m sedimentary layers of the Lower Silurian (deposited during 436–421 Ma) (**Figure 11c**).

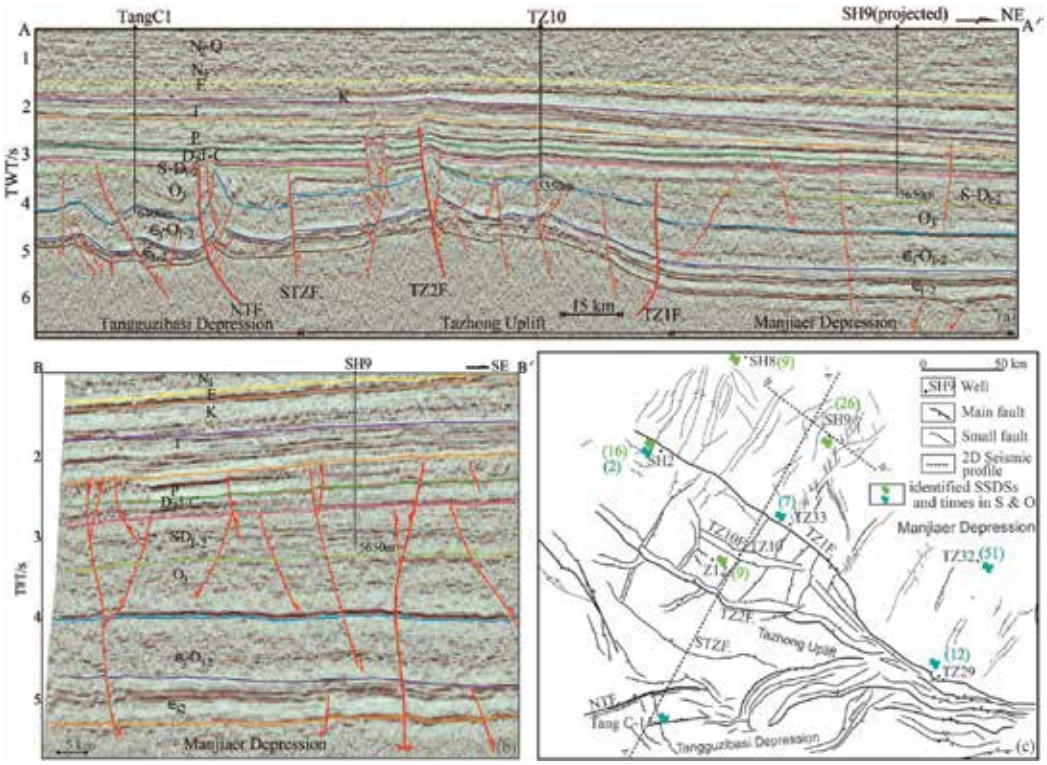

Figure 11. 2D seismic interpretation profiles of the Tazhong uplift and its adjacent area (A-A′, B-B′), (c) the fault systems of the Silurian in the Tazhong uplift and its adjacent areas (modified after Northwest Oilfield Company of SINOPEC, 2015), showing the identified seismic event layers in the deep drilling cores.

Based on their characteristics, the inferred formation mechanism and the spatial association with faults, the SSDSs were triggered by the paleo-active NW-trending TZ1F and a series of NE-trending small faults. The TZ1F was a seismogenic fault during the late Ordovician, whereas the reversed-direction secondary faults and multiple small NE-trending faults were the seismogenic faults in the Early-Middle Silurian. The SSDSs triggered by the paleo-active faults may be represented as records of the high-frequency tectonic events with the pulsation and circularity during the main tectonic movement phases.

3.4. Triggered by the Mesoproterozoic earthquake activities in the northern margin of the North China Craton

3.4.1. SSDSs of the Mesoproterozoic in the Yan-Liao Aulacogen

The SSDSs of the Mesoproterozoic in the Yan-Liao Aulacogen, which is located in the northern margin of the North China Craton, were recognised first by Song [62], and the oldest SSDSs have been observed in China [61–63]. In the Chuanlinggou and Gaoyuzhuang Formation of the Changcheng System (1800–1400) and Wumishan Formation of the Jixian

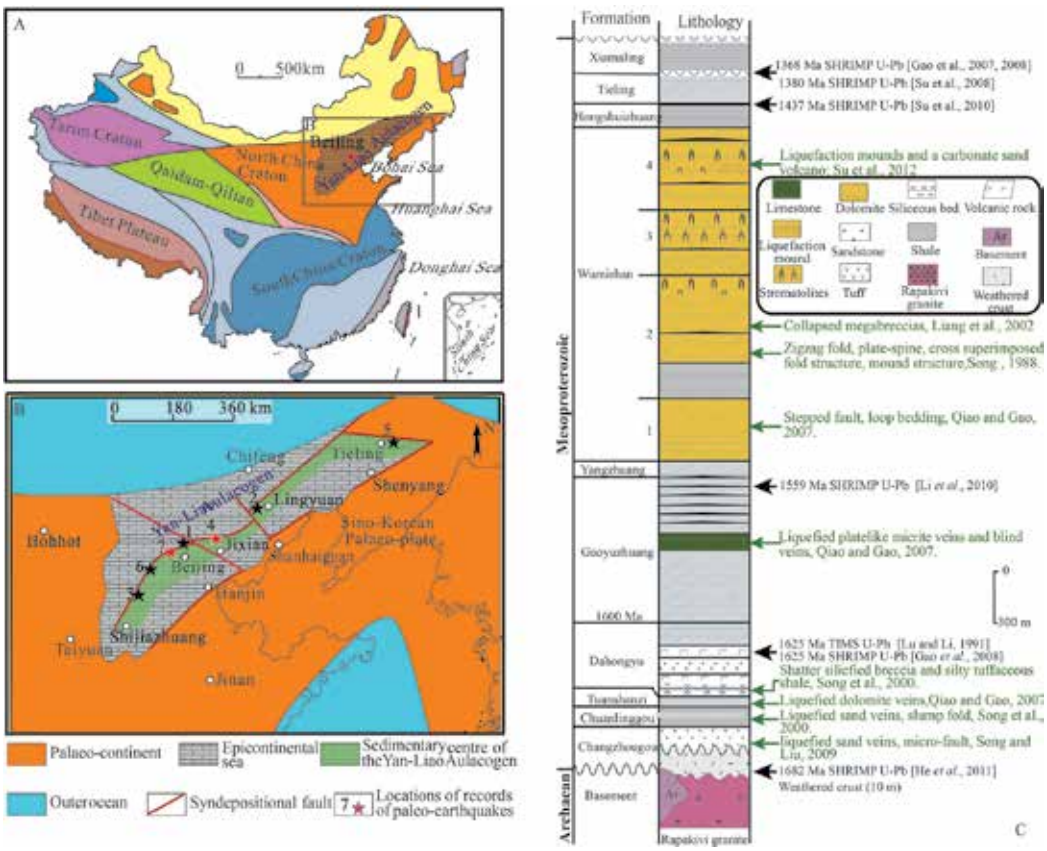

Figure 12. (A) Paleo-plate sketch map of China, showing the distribution of the major paleo-plates of different ages (after [62]). (B) Paleo-geographical map of the Yan-Liao Aulacogen from the Proterozoic Gaoyuzhuang Stage to the Wumishan Stage showing an epicontinental sea opened to the north, and the approximate positions of the discovered seismites (after [63–66]). The identified outcrops of earthquake-triggered SSDSs are marked by stars, 1—[60]; 2—[67]; 3—[68]; 4 and 5—[64]; 6—[32, 69]; 7—[66]. The red stars show the position of the seismites in this paper. (C) Lithostratigraphy of the Mesoproterozoic of the Yan-Liao Aulacogen (modified from [66–74, 77–79]), the records of multiple paleo-earthquake events in green words and volcanic events in black words are shown.

System, various SSDSs have been observed, which mainly developed in the epicontinental sea (**Figure 12**). They are liquefied sand veins, liquefied carbonate mounds, liquefied breccia, hydroplastic deformation, various curly deformation, looping bedding and graded faults. Deformed layers are separated by the undeform layers. The SSDSs in the Chuanlinggou Formation are composed of clastic rocks in the intertidal and subtidal environments, and the others are composed of carbonate rocks deposited in carbonate platform (**Figure 12C**).

3.4.1.1. Liquefaction mound and carbonate sand volcano

They are typical SSDSs in the Wumishan Formation (1550–1400 Ma) of the Mesoproterozoic, with the mound and crater in shape (**Figure 13a–c**), linear arrangement along a roadcut near Zhuanghuwa Village, ca. 70 km west of Beijing. Liquefaction mounds have generally

http://dx.doi.org/10.5772/intechopen.72941

Figure 13. Typical seismites triggered by the Mesoproterozoic earthquakes in the Yanliao Aulacogen, the northern margin of North China Craton. (a) Linear distribution of liquefied carbonate mounds of the Wumishan Formation, the orientation of mounds paralleled to the trending of the Shijiazhuang-Lingyuan Fault of the Yanliao Aulacogen, spot 7 illustrated in **Figure 12**. (b) Close-up views of mound 1 at the Zhuanghuwa sections, note the concentric circular rings and the radial fissures (arrowed). (c) The fine-grained carbonate-sand volcano of the Wumishan Formation, Zhuanghuwa section, spot 7 illustrated in **Figure 12**. (d) Loop bedding of the Wumishan Formation in Yongding River Valley, Beijing. (e) Netlike liquefied dolomite veins and argillaceous dolomite breccia, Tuanshanzi Formation, spot 4, Tuanshanzi village, Jixian, Tianjing. (f) Plate-spine breccias and intense folds, algal dolostones, Wumishan Formation, in Yongding River Valley, Beijing.

rounded shapes, with some concentric and radial fissures. They are composed of grey dolostone with minor amount of black siliceous (chert) rock, especially on the top of the mounds. The diameter of the mounds varies between 1.5 m and 4 m and their height from 10 cm to 30 cm. **Figure 13b** shows the best-exposed mound has an almost perfectly circular shape, with a diameter of 2.8 m, 6 concentric circular fissures and 13 radial direction

fissures. The fissures are filled with dark siliceous chert rock. A carbonate sand volcano also remains, which is shaped just like a small volcano with a crater (**Figure 13c**). It has a diameter of 110 cm and a thickness of about 30 cm. And a thin layer of black siliceous rock is built up in the centre of the depression. There are also at least three (possibly five) radial fissures exposed, which are filled with dark siliceous material.

3.4.1.2. Loop bedding

Loop beddings are ductile deformation structures, which consist of lacustrine finely laminated sediments and are induced by extension stress, presented as loops or chains (**Figure 13d**), and the adjacent layers are undeformed. In the Wumishan Formation of the Mesoproterozoic near Yongding River Valley, they are formed in a deep-water carbonate platform setting and suffered the horizontal shear stress. Loop beddings can be also formed in epicontinental seas and a low energy environment below the wave base of marine settings [66, 72, 76]. It is a result of stretching from unlithified to progressively lithified laminated sediments in response to successive minor seismic shocks, ultimately related to the slow movement of extensional faults [74, 75].

3.4.1.3. Intense intrastratal folds and plate-spine breccias

The strong intrastratal folds occur in the upper part of the Zhuanghuwa section and Yongding River Valley and are about 10–20 cm thick. They are deposited in a very shallow-water depositional environment indicated by the mud cracks and ripple marks beneath this deformed layer.

Plate-spine breccias are widely observed in lamellose or ribbon stripped layers of the Mesoproterozoic in the North China craton. These deformations are formed when the incomplete consolidated laminated layers experience continued compression and completely crack along the axial plane of folds. **Figure 12f** is a superimposed deformation structure of the intrastratal fold and plate-spine breccias, which are formed on two wings of folds, and the top of the fold layer without erosion looks like clouds and is covered by undeformed laminated layers. The formation mechanism of plate-spine breccias may be seismic activities [60]. Ettensohn et al. called the intense folds accordion-like folds, which are induced by earthquakes [34].

3.4.2. SSDSs triggered by the paleo-activity of the Shijiazhuang-Lingyuan Fault Belt

The Yanliao taphrogenic trough is a NE-trending rifting basin in the northern part of North China Craton and is open to the north [63–65]. The Shijiazhuang-Lingyuan Fault Belt (>800 km long) is the main fault belt with the NE-trending (**Figure 12B**), which is extended along the axial part of the Yan-Liao Aulacogen, activated during the early Mesoproterozoic in an extension tectonic environment [63]. The observed SSDSs are mainly distributed approximately less than 20 km from the fault in vertical distances. Identified SSDSs include intrastratal faults, liquefaction sand veins, liquefaction carbonate mounds and volcanos along the paleo-active fault belts. The SSDS layers have been interbedded by the many undeform layers. And some of them have the abnormal geochemical records such as Re, Os, Ir and other rare elements in black silty mudstones or shale of Chuanlinggou Formation that give a clue that volcanic and seismic events existed [77]. The liquefaction carbonate mounds and sand volcanos in the Mesoproterozoic have similar features which induced by the recent Wenchuan earthquake

(Ms 8.0) in Sichuan Province, SW China in 2008. According to the mechanism of SSDSs and the relationship of the activity of SSDSs and faults, they may be triggered by paleo-seismic events of the Shijiazhuang-Lingyuan Fault Belts. There are about 29 times deformation layers or seismic event layers have been observed in the Zhuanghuwa section, and the occurrence frequency of the strong paleo-earthquakes is about 20 thousand years to 32 thousand years [78, 79]. Multiple seismic events and activities of the Shijiazhuang-Lingyuan Fault Belt are responded on the break-up of the Columbian supercontinent.

4. Implication and prospects of the high-frequency tectonic events studied

4.1. Understanding the history of fault activities

The typical cases of seismites at different times in China reveal the sequence of paleo-earthquake events, and the activities of seismogenic faults can help us understand the dynamics of tectonic developments in different regions.

Seismites research may provide geo-history evidences for active seismic fault belts. The vertical sequences of paleo-earthquakes (seismites) are separated by undeformed sedimentary layers. They will provide a history of gradual and abrupt changes of the tectonic development and evolution in a particular region and regular patterns of seismicity of this region. Correlation of the paleo-earthquake activity sequences will help us to know spatial and temporal characteristics of paleo-seismic events in the main tectonic movement. This will provide important supplementary evidences of the impulsive and cyclicity of tectonism of the main tectonic movement. And they can also provide evidences for the tectonic records during a period from 10^2 to 10^6 yr (The white paper resulting from a workshop held at Denver Colorado, 2002), which is a difficult issue in the frontier research of structural geology and tectonic science. Paleo-earthquake events will build a link between orogenesis, high-frequency tectonism (in basin-mountain system) and a seismic activity.

4.2. Dating precisely of the tectonic events

Since seismites formed before sediments are completely consolidated, the age of depositing sediments in seismites could indicate the approximate time of a paleo-seismic event, and the ages of syn-depositional volcanism and organic debris in relative layers of seismites can provide evidence for the absolute age of seismicity and the tectonic events. The ^{14}C dating (radiocarbon dating), the U-Th disequilibrium technique (speleothem calcite), the electronic spin (ESR) (fossil dating), the K-Ar and ^{40}Ar-^{39}Ar dating (syntectonic illite) and the detrital zircon U/Pb dating (LA-MC-ICP-MS) can provide the different time-scale dating.

4.3. Effects on paleo-ecological environments and energy resources

Paleo-seismic research may help us understand more the changes of sedimentary paleogeographic and ecological on different scales. It is a new research direction to combine paleo-earthquake, which is an unexpected and catastrophic event, with life and environmental change.

He et al. analysed a host of identified Cretaceous seismites in Zhucheng faulted depression in Shandong Province, discussed the relationship between the distribution of seismites and the mass buried dinosaur fossils and pointed out that paleo-seismicity and environment change may result in migration of dinosaurs [80].

Faults and fractures can be channels for fluid flow, especially hydrocarbon migration and mineral accumulation in different times, but also as destroyers for them when the faults and fractures are active later. The paleo-seismicity accompanied by development of faults and fractures will affect the lithology, structural deformation, fluid properties, pressure-temperature and anisotropy of consolidated rocks. The research of intensity, frequency and distribution of paleo-seismic events help us to understand structural deformation, fracture development, characteristics of porosity and permeability and fluid migration. Integrated research of paleo-seismicity, basin structural and paleogeographic evolution may provide the reallocation and final determination of positions of oil and gas reservoirs and mineral resources.

Acknowledgements

This study was supported by the Science Research from the Northwest Subcompany of SINOPEC (no: KY2013-S-024), the work project of China Geological Survey (no. 12120115002001, DD20160169), a Special Research Grant from Ministry of Land and Resources of the People's Republic of China (no. 201011034), the Major Project of National Natural Science Foundation of China (no. 41630207).

Author details

Bizhu He*, Xiufu Qiao, Haibing Li and Dechen Su

*Address all correspondence to: hebizhu@vip.sina.com; hebizhu@cags.ac.cn

Key Laboratory of Continental Tectonics and Dynamics, Institute of Geology, Chinese Academy of Geological Sciences, Beijing, China

References

[1] Scholz CH. Earthquakes and friction laws. Nature. 1998;**391**:36-42

[2] Deng QD, Zhang PZ, Rang YK, Yang XP, Min W, Chu QZ. Basic characteristics of active structure in mainland of China. Science China (Earth Sciences). 2002;**32**:1020-1030 (in Chinese)

[3] Zhang PZ, Deng QD, Zhang ZQ, Li HB. Active faults, earthquake hazards and associated geodynamic processes in continental China. Scientia Sinica Terrae; **43**:1607-1620 (in Chinese)

[4] Kanamori H. 1977. The energy release in great earthquakes. Journal of Geophysical Research. 2013;**82**:2981-2987

[5] Stein S, Klosko E. Earthquake mechanisms and plate tectonics. International Geophysics. 2002;**81**(A):69-78. DOI: 10.1016/S0074-6142(02)80210-8

[6] Chen YT. Classification of earthquakes. City and Disaster. 2003;**1**:13-15 (in Chinese)

[7] Simms MJ. Uniquely extensive seismites from the latest Triassic of the United Kingdom: Evidence for bolide impact? Geology. 2003;**31**(6):557-560

[8] Wallace RE. Profiles and ages of young fault scarps, north-central Nevada. Geological Society of America Bulletin. 1977;**88**(9):1267-1278

[9] Yang ZE, Ying SH, Lin CY, Yu LB. Characteristics of fault rocks and their potential evidences for seismic events. Seismology and Geology. 1984;**3**(4):1-4 (in Chinese)

[10] Deng QD, Chen SF, Zhao XL. Tectonics, seismicity and dynamics of Longmenshan Mountains and its adjacent regions. Seismology and Geology. 1994;**16**(4):387-403 (in Chinese)

[11] Liu-Zeng J, Klinger Y, Xu X, Lasserre C, Chen G, Chen W, Tapponnier P, Zhang B. Millennial recurrence of large earthquakes on the Haiyuan fault near Songshan, Gansu Province, China. Bulletin of the Seismological Society of America. 2007;**97**(1B):14-34. DOI: 10.1785/0120050118

[12] McCalpin JP. Paleoseismology. San Diego: Academic Press; 2009. 647 p

[13] Ran YK, Li YB, Du P, Chen LC, Wand H. Key techniques and several cases analysis in paleoseismic studies in mainland China (3): Rupture characteristics, environment impact and paleoseismic indicators on normal faults. Seismology and Geology. 2014;**36**(2):287-301. DOI: 1.3969/j.issn.0253-4967.2014.02.001 (in Chinese with English abstract)

[14] Montenat C, Barrier P, d'Estevou PO, Hibsch C. Seismites: An attempt at critical analysis and classification. Sedimentary Geology. 2007;**196**:5-30

[15] Seilacher A. Fault-graded beds interpreted as seismites. Sedimentology. 1969;**13**:155-159

[16] Maltman A. On the term 'soft-sediment deformation. Journal of Structural Geology. 1984;**6**:589-592

[17] Brodzikowski K, van Loo AJ. A systematic classification of glacial and periglacial environments, facies and deposits. Earth-Science Reviews. 1987;**24**:297-381

[18] Qiao XF, Song TR, Gao LZ, Peng Y, Li HB, Gao M, Song B, Zhang QD. Seismic sequence in carbonate rocks by vibration liquefaction. Acta Geologica Sinica (English Edition). 1994;**7**(3):243-265

[19] Owen G, Moretti M, Alfaro P. Recognising triggers for soft-sediment deformation: Current understanding and future directions. Sedimentary Geology. 2011;**235**:133-140

[20] Qiao XF, Li HB, Qiu ZL. Seismites-paleoearthquake Records in Sedimentary Rock (the 10th paragraph). In: Feng ZZ. editor-in-chief. Beijing: Petroleum Industry Press; 2013. pp. 507-606 (in Chinese)

[21] He BZ, Qiao XF. Advances and overview on researching paleo-earthquake events: A review of seismites. Acta Geological Sinica. 2015;**89**(5):1702-1746

[22] Maltman AJ. Shear zones in argillaceous sediments—An experimental study. In: Jones ME, Preston RMF, editors. Deformation of Sediments and Sedimentary Rocks. Geological Society: London, Special Publication; 1987. 29 p

[23] Owen G. Deformation processes in Unconsolidated Sands. In: Jones ME, Preston RF. editor. Deformation of Sediments and Sedimentary Rocks. Geological Society of London Special Publication, 29. 1987. pp. 11-24

[24] Lowe DR. Water escape structures in coarse-grained sediments. Sedimentology. 1975; **22**:157-204

[25] Guiraud M, Plaziat JC. Seismites in the fluviatile bima sandstone: Identification of paleoseismism and discussion of their magnitudes in a cretaceous synsedimentary strike-slip basin (Upper Benue, Nigeria). Tectonophysics. 1993;**225**(4):493-522

[26] Allen JRL. Sedimentary Structures, their Character and Physical Basis, Vol. 2. Developments in Sedimentology. Vol. 30B. Amsterdam: Elsevier; 1982. 663 p

[27] Owen G, Moretti M. Identifying triggers for liquefaction-induced soft-sediment deformation in sands. Sedimentary Geology. 2011;**235**:141-147

[28] Van Loon AJ. Soft-sediment deformation structures in siliciclastic sediments: An overview. Geologos. 2009;**15**:3-55

[29] Du YS. Discussion about studies of earthquake event deposit in China. Journal of Palaeogeography. 2011;**13**(6):581-590 (in Chinese with English abstract)

[30] Obermeie SF. Use of liquefaction-induced features for paleoseismic analysis-an overview of how seismic liquefaction features can be distinguished from other features and how their regional distribution and properties of source sediment can be used to infer the location and strength of Holocene paleo-earthquakes. Engineering Geology. 1996;**44**:1-76

[31] Moretti M, Alfaro P, Caselles O, Canas JA. Modelling seismites with a digital shaking table. Tectonophysics. 1999;**304**:369-383

[32] Qiao XF, Song TR, Gao LZ, Li HB, Peng Y, Zhang CH, Zhang YX. Seismic Records in Strata (Ancient Earthquake). Beijing: Geological Publishing House; 2006. 1-263 p (in Chinese with English abstract)

[33] Van Loon AJ. The life cycle of seismite research. Geologos. 2014;**20**(2):61-66

[34] Ettensohn FR, Zhang C, Lierman R. Soft-sediment deformation in epicontinental carbonates as evidence of paleoseismicity with evidence for a possible new seismogenic indicator: Accordion folds. Sedimentary Geology. 2011;**235**:222-233

[35] Sims JD. Determining earthquake recurrence intervals from deformational structures in young lacustrine sediments. Tectonophysics. 1975;**29**:141-152

[36] Li HB, Fu XF, Van der Word J, Si JL, Wang ZX, Hou LW, Qiu ZL, Li N, Wu FY, Xu ZQ, Tapponnier P. Co-seisimic surface rupture and dextral-slip oblique thrusting of the Ms 8.0 Wenchuan earthquake. Acta Geologica Sinica. 2008;**82**(12):1623-1643 (in Chinese with English abstract)

[37] Li HB, Wang H, ZQ X, Si JL, Pei JL, Li TF, Huang Y, Song SR, Kuo LW, Sun ZM, Chevalie ML, Liu DL. Characteristics of the fault-related rocks, fault zones and the principal slip zone in the Wenchuan Earthquake Fault Scientific Drilling Project Hole—1 (WFSD-1). Tectonophysics. 2013;**584**:23-42

[38] Zhang PZ, We XZ, Shen ZK, Chen JH. Oblique high-angle listric-reverse faulting and associated straining processes: The Wenchuan earthquake of 12 May 2008, Sichuan, China. Annual Review of Earth and Planetary Sciences. 2010;**38**:353-382

[39] Fu BH, Shi PL, Wang P, Li Q, Kong P, Zheng GD. Geometry and kinematics of the Wenchuan earthquake surface ruptures around the Qushan Town of Beichuan County, Sichuan: Implications for mitigation of seismic and geologic disasters. Chinese Journal of Geophysics. 2009;**52**(2):485-495 (in Chinese with English abstract)

[40] Ran YK, Shi X, Wang H, Chen LC, Chen J, Liu RC, Gong H. The maximum coseismic vertical surface displacement and surface deformation pattern accompanying the Ms 8.0 Wenchuan earthquake. Chinese Science Bulletin. 2010;**55**(9):841-850

[41] Nichols RJ, Sparks RSJ, Wilson CJN. Experimental studies of the fluidization of layered sediments and the formation of fluid escape structures. Sedimentology. 1994;**41**:233-253

[42] Sobel ER, Arnaud N. Cretaceous-Paleogene basaltic rocks of the Tuyon basin, NW China and the Kyrgyz Tianshan: The trace of small plume. Lithos. 2000;**50**:191-215

[43] Li JH, Cai ZZ, Luo CS, Geng YH. The structure transfer at the southern end of Talas-Ferghana fault and its regional tectonic response in the Cenozoic. Acta Geologica Sinica. 2007;**81**(1):23-31 (in Chinese with English abstract)

[44] Luo JH, Zhou XY, Qiu B, Yang ZL, Yin H, Li JL. Controls of Talas-Ferghana fault on Kashi Sag. Northest Tarim Basin, Xinjiang. Petroleum Geology. 2004;**25**(6):584-587 (in Chinese with English abst)

[45] Owen G. Soft-sediment deformation in upper Proterozoic Torridonian sandstones (Applecross Formation) at Torridon, Northwest Scotland. Journal of Sedimentary Research. 1995;**A65**:495-504

[46] Liu Y, Xie JP. Vibration Liqueication of Sandy Soil. Beijing: Seismological press; 1984. pp. 1-327 (in Chinese with English abstract)

[47] Qiao XF, Jiang M, Li HB, et al. Soft-sediment deformation structures and their implications for tectonic evolution from Mesozoic to Cenozoic in the Longmen Shan. Earth Science Frontiers. 2016;**23**(6):80-106

[48] Li TD (Chief compiler). Geological Map of Western China and Adjacent Regions, 1:2500000. Beijing: Geologidal Pubulishing House. 2006

[49] Jia CZ, Wei GQ, Yao HJ. Oil and Gas Exploration Books in Tarim Basin- Tectonic Evolution and Regional Structural Geology. Beijing: Petroleum Industry Press; 1995; 70 p (in Chinese with English abstract)

[50] He DF, Jia CZ, Li DS, Zhang CJ, Meng QR, Shi X. Formation and evolution of polycyclic superimposed Tarim Basin. Oil & Gas Geology. 2005;**26**:64-77 (in Chinese with English abstract)

[51] Tang LJ, Jia CZ. Structure Interpretation and Stress Field Analysis in Superposition Tarim Basin/Series of Typical Superposition Basin Hydrocarbon Formation and Distribution Prediction in China. Beijing: Science Publishing House. 149 p; 2007 (in Chinese with English abstract)

[52] He BZ, Xu ZQ, Jiao CL, Li HB, Cai ZH. Tectonic unconformities and their formation: Implication for hydrocarbon accumulations in Tarim Basin. Acta Petrologica Sinica. 2011;**27**:253-265 (in Chinese with English abstract)

[53] He BZ, Jiao CL, Xu ZQ, Cai ZH, Zhang JX, Liu SL, Li HB, Chen WW, Yu ZY. The paleotectonic and paleogeography reconstructions of the Tarim Basin and its adjacent areas (NW China) during the late Early and Middle Paleozoic. Gondwana Research. 2016;**30**:191-206 http://dx.doi.org/10.1016/j.gr.2015.09.011

[54] He BZ, Qiao XF, Jiao CL, Xu ZQ, Cai ZH, Guo XP, Zhang YL. Palaeo-earthquake events during the late Early Palaeozoic in the central Tarim Basin (NW China): Evidence from deep drilling cores. Geologos. 2014;**20**(2):105-123. DOI: 10.2478/logos-2014-0006

[55] Rossetti DF, Bezerra FHR, Goes M, Neves BBB. Sediment deformation in Miocene and post-Miocene strata, Northeastern Brazil:Evidence for paleoseismicity in a passive margin. Sedimentary Geology. 2011;**235**:172-187

[56] Zhang HC. Thixotropic research of mud foundation triggered by earthquake. Journal of Geotechnical Engineering. 1989;**11**(3):78-85 (in Chinese)

[57] Tian HS, Zhang SH, Zhang AS. Test investigation on liquefied deformation structure in saturated lime-mud composites triggered by strong earthquakes. Acta Geological Sinica (English Edition). 2016;**90**(6):2008-2021

[58] Yang JS, Robinson PT, Jiang CF, Xu ZQ. Ophiolites of the Kunlun Mountains, China andtheir tectonic implications. Tectonophysics. 1996;**258**:215-231

[59] Xu ZQ, Yang JS, Li HB, Zhang JX, Wu CL. Orogenic Plateau: Terrain Amalgamation, Collision and Uplift in the Qinghai-Tibet Plateau. Beijing: Geological Publishing House; 2007. 458 pp (in Chinese with English abstract)

[60] Xu ZQ, Li ST, Zhang JX, Yang JS, He BZ, Li HB, Ling CS, Cai ZH. Paleo-Asian and Tethyan tectonic systems with docking the Tarim block. Acta Petrologica Sinica. 2011;**27**:1-22 (in Chinese with English abstract)

[61] Qiao XF, Gao LZ, Peng Y. Mesoproterozoic earthquake event and breakup of the Sino-Korean Plate. Acta Geologica Sinica (English Edition). 2007;**81**(3):385-397

[62] Song TR. A set of earthquake-tsunami sequences in carbonate stratigraphy of the Precambrian at thirteen imperial in Beijing. Sci. Rev. 1988;**38**(8):609-611 (in Chinese)

[63] Su DC, Qiao XF, Sun AP, Li HB, Somerville ID. Large earthquake-triggered liquefaction mounds and a carbonate sand volcano in the Mesoproterozoic Wumishan formation, Beijing, North China. Geological Journal. 2014;**49**:69-89

[64] Liu XY, Wang Q. Plate tectonic map of China's lithosphere. In: Ma LF, Qiao XF, Min LR, Fan BX, Ding XZ, editors. Geological Atlas of China. China: Geological Publishing House; 2007. pp. 41-44 (in Chinese)

[65] He ZJ, Song TR, Ding XZ, Zhang Q, Meng XH, Ge M. Early synsedimentary faulting of the Meso-Proterozoic Yanshan rift and its influence on event sedimentation. Journal of Palaeogeography. 2000;**2**:83-91 (in Chinese, with English abstract)

[66] Qiao XF, Gao LZ. Mesoproterozoic palaeoearthquake and palaeogeography in Yan-Liao Aulacogen. Journal of Palaeogeography. 2007;**9**:337-352 (in Chinese, with English abstract)

[67] Qiao XF. Intraplate seismic belt and basin framework of Sino-Korean plate in the Proterozoic. Earth Science Frontiers. 2002;**9**:141-150 (in Chinese, with English abstract)

[68] Su DC, Sun AP. Typical earthquake-induced soft-sediment deformation structures in the Mesoproterozoic Wumishan Fm., Yongding River valley (China) and interpreted earthquake frequency. Journal of Palaeogeography (English Edition). 2012;**1**:71-89

[69] Liu PJ. Seismite and its rhythm in the Gaoyuzhuang Formation of Mesoproterozoic in Pingquan County, Hebei Province. Geoscience. 2001;**15**:266-269 (in Chinese, with English Abstract)

[70] Liang DY, Song ZM, Zhao CH, Nie ZT. Discovery of Mesoproterozoic seismites at Baishi Mountain, Hebei Province and its geological significance. Geological Bulletin of China. 2002;**21**:625-630

[71] Liang DY, Nie ZT, Song ZM, Zhao CH, Chen KG, Gong HB. Seismic-tsunami sequence and its geological features of Mesoproterozoic Wumishan Formation in Fangshan Global Geopark, Beijing, China: A case study on Yesanpo scenic district. Geological Bulletin of China. 2009;**28**:30-37 (in Chinese, with English Abstract)

[72] Su WB, Zhang SH, Huff WD, Li HK, Ettensohn FR, Chen XY, Yang HM, Han YG, Song B, Santosh M. SHRIMP U-Pb ages of K-bentonite beds in the Xiamaling Formation: Implications for revised subdivision of the Meso- to Neoproterozoic history of the North China Craton. Gondwana Research. 2008;**14**:543-553

[73] Su WB, Li HK, Huff WD, Ettensohn FR, Zhang SH, Zhou HY, Wan YS. SHRIMP U-Pb dating for a K-bentonite bed in the Tieling Formation, North China. Chinese Science Bulletin. 2010;**55**:3312-3323

[74] Zhang CL, Wu ZJ, Gao LZ, Wang W, Tian YL, Ma C. Structure and significance of soft-sediment deformation structure of Wumishan formation triggered by earthquake. Science China Earth Sciences. 2007;**27**(3):336-342 (in Chinese with English abstract)

[75] Calvo JP, Rodriguez-Pascua M, Martin-Velazquez S, Jimenez S, Vicente GD. Micro-deformation of lacustrine laminite sequences from Late Miocene formations of SE Spain: An interpretation of loop bedding. Sedimentology. 1998;**5**(2):279-292

[76] Rodríguez-López JP, Meléndez N, Soria AR, Liesa CL, Van Loon AJ. Lateral variability of ancient seismites related to differences in sedimentary facies (the syn-rift Escucha formation, mid-cretaceous, eastern Spain). Sedimentary Geology. 2007;**201**:461-484

[77] Song TR, He ZJ, Ding XZ, Zhang QD. A study of geologidal event records in the proterozoic Chuanglinggou Formation of the Ming Tombs District, Beijing. Geological Review, 406. 2000;**46**(4):400 (in Chinese with English abstract)

[78] Su DC, Sun AP. Typical earthquake-induced soft-sediment deformation structures in the Mesoproterozoic Wumishan Formation, Yongding River Valley, Beijing, China and interpreted earthquake frequency. Journal of Palaeogeography. 2011;**1**(1):71-89

[79] Su DC, Sun AP. Soft-sediment deformation and occurrence frequency of palaeo-earthquake in the Mesoproterozoic Wumishan Formation, Yongding river valley, Beijing. Jourunal of Palaeogeography. 2011;**13**(6):591-614 (in Chinese with English abstract)

[80] He BZ, Qiao XF, Zhang YL, Tian HS, Cai ZH, Chen SQ, Zhang YX. Soft-sediment deformation structures in the Cretaceous Zhucheng depression, Shandong Province, East China; their character, deformation timing and tectonic implications. Journal of Asian Earth Sciences. 2015;**110**:101-122. DOI: 10.1016/j.jseaes.2014.12.005

Chapter 8

Evolution of Drainage in Response to Brittle - Ductile Dynamics and Surface Processes in Kachchh Rift Basin, Western India

Girish Ch Kothyari, Ajay P. Singh, Sneha Mishra, Raj Sunil Kandregula, Indu Chaudhary and Gaurav Chauhan

Additional information is available at the end of the chapter

http://dx.doi.org/10.5772/intechopen.73653

Abstract

The eastern part of Kachchh Rift basin was reactivated after 2001 Bhuj earthquake of Mw 7.7 and continuous seismicity has been recorded since then. The northern part of Wagad upland also experienced moderate earthquakes Mw ≥ 5.7 in February 2006 and March 2007. These moderate to major Intraplate earthquakes provide a unique opportunity to study the effects and linkage between brittle-ductile dynamics, surface processes and drainage evolution. We presented a geomorphological analysis of the Wagad highland providing new constraints on the evolution of river network. The shallow to deeper nature of fault and their response to development of hydrological networks has been analyzed using seismic tomography. Based on surface drainage offset and seismic structures several E-W oriented faults controlling fluvial dynamics are identified. From seismic structures and drainage offset it is clear that the fluvial dynamics is controlled by shallower to deeper faults. The estimated attributes are well supported with seismic structures and focal mechanisms solutions. Based on fluvial offset and seismic structure analysis a new tectonic model has been proposed for WH. The tectonic model shows that the faults WH are well connected at deeper level and generated negative flower structures and significantly controlling surface fluvial dynamics.

Keywords: drainage, geomorphology, fluvial dynamics, seismic structure, focal mechanisms

1. Introduction

Spatial distributions of geomorphic landforms in active regions are the results of the complex interaction of shallow and deep earth processes [1]. The imprints of these processes are reflected in the form of changes of local relief, drainage pattern, hypsometry, steepness, and channel slope relationship [2–8]. These parameters can be used to quantitatively characterize the relationship between shallow and deeper crustal structure, and geomorphic processes [1, 9]. The dry land fluvial systems of intraplate Kachchh rift basin, allow us to study the effects and linkage between brittle - ductile dynamics and surface processes on landscape evolution. The Kachchh basin evolved during the Early Jurassic, bound by Nagar Parkar Fault to the north and North Kathiawar Fault to the south (**Figure 1A**). The rifting was aborted by the trailing edge uplift during the Late Cretaceous pre-collision stage of the Indian plate, when the leading edge of the plate was slab-pulled towards the Tethyan trench [10, 14, 16]. Lateral motion during the drift stage of the plate induced horizontal stress and near vertical normal faults, which were reactivated as reverse faults during initiation of the inversion cycle, and became strike-slip faults involving divergent oblique-slip movement [10, 14, 17, 18].

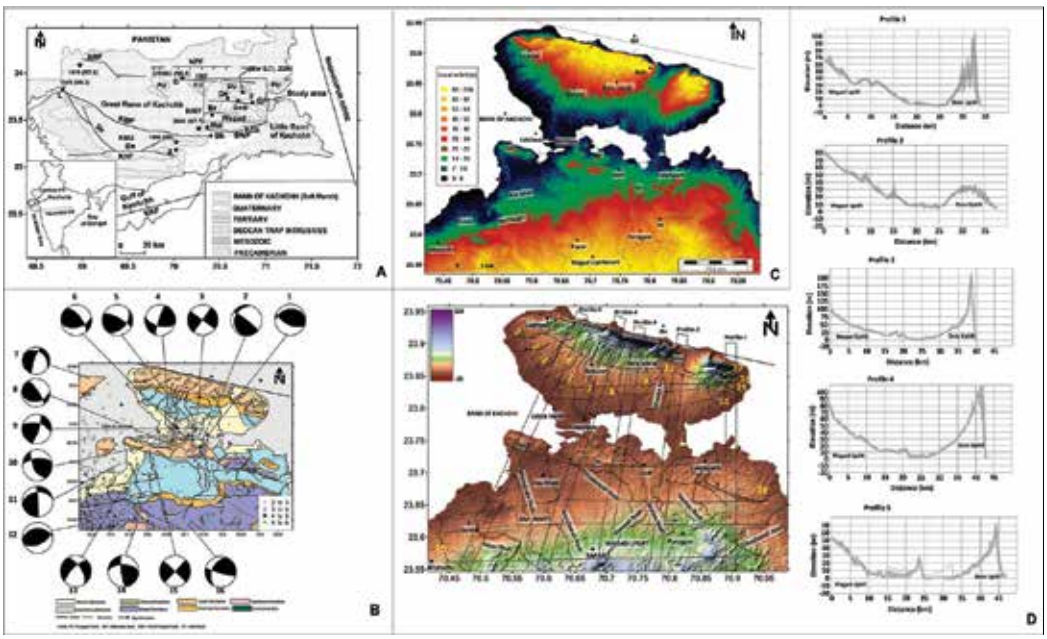

Figure 1. (A) Seismotectonic map of the Kachchh rift basin integrated with the geological map, showing the epicenters of significant earthquakes (modified after [10]). The Wagad area lies between the SWF and GF. Locations - A (Anjar), B (Bhuj), Ba (Bhachau), Br (Bharudia), Ch (Chitrod), D (Dholavira), De (Desalpar), L (Lakhpat), F (Fatehgarh) and G (Gedi); faults: NKF (North Kathiyawad Fault), KHF (Katrol Hill Fault), VF (Vigodi Fault), KMF (Kachchh Mainland Fault), SWF (South Wagad Fault), NWF (North Wagad Fault), GF (Gedi Fault), IBF (Island Belt Fault), ABF (Allah Bund Fault) and NPF (Nagar Parkar Fault); uplifts: KMU (Kachchh Mainland Uplift), PU (Patcham Uplift, KU (Khadir Uplift), BU (Bela Uplift), CU (Chorar Uplift). (B) Geological map of northern Wagad highland region [11]; shows location of earthquake epicenters. Focal mechanisms (1–16) plotted in the figure are after [12–15]. (C) CARTOSAT-DEM driven local relief map of Wagad Highland. Major and minor faults are marked by solid black line. (D) CARTOSAT DEM of the study and location of the five swath profiles; 1–5) swath profiles show the trends of the maximum, minimum and mean topography of the Wagad region. **Figure 1A** and **1B** *have been digitized in Surfer 14 software, while, we used MICRO-DEM 10 software for generation of* C and D, *and final editing has been done in golden software Surfer 14.*

Major structural features of the Kachchh region include east – west trending active faults [16, 19] (**Figure 1A**). The Wagad highland (WH) of Kachchh is bounded by the South Wagad Fault (SWF) in the south and Gedi Fault (GF) in the north comprises of Mesozoic sediments overlying a granitic basement [16]. The initiation and steadiness of dynamics support beneath Kachchh basin have been explored in several studies [10]. Earlier researchers argued that the impingement of a large intrusive body in the lower crust [19–21]. However, the fault adjacent to intrusive body at deeper depth gradually flattens close to magmatic body owing to listric nature of fault [20, 22]. The fault model proposed by [10] suggests that the GF is a sub-vertical fault and gradually changing listric nature in lower crust.

The chronometric and geomorphic attributes of the GF, suggests that the region is uplifting at the rate of 0.3–1.1 mm/y during the last 9 ka [23]. The results of geomorphic processes and subsurface dynamics of GF zone can be explored by investigating how base level fall at the WH region propagates through the drainage network. The subsurface nature of faults in WH and their association with landscape evolution is still unknown. However, in present study an attempt has been made to understand brittle and ductile dynamics of fault system controlling surface landscape pattern. In this study first time we proposed an integrated sub surface model of WH by combining seismic structure (Tomograph) and surface geomorphology. In this connection we analyzed the 27 basins of WH. In particular**,** we investigated the general topographic features e.g. swath profiles, local relief and the river network (river longitudinal profiles). We employed a knickpoint celerity approach in order to provide a chronological framework to the evolution of the river network. Furthermore, we made an attempt to image subsurface fault pattern of the area using the seismological approaches such as tomoDD and focal mechanisms. The results permitted us to trace the long-term evolution of the WH, to confirm dynamic support and documenting its impact on the contrasting development of the drainage basins.

2. General geomorphology and seismicity of Wagad Kachchh

The WH is second largest uplifted block of Kachchh basin, after mainland of Kachchh, covering an area of ~2432 km^2, and is bounded by GF to the north and SWF to the south [11, 16]. The area is drained by numerous ephemeral streams; flow direction regularly spaced around the upper planation surface [23, 24]. From north to south, the WH comprises of three E-W trending active faults, namely the GF between Deshalpar and Fatehgarh area, the North Wagad Fault (NWF) north of Bharudia and the SWF between Mai and east of Chitrod (**Figure 1A**).

Geomorphologically the WH is divided into 3 units; (i) the upper planation surface (Mesozoic) with juvenile streams, (ii) the middle incised slopes with piedmont (Tertiary), and (iii) the low-lying areas representing Quaternary deposits [23, 25]. The upper surface represents an early Quaternary erosional event, whereas the middle incised slopes with terraces were developed during late Quaternary [26]. These two geomorphic units provide sediments to the lower peripheral areas. Suvai, Bhimguda, Narelawali, Dhadawali, Karaswali, Malan, Baniyo, and Dabhodanwari are six ephemeral rivers that flow northward and originate from the WH, following the regional slope and drain into the Great Rann of Kachchh [23]. Along their longitudinal length, these rivers cross several E-W oriented faults (**Figure 2**).

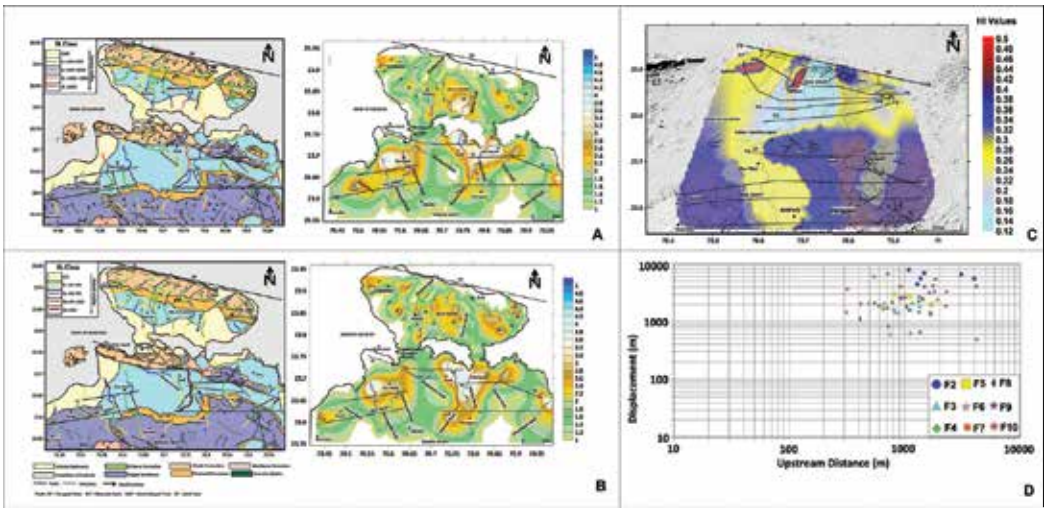

Figure 2. (A) Geological map of Wagad area shows especial distribution of SL along various geological units. Spatial distribution of SL class contour map of northern Wagad region. The higher activity is marked by higher order color (B) especial distribution of Ks along various geological units. Distribution of Ks class contour of northern Wagad region. Fault lines are shows by solid black line; dykes are marked by green lines; and bedding slope direction is highlighted by small black arrow. (C) Spatial variation of topography and statistics estimation for values of basin-wide hypsometric integral. The hotspots of higher uplift are marked by higher color values of hypsometric integral. (D) Relationship between amounts of stream offset along the fault and upstream length from the faults (F1–F10). *For generation of* **Figure 1A** and **B** *used Arc-GIS-10.4, Global mapper 18 software's and the final editing and contouring has been done in Surfer-11 software. We used River tool 3.0 for generation of hypsometric curves. The contour values of hypsometry Integral (HI) has been generated in Global mapper 18 and finally the contouring has been done in Surfer 14 software. We used excel for generation of* **D**.

The aftershocks of the January 26, 2001 Bhuj earthquake (Mw 7.7) are still continuing [15]. Distribution of the hypocenter of these aftershocks suggests that they are distributed mainly towards NE and SW directions. It has been observed that the WH is pronounced activated after the 2001 mainshock [12, 15, 27]. It is testified by a large number of aftershocks (Mw ≥ 2.5) occurred in the WH with focal depths ≥10 km. A few moderate earthquakes also occurred along the GF. Among these earthquakes, the most recent are the February 2006 (Mw 5.0); February 2006 (Mw 4.8); March 2006 Mw 5.7 and April 2008 Mw 4.1 [27] (**Figure 1B**). In the GF zone some 30 earthquakes (Mw 3.0–5.7) have been recorded at Seismic Network of Gujarat (SesisNetG) at shallow focal depths (≤ 20 km) during the period of 2006–2013 (**Figure 1B**).

3. Data and methodology

To investigate the relationship between brittle - ductile dynamics and surface processes in northern Wagad, we focused on topographic features (filtered topography, swath profiles, local relief), and hydrography (river longitudinal profiles), We used two elevation data sources: the CARTOSAT 2.5 m resolution digital elevation data (http://bhuvan.nrsc.gov.in) for regional scale analysis and the SRTM (http://srtm.csi.cgiar.org) of 90 m resolution for detailed analysis. Seismic tomography has been used to evaluate shallower to deeper surface dynamic

http://dx.doi.org/10.5772/intechopen.73653

process. The digital elevation model extracted from the SRTM was validated with the Survey of India topographic map (1:50,000) scale. To extract drainage network DEM data is used and 27 northward and south ward flowing rivers basins were generated. We calculated several tectonic attributes namely stream length-gradient Index (SL); steepness index (Ks), hypsometric integral (HI), asymmetric factor (AF) and Basin shape (BS). Based on results obtained from above analysis, spatial distributions of relative index of active tectonics (RIAT) are estimated for North Wagad/Bharudia, Gedi and Island fault zones. The dimensions of these drainage basins are given in **Table 1**.

3.1. Map of local relief

The map of local relief in the present study is produced from River-Tool by subtracting arithmetically a sub-envelope surface that describes the general pattern of valley bottoms elevations from an envelope surface (that connects peaks elevations) [28]. We obtained such surfaces by smoothing the minimum and maximum topography of the SRTM DEM by a 20 km wide circular moving window (**Figure 1C**). We chose the value of 20 km since it is the average spacing of the main valleys (5th, 6th and 7th Strahler order with respect to a critical area of ~4 km^2). This allowed us to remove small valleys, in effect operating like a low-pass filter that highlights the regional-scale features.

3.2. Swath profiles

We have considered five swath profiles across the study area to describe and quantify the topographic trend of the northern WH. The results show the trend of minimum, maximum and mean elevation into a single plot [29, 30] (**Figure 1D**). The statistical analyses such as maximum, minimum and mean elevations were calculated along each swath profile within a GIS platform. (**Figure 1D**). A rectangular swath of 300 m width was chosen to extract a series of parallel profiles that are separated by 1-cell (5 m). The width of the swath profile has been used to condense both elevated surfaces and streams. The higher elevation in swath depicts maximum elevation corresponds to the ridgelines; whereas, the lower elevation curve for the minimum elevation represents the valley floors. The Incision by river can be measured by the arithmetic difference between the maximum and minimum elevations within the longitudinal distance of the swath rectangle [31].

3.3. Stream length gradient index (SL)

The SL index is one of the quantitative geomorphic parameters included in morphotectonic assessment (Hack, [34]). This index will increase in value as rivers and streams flow over active uplifts and may have lesser values when flowing parallel to structures such as valleys made by strike-slip faulting [32]. The SL index seems to be a valid tool to detect local uplift as well as the incipient local response to regional processes [33]. Conventionally the SL index shows a quantitative approach to differential geomorphic studies related to erosion and depositional processes that include the river channel, long profile, and valley morphology as well as tectonically derived features such as fault scarps. This index was defined by [32] as:

Basins	Area (km²)	Area %	AF	BS	SL class	Ks class	HI class	AF class	BS class	RIAT value	RIAT class
1	30.759	2.05	7.70	3.4	2	2	2	2	4	2.4	3
2	8.962	0.60	1.90	3.2	1	1	4	1	4	2.2	2
3	49.538	3.31	14.21	3.4	2	2	2	2	4	2.4	3
4	22.855	1.53	16.59	5.3	1	2	2	3	5	2.6	3
5	49.991	3.34	12.06	4.8	1	2.5	1	2	5	2.3	3
6	17.051	1.14	5.12	3.9	2	2	3	2	4	2.6	3
7	20.658	1.38	15.41	5.4	2	2	2	3	5	2.8	4
8	7.733	0.52	13.51	3.6	1	1	4	1	4	2.2	3
9	56.53	3.77	3.60	3.5	2	2	1	1	4	2	3
10	52.989	3.54	8.07	2.8	2	2	1	2	3	2	3
11	40.325	2.69	1.48	3.6	1	1	2	1	4	1.8	1
12	20.395	1.36	8.76	1.5	1	2	3	2	2	2	2
13	11.269	0.75	5.24	3.2	2	2	3	2	4	2.6	3
14	13.33	0.89	14.92	6.2	2	2.5	2	2	5	2.7	4
15	16.705	1.12	35.33	1.6	1	1	2	4	2	2	2
16	9.342	0.62	20.88	3.4	1	2	1	3	4	2.2	3
17	5.188	0.35	4.82	3.7	1	3	2	1	4	2.2	3
18	53.91	3.60	25.82	2.3	1	2	3	4	3	2.6	3
19	134.73	8.99	10.92	1.6	2	1	3	1	2	1.8	1
20	48.422	3.23	13.31	9.4	2	2.5	3	1	5	2.7	6
21	209.47	13.98	8.26	1.9	2	2	2	2	2	2	2
22	71.57	4.78	15.51	3.7	2	2	3	1	4	2.4	3
23	151.26	10.10	3.18	3.9	3	3	3	1	4	2.8	5
24	129.46	8.64	14.02	4.9	3	2.4	4	2	5	3.28	5
25	96.119	6.42	4.32	2.5	2	2	3	1	3	2.2	2
26	64.618	4.31	31.38	1.9	1	2	4	1	2	2	2
27	104.85	7.00	2.10	1.5	2	2	4	1	2	2.2	3

Table 1. Spatial distribution of SL, HI, AF, Smf, SI, Bs, RSS, RIAT classes.

$$SL = (\Delta H/\Delta L)^{*} L \quad (1)$$

where $\Delta H/\Delta L$ is the local slope of the channel segment being evaluated, and L is the channel length from the divide to the midpoint of the channel reach. The SL index value increases as

streams flow over active uplifts and areas with high rock resistance and may decrease with low rock resistance. The integrated plot of stream longitudinal profile and SL index of all the rivers are presented graphically on the x- and y-axis of the longitudinal profile of the main channel (**Figure 3**).

3.4. Steepness index (Ks)

The normalized channel steepness index could be expected to vary with rock uplift rate (relative to base level), lithology, and climate [34, 35]. The method used for evolution of steepness index in the study area is based on the empirical power law equation of [36, 37] that relates the local slope (S) to the upstream contributing drainage basin area (A) [37, 38], However in present paper similar methodology has been:

$$S = k_s A^{-\Theta} \tag{2}$$

where k_s is the steepness index and Θ is concavity. Given Flint's law, the relationship between drainage area and distance downstream often described with Hack's law strongly influences the rate of change in channel gradient with distance downstream, which of course defines the concavity of river profiles. If there is no differential uplift, the value of Ks should remain constant. In the case of the river basin is undergoing differential uplift, Ks may change from one segment to another [38].

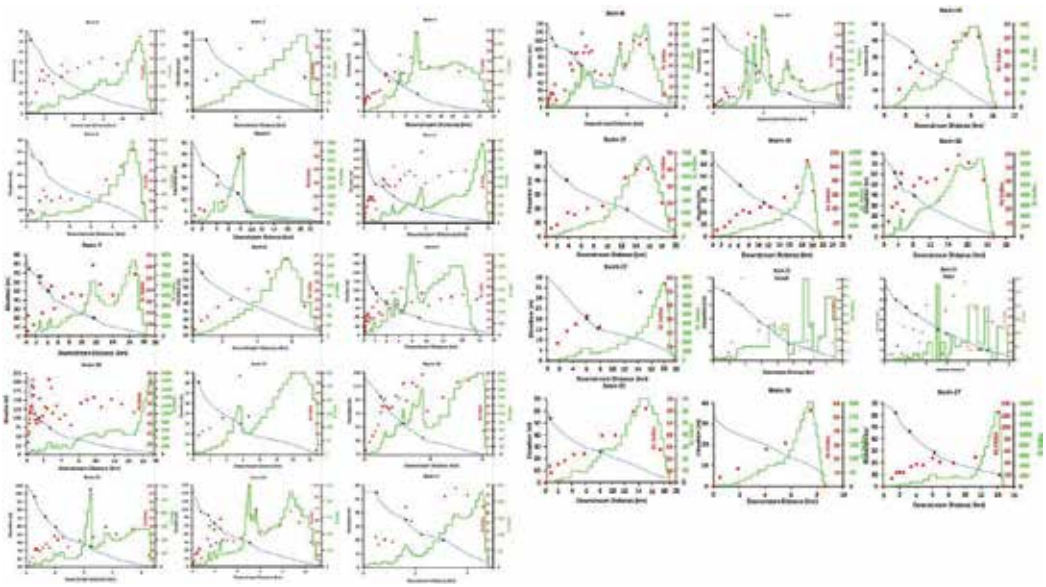

Figure 3. Integrated longitudinal river profiles and SL index of eight representative, rivers (Note: For details of all integrated river profiles, see **Figure 3**, SL is shown by small green line along the profile; solid thick red dots represents values of Ks along the long profile; knickpoints are marked by black star. *After collecting data in Arc GIS we used Microsoft excel for generating long river profiles and final editing has been done in golden software Surfer 14.*

3.5. Hypsometric integral (HI)

The hypsometric integral is an index that describes the distribution of elevation of a given area of a landscape [39]. The integral is generally derived for a particular drainage basin and is an index that is independent of basin area. The index is defined as the area below the hypsometric curve and thus expresses the volume of a basin that has not been eroded. The simple equation that may be used to calculate the index [32, 40] is:

$$HI = (average\ elevation - minimum\ elevation)/(maximum\ elevation - minimum\ elevation) \quad (3)$$

The hypsometric curve indicates degree of dissection of the basin, i.e., erosional stage of the basin. Concave profiles represent long-term equilibrium between uplift and erosion rates. Concave – convex profiles with erosion steps in the middle reaches indicate long-term predominance of erosional processes. Convex profiles are characteristic of areas where uplift (active tectonics) is dominant [41] The area below the hypsometric curve is known as the hypsometric integral (HI). The value of HI varies from 0 to 1 [41–43]. These profiles are drawn by projecting rivers onto a theoretical pre-incision surface that is obtained by interpolating the altitudes from present-day lateral divides of the basins (**Figure 4**). The values of elevation necessary for the calculation are obtained from a digital elevation mode.

3.6. Basin asymmetry (AF)

The asymmetric factor (AF) is a way to evaluate the existence of tectonic tilting at the scale of a drainage basin. The method may be applied over a relatively large area [32, 41] AF is defined by:

$$AF = 100\ (Ar/At) \quad (4)$$

where Ar is the area of the basin to the right (facing downstream) of the trunk stream and At is the total area of the drainage basin. If a basin has developed under stable conditions with little or no tilting, the Af factor is close to 50. The index is sensitive to change in inclination perpendicular to the channel direction. An AF factor above or below 50 may result from basin tilting, resulting either from active tectonics or lithologic, structural control, differential erosion. The AF value ranges from 18 to 85. The absolute difference (AF-50) has been calculated and the obtained values are grouped into four classes: class-1 ($AF \leq 5$; symmetric basins), class-2 ($6 \leq AF \leq 15$; gently asymmetric basins), class-3 ($16 \leq AF \leq 25$; moderately asymmetric basins), and class-4 ($AF \geq 26$; strongly asymmetric basins) (**Table 1**). The area of these drainage basins corresponding to asymmetric values is shown on the map (**Figure 5A**).

3.7. Basin shape (Bs)

The horizontal projection of a basin may be described by the basin shape index or the elongation ratio, Bs [43]:

$$Bs = Bl = Bw \quad (5)$$

http://dx.doi.org/10.5772/intechopen.73653

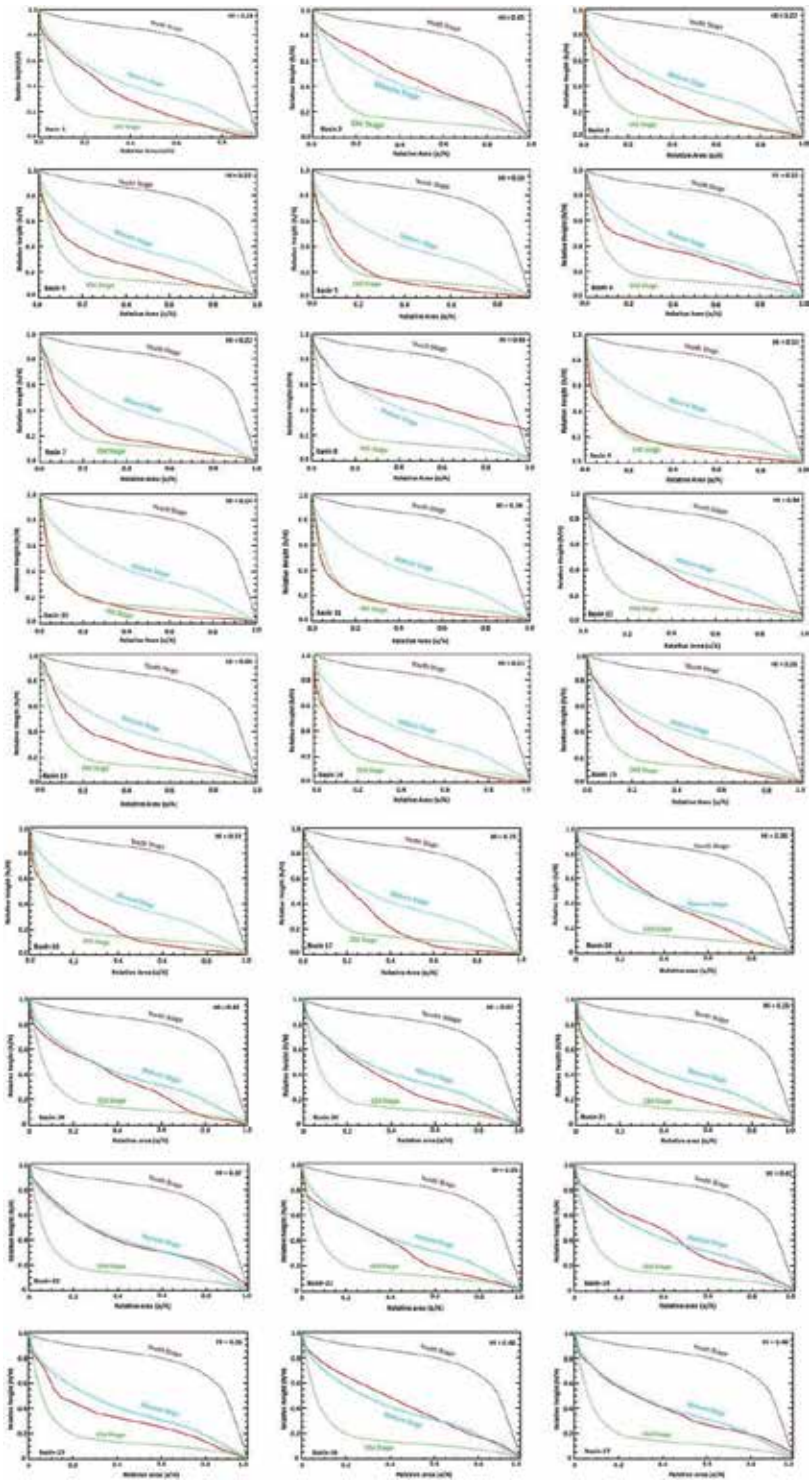

Figure 4. Hypsometry curves of all river basins integrated with youth (brown color), mature (cyan color), and old stages (green color) of river basin. *The hypsometric curves has been generated using River Tool 3.0 software and final editing has been done in golden software Surfer 14.*

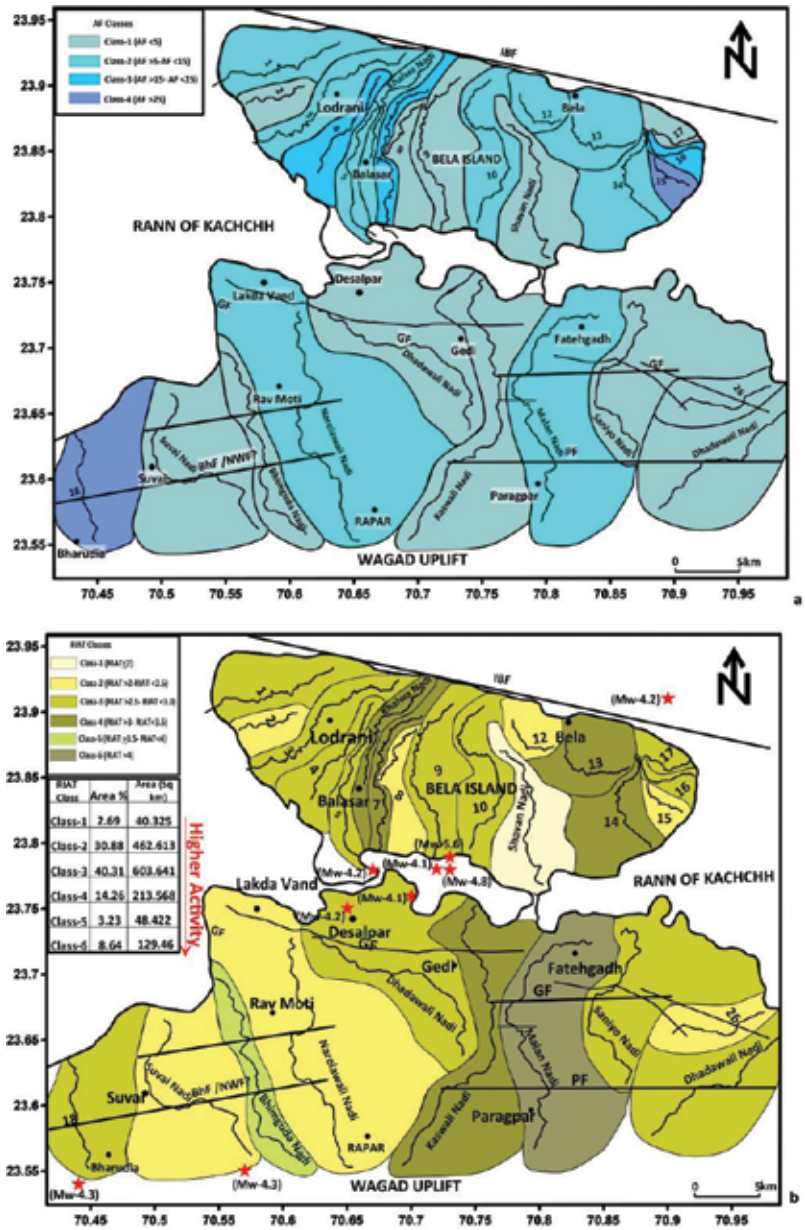

Figure 5. A spatial distribution of basin asymmetry along the northern Wagad area. (B) Estimated relative index of active tectonics (RIAT) distribution pattern of the area. A *and* B *have been generated using Global mapper 18 software and the final editing has been done in surfer 14 software.*

where *Bl* is the length of a basin measured from the highest point, and *Bw* is the width of a basin measured at its widest point. Relatively young drainage basins in tectonically active areas tend to be elongated in shape, normal to the topographic slope of a mountain [41, 43]. Therefore, *Bs* may reflect the rate of active tectonics.

http://dx.doi.org/10.5772/intechopen.73653

4. Relationship between fault displacements and drainage offset

Conventionally, quantitative displacement in a fault zone has been demonstrated by an offset of the river channel [25, 44, 45]. Usually, it has been widely observed that the maximum displacement occurred in the central part of the fault zone [46] and that the displacement decreases with increasing length. Decrease of river offset towards the west is possibly, westward propagation of the faults. These streams were taken into account to calculate offset ratio:

$$a = D/L \tag{6}$$

where D is the amount of stream offset along fault and L is upstream length of the displaced stream [47]. A relationship between long-term slip rate (S) along the lateral slip of a fault and offset ratio ($a = D/L$) has been roughly calculated as S (m/1000 years), *i.e.,* 10 a [25, 44, 45].

We investigated the major to north flowing rivers such as the Suvai, Bhimguda, Narelawali, Dhadawali, Karaswali, Malan, Baniyo, and Dabhodanwari rivers and adjoining streams to estimate river offset along the E-W faults F1–F4 (GF). However, 17 south flowing rivers such as 1–8, Khalwa River (9), 10, 11, Sharan Nadi (12), and rivers 13–17 have been analyzed to estimate offset along faults F6–F8. Based on offset of river channel we estimated net displacement along F2–F10 respectively.

5. Relative index of active tectonics (RIAT)

Several remote sensing studies have used the geomorphic indices to obtain index of relative tectonic activity [48–50]. To understand the RIAT of the fault segments, the results of all calculated geomorphic indices were synthesized. In this study we used geomorphic indices of active tectonics to obtained RIAT for the (NWF) North Wagad Fault, (GF) Gedi Fault, Bharudia Fault and (IBF) Island Belt Fault. Based on these classes we have considered each basin class average and combined to obtain the RIAT. The values of RIAT is assigned into five classes as Class- VI (RIAT >4), Class V: (> 3.5 RIAT <4), Class IV: (>3 RIAT <3.5), Class III: (>2.5 RIAT <3), Class II (>2 RIAT <2.5), and Class I (RIAT <2), (Supplementary Table 1; **Figure 5B**). Depending on the relative index of active tectonics classes, Western part of Wagad uplift covering basin 11, and Easterly covering 15 and 16 comes in highly active zone and shows offsetting drainage pattern (Class 5). Basin 1, 3, 4, 7 and 10 in Bela island, basin 13 and 18 in Wagad uplift are tectonically active and comes in (Class 4) zone and also delimiting by transverse fault between Basin 5, 6 and 9 in Bela Island 12, 14 and 17 in Wagad uplift are moderately active zones (Class 3) (**Figure 5B**). Basin 2 is intermediately active and comes in (Class 4) and Basin 8 is low active region.

6. Seismological approaches

The evidences of geomorphological in the Kachchh Rift Basin (KRB) is also supported by available high resolution seismic structures, fault plane solutions and recorded seismicity at

SeisNetG [13, 15, 51]. Theses integrated approaches provide a clue to understand what instigate to generating a negative flower structure of drainage patterns and its role in the seismicity in the regions. The snapshot of the seismic images play important role to understand brittle-ductile dynamics. It also shed light about hidden causative faults and the drainage patterns that can dictate the degree of damage through shaking (**Figure 1B**). Several faults in the Kachchh areas are mapped on the surface but still there are many among the existing factory of faults which still remains undiagnosed and not mapped on the surface [15, 51]. That is why we have determined almost all geological evidences and crustal heterogeneities parameters in the present study to understand the nature and extent of underlain structures controlling drainage network. The available 16 fault-plane solutions of the inferred fault planes of the events (Mw ≥ 3.5) recorded during 2007–2014 [13, 15, 51] (**Figure 1B**). The results obtained from morphotectonic analysis of fluvial networks and seismological approaches are jointly analyzed in the next section.

7. Imprints of active tectonics

The rivers in WH containing the knickpoints over the Mesozoic formations; are related to active geological structures. The maps of local relief, swath, stream length gradient index, and channel steepness (**Figures 1D** and **2**) represents two major topographic zones. The high elevated zones are located between 28 and 228 m. The high relief locations represent remnants of a relict landscape that was preserved at high elevations caused by erosionally balanced rapid Late Quaternary uplift [23]. The low relief zones are marked by Banni and Rann surfaces (**Figure 1C**). The DEM generated swath profiles shows incision into the alluvial surfaces. This incision is associated with multiple phases of tectonic events and intensified climate forcing during early to mid-Holocene [23]. The sedimentation in lower reaches of river valleys is predominantly controlled by processes that act in response to tectonically triggered and climatically enhanced events [23]. The uplift involve the Bela and WH that shows abrupt and anomalous variation in elevation as noticed in the swath profiles (**Figure 1D**). The swath profiles shows maximum elevation correspond to uplifted region and low elevation correspond to valley floor. The swath analysis of each profile shows asymmetrical nature of valley shape. The results of the SL index are shown in **Figure 2A**. Integrated longitudinal river profiles with SL and Ks longitudinal profiles of all rivers are illustrated in **Figure 3**. The SL values range from 5 to 2300 which are grouped into five classes: class-1 (low activity: 5 ≤ SL ≤ 100), class-2 (intermediate activity: 101 ≤ SL ≤500), class-3 (moderate activity: 501 ≤ SL ≤ 1000), class-4 (active: 1001 ≤ SL ≤ 1500), class-5 (very active: SL ≥ 1501) (**Figure 2A**). The high and moderate classes of the SL values correspond to significant faults except for the Bela zone, may be caused by the high rock resistance prevailed in that area. The *Ks* and Θ were estimated from the log–log plot of *S* vs. *A*. The Ks values range from 5 to 125. To evaluate segmental tectonic activity; these values were also grouped into five classes: class-1 (low activity: 5 ≤ Ks ≤ 25), class-2 (intermediate activity: 26 ≤ K_S ≤ 50), class-3 (moderate activity: 51 ≤ K_S ≤ 75), class-4 (active: 76 ≤ Ks ≤ 100), and class-5 (very active: Ks >101) (**Table 1**; **Figure 2B**). It is observed that the Ks values are high close to the E-W faults.

Equation	References	Fault	(SRL km)	(RLD km)	Average RLD	Coefficient		MD (km)	AD (km)	Offset ratio (m)	Magnitude (M)	Slip rate (mm/y)
						A	B					
M = A + B * log (SRL)	[55]	F1	56	21	21	5.16	1.22				6.3-6.3-7.3	—
M = A + B * log (RA)		F2	55.6	26	5.2	3.98	1.02	3.9	1.1	0.34	5.4-6.4-7.3	3.4
M = A + B * log (MD)		F3	55.8	42.8	16.6	6.81	0.78	0.49	1.3	0.11	6.1-6.7-7.3	1.1
M = A + B*log (RLD)		F4	55.6	40.6	40.6	4.33	1.49	0.63	4.3	0.14	6.7-6.7-7.3	1.4
		F5	15.2	38.6	38.6			0.8	1.8	0.09	6.7-6.6-6.6	0.9
		F6	56.7	43.8	37.6			0.79	3.1	0.07	6.7-6.7-7.3	0.71
		F7	50	38.6	38.6			0.3	0.9	0.08	6.7-6.7-7.2	0.84
		F8	54.13	48	17.2			0.4	1	0.06	6.2-6.8-7.2	0.67
Mw = 1.36*log SRL+ 4.67	Johnston [56]	F9	21.17	19	7.2	1.36	4.67	0.8	0.9	0.14	5.6-6.2-6.7	1.4
		F10	34	33	6.6			0.3	2.2	0.31	5.6-6.5-7.0	3.1

Surface rupture length (SRL).
Sub-surface rupture length (RLD).
Standard deviation (s).
Maximum displacement (MD).
Average displacement (AD).
Moment magnitude (M).

Table 2. Regression analysis of surface rupture, subsurface rupture length, and displacement.

Conventionally the hypsometric integrals reveal complex interactions between erosion and tectonics [39, 52, 53]. Hypsometric integrals are thought to be affected by basin parameters such as geometry, area and rapid lowering of basin elevations [53, 54]. The hypsometric integral of each basin has been computed based on drainage area and basin geometry. Hypsometric integrals are thought to be affected by basin parameters such as geometry, area and rapid lowering of basin elevations [53, 54]. The HI of each basin has been computed based on drainage area and basin geometry. However, we deployed conventional statistical technique for the entire basin as well as the computation is implemented to individual squire where high and low values can be obtained together. The contour map shows spatial distribution of high and low values, imply that the WH experiencing rapid changes in elevation and incision; owing to tectonic and climatic variations [23]. The higher values of HI clustered around the uplifted regions however the lower values representing low lying areas (**Figure 2C**). In the analysis of HI, it is considered whether the curve is convex in its upper portion, convex to concave, or convex in the lower portion. The HI curves of all basins are given in **Figure 4**. It is assumed that if part of the hypsometric integral is convex in the lower portion, it could be associated with uplift along a fault or associated with recent folding.

In present study 10 north flowing and 17 south flowing rivers of WH were analyzed in order to estimate river offset and tectonic control by the faults that cut across the area (**Figure 2A, B**). The estimated values of offset along F2 ranges between 1.1 and 3.9 km, along F3, 0.49–1.3 km, along F4 0.63–4.3 km, along F5 0.8–1.8 km, along F6 0.79–3.1 km, along F7 0.3–0.9 km, along F8 0.4–1 km, along F9 0.8–0.9 km, and along 10 the offset ranges between 0.3 and 2.2 km respectively (**Figure 2D**). The stream offset along the F2–10 is comparatively less westward. However, the computed values of offset ratio of about 0.34 km for F2, 0.11 km for F3, 0.14 km for F4, 0.09 km for F5, 0.07 km for F6, 0.08 km for F7, 0.06 km for F8, 0.14 km for F9 and 0.31 km for F10 respectively (**Table 2**).

8. Geomorphic evidences controlling fluvial network

We identified various geomorphic features associated with active movement along F1 such as block tilting, fault scarps, co-seismic uplift and drainage offset, are well characterized by [57]. At a place the Mesozoic sandstone ridded over Quaternary deposits, resulted ~2 m high active fault scarp (**Figure 6A–E**). The Mesozoic strata are tilted by 8° southward. We identified secondary surface deformation ~10 km along the strike of the F2 (**Figure 6A**). The co-seismic movement has developed tensional fractures along the strike of F2 (**Figure 6D–E**). The north dipping tensional fractures near F2 reflect "en echelon" pattern having step-overs with strike-slip component; probably developed during the northward movement of the hanging wall followed by surface bending (**Figure 6D** and **E**) [23].

Further Kothyari et al. [23] documented remarkable geomorphic features such as (a) E-W trending fault across gently folded Mesozoic strata, (b) steeply dipping strata with south facing active fault scarp at Deshalpar, (c) wide tensional in E-W direction, (d) highly fractured and sheared litho-units within faulted blocks, (e) subsidence of ground, and drainage offset

http://dx.doi.org/10.5772/intechopen.73653

along the structures (**Figure 6F**). The tectonic movement in this region resulted changes in surface elevation by forming approximately 9 m high fault scarp (**Figure 6G**). A significant gradient change in the valley floor causes development of 3 m high knickpoint (**Figure 6H**). The litho-units are tightly folded within the fault zone. The southern limb of the fold is steeply (~75°) dipping towards south. These steeply dipping beds are characterized by presence of slickensides parallel to the strike direction (E-W) of the F5 (**Figure 6I**). Kothyari et al. [23] believe that these features are results of middle to late Holocene tectonic reactivation of GF. Furthermore, the significant amount of changes have been observed within the hydrological network between 8 to 4 ka [23]. The north flowing Karaswali River takes 90° turn and flows in west direction, parallel to GF (F4). East–west offsetting of the two rivers is also observed south of the Gedi village (**Figure 6F**).

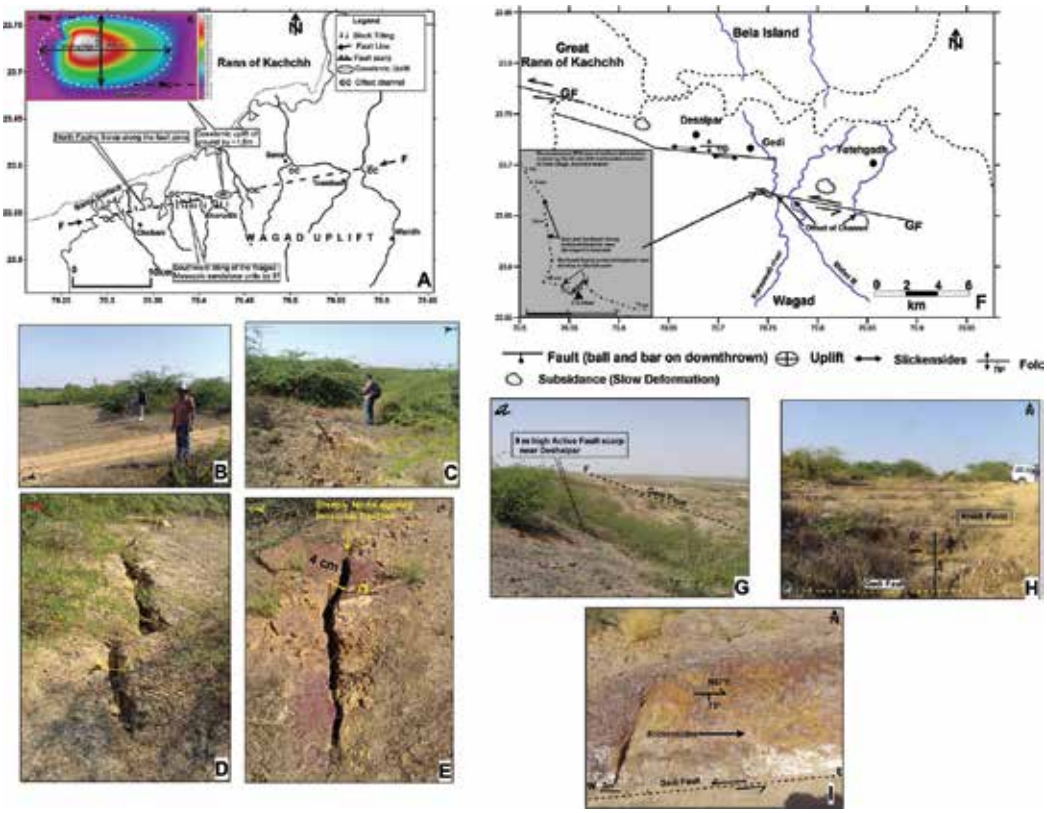

Figure 6. (A) Detailed map showing major tectonic features observed in the F2 zone (inset; DEM of growing ridge showing ground uplift (~1.5 m) near the fault zone (modified after [57]); (B and C) fault scarp; (D and E) development of E-W oriented tensional cracks within the fault zone. These tensional cracks are displaced by small scale strike slip faults. (F) Map shows locations of ground deformation observed along the trace of F4. Inset shows development of tensional fractures within the tertiary sandstone bed (modified after [23]); (G) development of ~9 m high fault scarp near Deshalpar, (H) lateral spreading of ground east of Deshalpar, and 3 m waterfall was developed along the F3, (I) well developed slickensides are visible parallel to strike of F4. *The drainage map of* **A** and **F** *are generated using georeference SOI topographic map in Global mapper 18 software and for final editing we used Surfer 14 software. The inset DEM of the area has been generated with the help of reconnaissance Real Time Kinematic (RTK) survey. The DEM has been generated in Surfer Software.*

9. Seismic tomography and fault plane solutions

The estimated velocity images and fault-plane solutions are shed new light in understanding the fluvial network and geomorphic development in the intraplate region of Western India [15]. The epicenters of the relocated earthquakes show that the majority of the events are confined along F1–F4 (**Figure 1B**) during the recorded period. It is also noticed that some of small to moderate events are located north of F4 and north of F1 (**Figure 1B**). Interestingly, epicenters of small to moderate earthquakes are associated with the offset zone of fluvial network. Theses fluvial network are plotted over seismic tomography images at 5.0 km, 10.0 km, 15.0 km, 20.0 km, 25.0 km, and 30.0 km depths to understand brittle - ductile dynamics (**Figure 7A**). Based on significant perturbations in Vp anomalies, several shallow and deep fault controlling surface fluvial network are identified. Conventionally the low velocity of Vp anomalies at shallower to deeper depths represents presence of fluid, unconsolidated rocks fault gauge, cracks and fractured basement [15, 51, 58, 59]. Based on surface fluvial offset and velocity perturbation in depth sections of tomography data, the slow velocity is interpreted as a subsurface fracture pattern or strong heterogeneities. The high velocity zones at deeper depth are associated with the surface offset of drainage network [15].

The depth slices of tomography images are critically examined to identify subsurface fault pattern (**Figure 7A**). Both combined seismological and geological results clearly show that the zone between Bharudia/NWF and IBF is controlled by eight (F1–F8) E-W oriented parallel faults. Seismic tomograms at depths 5–15 km shows NW-SE and NE-SE oriented transverse faults. The Fault F4 is a vertical fault, which is well defined by velocity perturbations sections down to the depth of 30 km depth. Faults F1, F2, F3, F5, and F6 are connected with the F4 at 25 km deeper level (**Figure 7A**, **B**). However, the fault F7 is connected with F5 at 15 km depth, whereas the F8 joints with F7 down to the depth of 10 km. **Figure 7B** represents inferred depth geometric relationship of all these faults. Geometrically all these faults are converge at depth along a single sub-vertical fault (F4), making an E-W oriented negative flower structure, where all branches of faults are interacting at different depth resulting rhomb shape graben structure (**Figure 7B**). From the experimental model of [60] it is clear that the strike–slip fault zone is generally composed of several branches that join together at depth into a single vertical plane. As a consequence, bulk displacement accommodated at depth on the basement fault is distributed towards the surface among several faults whose tectonic activity evolves through time. Some branches remain inactive during a certain period, and then they are reactivated later when their geometry becomes compatible again with the evolving strain field in the wrench zone [60]. The model shows that the local relief apparently has a clear influence on subsurface fault geometries (**Figure 7A**). In the regions of low topography or where strong river incision traverses the wrench zone, a narrow releasing bend generally develops when the fault trace is deviated towards topographic lows. In regions of higher relief, compression is often associated with shearing, and the fault zone appears much more deformed and segmented [60]. From the earthquake fault plane solution data, it is clear that all these faults are strike slip pattern in nature (**Figures 1B, 6** and **7A**). However, a few solutions show thrust motions may be due to local tectonic adjustment between segmented fault blocks.

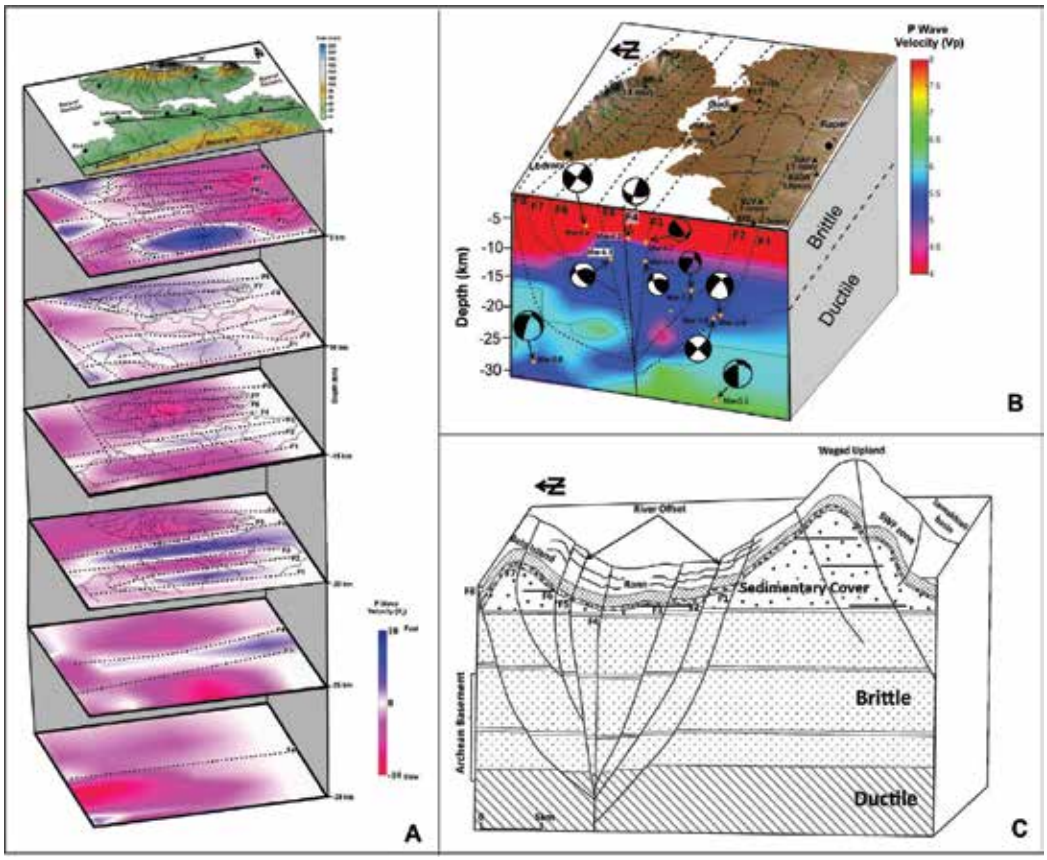

Figure 7. (A) Stack map shows horizontal depth slices of P-wave seismic structures [51] at 5, 10, 15, 20, 25, and 30 km. The topographic surface level is highlighted by digital elevation model of the area. The fault lines F1 to F10 are marked based on offset of river along the wave velocity transition phase and highlighted by black dotted lines. (B) Dimensional block model of northern Wagad areas shows development of negative flower structure at deeper level as inferred from seismic structures. The position of faults on the top surface is marked by stream offset pattern. The depth behavior of fault is shown by fault plane solutions of [12–15]. Locations on the surface are marked by black filled circles; solid fill triangles represent location of GPS stations. (C) Schematic block model of Wagad region based on geological and seismological data shows development of negative flower structure towards the northern part of the area. The streams crossing these faults show prominent offset on the surface. *The, horizontal depth slices in* **Figure 1A** *are generated using MATLAB R2010 software and depth wise stack map of horizontal slices has been generated using Surfer-14 software. The P wave velocity slice* (**B**) *has been generated in MATLAB R2010 and the final editing has been done in Surfer software. For generation of* **C** *we used CARTOSAT satellite data to generate N-S topographic profile and final map has been generated using Surfer-14 software.*

10. Combined interpretation and discussion

Globally, the rift basins are controlled by extensional tectonic forces. Changes of stress regime may cause inversion of such system from normal strike slip and reverse Coward [61], Scisciani [62] or by development of new faults between the basement rocks and overlying sedimentary succession [62, 63]. The wrench zone of a strike slip fault system shows complex arrays of structures in brittle upper crust in which fault splays are oblique to the principal fault trend

and generate a wide deformation zone [60, 64, 65]. The depth section of such faults tend to be steep at deeper level and to splay upwards, forming characteristic flower structures; have reverse (positive flower) or normal (negative flower) components [66, 67]. In such tectonic environment the shape of fault pattern is influenced by degradation and aggradation surface processes [68]. Conventionally in a negative flower zone the faults splays become listric as a result of synchronous deformation and sedimentation [69]. However, in a positive flower setting, faults tend to become steeper towards the surface as a result of aggradation in the footwall and degradation in the hanging wall [70–75].

A wide zone of fault rupture pattern is investigated in WH of Kachchh peninsula. The seismic structures, seismicity and fault plane solution investigation show that the GF (F4) is a nearly vertical fault (**Figure 7B**, **C**) having dominant strike-slip deformation [15, 18, 51]. Using double difference tomography, we identified several shallower and deeper faults (F1–10); these faults are well connected with sub-vertical south dipping GF (F4) at different level (**Figure 7B** and **C**). Geometrical relationship inferred from seismic structures show all these faults are converge at certain depth along GF and making E-W oriented negative flower structure. All fault branches are interacting at different depth level and generating rhomb shape graben structure, which is well imaged in the seismic structures (**Figure 7B** and **C**). Depth section of tomography suggested that the faults F1, F2, F3, F5 and F8 are deeper faults. However, the F6 and F7 are imaged at shallower depth. It is also clear from the seismic structures that the fault F1 is a north dipping fault plane and connected with the F4 at 27 km depth level. The north dipping faults F2 and F3 and the south dipping faults F5 and F8 are connected with F4 at 25 km depth level. On the other hand the fault F6 is a southward dipping splay of F5 and connected with F5 at 15 km depth. The F7 is a small south dipping subsidiary branch of F6. The fault is connected with F6 at 12 km depth.

Conventionally, an extensional overstep zone of a strike–slip fault several branches that join together at depth into a single vertical plane [18]. As a consequence, bulk displacement accommodated at depth on the basement fault is distributed towards the surface among several faults whose tectonic activity evolves through time [60]. Some branches remain inactive during a certain period, and then they are reactivated later when their geometry becomes compatible again with the evolving strain field in the wrench zone [60]. A few researchers argued that KRB regions show dominantly strike-slip with the slightly reverse faulting natures [13, 51, 76]. However, a few solution shows reverse type of motion could be associated with the local tectonic adjustment between segmented fault blocks.

The archeological records from the WH experience several damaging earthquakes of magnitude 6.0–7.8; that have occurred between 2900 BC and 1300 BC (**Table 3**). The archeological evidences observed from 40 km west of study area (e.g. Dholavira) suggested that the ancient town was damaged by several major earthquakes between 2900BC and 1300BC [63, 77–79]. Presence of geomorphic and paleoseismic features within the WH, studied by previous workers are correlated with these historical earthquakes [23, 25, 63]. Further, based on trench investigation and optical chronology identified three earthquake events during last 7000 years [63]. The displaced fluvial sediment and optical chronology in the area suggested that the SWF reactivated during Middle to Late Holocene period i.e., between 3 ka and 1 ka [25]. Similarly other geomorphic studies suggest that the F4 reactivated during Middle Holocene around 4 ka [23].

In-SAR measurements show current deformation rate as ~16 mm/y in the western part and 7–16 mm/y in the southern part of the GF zone [14, 23, 80]. Based on trench investigation [63] estimated uplift rate of 0.5 ± 0.05 mm/y, horizontal shortening rate of 1.1 ± 0.12 mm/y along SWF. However based of fluvial offset [25] estimated slip rate 2.2 mm/y along the SWF zone which is compatible with the slip rate 1.19 ± 0.13 mm/y observed by [63]. Based on strath terraces [23] estimated the uplift rates 0.3 to 1.1 mm/y along F4, during the last 9 ka. Further, based on fluvial offset, we estimated slip rates for faults (F2–F10) using the imperial relationship given by [45]. The estimated slip rate along F2 of about 3.4 mm/y, along F3 of about 1.1 mm/y, along F4 of about 1.4 mm/y. along F5 of about 0.9 mm/y, along F6 of about 0.71 mm/y, along F7 of about 0.84 mm/y, along F8 of about 0.67 mm/y, along F9 of about 1.4 mm/y, and along F10 of about 3.1 mm/y (**Table 2**). The observed slip rate of F2–F10 are well corroborated with the uplift rate 0.3 to1.1 mm/y during the last 9 ka as estimated from the OSL dates. The slip rates obtained from drainage analysis are well correlated with the published results of GPS from the WH (ISR technical report by [81]. Four sites located in the southern part of study area shows variations in localized deformation (**Figure 7B**). The site Ekal shows deformation rate 2.5 ± 0.12 mm/y, Suvai is deforming at the rate of 1.9 ± 0.03 mm/yr., Badargadh is deformation at the rate of 1.8 ± 0.13 mm/y, and the site located near Rapar shows deformation rate of 2.1 ± 0.11 mm/y [81]. To sites Deshalpar and Fatehgadh shows deformation rates of 1.0 ± 0.04 mm/y and 1.7 ± 0.04 mm/y (**Figure 7B**). However, a site located in the northern part of study area shows crustal deformation rate 3.8 ± 0.14 mm/y [81]. The estimated slip rates and GPS driven deformation rates together suggests that the landform development in the area is controlled by localized crustal deformation.

The future earthquake along active faults can be evaluated from estimates of fault rupture parameter in turn, released to earthquake magnitude [55]. Active fault studies require an assessment of seismic hazard analysis for the future potential earthquakes [55]. More specifically to estimate the size of earthquake that might be generated by a particular fault may be correlated with rupture parameter such as length, strike and displacement [55, 82, 83]. Moreover, the timing of the past earthquake and size of magnitude can be estimated with the help of geomorphic and paleoseismic records [84, 85]. We used regression analysis proposed by Wells and Coppersmith [55] and by Johnston [56] and Johnston and Kanter [86] for intraplate region to estimate moment magnitude. The detail regression analysis is expressed

S. No	Year	Remarks	References
1	2900BC	Damage in Dholavira, dislocation of walls, subsidence of floors and crushed bricks	[77]
2	2700BC	Damage in Dholavira, 4 m wide fissured wall, collapse of southern features and multiple cracks running E-W	[78]
3	2100BC	Damage in Dholavira; tremendous damage to the gates of castle, tilting and arching of thick inner walls and collapse of outer walls at north gate	[79]
4	2000BC		
6	1900BC	Abandonment of settlements	[63]
7	1300BC		

Table 3. List of historic earthquakes occurred in Kachchh region of western India.

in **Table 2**. The regression analysis proposed by Wells and Coppersmith [55] and Johnston [56] shows strong correlation between surface rupture length and magnitude of earthquakes. However the regression analysis shows that probability of occurrence of earthquake magnitude range between 6.3 and 7.3) along F1, magnitude (M 5.4–M 7.3) along F2, magnitude (M 6.1–M 7.3) along F3, magnitude (M 6.7–M 7.3) along F4, magnitude (M 6.0–M 6.6) along F5, magnitude (M 6.7–M 7.3) along F6, magnitude (M 6.7–M 7.2) along F7, magnitude (M 6.2–M 7.2) along F8, magnitude (M 5.6- M 6.7) along F9, magnitude (M 5.6–M 7.0) along F10 respectively (**Table 2**). From the regression analysis it is clear that the faults (F1–F10) passes through the WH are capable for generating earthquake magnitude M 5.4 and M 7.3. Occurrence of February 2006M-5.6 along F9 validates our results and significant level.

Geomorphic indices are widely used to obtain index of active tectonics [25, 48–50]. Here we synthesized conventional geomorphic indices of active tectonics to calculate relative index of active tectonic (RIAT) distribution along the all fault segments (F1–F10). The RIAT classes show that the deformation is higher along the offset zone of fault segment (**Figure 5B**). Conventionally the SL and KS values show abnormal increase of gradient within normal and reverse faults. Minor changes of SL and KS observed within the zone of strike slip fault. At few places the SL and KS values do not shows any variation, which is compared with the strike slip motion of fault. The strike slip motion is well corroborated with the results of seismic tomography and fault plane solution (**Figure 7B**). The existing studies suggest that the terrain close to the GF (F4) experienced occurrence of moderate earthquakes during recent time [23, 27]. The strike slip motion observed from focal mechanism is well correlated with drainage offset along E-W oriented faults within the north and south flowing river system.

Further the observations gathered from the SL, KS and RIAT distribution are corroborated with the geomorphological studies carried out by [23]. The geomorphic expressions such as active fault scarp, shifting and offset of channels indicates that the area is controlled by E-W oriented strike slip faults. Further, steepening of river gradient as observed from tectonic proxy (SL and KS) and uplift of ground further support that the area is tectonically active. Previous studies by [23] suggests that the uplifts in GF zone were associated with interlinking of strike slip fault segments. Further major two phase of tectonic uplift have been identified by [23] based on uplifted fluvial strath terraces. The study shows that the first phase of enhanced uplift took place round 8.0 ± 0.9 ka; however, the second phase of uplift is began after 4 ka and continued till today [23]. In present study, several E-W oriented knickpoints were identified across north and south flowing drainage basins of WH. At several locations these knick points have migrated primarily due to river response to sudden base level fall and secondly incision owing to vertical tectonic forces. As sudden base-level fall can be triggered by tectonic upheaval, climatic change, river capture, or channel incision [87–89]. The incision by river and the formation of knickpoints are well correlated with tectonic upheaval along F1–F8 (**Figure 2A**).

11. Conclusions

The study of the topographic configuration morphometric analysis and the subsurface imaging of the fluvial network from WH permitted us to develop a model for the long-term

evolution of the drainage basin which is influence by deep tectonic processes. Based on present observations the following conclusions have been drawn.

1. Based on analysis of fluvial offset and subsurface velocity images major 10 traces of active fault (F1–F10) controlling hydraulic network have been identified.
2. The surface geomorphology, velocity imaging and fault plane solution data together suggest that the subsurface structure of WH is controlled by strike slip faulting.
3. The fault geometry inferred from seismic images show presence of negative flower structure at a deeper level.
4. The depth wise images show that the GF (F4) is steeply dipping towards south. The fault F1, F2 and F3 are dipping towards north, whereas, the fault F5–F8 are dipping towards south. All these faults are connected with GF (F4) at different depth level, which is well imaged in the seismic structures.

Acknowledgements

The authors are thankful to Ministry of Earth Science, Government of India (MoES/P.O.(Seismo)/1(270)/AFM/2015) for financial support under the active fault mapping program. We are thankful to Dr. M. Ravikumar, Director General and Dr. Sumer Chopra, Director, Institute of Seismological Research, Gandhinagar for fruitful discussion.

Conflict of interest

There is no conflict of interest between all co-authors.

Author's contribution

All the authors have made equal contribution in this manuscript.

Author details

Girish Ch Kothyari*, Ajay P. Singh, Sneha Mishra, Raj Sunil Kandregula, Indu Chaudhary and Gaurav Chauhan

*Address all correspondence to: kothyarigirish_k@rediffmail.com

Institute of Seismological Research, Gandhinagar, Gujarat, India

References

[1] Sembroni A, Molin P, Pazzaglia FJ, Faccenna C, Abebe B. Evolution of continental-scale drainage in response to mantle dynamics and surface processes: An example from the Ethiopian highlands. Geomorphology. 2016;**261**:12-29

[2] Pazzaglia FJ, Gardner TW, Merritts DJ. Bedrock fluvial incision and longitudinal profile development over geologic time scales determined by fluvial terraces. In: Wohl E, Tinkler K, editors. River over Rock: Fluvial Processes in Bedrock Channels American Geophysical Union Geophysical Monograph 107. Washington, DC: American Geophysical Union; 1998. pp. 207-235

[3] Scotti VN, Molin P, Faccenna C, Soligo M, Casas-Sainz A. The influence of surface and tectonic processes on landscape evolution of the Iberian chain (Spain): Quantitative geomorphological analysis and geochronology. Geomorphology. 2014. DOI: 10.1016/j.geomorph.2013.09.017

[4] Tomkin JH, Brandon MT, Pazzaglia FJ, Barbour JR, Willett SD. Quantitative testing of bedrock incision models, Clearwater River, NW Washington state. Journal of Geophysical Research. 2003;**108**(B6). DOI: 10.1029/2001JB000862

[5] Wegmann KW, Zurek BD, Regalla CA, Bilardello D, Wollenberg JL, Kopczynski SE, Ziemann JM, Haight SL, Apgar JD, Zhao C, Pazzaglia FJ. Position of the Snake River watershed divide as an indicator of geodynamic processes in the greater Yellowstone region, western North America. Geosphere. 2007;**3**(4):272-281

[6] Wegmann KW, Pazzaglia FJ. Holocene strath terraces, climate change, and active tectonics: The Clearwater River basin, Olympic peninsula, Washington state. Geological Society of America Bulletin. 2002;**114**:731-744

[7] Wells SG, Bullard TF, Menges CM, Drake PG, Karas PA, Kelson KI, Ritter JB, Wesling JR. Regional variations in tectonic geomorphology along a segmented convergent plate boundary, Pacific coast of Costa Rica. Geomorphology. 1988;**1**:239-265

[8] Wobus C, Whipple KX, Kirby E, Snyder N, Johnson J, Spyropolou K, Crosby B, Sheehan D. Tectonics from topography: Procedures, promise, and pitfalls. In: Willett SD et al., editors. Tectonics, Climate, and Landscape Evolution. Geol. Soc. Am. Vol. 398. 2013. pp. 55-74

[9] Molin P, Fubelli G, Nocentini M, Sperini S, Ignat P, Grecu F, Dramis F. Interaction of mantle dynamics, crustal tectonics and surface processes in the topography of the Romanian Carpathians: A geomorphological approach. Global and Planetary Change. 2012. DOI: 10.1016/j.gloplacha.2011.05.005

[10] Biswas SK. A review of structure and tectonics of Kutch basin, western India with special reference to earthquakes. Current Science. 2005;**88**(10):1592-1600

[11] Biswas SK, Deshpande SV. Geologic and tectonic maps of Kachchh. Bull ONGC. 1973;**7**: 115-116

[12] Mandal P, Chadha RK, Raju IP, Kumar N, Satyamurty C, Narsaiah R. Are the 7th march 2006 Mw 5.6 event and the 3rd February 2006 Mw 4-5.8 event triggered by the five years continued occurrence of aftershocks of the 2001 Mw 7.7 Bhuj event. Current Science. 2007;**92**:1114-1124

[13] Rao CN, Rao PC, Rastogi BK. Evidence for right–lateral strike-slip environment in the Kutch basin of northwestern India from moment tensor inversion studies. Journal of Asian Earth Sciences. 2014;**64**:158-167

[14] Rastogi BK, Mandal P, Biswas SK. Seismogenesis of earthquakes occurring in ancient rift basin of Kachchh, western India. In: Talwani P, editor. Intraplate Earthquakes. Cambridge; 2014. pp. 126-161

[15] Singh AP, Dorbath C, Kumar MR, Kumar S, Chaudhary I, Kayal JR. Fault geometry of the M 7.7 western India Intraplate earthquake: Constrained from double-difference tomography and fault-plane solutions. Bulletin of the Seismological Society of America. 2016a. DOI: 10.1785/0120150280

[16] Biswas SK. Regional tectonic framework, structure and evolution of the western margin basins of India. Tectonophysics. 1987;**135**:307-327

[17] Biswas SK. Tectonic framework, structure and tectonic evolution of Kutch Basin, western India. Special publication of the Geological Society of India. 2016;(6):129-150

[18] Kothyari GC, Dumka RK, Singh AP, Chauhan G, Thakkar MG, Biswas SK. Tectonic evolution and stress pattern of south Wagad fault at the Kachchh Rift Basin in western India. Geological Magazine. 2016c;**154**(4):875-887

[19] Mandal P, Rastogi BK, Satyanarayana HVS, Kousalya M, Vijayraghavan R, Satyamurty C, Raju IP, Sarma ANS, Kumar N. Characterization of the causative fault system for the 2001 Bhuj earthquake of Mw 7.7. Tectonophysics. 2004;**378**:105-121

[20] Kayal JR, De R, Ram S, Sriram BV, Gaonkar SG. Aftershocks of 26th January Bhuj earthquake in western India and its seismotectonic implication. Journal Geological Society of India. 2002;**59**:395-418

[21] Singh AP, Mishra OP, Rastogi BK, Kumar D. 3-D seismic structure of the Kachchh, Gujarat and its implications for the earthquake hazard mitigation. Natural Hazards. 2011;**57**:83-105

[22] Bodin P, Horton S. Source parameters and tectonic implications of aftershocks of the M 7.6 Bhuj earthquake of 26 January 2001. Bulletin of the Seismological Society of America. 2004;**94**:818-827

[23] Kothyari GC, Rastogi BK, Morthekai P, Dumka RK. Landform development in a zone of active Gedi fault, eastern Kachchh Rift Basin, western India. Tectonophysics. 2016b; **670**:115-126

[24] Bhattacharya F, Rastogi BK, Kothyari GC. Morphometric evidences of seismicity around Wagad and Gedi faults, eastern Kachchh, Gujarat. Journal of the Geological Society of India. 2013;**81**:113-121

[25] Kothyari GC, Rastogi BK, Morthekai P, Dumka RK, Kandregula RS. Active segmentation assessment of the tectonically active south Wagad fault in Kachchh, western peninsular India. Geomorphology. 2016a;**253**:491-507

[26] Biswas SK. Landscape of Kutch—A morphotectonic analysis. Indian Journal of Earth Sciences. 1974;**1**(2):177-190

[27] Mandal P, Satyamurty C, Raju IP. Iterative de-convolution of the local waveforms: Characterization of the seismic sources in Kachchh, India. Tectonophysics. 2009;**478**: 143-157

[28] Molin P, Pazzaglia FJ, Dramis F. Geomorphic expression of active tectonics in a rapidly deforming forearc, Sila massif, Calabria, southern Italy. American Journal of Science. 2004;**304**:559-589

[29] Duncan C, Masek J, Fielding E. How steep are the Himalaya? Characteristics and implications of along-strike topographic variations. Geology. 2003;**31**:75-78

[30] Ponza A, Pazzaglia FJ, Picotti V. Thrust-fold activity at the mountain front of the northern Apennines (Italy) from quantitative landscape analysis. Geomorphology. 2010;**123**: 211-231

[31] Andreani L, Gloaguen R. Geomorphic analysis of transient landscapes in the sierra Madre de Chiapas and Maya Mountains (northern central America): Implications for the north American–Caribbean–Cocos plate boundary. Earth Surface Dynamics. 2016;**4**:71-102

[32] Keller EA, Pinter N. Active Tectonics. Earthquake, Uplift, and Landscape. New Jersey: Prentice Hall; 2002. p. 362

[33] Troiani F, Troiani M, Della S. The use of the stream length-gradient index in morphotectonic analysis of small catchments: A case study from Central Italy. Geomorphology. 2008;(1):159-168

[34] Hack J. Drainage adjustment in the Appalachians. In: Morisawa M, editor. Fluvial Geomorphology. London: George llen and Unwin; 1973. pp. 51-69

[35] Merrits D, Vincent KR. Geomorphic response of coastal streams to low, intermediate, and high rates of uplift, Mendocino triple junction region, northern California. Geological Society of America Bulletin. 1989;**101**:1373-1388

[36] Flint JJ. Stream gradient as a function of order, magnitude, and discharge. Water Resources Research. 1974;**10**:969-973

[37] Goldrick G, Bishop P. Regional analysis of bedrock streamlong profiles: Evaluation of Hack's SL form, and formulation and assessment of an alternative (the DS form). Earth Surface Processes and Landforms. 2007;**32**(5):649-671

[38] Whipple KX, Di-Biase RA, Crosby BT. Bedrock Rivers. Treatise on Geomorphology. 2013;**9**:550-570

[39] Strahler AN. Hypsometric (area-altitude) analysis of erosional topography. Geological Society of America Bulletin. 1952;**63**:1117-1142

[40] Menéndez I, Silva PG, Martín-Betancor M, Pérez-Torrado FJ, Guillou H, Scaillet S. Fluvial dissection, isostatic uplift, and geomorphological evolution of volcanic islands (gran Canaria, Canary Islands, Spain). Geomorphology. 2008;**102**:189-203

[41] Bull WB, McFadden LD. Tectonic geomorphology north and south of the Garlock fault, California. In: Doehering DO, editor. Geomorphology in Arid Regions. Proceedings at the Eighth Annual Geomorphology Symposium. Binghamton, NY: State University of New York; 1977. pp. 115-138

[42] Pérez-Peña JV, Azor A, Azañón JM, Keller EA. Active tectonics in the sierra Nevada (Betic cordillera, SE Spain): Insights from geomorphic indeces and drainage pattern analysis. Geomorphology. 2010;**119**:74-87

[43] Ramírez-Herrera MT. Geomorphic assessment of active tectonics in the Acambay Graben, Mexican volcanic belt. Earth Surface Processes and Landforms. 1998;**23**:317-332

[44] Malik JN, Nakata T. Active faults and related late quaternary deformation along the northwestern Himalayan frontal zone, India. Annales de Geophysique. 2003;**46**(5):917-936

[45] Matsuda T. Active Fault Assessment for Irozaki Fault System, Izu Peninsula. Report on the Earthquake of the Izu Peninsula. 1975;**38**:409p

[46] Bull WB. Tectonic Geomorphology of Mountains: A New Approach to Paleoseismology. Malden: Blackwell; 1977

[47] Matsuda T. Strike-Slip Faulting along the Atera Fault, Japan. Univ. Tokyo Earthq. Res. Inst. Bull. vol. 44; 1966. pp. 103-111

[48] Azor A, Keller EA, Yeats RS. Geomorphic indicators of active fold growth: South Mountain, oak ridge anticline, Ventura basin, southern California. Geological Society of America Bulletin. 2002;**114**:745-753

[49] Rockwell TK, Keller EA, Johnson DL. Tectonic geomorphology of alluvial fans and mountain fronts near Ventura, California. In: Morisawa M, editor. Tectonic Geomorphology. In: Proceedings of the 15th Annual Geomorphology Symposium. Boston: Allen and Unwin Publishers; 1985. pp. 183-207

[50] Silva PG, Goy JL, Zazo C, Bardají T. Fault generated mountain fronts in Southeast Spain: Geomorphologic assessment of tectonic and seismic activity. Geomorphology. 2003;**50**:203-225

[51] Singh AP, Zhao L, Kumar S, Mishra S. Inversions for earthquake focal mechanisms and regional stress in the Kachchh rift basin, western India: Tectonic implications. Journal of Asian Earth Sciences. 2016b;**117**:269-283

[52] Hurtrez JE, Lucazeau F, Lave J, Avouac JP. Investigation of the relationships between basin morphology, tectonic uplift, anddenudation from the study of an active fold belt in the Siwalik Hills, Central Nepal. Journal of Geophysical Research: Solid Earth. 1999;**104**:12779-12796

[53] Pérez-Peña JV, Azañón JM, Booth-Rea G, Azor A, Delgado J. Differentiating geology and tectonics using a spatial autocorrelation technique for the hypsometric integral. Journal of Geophysical Research. 2009;**114**. DOI: 10.1029/2008JF001092

[54] Chen YC, Sung Q, Cheng KY. Along-strike variations of morphotectonic features in the western foothills of Taiwan: Tectonic implications based on stream-gradient and hypsometric analysis. Geomorphology. 2003;**56**:109-137

[55] Wells DL, Coppersmith KJ. New empirical relationships among magnitude, rupture length, rupture width, rupture area, and surface displacement. Bulletin of the Seismological Society of America. 1994;**84**:974-1002

[56] Johnston AC. Seismotectonic Interpretations and Conclusions from the Stable Continental Regions. The Earthquakes of Stable Continental Regions: Assessment of Large Earthquake Potential. Palo Alto: Electric Power & Research Institute; 1994. Report TR 10261 Ch.3

[57] Kothyari GC, Rastogi BK, Dumka RK, Chauhan M. Secondary surface deformation along the Bharudia/north Wagad fault zone in Kachchh Rift Basin, western India. Comunicações Geológicas. 2015;**102**(1):15-27

[58] Mishra OP, Singh AP, Rastogi BK. An insight crack density, saturation rate, and porosity model of the 2001 Bhuj earthquake in the stable continental region of western India. Journal of Asian Earth Sciences. 2014;**83**:48-59

[59] Singh AP, Mishra OP. Seismological evidence for monsoon induced micro to moderate earthquake sequence beneath the 2011 Talala, Saurashtra earthquake, Gujarat, India. Tectonophysics. 2015;**611**:38-48

[60] Graveleau F, Strak V, Dominguez S, Malavieille J, Manighetti I, Petit C. Experimental modelling of tectonics–erosion–sedimentation interactions in compressional, extensional, and strike–slip settings. Geomorphology. 2015. DOI: 10.1016/j.geomorph.2015.02.011

[61] Coward MP. Continental collision. In: Hancock PL, editor. Inversion Tectonics. New York: Pergamon Press; 1994. pp. 289-304

[62] Scisciani V. Styles of positive inversion tectonics in the central Apennines and in the Adriatic foreland: Implications for the evolution of the Apennine chain (Italy). Journal of Structural Geology. 2009;**31**:1276-1294

[63] Malik JN, Gadhavi MS, Kothyari GC, Sathuluri S. Paleo-earthquake signatures from the south Wagad fault (SWF), Wagad Island, Kachchh, Gujarat, western India: A potential seismic hazard Journal of Structural Geology. 2017;**95**:142-159

[64] Naylor MA, Mandl G, Sijpesteijn CHK. Fault geometries in basement-induced wrench faulting under different initial stress states. Journal of Structural Geology. 1986;**8**:737-752

[65] Tchalenko JS. Similarities between shear zones of different magnitudes. Geological Society of America Bulletin. 1970;**81**:1625-1640

[66] Harding TP. Seismic characteristics and identification of negative flower structures, positive flower structures, and positive structural inversion. AAPG Bulletin. 1985;**69**(4): 582-600

[67] Sylvester AG. Strike-slip faults. Geological Society of America Bulletin. 1988;**100**:1666-1703

[68] Guerroue EL, Cobbold PR. Influence of erosion and sedimentation on strike slip fault system: Insights from analogue model. Journal of Structural Geology. 2006;**28**:421-430

[69] Vendeville B, Cobbold PR. How normal faulting and sedimentation interact to produce listric fault profiles and stratigraphic wedges. Journal of Structural Geology. 1988;**10**:649-659

[70] Barrier L, Nalpas T, Gapais D, Proust JN, Casas AM, Bourquin S. Influence of syntectonic sedimentation on thrust geometry. Field examples from the Iberian chain (Spain) and analogue modelling. Sedimentary Geology. 2002;**146**(1-2):91-104

[71] Cobbold PR, Davy P, Gapais D, Rossello EA, Sadybakasov E, Thomas JC, Tondji Biyo JJ, De Urreiztieta M. Sedimentary basins and crustal thickening. Sedimentary Geology. 1993;**86**:77-89

[72] Davy P, Cobbold PR. Experiments on shortening of a 4-layer model of the continental lithosphere. Tectonophysics. 1991;**188**(1-2):1-25

[73] Persson KS, Sokoutis D. Analogue models of orogenic wedges controlled by erosion. Tectonophysics. 2002;**356**:323-336

[74] Storti F, McClay K. Influence of syntectonic sedimentation on thrust wedges in analogue models. Geology. 1995;**23**:999-1002

[75] Tondji Biyo JJ. Chevauchements et basins compressifs influence de l'erosion et de la sedimentation. Modelisation analogique et exemples naturels. Memoires de Geosciences-Rennes. 1995;**59**:1-411

[76] Mandal M, Horton S. Relocation of aftershocks, focal mechanisms and stress inversion: Implications toward the seismotectonics of the causative fault zone of Mw 7.6 2001 Bhuj earthquake (India), Tectonophysics. 2007;**429**:61-78

[77] Bisht RS. Major earthquake occurrences in archaeological strata of Harappan settlement at Dholavira (Kachchh, Gujarat) (abstract). In: International Symposium on the 2001 Bhuj Earthquake and Advances in Earthquake Science (AES-2011), Gandhinagar. 2011. pp. 22-24

[78] Gaur AS, Vora KH, Sundaresh RMM, Jayakumar S. Was the Rann of Kachhh naviagable during the Harappan times (mid-Holocene)? An archaeological perspective. Current Science. 2013;**105**(11):1485-1491

[79] Kovach RL, Grijalva K, Nur A. **earthquakes and civilizations of the Indus Valley: A challenge for archaeoseismology. In: Sintubin M, Stewart IS, Niemi TM, Altunel E, editors. Ancient Earthquakes: Geological Society of America Special Paper. 471. 2010. pp. 119-127

[80] Rastogi BK, Choudhury P, Dumka RK, Sreejith KM, Majumdar TJ. Stress pulse migration by viscoelastic process for long-distance delayed triggering of shocks in Gujarat, India, after the 2001 Mw 7.7 Bhuj earthquake. American Geophysical Union. 2012;**196**:63-73

[81] Dumka RK, Rastogi BK, Chodhury P, Kumar P, Prajapati S. Crustal Deformation Studies by GPS Measurements. ISR Annual Report; 2015. pp 64-66

[82] Chinnery MA. Earthquake magnitude and source parameters. Bulletin of the Seismological Society of America. 2003;**59**:1969-1982

[83] Tocher D. The Alaska earthquake of July 10, 1958-movement on the fairweather fault and field investigation of southern epicentral region. Bulletin of the Seismological Society of America. 1960;**50**:267-292

[84] Coppersmith KJ. Seismic source characterization for engineering seismic hazard analysis. In: Proc. 4th International Conference on Seismic Zonation. Vol. I. Oakland, California: Earthquake Engineering Research Institute; 1991. pp. 3-60

[85] Schwartz DP, Coppersmith KJ. Seismic Hazards New Trends in Analysis Using Geologic Data, in Active Tectonics. Washington, D.C.: National Academy Press; 2009. pp. 215-230

[86] Johnston AC, Kanter LR. Earthquakes in stable continental crust. Scientific American. 1990;**262**:68-75

[87] Seidl MA, Dietrich WE, Kirchner JW. Longitudinal profile development into bedrock: An analysis of Hawaiian channels. Journal of Geology. 1994;**102**:457-474

[88] Stock JD, Montgomery DR. Geologic constraints on bedrock river incision using the stream power law. Journal of Geophysical Research. 1999;**104**(B3):4983-4993

[89] Weissel JK, Seidl MA. Inland propagation of erosional escarpments and river profile evolution across the southeast Australian passive continental margin. In: Tinkler KJ, Wohl EE, editors. Rivers over Rock: Fluvial Processes in Bedrock Channels. Geophysical Monograph. Vol. 107. 1998. pp. 189-206

Edited by Evgenii V. Sharkov

This book is devoted to different aspects of tectonic researches. New results and interpretations are presented here for diverse tectonic settings. Most of the chapters include up-to-date materials of detailed geological investigations, often combined with geophysical data, which can help understand more clearly the essence of mechanisms of different tectonic processes.

Some chapters are devoted to the tectonic evolution of regions (East Antarctica, East Kazakhstan, Mongolo-Okhotsk orogenic belt), and others have dealt with the different aspects of tectonic events: influence of detachment structural deformation on pore structure evolution in shales, evolution of drainage in response to brittle-ductile dynamics and surface processes, soft sediment deformation structures triggered by the modern earthquakes, and post-opening deformation history of the Japan Sea back-arc basin.

Published in London, UK

IntechOpen

ISBN 978-1-83881-296-6